Springer Series in Light Scattering

Alexander Kokhanovsky *Editor*

Springer Series in Light Scattering

Volume 5: Radiative Transfer, Remote Sensing, and Light Scattering

Springer

Springer Series in Light Scattering

The main purpose of ***SPRINGER Series in Light Scattering*** is to present recent advances and progress in light scattering media optics. The topic is very broad and incorporates such diverse areas as atmospheric optics, ocean optics, optics of close-packed media, radiative transfer, light scattering, absorption, and scattering by single scatterers and also by systems of particles, biomedical optics, optical properties of cosmic dust, remote sensing of atmosphere and ocean, etc. The topic is of importance for material science, environmental science, climate change, and also for optical engineering. Although main developments in the solutions of radiative transfer and light scattering problems have been achieved in the 20th century by efforts of many scientists including V. Ambartsumian, S. Chandrasekhar, P. Debye, H. C. van de Hulst, G. Mie, and V. Sobolev, the light scattering media optics still have many puzzles to be solved such as radiative transfer in closely packed media, 3D radiative transfer as applied to the solution of inverse problems, optics of terrestrial and planetary surfaces, etc. Also it has a broad range of applications in many branches of modern science and technology such as biomedical optics, atmospheric and oceanic optics, and astrophysics, to name a few. It is planned that the Series will raise novel scientific questions, integrate data analysis, and offer new insights in optics of light scattering media.

More information about this series at http://www.springer.com/series/15365

Alexander Kokhanovsky
Editor

Springer Series in Light Scattering

Volume 5: Radiative Transfer, Remote Sensing, and Light Scattering

Springer

Editor
Alexander Kokhanovsky
VITROCISET Belgium
A Leonardo Company
Darmstadt, Germany

ISSN 2509-2790 ISSN 2509-2804 (electronic)
Springer Series in Light Scattering
ISBN 978-3-030-38695-5 ISBN 978-3-030-38696-2 (eBook)
https://doi.org/10.1007/978-3-030-38696-2

This Springer imprint is published by the registered company Springer Nature Switzerland AG
The registered company address is: Gewerbestrasse 11, 6330 Cham, Switzerland

Contents

Contributors

Jerzy Cierniewski Department of Soil Science and Remote Sensing of Soils, Adam Mickiewicz University, Poznań, Poland

André Ehrlich Leipzig Institute for Meteorology (LIM), University of Leipzig, Leipzig, Germany

Mark Flanner Department of Climate and Space Sciences and Engineering, University of Michigan, Ann Arbor, MI, USA

Cenlin He Advanced Study Program and Research Applications Laboratory, National Center for Atmospheric Research (NCAR), Boulder, CO, USA

Aleksey Malinka Institute of Physics, National Academy of Sciences of Belarus, Minsk, Belarus

Hajime Okamoto Research Institute for Applied Mechanics, Kyushu University, Kasuga, Fukuoka, Japan

Elena Ruiz-Donoso Leipzig Institute for Meteorology (LIM), University of Leipzig, Leipzig, Germany

Kaori Sato Research Institute for Applied Mechanics, Kyushu University, Kasuga, Fukuoka, Japan

Michael Schäfer Leipzig Institute for Meteorology (LIM), University of Leipzig, Leipzig, Germany

Manfred Wendisch Leipzig Institute for Meteorology (LIM), University of Leipzig, Leipzig, Germany

Application of Single and Multiple-Scattering Theories to Analyses of Space-Borne Cloud Radar and Lidar Data

Kaori Sato and Hajime Okamoto

1 Introduction

The possibility of generating an instrument for "light amplification by stimulated emission of radiation (LASER)" was proposed by Schalow and Townes (1958) and further realized by Maiman (1960) and by Javan et al. (1961), after pioneering works by e.g., Einstein (1917), V. A. Fabricant, C. H. Towns, N. G. Basov and A. M. Prokhorov (Townes 1999; Lukishova 2010; Gordon et al. 1954, 1955). For applications related to atmospheric physics, light detection and ranging (lidar) systems have been widely used to study aerosols and clouds from both ground and space (Winker 1996; Spinhirne et al. 2005; Winker et al. 2007). Observations of noctilucent clouds and planetary dust were made by Fiocco and Smulin (1963) by ground-based lidar. Scotland et al. (1971) conducted field experiments on the depolarization ratio of clouds. Lhermite (1987) observed clouds and precipitation using 94 GHz Doppler cloud radar (radiowave detection and ranging). Lidar and cloud radar provide valuable information on cloud microphysics and in-cloud vertical motion, which are critical parameters related to clouds in climate models (Tsushima et al. 2006; Satoh and Matsuda 2009; Sato et al. 2010; Gettelman and Sherwood 2016). Today, combined observations from lidar onboard the Cloud-Aerosol Lidar and Infrared Pathfinder Satellite Observations (CALIPSO) satellite and cloud profiling radar onboard CloudSat provide global distributions of aerosols, clouds, and precipitation (Winker et al. 2010; Stephens et al. 2018, and references therein). Such instruments will also be carried on future missions, including the Earth Clouds, Aerosols and Radiation Explorer (EarthCARE) (Illingworth et al. 2015 and references therein).

K. Sato (✉) · H. Okamoto
Research Institute for Applied Mechanics, Kyushu University, Kasuga, Fukuoka 816-8580, Japan
e-mail: sato@riam.kyushu-u.ac.jp

H. Okamoto
e-mail: okamoto@riam.kyushu-u.ac.jp

A. Kokhanovsky (ed.), *Springer Series in Light Scattering*,
Springer Series in Light Scattering,
https://doi.org/10.1007/978-3-030-38696-2_1

Many particles, such as ice cloud particles, snow, and aerosols are irregular in shape. At present, precise methods for obtaining single scattering properties of non-spherical particles over the entire size range of interest do not exist, and it is often necessary to rely on approximate approaches. Single scattering occurs when the separation between particles is sufficiently large that the scattering property of each particle can be added to represent that of the assemblage of particles. In many cases, conventional ground-based lidar and radar returns from aerosols and hydrometeors can be applied to the first-order multiple scattering approximation (Ishimaru 1997), which considers line-of-site two-way attenuation and single backscattering. This method can be employed depending upon receiver footprint size and the sensitivity limit of the sensor. As particle density increases and the receiver footprint size at the target position becomes larger than the mean scattering path of the scatterers, multiple scattering processes become important and efforts have been made to solve the time-dependent radiative transfer equation (Bissonnette 2005; Battaglia et al. 2010). When using data from lidar and high-frequency radar on space-borne missions for cloud and precipitation studies, these conditions are often met. However, analytical solutions are found under limited conditions, so the Monte Carlo method is widely used, despite being computationally inefficient for inversions. Characterization of single scattering properties of irregular particles and the treatment of multiple scattering effects on observable quantities are important issues for accurate inversion of cloud microphysics from active space-borne sensors.

This chapter is organized as follows. Single scattering theory for irregular particles at the wavelengths of lidar and radar is reviewed in Sect. 2. With the development of non-spherical light scattering theories, detailed analyses of ice crystal shape and orientation have become possible from lidar (Iwasaki and Okamoto 2001; Borovoi et al. 2012) and from its synergy with cloud radar (Okamoto et al. 2003, 2010; Sato and Okamoto 2011). In Sect. 3, application of this method to the CloudSat and CALIPSO satellites is further discussed. In Sect. 4, we discuss simulation methods for the inversion of cloud properties from the attenuated backscattering coefficient and depolarization ratio of space-borne lidars under multiple scattering conditions, as well as observations of lidar multiple scattering and introduce the example of multiple backscattered return from clouds with ground-based multiple-field-of-view (MFOV) multiple-scattering polarization lidar (MFMSPL; Okamoto et al. 2016). Finally, the paper is summarized in Sect. 5.

2 Single Scattering Properties of Cloud Particles

Mie theory has wide applicability. For a homogenous sphere, the scattering properties are estimated to be a function of particle size, the complex refractive index, and the wavelength of the incident electromagnetic wave. For non-spherical particles, no perfect scattering theory currently exists. The response of the particle to electromagnetic waves is determined by solving the Maxwell equations considering the particle boundary condition. Exact analytical solutions are possible for extremely

limited geometries, e.g., homogeneous spheres, spheroids, infinite cylinders, and aggregated spherical particles (Bohren and Huffman, 1983). Therefore, scattering from particles with arbitrary shapes is estimated using approximation methods. The applicability of these methods depends on the size parameter X of interest. For small ones (X < 50), numerical scattering methods such as the discrete dipole approximation (DDA; Draine 1988), T-matrix (Mishchenko 1993), and finite difference time domain (FDTD; Yang and Liou 1996) methods are popular. DDA is widely used in astronomy (Draine 1988), planetary sciences (e.g., West 1991; Okamoto et al. 1994), and atmospheric sciences (e.g., Flatau et al. 1990; Evans and Vivekanandan 1990; Dungey and Bohren 1993; Okamoto et al. 1995; Lemke and Quante 1999). When the size parameter is large, numerical simulations such as DDA are impractical and geometric optics (GO)-based methods such as the physical optics (PO) approach are applied (Borovoi 2013). In the following sections, we focus on PO and DDA as two major approaches that are considered effective for application to non-spherical cloud particles at the wavelengths of lidar and radar.

2.1 Discrete Dipole Approximation; DDA

DDA originated from Purcell and Pennypacker (1973), to study scattering from interstellar dust grains, and from Draine (1988), who extended the theory and developed the theoretical basis of DDA. DDA is easily applicable to any target geometry. In DDA, the target is approximated with N cubic sub-volume elements, and then each element is replaced with an electric dipole characterized by dipole polarizability, α. Differences among substances are expressed as α, which reflects the complex refractive index of the particle. Many methods have been proposed to determine α (Draine and Goodman 1993). Draine (1988) extended the estimation of α by introducing a radiative reaction correction term to the Clausius-Mossotti relation (CMRR). Other methods have also been proposed, such as the digitized Green's function approach or the volume integral equation formulation (DGF/VIEF; Liversay and Chen 1974; Goedecke and O'Brien 1988 and Hage and Greenberg 1990) and the lattice dispersion relation (LDR; Draine and Goodman 1993). In a comparison of various approaches, LDR was superior to CMRR and DGF/VIEF for the same number of dipoles (Draine and Goodman 1993; Okamoto 1995). DDAs with different α values generally have the same accuracy at the zero-frequency limit (Okamoto and Xu 1998).

Each of the N dipole elements is exposed not only to the incident field $\mathbf{E_{inc}}$ but also to the field generated by other elements. Therefore, retardation effects must be fully considered. The dipole moments $\mathbf{P}$ are calculated as,

$$\mathbf{P_j} = \alpha_j \left(\mathbf{E_{inc},}_j - \sum_{k \neq j}^{N} \mathbf{A}_{jk} \mathbf{P}_k \right) \quad (\mathrm{j} = 1, 2, \ldots, \mathrm{N}) \tag{1}$$

The second term represents the field from other elements that are excited by the incident field and can be rewritten as follows (Draine 1988),

$$\mathbf{A_{jk}P_k} = \frac{\exp(\mathrm{ikr}_{jk})}{\mathrm{r}_{jk}^3}\left\{\mathrm{k}^2\mathbf{r}_{jk}\times\left(\mathbf{r}_{jk}\times\mathbf{P_k}\right)+\frac{1-\mathrm{ikr}_{jk}}{\mathrm{r}_{jk}^2}\times\left[\mathrm{r}_{jk}^2\mathbf{P_k}-3\mathbf{r}_{jk}(\mathbf{r}_{jk}\cdot\mathbf{P_k})\right]\right\} \tag{2}$$

$\mathbf{A}_{jk}$ is the jk element of a 3 N × 3 N complex matrix **A,** $\mathbf{r}_{jk}$ is the distance between the jth and kth dipole, $\mathbf{r}_{jk} \equiv \mathbf{r}_j - \mathbf{r}_k$, $\mathrm{k} = 2\pi/\lambda$ and λ is the wavelength. Equation (1) includes 3 N unknowns, based on the components of the dipole moments. Because the incident field and the polarizability are known, the solution to Eq. (1) can be obtained by solving 3N independent equations. The scattering and absorption properties are derived from the sum of the fields generated by each dipole. The scattering cross-section $\mathrm{C_{sca}}$ can be obtained as follows (Draine 1988),

$$C_{sca} = \frac{\mathrm{k}^4}{|\mathbf{E_{inc}}|^2}\int d\Omega\left|\sum_{j=1}^{N}\mathbf{P_j}-\hat{\mathbf{n}}\left(\hat{\mathbf{n}}\cdot\mathbf{P_j}\right)\exp\left(-\mathrm{ik}\hat{\mathbf{n}}\cdot\mathbf{r_j}\right)\right|^2 \tag{3}$$

Ω and **n** are solid angle and unit vector in the scattering direction, respectively.

The accuracy of the DDA approximation has been examined using spherical particles, two cluster spheres (Draine and Flatau 1994) for which exact solutions can be obtained, and for hexagonal particles (Okamoto 2002). The applicability of the method can be described as a function of the complex refractive index m, wave number k, and the smallest separation distance among dipoles located in the cubic lattice d (lattice spacing). For angular dependent scattering properties, especially for backscattering coefficient with random orientation, this is (Okamoto 2002),

$$2\pi\frac{d}{\lambda}|m| < 0.5 \tag{4}$$

Generally, the computation time of the DDA increases with increasing N. For particles with large values of X, sufficiently larger N must be used. When the particle has a random orientation with respect to the incident electromagnetic wave, the computation time increases. Mainly due to its high memory requirements and long computational time, the applicability of this theory is practically limited to smaller X (<about 50). In the DDA, magnetic dipoles and high-order terms such as electric quadrupoles are ignored. The accuracy of DDA that neglects high-order terms was reported in detail by Okamoto et al. (1995).

To handle large X values with low computational cost, Okamoto (1995) developed the a_1-term method, which is suitable for calculating the scattering properties of clusters of spherical monomers. The $\mathrm{a_1}$-term procedure is a modification of the DDA method wherein each monomer is replaced by a dipole with α determined from the first scattering coefficient term of Mie theory (i.e., the $\mathrm{a_1}$-term) (Okamoto 1995).

$$\alpha = i\frac{3a_1}{2k^3}, \tag{5}$$

where

$$a_1 = \frac{m\psi_1(mX_m)\psi_1'(X_m) - \psi_1(X_m)\psi_1'(mX_m)}{m\psi_1(mX_m)\xi_1'(X_m) - \xi_1(X_m)\psi_1'(mX_m)} \tag{6}$$

The a_1-term depends on the complex refractive index m, the size parameter of the monomer X_m, and is also a function of the first terms of the Riccati-Bessel functions ψ_1 and ξ_1 and their derivatives (Okamoto and Xu 1998).
Fuller (1991), Mackowski (1991), and Xu (1995, 2001) explored rigorous analytic solutions for clusters of spherical monomers, referred to as modal analyses. Modal analyses can be applied to particles with components of isotropic and homogeneous spherical monomers that are similar to or larger than the wavelength and have different compositions. The accuracy of the a_1-term method tested against modal analyses revealed that the a_1-term method is applicable to clusters with total size parameters exceeding $X \sim 100$ with $N \sim 10^6$ dipoles (Okamoto and Xu 1998). The maximum size parameter of the monomers in the cluster is 1.

Because the component elements do not need to be further divided when using the a_1-term method, the scattering properties of fractals can be determined efficiently. Okamoto (1995) applied the a_1-term method to ballistic cluster-cluster aggregates (BCCAs) and ballistic particle-cluster aggregates (BPCAs). The scattering properties of BPCAs and BCCAs can be obtained using the a_1-term method when the components of the target are smaller than the wavelength of the electromagnetic wave (Okamoto 1995). Kimura et al. (2002) used the a_1-term method to estimate radiation pressure and the Poynting–Robertson effect to study the evolution of the trajectories of interplanetary dust aggregates in the solar system. Moteki (2016) proposed a hybrid method combining the monomer dipole approach and the original DDA. The magnetic dipole of the monomer (Mullholland et al. 1994) was considered for application to atmospheric aerosols containing black carbon monomers. Ishimoto (2008) used the FDTD method for fractal snowflakes (Maruyama and Fujiyoshi 2005) with the Maxwell–Garnett mixing rule to estimate the refractive index of the ice–air mixture for a lattice where the range of size parameters falls within the Rayleigh regime.

2.2 *Scattering Theory Based on Geometric Optics: Physical Optics*

When exact numerical simulation of the Maxwell equation is not practical for large size parameters, an approximation theory called geometric optics (GO) is widely used. Physical optics (PO) approximation extends the GO approach by accounting for the wave properties of light (Borovoi 2013).

In GO approximation, the incident electric fields on different parts of the particle do not interact with each other and behave independently. The incident wave undergoes reflection and refraction within the particle. Some rays are internally reflected and others are transmitted outside the particle according to the reflectance and transmittance values determined from Fresnel equations. To account for these processes, the electromagnetic wave is often approximated as rays using the ray-tracing technique based on the Monte Carlo method (Macke et al. 1996). In the conventional GO approach (GOM1), it is assumed that the scattering cross section of diffraction is equal to the geometrical cross section of the particle so that the total extinction efficiency equals 2 (Macke et al. 1996; Cai and Liou 1982).The differential scattering cross section at scattering angle θ from the transmitted and reflected components of the ray are estimated and the diffraction term are added to obtain the total differential scattering cross section at scattering angle θ.

In the backscattering direction, GO suffers from convergence (Iwasaki and Okamoto 2001; Borovoi et al. 2005, 2012) and thus has limited applicability for lidar. The backscattering cross-section C_{bk} is estimated as,

$$C_{bk} \cong 4\pi \left. \frac{\Delta C_{sca}(\theta)}{\Delta \Omega} \right|_{\Delta\Omega \to 0, \theta \cong 180^\circ} \tag{7}$$

where θ and Ω are the scattering and solid angles, respectively (Okamoto and Sato 2018a). In reality, when ΔΩ becomes small, the light scattered at ~ 180° decreases, and C_{bk} will converge. However, C_{bk} diverges as $\Delta\Omega \to 0^\circ$ at ~ 180° for the GO method (Iwasaki and Okamoto 2001), and the differential cross-section cannot always be obtained.

For application of PO to specific cases, Iwasaki and Okamoto (2001) considered Kirchhoff's diffraction theory to estimate backscattering from large non-spherical ice particles. Based on this theory, when the size parameter is sufficiently large and the particle is a cuboid, C_{bk} can be obtained analytically (Iwasaki and Okamoto 2001). For the horizontal orientation studied in Iwasaki and Okamoto (2001), C_{bk} was a few orders of magnitude larger than that of a mass-equivalent sphere, providing theoretical evidence of the frequently observed specular reflection phenomenon in lidar data (Platt 1978). Mishchenko et al. (1997) found that a similar tendency of high lidar backscattering can be obtained from a thin circular disk.

Borovoi et al. 2012 extended the approach based on PO to general particle geometry and orientation. In this method, the particle geometry consists of flat surfaces, and electromagnetic waves inside the particle are subjected to GO approximation to estimate the electric field at the surface of the polygon. The electric field generated by the polygon surface is derived analytically (Heffels et al. 1995). Scattering outside of the particle is estimated via diffraction according to the electric field at the polygon surface. The contributions from refraction and reflection estimated using GO and that from diffraction were treated appropriately, and therefore the singularities present in quantities dependent on scattering angles, such as the differential scattering cross-section, could be avoided. Konoshonkin et al. (2017) investigated

the computational accuracy of this method against FTDT. A similar approach was developed by Yang and Liou (1996), called the geometrical optics-integral equation model (GOM2), which allows the electric field at the particle surface to be estimated numerically. The numerical efficiency of GOM2 was further improved by Masuda et al. (2012). Because these methods fully incorporate the wave properties of light, they can be expected to play a role in bridging the gap in the size parameter range of 50 < X< 200 (Masuda et al. 2012).

To apply scattering theories to lidar, Borovoi et al. 2012 investigated lidar backscattering from the CALIPSO configuration for horizontally oriented ice plates; Bi et al. (2009) did the same for randomly oriented hexagonal columns and plates through an improved geometric optics method (IGOM). The depolarization ratios at 532 nm and 1064 nm wavelengths have been studied using Voronoi aggregates and hexagonal columns with the geometric optics integral equation (GOIE; Masuda and Ishimoto 2017). The laser tilt angle dependence of scattering properties has been investigated for quasi 2D oriented ice plates theoretically (Borovoi et al. 2012; Okamoto et al. 2012, 2019b) for the CALIPSO configuration.

3 Application of Scattering Theories to Analyze Lidar and Cloud Radar Data

3.1 Backscattering Properties of Cloud Particles at Lidar and Radar Wavelengths

The nonattenuated radar reflectivity factor $Z_{e,true}$ and lidar backscattering coefficient β_{true} are determined as follows,

$$Z_{e,true} = \frac{\lambda^4}{\pi^5 |K(\lambda)|^2} \int_{r_{min}}^{r_{max}} C_{bk,ra}(r_{eq}) \frac{dn(r_{eq})}{dr_{eq}} dr_{eq} \tag{8}$$

$$\beta_{true} = \frac{1}{4\pi} \int_{r_{min}}^{r_{max}} C_{bk,li}(r_{eq}) \frac{dn(r_{eq})}{dr_{eq}} dr_{eq} \tag{9}$$

r_{eq} is the radius of a mass-equivalent sphere. The backscattering cross-sections at the radar $C_{bk,ra}$ and lidar $C_{bk,li}$ wavelengths can be obtained through DDA and PO for nonspherical particles and from Mie theory for spherical particles. K is generally a function of the complex refractive index m of water at the radar wavelength, i.e., $|K(\lambda)| = \left|(m^2 - 1)/(m^2 + 2)\right|$. Effective radius is defined here as,

$$r_{eff} = \int_{r_{\min}}^{r_{\max}} r_{eq}^3 \frac{dn(r_{eq})}{dr_{eq}} dr_{eq} \Big/ \int_{r_{\min}}^{r_{\max}} r_{eq}^2 \frac{dn(r_{eq})}{dr_{eq}} dr_{eq} \tag{10}$$

For the size distribution of ice cloud particles, a modified gamma distribution is commonly used (Petty and Huang 2011, Stephens et al. 1990).

$$\frac{dn(r_{eq})}{dr_{eq}} = \frac{N_o}{\Gamma(p) r_m} \left(\frac{r_{eq}}{r_m}\right)^{p-1} \exp\left(-\frac{r_{eq}}{r_m}\right) \tag{11}$$

N_o, r_m, and p are the total number of cloud particles per unit volume, characteristic radius, and dispersion of the distribution, respectively (Okamoto et al. 2003). $Z_{e,true}$ is reportedly insensitive to variation in p from 1 to 4 for spheres when r_{eq} ranging from 1 to 1000 μm is considered in Eq. (8) (Sato and Okamoto 2006). For cloud droplets, a log-normal size distribution has also been used in the past (e.g., Frisch et al. 1995),

$$\frac{dn(r_{eq})}{dr_{eq}} = \frac{N_o}{\sqrt{2\pi} r_{eq} \ln \sigma} \exp\left(-\frac{\left(\ln(r_{eq}/r_o)\right)^2}{2(\ln \sigma)^2}\right) \tag{12}$$

r_o and σ are the mode radius and standard deviation of the distributions, respectively. Lidar and radar observations depend on the ice particle size (r_{eff}), number concentration or ice water content (IWC), particle shape, and orientation. Figure 1 shows the calculated $Z_{e,true}$ and β_{true} for ice and water. For ice, spherical ice and a perfectly oriented 2D plate are shown. For cloud radar, the nonsphericity effect on Z_e is within about 3 dB when $r_{eff} < 100$ μm, while particle shape and orientation must be considered at larger r_{eff} (Sato and Okamoto 2006). The effects of nonsphericity have a large impact on β_{true} with small r_{eff}. $Z_{e,true}$ and β_{true} values for 2D ice are larger than those for spherical ice. For 3D ice, $Z_{e,true}$ and β_{true} are generally considered to gradually

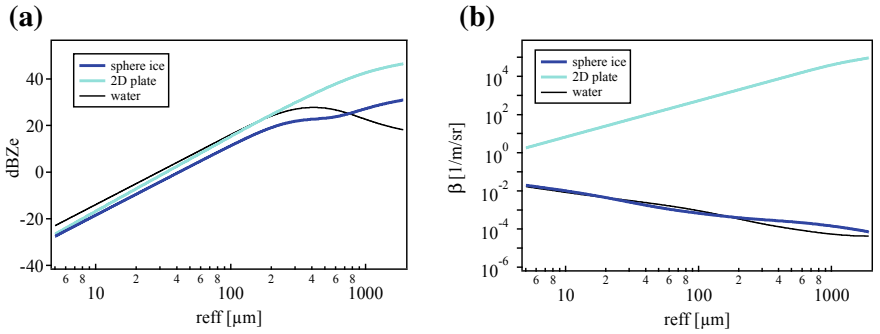

Fig. 1 **a** $Z_{e,true}$ and **b** β_{true} at nadir angle for spherical ice, perfectly oriented 2D plate ice at IWC = 1 g/m^3 and spherical liquid at LWC = 1 g/m^3

shift from those of perfectly oriented 2D ice to those of spherical ice. Radar and lidar have different size dependencies. $Z_{e,true}$ is generally more sensitive to large ice particles than to small ones of the same mass (Fig. 1a), while the opposite is true for β_{true} (Fig. 1b) for both water and ice, except for a perfectly oriented 2D plate. These differences in size dependency allow effective microphysics retrieval from radar and lidar synergy (Okamoto et al. 2000, 2003, 2010; Donovan and van Lammeren 2001; Wang and Sassen 2002; Deng et al. 2010; Sato and Okamoto 2011). Heymsfield et al. (2008) used comprehensive in situ measurement to determine that radar–lidar algorithms combining radar reflectivity Z_e with the lidar attenuated backscattering coefficient β are superior to radar reflectivity-only algorithms for ice cloud microphysics retrieval when the lidar signal is not fully attenuated.

3.2 *Retrieval of Ice Microphysics from Space-Borne Lidar and Radar*

CALIPSO launched in 2006 and carries the Cloud-Aerosol Lidar with Orthogonal Polarization (CALIOP), which is the first polarization lidar instrument in space (Winker 2009). CALIOP measures the depolarization ratio δ, which is a strong indicator of particle shape (Sassen 1991). For ground-based lidar, discriminating 2D ice from super-cooled water using δ alone is difficult, as both produce low δ values, but 3D ice can be separated. For space-borne lidar, multiple scattering increases the δ of water clouds, which makes discrimination of particle type using only δ difficult for 3D ice and super-cooled water. Hu et al. (2007) proposed the use of column-integrated β and δ for phase classification. Yoshida et al. (2010) combined the ratio of the attenuated backscattering coefficients β for two vertically consecutive cloud layers x and δ to discriminate among lidar grids dominated by 2D ice, 3D ice, and super-cooled water (Kyushu University (KU)-C2type scheme). x is given as,

$$x(R_i) = \log_{10}\left[\frac{\beta(R_i)}{\beta(R_{i+1})}\right] \tag{13}$$

The ratio x is considered an indicator of the optical thickness of layer R_i, which generally indicates water clouds with larger x values and ice clouds with smaller x values at 532 nm. Because this method provides range-resolved particle type data, it can be used to evaluate liquid/ice partitioning in a general circulation model (GCM) with respect to temperature (Watanabe et al. 2010). Yoshida et al. (2010) found that the zonal mean ratio of super-cooled water occurrence derived from CALIOP observations was larger than 50% over the temperature (T) range 0 °C > T > –10 °C with latitude dependence, indicating that the separation of super-cooled water from ice is crucial to the retrieval of accurate ice microphysics (Okamoto et al. 2010). Figure 2 shows an example of type discrimination from CALIOP β and δ data after cloud masking at $-70° \leq$ latitude $\leq -40°$. To construct the cloud mask shown in

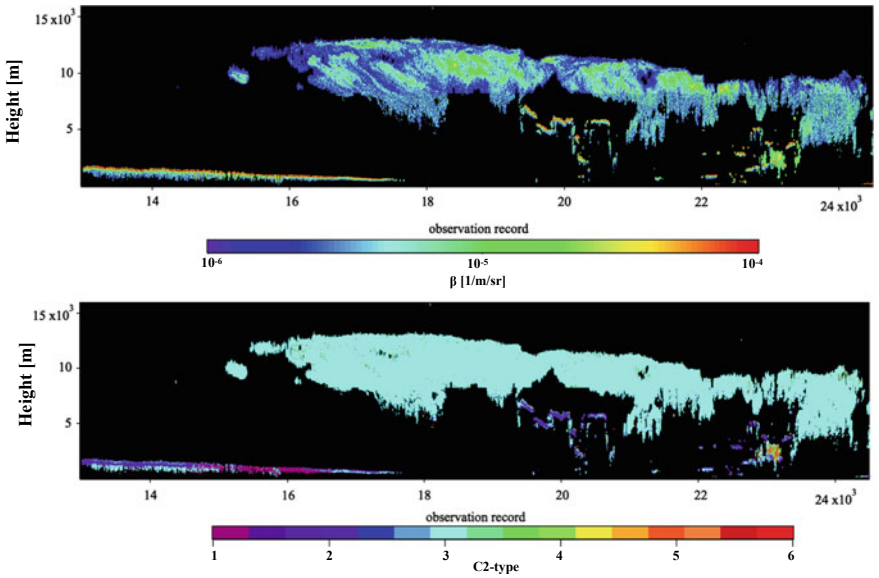

Fig. 2 Time–height cross-section of (top) the attenuated backscattering coefficient β from CALIOP after cloud masking (KU-mask) and (bottom) cloud particle type determined using the KU-C2 type algorithm, i.e., (1) warm water, (2) super-cooled water, (3) 3D ice, (4) 2D ice, (5) likely 3D ice crystals with horizontally oriented plates, (6) likely liquid droplets or randomly oriented ice crystals. For this figure, the extended version of the KU-mask originally developed by Hagihara et al. (2010) was used, and the KU-C2 type was applied to the original CALIOP vertical and horizontal resolutions (see text)

the figure, the cloud detection algorithm developed by Hagihara et al. (2010) (KU-mask scheme) was extended to account for CALIOP's transient response function (Lu et al. 2014) and thus better detect low-level water clouds and fully attenuated pixels (Cesana et al. 2016). The KU-C2type scheme was extended for application to the original CALIOP vertical (i.e., 30 m and 60 m below and above 8.2 km, respectively; Winker et al. 2009) and horizontal resolutions, as it was originally developed for application to the CloudSat-CALIPSO KU-merged dataset (Hagihara et al. 2010) with a vertical resolution of 240 m. At lower to middle altitudes, detailed structures of ice precipitation from super-cooled layers were observed, while high clouds contained mostly 3D ice in this case.

In late 2007, CALIOP changed its laser tilt angle from 0.3° to 3° off the nadir, while the observation conditions for CloudSat remained the same. The height–latitude plot of monthly mean CALIOP β of ice classified with a particle type algorithm for 2 months in September and October of the years before (i.e., 2006 and 2007) and after (i.e., 2008 and 2009) the change is investigated. The interannual variability of β is marginal between the observation years with the same laser tilt angle. The year-to-year difference in β profiles is greatest between 2007 and 2008 (Fig. 3), indicating that the drastic change seen in β reflects the tilt angle effect more than the difference in

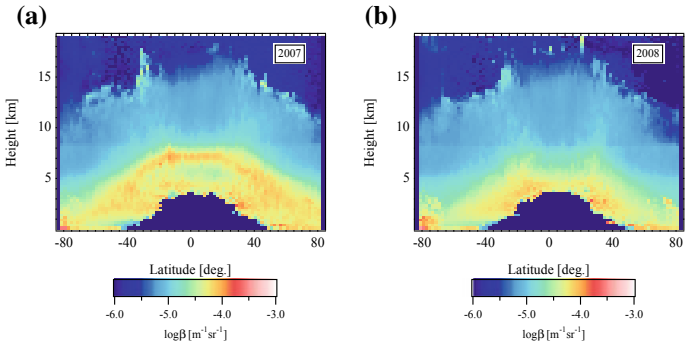

Fig. 3 Zonal mean attenuated β profiles for ice obtained from CALIOP for 2 months in September and October of **a** 2007 and **b** 2008 for ice phases identified by the KU-C2 type algorithm

mean microphysical properties among years. The zonal mean profiles for Z_e (Fig. 4) and CALIOP observations of water (figure not shown) did not show significant year-to-year variability, further supporting the argument that the laser angle affected ice detection. After pointing the laser 3° off-nadir, the probability of observing a strong specular return decreased, particularly around the temperature range of $-20\,°C < T < -10\,°C$. This temperature range corresponds to the region of high 2D ice occurrence reported by Yoshida et al. (2010) for the period when the laser was 0.3° off-nadir. β was reduced nearly an order of magnitude in some regions, consistent with the level reported in theoretical research (Iwasaki and Okamoto 2001).

A similar comparison among mean δ values also showed notable differences in data collected before and after late 2007 (Fig. 5). δ values around 15 km in the polar regions represent polar stratospheric clouds. Sassen and Zhu (2009) and Sassen et al. (2012) reported evidence of horizontally orientated plates lowering the depolarization ratio from the first 1–2 years of CALIOP observations. If we consider a mixture of 2D and 3D ice, δ can be described as the ratio of their backscattering coefficients for the perpendicular (cr) and parallel channels (co), i.e.,

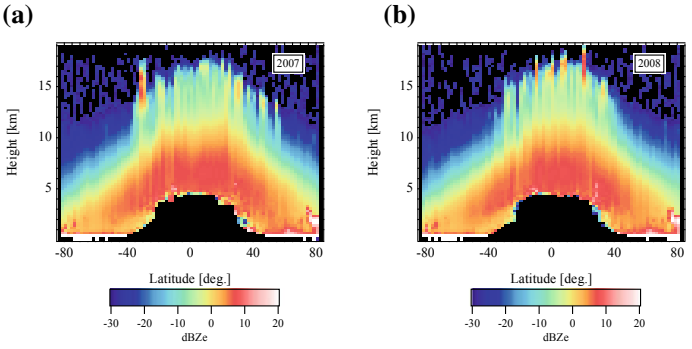

Fig. 4 As described in Fig. 3, but showing mean attenuated Z_e profiles obtained from CloudSat for temperatures lower than 0 °C

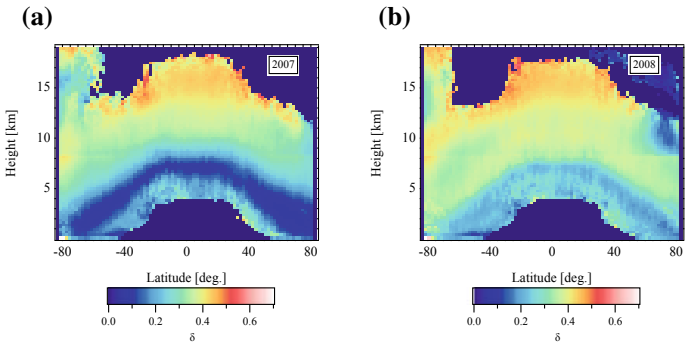

Fig. 5 As described in Fig. 3, but showing mean depolarization ratio profiles from CALIOP. The CALIOP cloud occurrence of frequencies greater than 2.0×10^{-4} is shown

$$\delta = \frac{\beta_{cr,2D}\mathrm{IWC}_{2D} + \beta_{cr,3D}\mathrm{IWC}_{3D}}{\beta_{co,2D}\mathrm{IWC}_{2D} + \beta_{co,3D}\mathrm{IWC}_{3D}} \tag{14}$$

β_{co} and β_{cr} are the values for ice water content IWC = 1 g/m^3, and IWC_{2D} and IWC_{3D} are the IWC for the 2D and 3D ice categories, respectively. For the same cloud, when the laser tilt angle changed, $\beta_{co,2D}\mathrm{IWC}_{2D}$ (3°) < $\beta_{co,2D}\mathrm{IWC}_{2D}$ (0.3°), while $\beta_{cr,2D}\mathrm{IWC}_{2D}$ will not vary much from 0. Given that $\beta_{co,3D}\mathrm{IWC}_{3D}$ and $\beta_{cr,3D}\mathrm{IWC}_{3D}$ remain unchanged between 0.3° and 3° tilt angles, Eq. (14) shows that δ will become larger after the change in tilt angle, as shown in Fig. 5.

To determine quantitative ice microphysics from CALIOP and CloudSat measurements, Okamoto et al. (2010) applied PO and DDA to lidar and radar, respectively, using consistent ice particle geometries. By explicitly considering the effects of ice particle nonsphericity and incorporating specular reflection for the nadir tilt of the laser, r_{eff}, IWC and the mass ratio of the 2D plate category to the total IWC (defined as $X' = \mathrm{IWC}_{2D}/(\mathrm{IWC}_{2D} + \mathrm{IWC}_{3D})$) at each vertical grid was individually retrieved from the combination of CALIOP β and δ with CloudSat Z_e in their overlap region (C3 region) (Fig. 6). For cloud regions observed only by CALIOP or CloudSat (C4 region), Kikuchi et al. (2017) developed a particle discrimination scheme trained with CALIOP and Tropical Rainfall Measuring Mission (TRMM) radar, and further classified them into mixed-phase, snow, and rain clouds. Sato and Okamoto (2011) extended the ice microphysics retrieval method (Okamoto et al. 2010) to ice and snow clouds for the C4 region. They compared the global statistics of the retrieved monthly mean r_{eff} and IWC at the C3 and C4 regions. They found that the C4 region contained a larger fraction of large IWC than the C3 region, whereas r_{eff} was similar between C3 and C4, except at lower altitudes, where snow with large particle sizes was retrieved. These results indicate the presence of clouds with much higher ice concentrations in C4. Detection of cloud type and microphysics will be further improved when Doppler cloud radar information becomes available from the EarthCARE mission (Illingworth et al. 2015), as well as with separation of air motion and the particle fall speed (Sato et al. 2009).

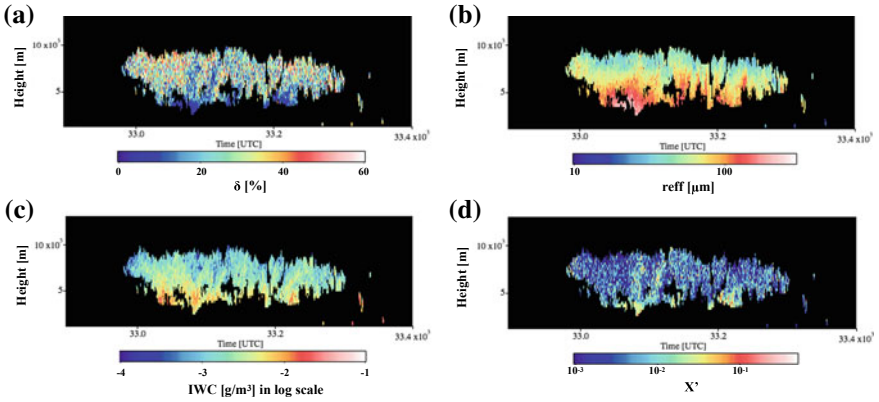

Fig. 6 Time–height cross-section of **a** the CALIOP 532 nm depolarization ratio after application of the KU-cloud masking algorithm (Hagihara et al. 2010), which discriminates clouds and precipitation from aerosols and noisy pixels in the case of lidar, **b** effective radius of ice particles, **c** ice water content, and **d** mass mixing ratio of 2D ice to total ice retrieved with the microphysics retrieval scheme of Okamoto et al. (2010) for the 0.3° off-nadir period

The impacts of ice particle shape and orientation on microphysics retrieval with regard to the change in laser tilt angle remain unclear without an appropriate scattering theory. Recently, PO has been applied to various shapes and laser incident angles (Borovoi et al. 2012; Okamoto et al. 2012). Using PO, Okamoto et al. (2012) studied the effects of 2D ice on microphysics retrieval at different laser tilt angles. The scattering properties of quasi-2D ice and 3D ice have notable differences (see also Okamoto et al. 2019b). These studies suggest that the effects of shape and orientation require further consideration of microphysics retrieval from CALIOP's 3° off-nadir laser period.

4 Simulation and Observation of Multiple Scattering Effects from Clouds

Multiple scattering is a widely observed phenomenon in space-borne lidar (Hu 2007) and short-wavelength space-borne radar measurements (Battaglia et al. 2010, 2015). Pulse stretching, where the apparent and actual range of the backscattered return differ due to multiple scattering, was observed during the Lidar In-space Technology Experiment (LITE) space shuttle mission (Winker et al. 1996) from optically thick water clouds (Miller and Stephens 1999). For radar, pulse stretching effects are sometimes observed as long tails below the surface or become apparent in later profiles of W band (94 GHz) CloudSat radar reflectivity data (Battaglia et al. 2008; Battaglia et al. 2010). These effects are also revealed by ghost echoes in Ku (13.6 GHz) and Ka

(35.5 GHz) band or by Ku-Ka band dual wavelength ratio knees in the Global Precipitation Measurement (GPM) Mission data (Battaglia et al. 2014, 2016). Multiple scattering between the surface and precipitation appears as mirror images below the surface and is often observed with Tropical Rainfall Measuring Mission (TRMM) Ku band (13.8 GHz) precipitation radar measurements (Li and Nakamura 2002). In this section, we focus on the effects of multiple scattering from clouds on lidar observations.

Conventional ground-based lidar systems are typically designed to avoid multiple scattering effects (Polonsky et al. 2005), and the detectable optical thickness is usually around 3–4 (Davis 2008). Figure 7a shows the optical thicknesses of water clouds at visible wavelengths from Moderate-Resolution Imaging Spectroradiometer (MODIS) cloud product (MODIS Science Team et al. 2006). A large population of data exceeds the range that is measurable with conventional ground-based lidar. The observed maximum depolarization ratio δ of water clouds in a vertical profile obtained from CALIOP increased as a function of optical thickness due to multiple scattering and was much larger than those typically observed from ground-based lidar instruments (Fig. 7b).

Multiple scattering effects on lidar have been investigated through Monte Carlo simulations (Winker and Poole 1995; Hu et al. 2007; Yoshida et al. 2010). Some studies that have used that method have indicated that the combination of β and δ may be effective for retrieving water cloud microphysics from the ground (Donovan et al. 2015) and from space (Sato et al. 2016). However, Monte Carlo simulations are often impractical for lidar inversion due to their high computational cost, particularly for global observation data. Many efforts have been made to simulate multiple scattering by a practical model (e.g., Eloranta 1998; Bissonnette 1996), by developing solutions to polarized radiative transfer equations (e.g., Zege and Chaikovskaya 1996) or using diffusion models (e.g., Davis et al. 1999) (Bissonnette 2005 and references therein). Wandinger (1998) studied multiple scattering effects on the extinction coefficient from ground-based Raman and high-spectral-resolution lidar. For the inversion of cloud properties from β observed with space-borne lidar, Hogan (2008) and Hogan

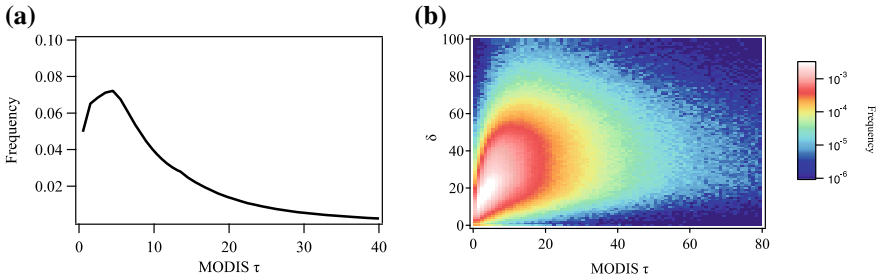

Fig. 7 **a** Frequency distribution of water cloud optical thickness from the level 2 MODIS cloud product (MODIS Science Team et al. 2006). **b** Relation between the MODIS water cloud optical thickness in panel **a** and the maximum CALIOP depolarization ratio of water in a vertical column determined from the Kyushu University lidar cloud type product (KU-C2 type) (Yoshida et al. 2010)

and Battaglia (2008) proposed an efficient method based on time-dependent two-stream approximation, and Sato et al. (2018) applied a physical model (PM) based on the multiple scattering phase function (hereafter, high-order phase function) and a path integral approach for lidar backscattering.

To investigate the information content of the lidar depolarization ratio for multiple scattering, models have been developed that consider double scattering (Roy and Roy 2008; Roy et al. 2018) and triple scattering (Cai and Liou 1981). Space-borne lidar returns are strongly affected by high-order scattering. Based on the simulation for LITE space shuttle mission, Winker and Poole (1995) found that as much as 30 orders of scattering must be considered with a large receiver footprint size. Sato et al. (2019) extended the PM approach with a polarization function and introduced the vectorized physical model (VPM) to analyze the transition of backscattered returns of space-borne polarization lidar from water clouds in regimes of single scattering and multiple scattering to diffusion with regard to high-order scattering. For pulsed space-borne radar, second-order analytical solutions to the vectorized time-dependent radiative transfer equation have been derived (e.g. Kobayashi et al. 2007) that are applicable for optical thicknesses up to about 2 (Kobayashi et al. 2007). Extension of the VPM to radar data is straightforward.

4.1 Introduction of the PM Approach for Space-Borne Lidar Application

For simplicity in the following discussion, we consider nadir-pointing space lidar in Fig. 8 and assume that the backscattered irradiance I is azimuth-independent. The general formulation of the PM for application to inhomogeneous profiles was investigated by Sato et al. (2018).

$I_{\mathrm{tot}}(\mathrm{t})$ is the total backscattered irradiance within the receiver footprint from the apparent in-cloud z-axis position $z = \mathrm{c}t$ at an in-cloud half-round-trip time t. c is the speed of light in a vacuum. $I_{\mathrm{tot}}(\mathrm{t})$ consists of the lidar returns from different in-cloud z-axis positions ($z \leq \mathrm{c}t$). To estimate $I_{\mathrm{tot}}(\mathrm{t})$, the PM includes three scattering processes contributing to I_{tot}: single scattering (*ss*) $I_{\mathrm{ss}}(t)$, on-beam multiple scattering (*ms*,*on*) $I_{\mathrm{ms,on}}(t)$, and off-beam multiple scattering (*ms*,*off*) $I_{\mathrm{ms,off}}(z, t)$ ($z \leq \mathrm{c}t$), i.e., the pulse stretching component (Fig. 8):

$$
\begin{aligned}
I_{\mathrm{tot}}(t) &= I_{\mathrm{ss}}(t) + I_{\mathrm{ms,on}}(t) + \sum_{i} I_{\mathrm{ms,off}}(z_i, t), \quad (z_i < ct) \\
&= I_{\mathrm{ss}}(t) + I_{\mathrm{ms,on}}(t) + \sum_{k=1}^{i} \sum_{i} I_{\mathrm{ms,off,k}}(z_i, t), \quad (z_i < ct)
\end{aligned} \tag{15}
$$

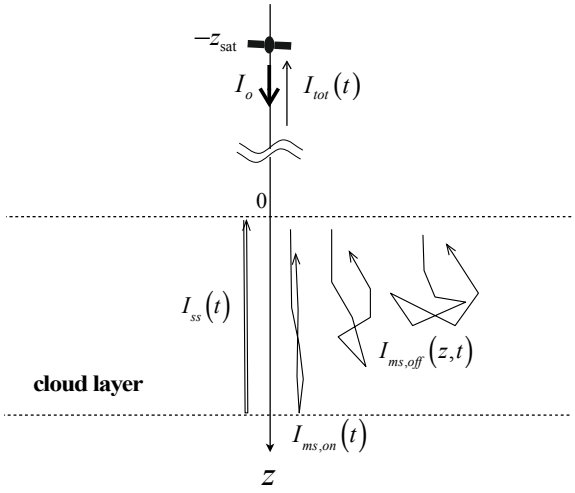

Fig. 8 Geometry of cloud observation from space lidar. $I_{\mathrm{tot}}(\mathrm{t})$ is the total backscattered irradiance at an in-cloud half-round-trip time t. Schematic of the single scattering component $I_{\mathrm{ss}}(t)$, on-beam multiple scattering component $I_{\mathrm{ms,on}}(t)$ and off-beam multiple scattering components $I_{\mathrm{ms,off}}(z, t)$ ($z <$ ct) of $I_{\mathrm{tot}}(\mathrm{t})$ are shown in the figure. The round path for $I_{\mathrm{ss}}(t)$, $I_{\mathrm{ms,on}}(t)$ and $I_{\mathrm{ms,off}}(z, t)$ is the same, and the path of $I_{\mathrm{ms,on}}(t)$ does not deviate significantly from those of $I_{\mathrm{ss}}(t)$

The variable z in $I_{\mathrm{ms,off}}(z, t)$ is defined as the maximum z-axis position of the photon trajectories contributing to $I_{\mathrm{ms,off}}$. *ms*,*on* and *ms*,*off* include contribution from high-order scattering, where the number of scattering event is determined by the scattering mean free path length l as ct/l. The portion of the *ss* component that is scattered out of the initial incident direction during the first scattering event becomes the source term $J_{\mathrm{on}}(\mathrm{z_k})$ for $I_{\mathrm{ms,on}}(\mathrm{t} = \mathrm{z_k/c})$. The *ms*,*on* component previously scattered at $\mathrm{z_k}$ ($\mathrm{k} \leq \mathrm{i}$,) becomes the source term $J_{\mathrm{off}}(z_{\mathrm{k}}, z_{\mathrm{i}}, t)$ for $I_{\mathrm{ms,off}}(\mathrm{z_i}, \mathrm{t})$. $I_{\mathrm{ms,off,\,k}}(z_{\mathrm{i}}, t)$ in Eq. (15) are components of $I_{\mathrm{ms,off}}(\mathrm{z_i}, \mathrm{t})$, which arise from different source terms $J_{\mathrm{off}}(z_{\mathrm{k}}, z_{\mathrm{i}}, t)$. The *ms*,*off* component is not the source of other quantities. The relations among the three components in the model are depicted in Fig. 9. The PM considers many fewer representative photon path trajectories than Monte Carlo simulations.

Figure 10 shows an example of the z–t dependence of $I_{\mathrm{tot}}(\mathrm{t})$ for a simulated space-borne lidar return from three different z-axis position in a water cloud in the Monte Carlo model (solid lines) and in the PM (circle symbols). The lines and symbols in navy, cyan and red show the t-dependence of the lidar return from $z = 64$, 255, and 511 m, respectively. For example, the first navy circle symbol (on the right most of Fig. 10) corresponds to the sum of the on-beam returns from $\mathrm{z} = 64$ m, i.e., $I_{\mathrm{ss}}(t = z/\mathrm{c}) + I_{\mathrm{ms,on}}(\mathrm{t} = z/\mathrm{c})$, while other navy circles correspond to the time-delayed returns $I_{\mathrm{ms,off}}(z, t > z/\mathrm{c})$ from $z = 64$ m. In the region enclosed by a square in Fig. 10, lidar returns from different z-axis position but for the same t are compared. For this case, it is seen that the on-beam return from $z = 511$ m (red) is larger than the off-beam

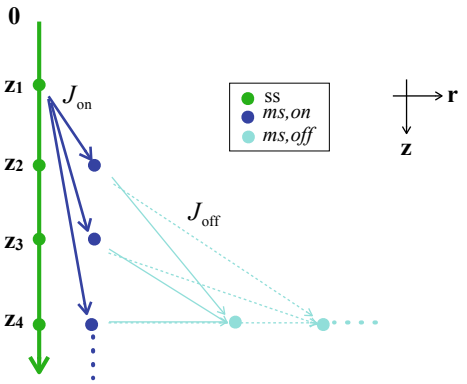

Fig. 9 Relations among the single scattering components, on-beam multiple scattering components, and off-beam multiple scattering components. r is the radial component of z

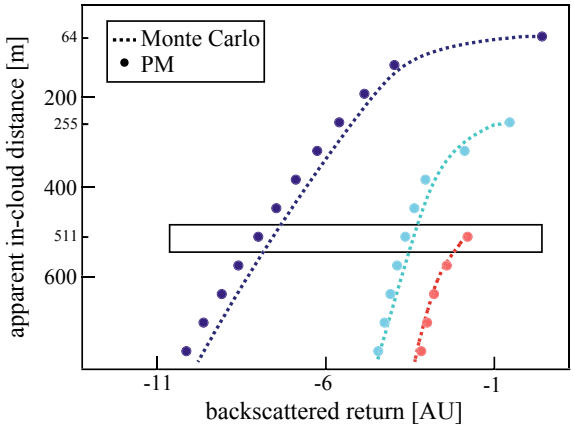

Fig. 10 The t dependence of the backscattered returns from a fixed in-cloud distance z of about 64 m (navy), 255 m (cyan), and 511 m (red) simulated with the PM (symbol) and a Monte Carlo method (dotted line). The vertical axis is the apparent in-cloud distance corresponding to time t and the horizontal axis is in logarithmic scale. The results for PM are plotted at discrete time steps $\Delta t = l/\mathrm{c}$, where l is the scattering mean path length. For the symbols with the same color, the right most symbol corresponds to the sum of the on-beam backscattered returns ($ss + ms$, on) and the others correspond to the off-beam returns (ms,off) from the same cloud layer but received at a later time. The region enclosed by a square shows an example of the lidar returns at $t = z/\mathrm{c}$ ($z = 511$ m) from three different in-cloud distance, i.e., ms,off for navy and cyan, and $ss + ms$, on for red

returns from $z = 64$ m (navy) and 255 m (cyan), and that these features seen in the Monte Carlo method are well captured by the PM.

4.1.1 The Scattering Phase Function and Effective Extinction After the *n*th Scattering Event

The PM modeled lidar multiple scattering by introducing the effective extinction coefficient $\sigma_{ext,w}$ (w = *ms*,*on*, *ms*,*off*) and the phase function after the *n*th scattering event $p_n(\theta)$ (n = 1, 2, …, *N*). In analogy to the single scattering lidar equation, $I_{ss}(t)$, $I_{ms,on}(t)$, and $I_{ms,off}(z, t)$ can be written in their simplest form as:

$$I_w(z,t) = C_{li} J_w \sigma_{sca} p_{bk,w} \Big/ (4\pi) F_{2way}(\sigma_{ext,w}) \quad (w = ss, mson, msoff) \tag{16}$$

C_{li} depends on the lidar specification. Equation (16) is constructed from a source term J_w for each component, the backscattering coefficient $\sigma_{sca}p_{bk,w}$, and the two-way attenuation term F_{2way}, which is characterized by the effective extinction coefficient $\sigma_{ext,w}$ (w = *ms*,*on*, *ms*,*off*) after multiple scattering. $p_{bk,w}$ represents either the single scattering phase function p_{ss} or p_n for backscattering angles depending on the value of w. In the following p_n and $\sigma_{ext,w}$ are introduced.

Multiple Scattering Phase Function

p_n is derived as follows. An arbitrary phase function can be expanded using a Legendre polynomial P_l (l = 0, 1, … ∞) series. After *n* scattering events, the average value of the polynomial equals its *n*th order after a single scattering event when scattering is cylindrically symmetrical (Goudsmit and Saunderson 1940). Based on this relation, p_n is expressed as follows,

$$p_n(\theta) = \sum_{l=0}^{\infty} (2l+1) A_l^n P_l(\cos\theta) \tag{17}$$

where A_l is the *l*th order expansion coefficient of the single scattering phase function. Goudsmit and Saunderson (1940) used the property of Legendre polynomials and further considered the probability distribution of the number of collisions within a given path length to derive the angular distribution from multiple elastic scattering of charged particles. In electron scattering, the scattering can be considered elastic at path lengths where the energy loss of the electrons is negligibly small; otherwise, corrections can be made using appropriate approximations for inelastic scattering (Fernández-Varea et al. 1993). The angular distribution of charged particles after multiple scattering and the moments of their spatial distributions were further studied by Lewis (1950). These methods have also been incorporated in high-energy Monte Carlo simulations (Kadri et al. 2009).

In Sato et al. (2018), p_n is considered within the framework of the PM rather than in Monte Carlo simulations. For a typical water cloud particle size at visible wavelengths, p_n gradually evolves from the initial forward peaked shape representing single scattering with minimal side scattering into an isotropic shape as the number of

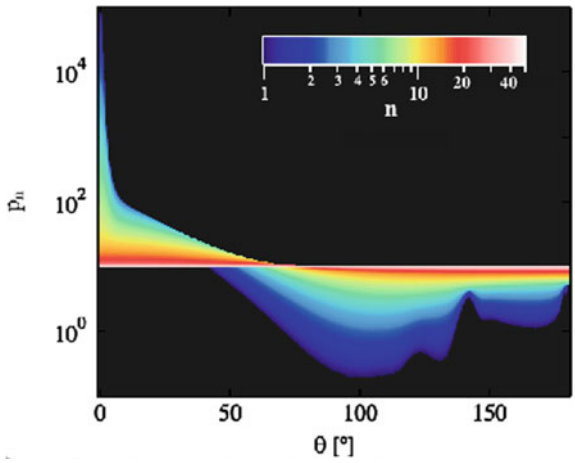

Fig. 11 An example of p_n estimated at different scattering order n values (indicated by colors) in visible wavelengths for an effective radius r_{eff} of 10 μm

scattering events increases (Fig. 11). With this evolution of the distribution function, the probability of scattering at larger angles gradually increases, and the transition from the single scattering regime to the multiple scattering regime and then to the diffusion regime is naturally accommodated in the PM.

Effective Extinction

For light propagation in a multiple scattering medium, Perelman et al. (1994) introduced Feynman path integrals (Feynman 1949) and determined the escape probability of photons from the surface after interaction with a semi-infinite medium in relation to the number of scattering events, the escape zenith angle, and single scattering properties. This approach was considered effective for inversion problems in medical applications (Perelman et al. 1994). Analogous treatment has also been considered in PM to model $\sigma_{ext,off}$ according to the photon trajectories contributing to the time-delayed backscattered returns, where $\sigma_{ext,off}$ in Eq. (16) is expressed as a function of the number of scattering events, the zenith angle of the propagation direction, and p_n, such that at larger optical thickness (1) the attenuation of the backscattered irradiance is reduced for a photon path with a scattering angle larger than that of the more forward scattering paths when the same phase function shape is considered, and (2) $\sigma_{ext,off}$ is smaller with a more isotropic single scattering phase function compared to that with a more forward-peaked single scattering phase function (Sato et al. 2018). For *ms,on*, the photon trajectories contributing to $I_{ms,on}$ does not deviate significantly from those contributing to I_{ss}. It is assumed that the extinction coefficient is reduced from σ_{ext} by accounting for the amount of photons scattered into the *ms,on* path within the FOV due to multiple scattering using p_n to obtain $\sigma_{ext,on}$ (Sato et al. 2018).

The treatment of effective extinction in the PM may correspond to a modification of the "η factor" approach. To account for multiple scattering effects on β, Platt (1981) introduced this approach, which can be written as follows:

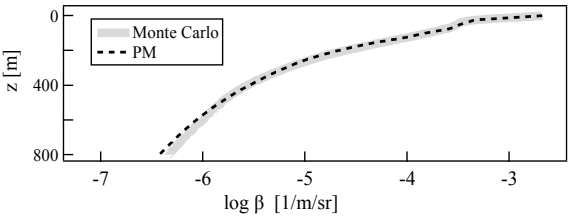

Fig. 12 The total backscattering coefficient estimated with the PM and a Monte Carlo simulation for a water cloud with extinction profile $\sigma_{\text{ext}} = 40$/km under CALIOP specifications. The mean value of the Monte Carlo simulation at 1 m resolution is shown. Note that the PM can also be applied to vertically inhomogeneous clouds

$$\eta = 1 - \frac{1}{2\int_0^R \sigma_{ext} dz} \ln \frac{P_{rec,t}(R)}{P_{rec,ss}(R)} \tag{18}$$

where $P_{rec,t}$ and $P_{rec,ss}$ are the total received power from the target at range R and that calculated assuming single scattering, respectively. The η factor is a useful concept for deriving cloud microphysics (Platt 1981). The drawback is that the value of η is an unknown parameter that must be determined from instrument specifications and hydrometeor profiles. Further, the backscattering efficiency from the target volume may change during the multiple scattering process (Bissonnette 2005), which is accommodated in the PM.

The validity of the present method can be evaluated against a Monte Carlo approach (Fig. 12). For CALIOP, the overall uncertainty in the estimated total backscattering coefficient of the PM with respect to a Monte Carlo simulation is about $15 \pm 11\%$ for a variety of extinction and field-of-view (FOV) profiles and optical depths (Sato et al. 2018). The z–t dependence of the backscattered return also shows good correspondence with true values (Fig. 10).

4.2 Polarimetric Property of Lidar Multiple Scattering in the VPM

The VPM (Sato et al. 2019) considered the polarimetric property of lidar backscattering by replacing p_n with Nth order 4×4 Mueller matrices $\mathbf{S}_n$. Elements in the Mueller scattering matrix $\mathbf{S}_n$ are related to those of the scattering phase matrix $\mathbf{p}_n$ in analogy to the single scattering process as $\mathbf{S}_n = \sigma_{sca} k^2 \mathbf{p}_n/(4\pi)$. $\mathbf{p}_n$ is obtained by considering the expansion coefficient of the single scattering phase matrix for A_l in eq. (17). For randomly oriented particles in space, the Mueller matrix $\mathbf{S}_n$ can be written as (Liou 2002),

$$\mathbf{S}_n = \begin{bmatrix} S_{11,n}(\theta) & S_{12,n}(\theta) & 0 & 0 \\ S_{12,n}(\theta) & S_{22,n}(\theta) & 0 & 0 \\ 0 & 0 & S_{33,n}(\theta) & S_{34,n}(\theta) \\ 0 & 0 & -S_{34,n}(\theta) & S_{44,n}(\theta) \end{bmatrix} \tag{19}$$

Nth order lidar multiple scattering can be written in simplified form as (Cai and Liou 1981; Sato et al. 2019):

$$\mathbf{I}_{\text{tot}}\left(t_{j=N}\right) = \mathbf{I}_o \iiint_{v_1} \cdots \iiint_{v_N} \mathbf{L}'_N \mathbf{p}(\theta_N) \cdots \mathbf{L}'_3 \mathbf{p}(\theta_2) \mathbf{L}'_2 \mathbf{p}(\theta_1) \mathbf{L}'_1 dv_1 \cdots dv_N. \tag{20}$$

dv_n (n = 1,2,…N) are infinitesimal scattering volumes at the location of the nth scattering point of the incident light. θ_n (n = 1,2,…N) are scattering angles for the nth scattering event. Equation (20) is an Nth order volume integration of a set of N 4 × 4 scattering phase matrices and the transformation matrix for the Stokes parameter related to the rotation of the scattering plane $\mathbf{L}_n$ (n = 1,2,…N). $\mathbf{L}_n{}'$ is a function of $\mathbf{L}_n$, scattering coefficient at dv_n, extinction and distance between dv_n and dv_{n+1}.

For VPM, the multiple scattering process determined from Eq. (20) can be modeled by considering one set of transformation matrices between the incident plane and the Nth scattering plane, in an analogous manner to that used for the single scattering framework (Sato et al. 2019).

$$\mathbf{I}_{\text{tot}}\left(t_{j=N}\right) = \mathbf{I}_o \mathbf{F}\left(\mathbf{L}'_N \mathbf{p}_N \mathbf{L}'_1\right). \tag{21}$$

The term F in Eq. (21) indicates that in addition to the introduction of the scattering phase matrix after Nth scattering event $\mathbf{p}_\text{N}$, the VPM was further modified to implement the accumulated effects of depolarization: (1) depolarization of the incoming wave Q^{in} at the cloud layer of interest in the forward direction due to rotation of the scattering plane during multiple scattering and (2) depolarization produced by the backward scattering processes within the FOV (geometric effect) (Sato et al. 2019). For single scattering from spherical particles, the angular dependence of the linear depolarization ratio $\delta_{ss}(\theta)$ can be estimated from the ratio of the azimuthally-averaged scattered intensities parallel and perpendicular to the linearly polarized light with the following equation (Bissonnette et al. 2001; Roy and Roy 2008),

$$\delta_{ss}(\theta) = \frac{\left(S_{11,n} + S_{12,n}\right)\cos^2\theta - 2S_{33,n}\cos\theta + \left(S_{11,n} - S_{12,n}\right)}{3\left(S_{11,n} + S_{12,n}\right)\cos^2\theta + 2S_{33,n}\cos\theta + 3\left(S_{11,n} - S_{12,n}\right)} \quad (n = 1) \tag{22}$$

δ_{ss} is non-zero at backscattering angles other than 180°. Depolarization in forward scattering directions ($0° \le \theta < 90°$), Q^{in}, is generally small for single scattering of a typical liquid cloud particle estimated by Eq (22) at the lidar wavelength for scattering angles smaller than 20 °, and the polarization state of the incoming wave at the layer of interest can be assumed to remain unchanged (Roy and Roy 2008). Under multiple scattering conditions, the polarization state of the incoming wave at

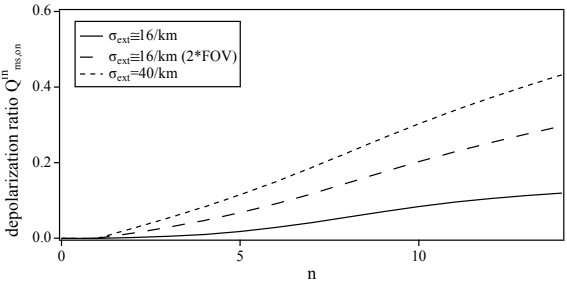

Fig. 13 Mean depolarization of the incoming wave at the *n*th scattering event for the *ms*, *on* component. Calculations were performed for water clouds with different σ_{ext} profiles and CALIOP FOV

the layer of interest may change due to rotation of the scattering plane. In the VPM, in addition to depolarization generated from backscattering, a procedure is introduced that allows instant estimation of Q^{in} at the layer of interest without tracking of every scattering event, which is represented by the term F in Eq. (21). The accumulated effects that produce non-zero Q^{in} of the incoming wave at the Nth scattering event are treated separately for *ms*,*on* and *ms*,*off* and are estimated to be a function of $\mathbf{S}_{\text{n}}$ (i.e., the profile of cloud microphysics), the horizontal spread of the photons at the Nth scattering event, and the receiver FOV (Sato et al. 2019). Figure 13 shows an example of Q^{in} for *ms*,*on* (hereafter $Q^{in}_{ms,on}$). $Q^{in}_{ms,on}$ increases with scattering order (i.e., optical thickness), σ_{ext}, and FOV. Cases with larger FOV show larger $Q^{in}_{ms,on}$ values for the same scattering order and microphysics. For the same cloud microphysics, as the receiver FOV becomes larger, the receiver footprint size at the target position exceeds the scattering mean path of the scatterers and photons scattered at larger angles likely remain within the receiver FOV. For a similar reason, cases with smaller scattering mean free path lengths are considered to show larger $Q^{in}_{ms,on}$ values for the same scattering order and receiver FOV.

The linear depolarization ratio $\delta(t)$ is estimated by considering the contributions of the parallel and perpendicular components of I_{tot} with respect to the incident electric field of the emitted light as:

$$\delta(t_j) = \frac{I_{\text{tot},y}(t_j)}{I_{\text{tot},x}(t_j)} = \frac{I_{\text{ss},y}(t_j) + I_{\text{ms,on},y}(t_j) + \sum_{i=1}^{j} I_{\text{ms,off},\,y}(z_i, t_j)}{I_{\text{ss},x}(t_j) + I_{\text{ms,on},x}(t_j) + \sum_{i=1}^{j} I_{\text{ms,off},x}(z_i, t_j)} \tag{23}$$

The parallel and perpendicular components of $\mathbf{I}_{\text{tot}}$ are functions of $\mathbf{S}_{\text{n}}$ and the polarization state of the incoming wave Q^{in} at the layer of interest. These components are estimated for each *ss*, *ms*,*on*, and *ms*,*off* category to obtain $\delta(t)$ (Fig. 14).

Sato et al. (2019) evaluated the VPM by comparing it to Monte Carlo simulations. Q^{in} became increasingly important to δ as the multiple scattering effect increased. The uncertainty of $\delta(t)$ estimation was reported to be about $2 \pm 3\%$ overall, which is comparable to the 1% calibration uncertainty of δ from CALIOP (Hunt et al. 2009).

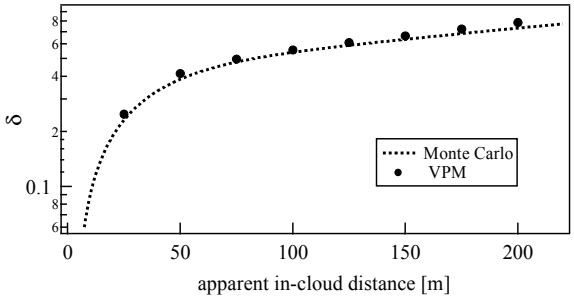

Fig. 14 Depolarization ratio estimated using the VPM against that of the mean value obtained from a Monte Carlo simulation for a water cloud case with $\sigma_{ext} = 40$/km with the configuration of CALIOP. Results are shown for instantaneous values at 1 m resolution. Note that the VPM can also be applied to vertically inhomogeneous clouds

4.3 Observation of Lidar Multiple Scattering from Ground-Based Lidar

Several attempts have been made to extend the limits of ground-based Mie-type lidar observations using multiply scattered lidar returns (Okamoto et al. 2016). For MFOV lidar measurements, Roy et al. (1999) considered a FOV of about 12 mrad and used the secondary polarization returns to infer the particle size density distribution at cloud base (Roy et al. 1999). Multiple scattering or off-beam lidar (Polonsky et al. 2005; Davis 2008) collects multiply scattered signals off-beam from the emitted laser beam direction with a very wide FOV. One off-beam lidar instrument, Wide-Angle Imaging Lidar (WAIL) (Polonsky et al. 2005), has detected lidar returns ~30° (half angle) off-beam at 532 nm wavelength using a CCD imager. In that case, a wide FOV was used to gain information on cloud boundaries, which are not detectable with conventional lidar. Cahalan et al. (2005) studied an airborne MFOV-multiple scattering lidar using the Cloud Thickness from Offbeam Returns (THOR) system to investigate the information obtainable from bright halos. Retrieval of the extinction coefficient profiles in water clouds from the THOR system was further investigated in Pounder et al., (2011). Okamoto et al. (2016) utilized the polarization capability of MFOV Multiple-Scattering Polarization Lidar (MFMSPL) in the off-beam direction for the first time operating at the 532 nm wavelength during both day and night (Fig. 15). In the first version of MFMSPL-1, four detectors for parallel channels and four detectors for perpendicular channels, each with an FOV of 10 mrad, were employed to measure the depolarization ratio. The detectors were tilted with angles ranging from 0 to 30 mrad in the vertical direction at a 10-mrad interval to observe on-beam and off-beam returns. The on-beam channels detected returns from atmospheric molecules, aerosols, clouds, and precipitation. The off-beam channels detected multiple scattered returns, mainly from clouds and precipitation. Further,

Fig. 15 Initial version of the MFMSPL system (MFMSPL-1) operated at the National Institute for Environmental Studies (NIES). The figure shows a total of eight channels, with odd-numbered channels and even-numbered channels detecting parallel and perpendicular signals, respectively

backscattered returns from drizzle and precipitation appeared to be different in on-beam and off-beam channels depending on the degree of multiple scattering that occurred (Okamoto et al. 2016).

4.4 Observation of Water and Mixed-Phase Clouds with MFMSPL

The 35-mrad half-angle FOV of MFMSPL-1 corresponds to a receiver footprint radius size of about 70 m at 1 km of height. This is comparable to that of CALIOP. The MFMSPL system is expected to offer unique opportunities to simulate lidar returns similar to those observed with space-borne lidar. This will further fill the gap between ground-based and space-borne polarimetric lidar measurements and improve cloud retrieval from space-borne lidar that is affected by multiple scattering. In the following sections, observations made with MFMSPL-1 are shown for water cloud and mixed-phase cloud cases.

4.4.1 Water Cloud Observation

Figures 16 shows the attenuated backscattering coefficient and depolarization ratio of a water cloud obtained with MFMSPL-1. The off-beam channels recorded a higher cloud top than the on-beam channels. The depolarization ratio generally grew with increasing height and further off-beam channels. The maximum depolarization ratio

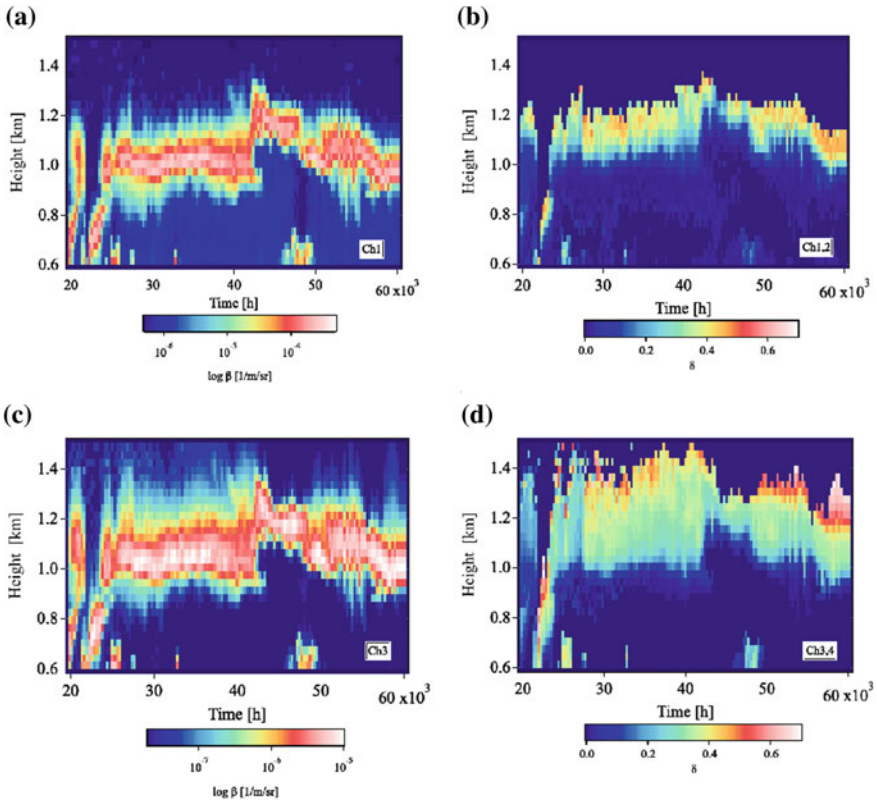

Fig. 16 Backscattering coefficients obtained from the parallel **a** on-beam channel Ch1 and **c** the first off-beam channel Ch3 of MFMSPL-1 in July 2016 and the depolarization ratios obtained from the **b** on-beam channels $\delta(1,2) = \beta(\text{Ch2})/\beta(\text{Ch1})$ and **d** the first off-beam channels $\delta(3,4) = \beta(\text{Ch4})/\beta(\text{Ch3})$. The cloud was located in the temperature range of 13–19 °C

was around 40% for the on-beam channel, while it reached about 60–80% for the outermost off-beam channel.

4.4.2 Mixed-Phase and Ice-Phase Cloud Observations

Figure 17 depicts the on-beam and off-beam lidar returns for mixed-phase conditions at a sub-freezing temperature range of −6 to −1 °C. The hydrometeor occurrences recorded with Ch1 and Ch3 were almost the same at lower altitudes, while the off-beam channels Ch5 and Ch7 detected smaller ice precipitation fractions below about 1.9 km altitude compared to Ch1 and Ch3, probably due to a lower ice concentration and a smaller multiple scattering effect within these regions (Fig. 17). Similar to the water cloud case, all parallel off-beam channels showed the cloud top about 300 m higher than the on-beam channel.

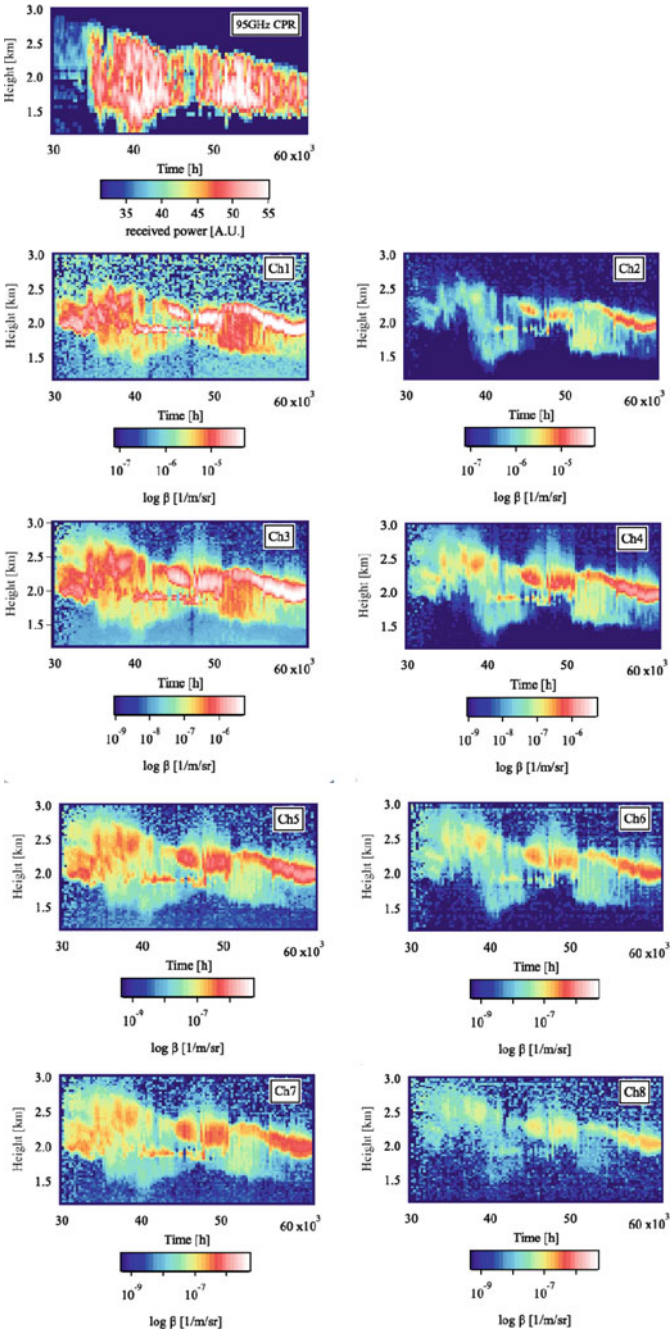
95GHz CPR
Height [km]
3.0
2.5
2.0
1.5
30
40
50
60 x10^3
Time [h]
35 40 45 50 55
received power [A.U.]
Ch1
Ch2
Ch3
Ch4
Ch5
Ch6
Ch7
Ch8
10^-7 10^-6 10^-5
10^-9 10^-8 10^-7 10^-6
10^-9 10^-7
log β [1/m/sr]

◀**Fig. 17** Simultaneous observations of a mixed-phase cloud with MFMSPL-1 and the 95 GHz cloud profiling radar conducted at the National Institute of Environmental Studies (NIES) in April 2015. The time–height plot of the backscattering coefficient obtained with MFMSPL-1 is shown for channels 1–8. The range of backscattering coefficient s indicated by the color bars in the figures differs between on-beam and off-beam channels

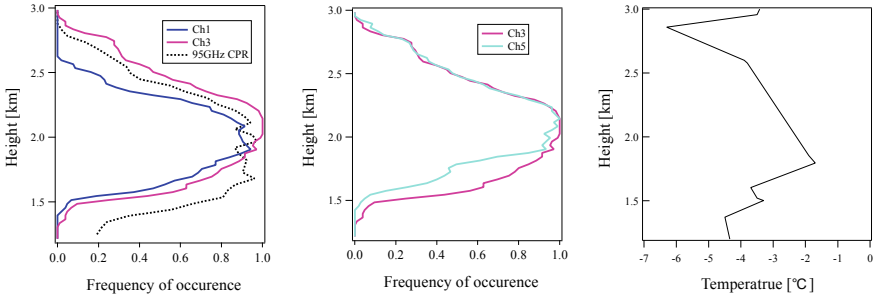

Fig. 18 Vertical profiles of (left two) hydrometeor occurrence corresponding to the observation period of Fig. 17, and (right) the temperature profile at Tateno on the same day from the atmospheric sounding data reported by the University of Wyoming

MFMSPL-1 was operated on the same day as a collocated 95 GHz cloud radar measurement (Yamaguchi et al. 2006). The cloud top height of the off-beam channel and that from the cloud radar corresponded well with each other and with the altitude of a temperature inversion observed around 2.9 km (Fig. 18), and the radar–lidar overlap region increased when off-beam returns were considered. Layers that likely contained super-cooled liquids were apparent from both the on-beam and off-beam detectors (e.g., around 13:00 UTC). However, only the off-beam channels observed the return from the ice phase above the uppermost super-cooled layer, which was recorded by cloud radar (Fig. 17). The morphologies of cloud top boundaries detected by cloud radar and the off-beam channels showed good overall consistency.

The hydrometeor fraction observed with the off-beam channel was comparable to that of cloud radar, except at lower altitudes, where cloud radar showed more ice precipitation. A large backscattering coefficient and low depolarization ratio for the on-beam channel was observed just below 2 km height (Figs. 17, 19), and the off-beam channels showed the same tendency (Fig. 19). This suggests the presence of horizontally oriented ice particles such as 2D plates, as the depolarization ratio at small canting angles estimated from PO (Okamoto et al. 2012) is negligible. The range of −2 to −1 °C corresponds to the temperature where the typical habit is plate-like in laboratory studies (Wallace and Hobbs 2005). The habit is also reported to change from hexagonal plates to dendrites according to whether the supersaturation level falls between ice and water saturation or is greater than water saturation in the same temperature range (Wallace and Hobbs 2005). Mixed-phase drizzle precipitating from the super-cooled and 2D plate layers had depolarization ratios around 20% for on-beam returns. Radar reflectivity also increased in these regions, likely

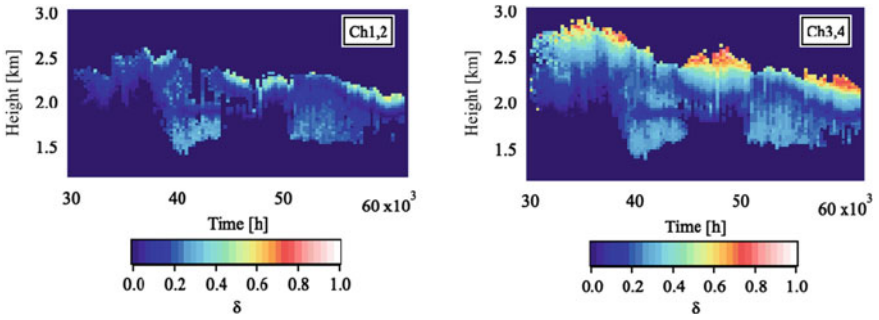

Fig. 19 Example of the time–height cross-section of the depolarization ratio obtained using MFMSPL-1 for Ch 1, 2 and Ch 3, 4 after applying a cloud masking scheme to the observational data shown in Fig. 17

indicating an increase in optical thickness, and depolarization increased in off-beam channels to about 30% for the first off-beam channel (Fig. 19).

Another mixed-phase cloud case was observed at a lower temperature range of −18 to −11 °C, and is shown in Fig. 20. Temperature inversions occurred near altitudes of 3.9 km and 5.6 km. The high backscattering coefficient for Ch1 and the low on-beam and off-beam depolarization ratios at 4–4.5 km altitude in Fig. 20 indicate the presence of 2D plate-like ice particles. The temperature zone around −15 °C also corresponds to the preference of plate-like ice particles observed in a laboratory experiment (Wallace and Hobbs 2005) as well as in a global analysis based on CALIOP (Yoshida et al. 2010).

Depolarization ratios in super-cooled and ice or mixed-phased regions near the cloud top had similar features as the previous case. In contrast to the previous case, the depolarization ratio in ice fallout regions below about 4 km was larger for on-beam observations than off-beam observations (Fig. 20), suggesting relatively low optical thickness in the region.

Characterization of lidar multiple scattering theories often relies on comparison with Monte Carlo simulations. MFMSPL may provide the opportunity to test multiple scattering theories from observational and experimental perspectives.

Different space-borne lidar missions have different receiver FOVs, being 130 μrad, 65 μrad, and 13 μrad for CALIOP, EarthCARE 355 nm Atmospheric Lidar (ATLID), and ADM-Aeolus 355 nm Atmospheric Laser Doppler Instrument (ALADIN) (Stoffelen et al. 2005), respectively. These differences produce different multiple scattering effects on the lidar returns from clouds with the same physical properties. Recently, MFOV high-spectral-resolution polarization lidar (HSRL) was developed (Okamoto et al. 2019a). Wide-field-of-view HSRL at 532 nm wavelength showed smaller extinction observations compared to a narrow-field-of-view HSRL system, indicating that the multiple scattering effect on extinction measurement can be inferred (Jin et al. 2019). By investigating such effects at footprints comparable to that of space-borne lidar, these observation systems may support retrieval algorithm

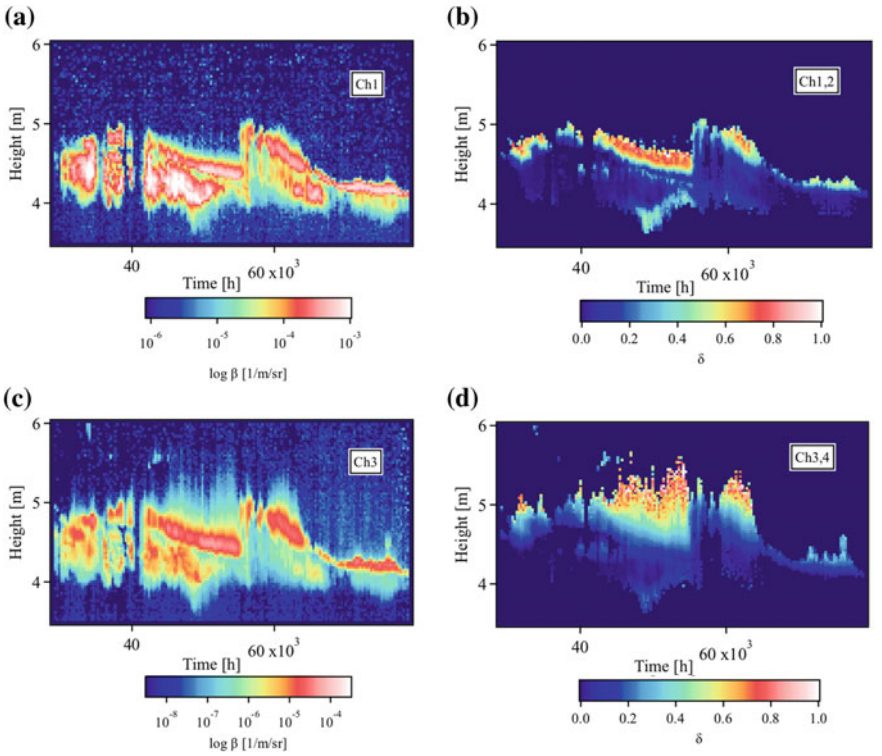

Fig. 20 As described in Fig. 16, but showing the **a**, **c** backscattering coefficient and **b**, **d** depolarization ratio observation of a mixed-phase cloud from MFMSPL-1 obtained at NIES in December 2015

development for the first space-borne HSRL measurement from the EarthCARE mission (Okamoto et al. 2019a).

5 Summary and Future Studies

In this paper, we introduced two single scattering theories for non-spherical particles that are effective over different size parameter ranges, i.e., PO theory and DDA. Efforts are being made by several research groups to reduce computational cost and extend the applicable size parameter range of these theories. One example of modification of the DDA involves the dipole polarizability being replaced with the a_1-term of the scattering coefficient from Mie theory to reduce computational cost. PO and DDA were applied to analyses of CloudSat radar and CALIPSO lidar measurements. Ice particle size, IWC, and mass mixing ratio of 2D and 3D ice could be retrieved. Progress is also being made with PO to infer the effects of particle shape, orientation,

and wavelength at different laser tilt angles, which is essential for the development of continuous datasets of clouds and aerosols for use in climate research (Okamoto et al. 2019b).

For multiple scattering, physical models that incorporate mechanisms to capture the major physical processes are effective when analytical solutions cannot be obtained, as the a_1-term method for the single scattering problem. In this paper, we introduced the recently developed PM approach and its vectorized version (VPM) to analyze global data from space-borne lidar with depolarization measurements affected by high-order scattering. These methods accommodate analytical expression for the high-order scattering matrix and employ the path integral approach to estimate effective extinction due to the presence of multiple scattering processes in lidar returns. The computational costs were drastically reduced compared to Monte Carlo simulations. The forthcoming EarthCARE mission (JAXA/ESA 2021) will carry a high-sensitivity 94 GHz Doppler cloud profiling radar (CPR), 355 nm high-spectral-resolution lidar (ATLID), 7-channel multi-spectral imager (MSI), and broadband radiometer (BBR). New challenges, such as multiple scattering effects on Doppler velocity (Battaglia and Tanelli 2011) and the Rayleigh channel of high-spectral-resolution lidar (Jin et al. 2019), will arise with these new technologies.

MFOV measurements from space may be useful, as suggested by ground-based MFMSPL observation results. Observations with MFMSPL have revealed interesting changes in the depolarization ratios of water clouds and mixed-phase clouds between on-beam and off-beam detectors. Extension of this ground-based satellite simulator based on multiple scattering is underway to clarify the information content of single scattering and multiple scattering returns from current and forthcoming space-borne active sensor missions including the CALIPSO/CloudSat, ADM-Aeolus, and EarthCARE satellites (Okamoto et al. 2018b).

Acknowledgements This study was supported by the JSPS KAKENHI Grant Numbers JP18K03745, JP17H06139, in part by The Japan Aerospace Exploration Agency (EarthCARE satellite mission), Ministry of Education, Culture, Sports, Science and Technology (The Arctic Challenge for Sustainability (ArCS)) and by the Collaborated Research Program of Research Institute for Applied Mechanics, Kyushu University (Fukuoka, Japan). We acknowledge Drs. T. Nishizawa, N. Sugimoto, Y. Jin, A. Shimizu (National Institute of Environmental Studies) and Mr. M. Fujikawa (Kyushu University) for the MSFMPL-1 data, and Dr. T. Takano (Chiba University) for the 95-GHz cloud radar (FALCON-1) data, which were operated under the JSPS KAKENHI Grant Number JP25247078. We also thank Drs. Y. Hagihara, M. Kikuchi (JAXA) and E. Oikawa (Kyushu University) for the KU-products. The CloudSat and CALIPSO data were provided by the CloudSat data processing center and NASA Atmospheric Science Data Center, respectively. The atmospheric sounding data was provided by the University of Wyoming.

References

Battaglia A, Tanelli S (2011) Doppler multiple scattering simulator. IEEE Trans Geosci Remote Sens 49:442–450. https://doi.org/10.1109/TGRS.2010.2052818

Battaglia A, Haynes JM, L'Ecuyer T, Simmer C (2008) Identifying multiple- scattering affected profiles in CloudSat observations over the oceans. J Geophys Res 113, D00A17. 10.1029/2008JD009960

Battaglia A et al (2010) Multiple-scattering in radar systems: a review. JQSRT. https://doi.org/10.1016/j.jqsrt.2009.11.024

Battaglia A, Tanelli S, Heymsfield GM, Tian L (2014) The dual wavelength ratio knee: a signature of multiple scattering in airborne Ku–Ka observations. J Appl Meteor Climatol 53:1790–1808. https://doi.org/10.1175/JAMC-D-13-0341.1

Battaglia A, Tanelli S, Mroz K, Tridon F (2015) Multiple scattering in observations of the GPM dual-frequency precipitation radar: evidence and impact on retrievals. J Geophys Res Atmos 120:4090–4101. https://doi.org/10.1002/2014JD022866

Battaglia A, Mroz K, Tanelli S, Tridon F, Kirstetter P (2016) Multiple-scattering-induced "ghost echoes" in GPM DPR observations of a tornadic supercell. J Appl Meteor Climatol 55:1653–1666. https://doi.org/10.1175/JAMC-D-15-0136.1

Bi L, Yang P, Kattawar GW, Baum BA, Hu YX, Winker DM, Brock RS, Lu JQ (2009) Simulation of the color ratio associated with the backscattering of radiation by ice particles at the wavelengths of 0.532 and 1.064 μm. J Geophys Res 114:D00H08. https://doi.org/10.1029/2009jd011759

Bissonnette LR (1996) Multiple-scattering lidar equation. Appl Opt 35:6449–6465

Bissonnette (2005) Lidar and multiple scattering in lidar. In: Weitkamp C (ed) Springer, Newyork

Bissonnette LR, Roy G, Fabry F (2001) Range–height scans of lidar depolarization for characterizing properties and phase of clouds and precipitation. J Atmos Oceanic Technol 18:1429–1446. https://doi.org/10.1175/1520-0426(2001)018%3c1429:RHSOLD%3e2.0.CO;2

Bohren CF, Huffman DR (1983) Absorption and scattering of light by small particles. Wiley

Borovoi AG (2013) Light scattering by large particles: physical optics and the shadow-forming field. In: Kokhanovsky A (ed) Light scattering reviews, vol 8. Springer Praxis Books. Springer, Berlin, Heidelberg

Borovoi A, Konoshonkin A, Kustova N, Okamoto H (2012) Backscattering mueller matrix for quasi-horizontally oriented ice plates of cirrus clouds: application to CALIPSO signals. Opt Express 20:28222–28233. https://doi.org/10.1364/OE.20.028222

Borovoi AG, Kustova NV, Oppel UG (2005) Light backscattering by hexagonal ice crystal particles in the geometrical optics approximation. Opt Eng 44(7):071208

Cahalan RF, McGill M, Kolansinski J (2005) THOR-cloud thickness from offbeam lidar returns. J Atmos Ocean Technol 22(6):605–627

Cai Q, Liou K (1981) Theory of time-dependent multiple backscattering from clouds. J Atmos Sci 38:1452–1466

Cai Q, Liou K (1982) Polarized light scattering by hexagonal ice crystals: theory. Appl Opt 21:3569–3580

Cesana G, Chepfer H, Winker D, Getzewich B, Cai X, Jourdan O, Mioche G, Okamoto H, Hagihara Y, Noel V, Reverdy M (2016) Using in situ airborne measurements to evaluate three cloud phase products derived from CALIPSO. J Geophys Res 121:5788–5808

Davis AB, Cahalan RF, Spinhirne JD, McGill MJ, Love SP (1999) Offbeam lidar: an emerging technique in cloud remote sensing based on radiative green-function theory in the diffusion domain. Phys Chem Earth B 24:177–185

Davis A (2008) Multiple-scattering lidar from both sides of the clouds: addressing internal structure. J Geophys Res 113(D14):D14S10

Deng M, Mace GG, Wang Z, Okamoto H (2010) Tropical composition, cloud and climate coupling experiment validation for cirrus cloud profiling retrieval using CloudSat radar and CALIPSO lidar. J Geophys Res 115(D00J15):1–18

Donovan DP, van Lammeren ACAP (2001) Cloud effective particle size and water content profile retrievals using combined lidar and radar observations, 1, Theory and simulations. J Geophys Res 106:27,425–27,448

Donovan DP, Baltink K, Henzing H, de Roode SR, Siebesma AP (2015) A depolarisation lidar-based method for the determination of liquid-cloud microphysical properties. Atmos Meas Tech 8:237–266. https://doi.org/10.5194/amt-8-237-2015

Draine BT (1988) The discrete-dipole approximation and its application to interstellar graphite grains. Astrophys J 333:848–872

Draine BT, Flatau PJ (1994) Discrete-dipole approximation for scattering calculations. J Opt Soc Am A 11:1491–1499

Draine BT, Goodman J (1993) Beyond Clausius-Mossotti: wave propagation on a polarizable point lattice and the discrete dipole approximation. Astrophys J 405:685–697

Dungey CE, Bohren CF (1993) Backscattering by nonspherical hydro- meteors as calculated by the coupled-dipole method: an application in radar meteorology. J Atmos Oceanic Technol 10:526–532

Einstein A (1917) Zur Quantentheorie der Strahlung (On the quantum theory of radiation). Phys Z 18:121–128

Eloranta EW (1998) Practical model for the calculation of multiply scattered lidar returns. Appl Opt 37:2464–2472

Evans KF, Vivekanandan J (1990) Multiparameter radar and microwave radiative transfer modeling of nonspherical atmospheric ice particles. IEEE Trans Geosci Remote Sens 28:423–443

Fernández-Varea JM, Mayol R, Baró J, Salvat F (1993) On the theory and simulation of multiple elastic scattering of electrons. Nucl Instrum Methods Phys Res, Sect B 73:447–473

Feynman RP (1949) Space-time approach to quantum electrodynamics. Phys Rev 76(6):769–789

Fiocco G, Smulin LD (1963) Detection of scattering layers in the upper atmosphere (60–140 km) by Optical radar. Nature 199:1275–1276. https://doi.org/10.1038/1991275a0

Flatau PJ, Stephens GL, Draine BT (1990) Light scattering by rectangular solids in the discrete-dipole approximation: a new algorithm exploiting the Block-Toeplitz structure. J Opt Soc Am A 7:593–600

Frisch AS, Fairall CW, Snider JB (1995) Measurement of stratus cloud and drizzle parameters in ASTEX with a Ka-band Doppler radar and a microwave radiometer. J Atmos Sci 52:2788–2799. https://doi.org/10.1175/1520-0469(1995)052%3c2788:MOSCAD%3e2.0.CO;2

Fuller KW (1991) Optical resonances and two-sphere systems. Appl Opt 30:4716–4731

Gettelman A, Sherwood SC (2016) Processes responsible for cloud feedback. Curr Clim Change Rep 2:179. https://doi.org/10.1007/s40641-016-0052-8

Goedecke GH, O'Brien SG (1988) Scattering by irregular inhomogeneous particles via the digitized Green's function algorithm. Appl Opt 28:2431–2438

Gordon JP, Zeiger HJ, Townes CH (1954) Molecular microwave oscillator and new hyperfine structure in the microwave spectrum of NH_3. Phys Rev 95(1):282–284. https://doi.org/10.1103/PhysRev.95.282

Gordon JP, Zeiger HJ, Townes CH (1955) The maser—new type of microwave amplifier, frequency standard, and spectrometer. Phys Rev 99:1264–1274. https://doi.org/10.1103/physrev.99.1264

Goudsmit S, Saunderson JL (1940) Multiple scattering of electrons. Phys Rev 57:24–29

Hage JI, Greenberg JM (1990) A model for the optical properties of porous grains. Astrophys J 361:260–274

Hagihara Y, Okamoto H, Yoshida R (2010) Development of a combined CloudSat-CALIPSO cloud mask to show global cloud distribution. J Geophys Res 115(D00H33):1–17

Heffels C, Heitzmann D, Hirlemann ED, Scarlett B (1995) Forward light scattering for arbitrary sharp-edged convex crystals in Fraunhofer and anomalous diffraction approximations. Appl Opt 34(28):6552–6560

Heymsfield AJ, Protat A, Austin R, Bouniol D, Hogan R, Okamoto H, Sato K, Zadelhoff G, Donovan D, Wang Z (2008) Testing and evaluation of ice water content retrieval methods using radar and ancillary measurements. J Appl Meteorol Climatol 47:135–163. https://doi.org/10.1175/2007JAMC1606.1

Hogan RJ (2008) Fast lidar and radar multiple-scattering models. Part I: small-angle scattering using the photon variance-covariance method. J Atmos Sci 65:3621–3635

Hogan RJ, Battaglia A (2008) Fast lidar and radar multiple-scattering models. Part II: wide-angle scattering using the time-dependent two-stream approximation. J Atmos Sci 65:3636–3651

Hu Y et al. (2007) Depolarization ratio-effective lidar ratio relation: theoretical basis for space lidar cloud phase discrimination. Geophys Res Lett 34(11):L11812

Hunt WH, Winker DM, Vaughan MA, Powell KA, Lucker PL, Weimer C (2009) CALIPSO lidar description and performance assessment. J Atmos Oceanic Technol 26:1214–1228

Illingworth AJ, Barker HW, Beljaars A, Ceccaldi M, Chepfer H, Clerbaux N, Cole J, Delanoë J, Domenech C, Donovan DP, Fukuda S, Hirakata M, Hogan RJ, Huenerbein A, Kollias P, Kubota T, Nakajima T, Nakajima TY, Nishizawa T, Ohno Y, Okamoto H, Oki R, Sato K, Satoh M, Shephard MW, Velázquez-Blázquez A, Wandinger U, Wehr T, van Zadelhoff G (2015) The EarthCARE satellite: the next step forward in global measurements of clouds, aerosols, precipitation, and radiation. Bull Am Meteor Soc 96:1311–1332. https://doi.org/10.1175/BAMS-D-12-00227.1

Ishimaru A (1997) Wave propagation and scattering in random media. Wiley-IEEE Press

Ishimoto H (2008) Radar backscattering computations for fractal-shaped snowflakes. J Meteorol Soc Jpn Ser II 86(3):459–469. https://doi.org/10.2151/jmsj.86.459

Iwasaki S, Okamoto H (2001) Analysis of the enhancement of backscattering by nonspherical particles with flat surfaces. Appl Opt 40(33):6121–6129

Javan A, Bennett WR Jr, Herriott DR (1961) Population inversion and continuous optical maser oscillation in a gas discharge containing a He-Ne mixture. Phys Rev Lett 6:106. https://doi.org/10.1103/PhysRevLett.6.106

Jin Y, Nishizawa T, Sugimoto N, Okamoto H, Sato K (2019) Development of a wide-field-of-view high-spectral-resolution lidar at 532 nm, paper presented at ISALSaRS'19

Kadri O, Ivanchenko V, Gharbi F, Trabelsi A (2009) Incorporation of the Goudsmit–Saunderson electron transport theory in the Geant4 Monte Carlo code. Nucl Instrum Methods Phys Res Sect B Beam Interact Mater Atoms 267(23–24):3624–3632. ISSN 0168-583X, https://doi.org/10.1016/j.nimb.2009.09.015

Kikuchi M, Okamoto H, Sato K, Suzuki K, Cesana G, Hagihara Y, Takahasi N, Hayasaka T, Oki R (2017) Development of algorithm for discriminating hydrometeor particle types with a synergistic Use of CloudSat and CALIPSO. J Geophys Res 122:11022–11044

Kimura H, Okamoto H, Mukai T (2002) Radiation pressure and the Poynting-Robertson effect for fluffy dust particles. Icarus 157(2):349–361. https://doi.org/10.1006/icar.2002.6849

Kobayashi S, Ito S, Tanelli S, Oguchi T, Im E (2007) A time-dependent multiple scattering theory for a pulsed radar with a finite beam width. Radio Sci 42:RS4001. https://doi.org/10.1029/2006rs003555

Konoshonkin A, Borovoi A, Kustova N, Okamoto H, Ishimoto H, Grynko Y, Foestner J (2017) Light scattering by ice crystals of cirrus clouds: from exact numerical methods to physical-optics approximation. J Quant Spectrosc Radiat Transfer 195:132–140. https://doi.org/10.1016/j.jqsrt.2016.12.024

Lemke H, Quante M (1999) Potential of polarimetric radar measurements. J Geophys Res 104:31739–31751

Lewis HW (1950) Multiple scattering in an infinite medium. Phys Rev 78:526–529

Lhermite R (1987) A 94-GHzDoppler radar for cloud observations. J Atmos Oceanic Technol 4:36–48

Li J, Nakamura K (2002) Characteristics of the mirror image of precipitation observed by the TRMM precipitation radar. J Atmos Oceanic Technol 19:145–158. https://doi.org/10.1175/1520-0426(2002)019%3c0145:COTMIO%3e2.0.CO;2

Liou KN (2002) An introduction to atmospheric radiation Academic Press

Liversay DE, Chen K (1974) Electromagnetic fields induced inside arbitrarily shaped biological bodies. IEEE Trans Microwave Theory Tech MTT-22 1273–1280

Lu X, Hu Y, Trepte C, Zeng S, Churnside JH (2014) Ocean subsurface studies with the CALIPSO spaceborne lidar. J Geophys Res Oceans 119:4305–4317. https://doi.org/10.1002/2014jc009970

Lukishova SG (2010) Valentin A. Fabrikant: negative absorption, his 1951 patent application for amplification of electromagnetic radiation (ultraviolet, visible, infrared and radio spectral regions) and his experiments. J Eur Opt Soc Rapid Publ Eur 5

Macke A, Mueller J, Raschke E (1996) Single scattering properties of atmospheric ice crystals. J Atmos Sci 53:2815–2825

Mackowski DW (1991) Analysis of radiative scattering for multiple sphere configurations. Proc R Soc Lond Ser A 433:599–614

Maiman TH (1960) Stimulated optical radiation in ruby. Phys Rev Lett 4(11):564–566

Maruyama K, Fujiyoshi Y (2005) Monte Carlo simulation of the formation of snow akes. J Atmos Sci 62:1529–1544

Masuda K, Ishimoto H (2017) Backscatter ratios for nonspherical ice crystals in cirrus clouds calculated by geometrical-optics-integral-equation method. J Quant Spectrosc Radiat Transfer 190:60–68. https://doi.org/10.1016/j.jqsrt.2017.01.024

Masuda K, Ishimoto H, Mano Y (2012) Efficient method of computing a geometric optics integral for light scattering by nonspherical particles. Pap Meteorol Geophys 63:15–19

Miller SD, Stephens GL (1999) Multiple scattering effects in the lidar pulse stretching problem. J Geophys Res 104(D18):22205–22219. https://doi.org/10.1029/1999JD900481

Mishchenko MI (1993) Light scattering by size-shape distributions of randomly oriented axially symmetric particles of a size comparable to a wavelength. Appl Opt 32:4652–4666

Mishchenko MI, Wielaard DJ, Carlson BE (1997) T-Matrix computations of zenith-enhanced lidar backscatter from horizontally oriented ice plates. Geophys Res Lett 24:7. https://doi.org/10.1029/97GL00545,771-774

MODIS Science Team, Gao B-C, Menzel P, King M (2006) MODIS/Aqua Clouds 1 km and 5 km 5-Min L2 Narrow Swath Subset along CloudSat, Edited by GES DISC, Greenbelt, MD, USA, Goddard Earth Sciences Data and Information Services Center (GESDISC). https://disc.gsfc.nasa. gov/datacollection/MAC06S0_002.html

Moteki N (2016) Discrete dipole approximation for black carbon-containing aerosols in arbitrary mixing state: a hybrid discretization scheme. J Quant Spectrosc Radiat Transfer 178:306–314. https://doi.org/10.1016/j.jqsrt.2016.01.025

Mullholland GW, Bohren CF, Fuller KA (1994) Light scattering by agglomerates: coupled electric and magnetic dipole method. Langmuir 10:2533–2546

Okamoto H (1995) Light scattering by clusters: the a_1-term method. Opt Rev 2:407–412

Okamoto H (2002) Information content of the 95-GHz cloud radar signals: theoretical assessment of nonsphericity and error evaluation of the discrete dipole approximation. J Geophys Res 107:4628. https://doi.org/10.1029/2001jd001386

Okamoto H, Xu Y (1998) Light scattering by irregular interplanetary dust particles. Earth Planets Space 50:577. https://doi.org/10.1186/BF03352151

Okamoto H, Mukai T, Kozasa T (1994) The 10 μm-feature of aggregates in comets. Planet Space Sci 42:643–649

Okamoto H, Macke A, Quante M, Raschke E (1995) Modeling of backscattering by non-spherical ice particles for the interpretation of cloud radar signals at 94 GHz. An error analysis. Beitr Phys Atmosph 68:319–334

Okamoto H, Iwasaki S, Yasui M, Horie H, Kuroiwa H, Kumagai H (2000) 95-GHz cloud radar and lidar systems: Preliminary results of cloud microphysics. Proc SPIE 4152:355–363

Okamoto H, Iwasaki S, Yasui M, Horie H, Kuroiwa H, Kumagai H (2003) An algorithm for retrieval of cloud microphysics using 95-GHz cloud radar and lidar. J Geophys Res 108(D7):4226. https://doi.org/10.1029/2001jd001225.2003

Okamoto H, Sato K, Hagihara Y (2010) Global analysis of ice microphysics from CloudSat and CALIPSO: incorporation of Specular Reaction in Lidar Signals. J Geophys Res 115:D22209. https://doi.org/10.1029/2009JD013383

Okamoto H, Sato K, Hagihara Y, Matsumoto T, Borovo A (2012) Retrieved ice microphysics from Calipso and Cloudsat and horizontally oriented ice plate. In: 26th International laser radar conference on reviewed and revised papers, pp 687–690

Okamoto H, Sato K, Nishizawa T, Sugimoto N, Makino T, Jin Y, Shimizu A, Takano T, Fujikawa M (2016) Development of a multiple-field-of-view multiple-scattering polarization lidar: comparison with cloud radar. Opt Express 24:30053–30067. https://doi.org/10.1364/OE.24.030053

Okamoto H, Sato K (2018a) Cloud remote sensing by active sensors: new perspectives from CloudSat, CALIPSO and EarthCARE, Remote sensing of clouds and precipitation. Springer Remote Sensing/Photogrammetry. https://doi.org/10.1007/978-3-319-72583-3_8

Okamoto H, Sato K, Ishii S, Aoki M, Nishizawa T, Sugimoto N, Jin Y, Ohno Y, Horie H (2018b) Next-generation-synergetic-observation-system for the unified analysis of CALIPSO, ADM-Aeolus and EarthCARE-ATLID. In: Proceedings of CLRC2018, We6, pp 1–4

Okamoto H, Sato K, Fujikawa M, Oikawa E, Nishizawa T, Ishii S, Jin Y, Aoki M, Sugimoto N (2019a) Development of synergetic-active sensor-system for evaluation of observations by earthcare. ProcILRC29

Okamoto H, Sato K, Borovoi A, Ishimoto H, Masuda K, Konoshonkin A, Kustova N (2019b) Interpretation of lidar ratio and depolarization ratio of ice clouds using spaceborne high-spectral-resolution polarization lidar. Opt Express 27:36587–36600. https://doi.org/10.1364/OE.27.036587

Perelman LT, Wu J, Itzkan I, Feld MS (1994) Photon migration in turbid media using path integrals. Phys Rev Lett 72(9):1341–1344

Petty GW, Huang W (2011) The modified gamma size distribution applied to inhomogeneous and nonspherical particles: key relationships and conversions. J Atmos Sci 68:1460–1473. https://doi.org/10.1175/2011JAS3645.1

Platt CMR (1978) Lidar backscatter from horizontal ice crystal plates. J Appl Meteorol 17:482–488

Platt CMR (1981) Remote sounding of high clouds. III: Monte Carlo calculations of multiple-scattered lidar returns. J Atmos Sci **38**(1):156–167

Polonsky NI, Love SP, Davis AB (2005) Wide-angle imaging lidar development at the ARM southern great plains site: intercomparison of cloud property retrievals. J Atmos Ocean Technol 22(6):628–648

Pounder NL, Hogan RJ, Varnai T, Battaglia A, Cahalan RF (2011) A variational method to retrieve the extinction profile in liquid clouds using multiple-field-of-view lidar. J Appl Meteorol Climatol 51:350–365

Purcell EM, Pennypacker CR (1973) Scattering and absorption of light by nonspherical dielectric grains. Astrophys J 186:705–714

Roy G, Roy N (2008) Relation between circular and linear depolarization ratios under multiple-scattering conditions. Appl Opt 47:6563–6579

Roy G, Bissonnette L, Bastille C, Vallée G (1999) Retrieval ofd roplet-size density distribution from multiple- field-of-view cross-polarized lidar signals: theory and experimental validation. Appl Opt 38(24):5202–5211

Roy G, Tremblay G, Cao X (2018) Scattering phase function depolarization parameter model and its application to water droplets sizing using off-axis lidar measurements at multiple angles. Appl Opt 57:969–977

Sassen K (1991) The polarization lidar technique for cloud research: a review and current assessment. Bull Am Meteorol Soc 72:1848–1866

Sassen K, Zhu J (2009) A global survey of CALIPSO linear depolarization ratios in ice clouds: initial findings. J Geophys Res 114(D00H07). https://doi.org/10.1029/2009jd012279

Sassen K, Kayetha VK, Zhu J (2012) Ice cloud depolarization for nadir and off-nadir CALIPSO measurements. Geophys Res Lett 39:L20805. https://doi.org/10.1029/2012GL053116

Sato K, Okamoto H (2006) Characterization of Ze and LDR of nonspherical and inhomogeneous ice particles for 95-GHz cloud radar: Its implication to microphysical retrievals. J Geophys Res 111:D22213. https://doi.org/10.1029/2005JD006959

Sato K, Okamoto H (2011) Refinement of global ice microphysics using space- borne active sensors. J Geophys Res 116:D20202. https://doi.org/10.1029/2011JD015885

Sato K, Okamoto H, Yamamoto MK, Fukao S, Kumagai H, Ohno Y, Horie H, Abo M (2009) 95-GHz Doppler radar and lidar synergy for simultaneous ice microphysics and in-cloud vertical air motion retrieval. J Geophys Res 114:D03203. https://doi.org/10.1029/2008JD010222

Sato K, Okamoto H, Takemura T, Kumagai H, Sugimoto N (2010) Characterization of ice cloud properties obtained by shipborne radar/lidar over the tropical western Pacific Ocean for evaluation of an atmospheric general circulation model. J Geophys Res 115:D15203. https://doi.org/10.1029/2009JD012944

Sato K, Okamoto H, Ishimoto H (2016) Modeling lidar multiple scattering. EPJ Web Conf 119:21005. https://doi.org/10.1051/epjconf/201611921005

Sato K, Okamoto H, Ishimoto H (2018) Physical model for multiple scattered space-borne lidar returns from clouds. Opt Express 26:A301–A319. https://doi.org/10.1364/OE.26.00A301

Sato K, Okamoto H, Ishimoto H (2019) Modeling the depolarization of space-borne lidar signals. Opt Express 27:A117–A132. https://doi.org/10.1364/OE.27.00A117

Satoh M, Matsuda Y (2009) Statistics on high cloud areas and their sensitivities to cloud microphysics using single cloud experiments. J Atmos Sci 66:2659–2677. https://doi.org/10.1175/2009JAS2948.1

Schalow AL, Townes CH (1958) Infrared and optical masers. Phys Rev 112(6):1940–1949

Scotland RM, Sassen K, Stone RJ (1971) Observations by lidar of linear depolarization ratios by hydrometeors. J Appl Meteorol 10:1011–1017

Spinhirne JD, Palm SP, Hart WD, Hlavka DL, Welton EJ (2005) Cloud and aerosol measurements from GLAS: overview and initial results. Geophys Res Lett 32:L2S03. https://doi.org/10.1029/2005GL023507

Stephens GL, Tsay S-C, Stackhouse PW Jr, Flatau PJ (1990) The relevance of the microphysical and radiative properties of cirrus clouds to climate and climatic feedback. J Atmos Sci 47:1741–1753

Stephens G, Winker D, Pelon J, Trepte C, Vane D, Yuhas C, L'Ecuyer T, Lebsock M (2018) CloudSat and CALIPSO within the a- train: ten years of actively observing the earth system. Bull Am. Met Soc 99:569–581. https://doi.org/10.1175/BAMS-D-16-0324.1

Stoffelen A, Pailleux J, Källén E, Vaughan JM, Isaksen L, Flamant P, Wergen W, Andersson E, Schyberg H, Culoma A, Meynart R, Endemann M, Ingmann P (2005) The atmospheric dynamics mission for global wind field measurement. Bull Am Meteorol Soc 86:73–88. https://doi.org/10.1175/BAMS-86-1-73

Townes CH (1999) How the laser happened. Adventure of a scientist. Oxford University Press, Oxford

Tsushima Y, Emori S, Ogura T, Kimoto M, Webb MJ, Williams KD, Ringer MA, Soden BJ, Li B, Andronova N (2006) Importance of the mixed phase cloud distribution in the control climate for assessing the response of clouds to carbon dioxide increase: a multi model study. Clim Dyn 27:113–126. https://doi.org/10.1007/s00382-006-0127-7

Wallace J, Hobbs P (2005) Atmospheric science, 2nd edn. An introductory survey. Academic Press

Wandinger U (1998) Multiple-scattering influence on extinction- and backscatter-coefficient measurements with Raman and high-spectral-resolution lidars. Appl Opt 37:417–427

Wang Z, Sassen K (2002) Cirrus cloud microphysical property retrieval using lidar and radar measurements: Part I. Algorithm description and comparison with in situ data. J Appl Meteorol 41:218–229

Watanabe M, Suzuki T, O'ishi R, Komuro Y, Watanabe S, Emori S, Takemura T, Chikira M, Ogura T, Sekiguchi M, Takata K, Yamazaki D, Yokohata T, Nozawa T, Hasumi H, Tatebe H, Kimoto M (2010) Improved climate simulation by MIROC5: mean states, variability, and climate sensitivity. J Clim 23:6312–6335

West RA (1991) Optical properties of aggregate particles whose outer diameter is comparable to the wavelength. Appl Opt 30:5316–5324

Winker DM, Poole LR (1995) Monte-Carlo calculations of cloud returns for ground-based and space-based lidars. Appl Phys B 60:341–344

Winker DM, Couchand RH, McCormich MP (1996) An overview of LITE: NASA's lidar in-space technology experiment. Proc IEEE 84:164–180

Winker DM, Hunt WH, McGil MJ (2007) Initial performance assessment of CALIOP. Geophys Res Lett 34:L19803. https://doi.org/10.1029/207GL030135

Winker DM, Vaughan MA, Omar A, Hu Y, Powell KA, Liu Z, Hunt WH, Young SA (2009) Overview of the CALIPSO mission and CALIOP data processing algorithms. J Atmos Oceanic Technol 26:2310–2323

Winker DM, Pelon J, Coakley JA, Ackerman SA, Charlson RJ, Colarco PR, Flamant P, Fu Q, Hoff RM, Kittaka C, Kubar TL, Le Treut H, Mccormick MP, Mégie G, Poole L, Powell K, Trepte C, Vaughan MA, Wielicki BA (2010) The CALIPSO mission. Bull Am Meteorol Soc 91:1211–1230. https://doi.org/10.1175/2010BAMS3009.1

Xu Y (1995) Electromagnetic scattering by an aggregate of spheres. Appl Opt 34:4573–4588

Xu Y (2001) Electromagnetic scattering by an aggregate of spheres. Appl Opt 34:4573–4588 (1995); errata Appl Opt 40:5508–5508. https://doi.org/10.1364/ao.40.005508

Yamaguchi J, Takano T, Nakajima T, Takamura T, Kumagai H, Ohno Y, Nakanishi Y, Akita K, Kawamura Y, Abe H, Futaba K, Yokote S (2006) Sensitivity of FMCW 95 GHz cloud radar for high clouds. In: Proceedings of Asia-Pacific microwave conference

Yang P, Liou K (1996) Finite-difference time domain method for light scattering by small ice crystals in three-dimensional space. J Opt Soc Am A 13:2072–2085

Yoshida R, Okamoto H, Hagihara Y, Ishimoto H (2010) Global analysis of cloud phase and ice crystal orientation from Cloud-Aerosol Lidar and Infrared Pathfinder Satellite Observation (CALIPSO) data using attenuated backscattering and depolarization ratio. J Geophys Res 115:D00H32. https://doi.org/10.1029/2009jd012334

Zege EP, Chaikovskaya LI (1996) New approach to the polarized radiative transfer problem. J Quant Spectrosc Radiat Transf 55(1):19–31

Airborne Remote Sensing of Arctic Clouds

André Ehrlich, Michael Schäfer, Elena Ruiz-Donoso and Manfred Wendisch

1 Introduction

Airborne remote sensing builds a bridge between long-term ground-based measurements and space-borne satellite observations. In the Arctic, only a few sites continuously run ground-based remote sensing measurements of the atmosphere. Satellite observations are limited to several daily overpasses and typically have a lower spatial resolution compared to airborne remote sensing. Airborne observations are mostly performed with a specific scientific objective during individual campaigns which cover a limited time period and area. A strong focus of Arctic airborne remote sensing measurements is the characterization of cloud and surface properties. Clouds and snow-covered land or sea ice reflect solar radiation more efficiently compared to the open ocean and, therefore, have a strong radiative impact on the Arctic surface energy budget (Wendisch et al. 2017). To quantify the radiative forcing of clouds and sea ice, their radiative and microphysical properties need to be retrieved by remote sensing observations. The cloud reflectivity, transmissivity, and absorptivity in the solar spectral range are determined by the cloud optical thickness, which is linked to the total water path and the cloud particle size. In the Arctic, cloud particles are formed by either liquid droplets or ice crystals of different shape. As both have significantly different scattering properties, the cloud thermodynamic phase is an important quantity to be retrieved by airborne remote sensing (Curry et al. 1996; Ehrlich et al. 2008).

The following sections will concentrate on the airborne remote sensing of Arctic cloud properties although a multitude of other components of the Artic climate system such as surface, aerosol and trace gases can be retrieved using airborne observations.

Snow and ice surfaces are characterized by a high surface albedo, which significantly depend on the type of sea ice, the thickness of the snow, and the grain size of

A. Ehrlich (✉) · M. Schäfer · E. Ruiz-Donoso · M. Wendisch
Leipzig Institute for Meteorology (LIM), University of Leipzig, Leipzig, Germany
e-mail: a.ehrlich@uni-leipzig.de

A. Kokhanovsky (ed.), *Springer Series in Light Scattering*,
Springer Series in Light Scattering,
https://doi.org/10.1007/978-3-030-38696-2_2

snow particles. Active airborne remote sensing techniques using radar provide geometric properties of the sea ice such as sea ice fraction, thickness, and the depth of the snow (Haas et al. 2017). On the other hand, passive solar remote sensing measurements characterize the optical snow and sea ice properties such as the spectral surface albedo, the directional reflectivity, and the effective snow grain size (Lyapustin et al. 2010; Carlsen et al. 2017).

Airborne remote sensing of Arctic aerosol particles is limited to active lidar techniques and sun-photometer observations (Nott and Duck 2011; Stone et al. 2014). Lidar observations provide vertical profiles of aerosol backscatter and extinction coefficients for a few wavelengths above or below the aircraft platform. Sun photometers measure the aerosol optical depth (AOD) at different spectral channels, which can be used to retrieve the size distribution of the aerosol particles. Over the bright Arctic snow and ice surfaces, airborne remote sensing measurements of the reflected solar radiation are almost insensitive to the rather low aerosol concentrations. Comparing lidar observation with airborne aerosol remote sensing of the reflected solar radiation, it was shown, that due to the bright Arctic snow and ice surfaces the later are almost insensitive to the rather low aerosol concentrations found in the Arctic and require multi-view observations which become capable to retrieve AOD (Tomasi et al. 2015).

Atmospheric trace gas concentrations, e.g., water vapor, ozone, nitrogen dioxide, bromine monoxide can be retrieved using airborne observations by the active differential absorption lidar technique (Wirth et al 2009), passive differential optical absorption spectroscopy (DOAS, Hüneke et al. 2017), and limb observations of the emitted spectral terrestrial radiation (Riese et al. 2014).

In the following Sect. 2, a typical combination of airborne remote sensing instruments applied to characterize clouds is introduced. The aircraft instrumentation includes active and passive remote sensing techniques which are based on solar and microwave radiation. For passive solar remote sensing of cloud properties, the Arctic environment poses an additional degree of complexity. These challenges are discussed by different exemplary observations in Sect. 3. Advanced airborne remote sensing techniques aim to overcome these challenges. Three examples of how airborne observations are used to analyse properties of Arctic clouds are introduced in the following sections. The use of spectral information of the reflected solar radiation to derive the cloud thermodynamic phase and a combined retrieval of snow and cloud radiative properties are explored in Sect. 4. The capabilities of directional radiation measurements to retrieve cloud properties of the uppermost cloud layer are discussed in Sect. 5. The benefits of imaging spectrometer observations which provide a two-dimensional view on Arctic clouds with high spatial resolution are discussed in Sect. 6. Concluding remarks are summarized in Sect. 7.

2 Airborne Remote Sensing Instrumentation

Instruments for airborne remote sensing of cloud properties mostly apply techniques similar to those on geostationary and polar orbiting satellite, which use observations of electromagnetic radiation at different wavelengths either reflected or emitted by the atmosphere and surface. On aircraft, advanced techniques can be applied, which can be used to validate satellite observations and help to develop new retrieval methods (Wendisch and Brenguier 2013). Due to the lower flight altitude, the spatial resolution of airborne observations is higher, however, the spatial coverage of airborne measurements is smaller than that of satellite observations. Active and passive remote sensing instruments are applied, which include solar and microwave spectro-radiometers, as well as lidar and radar.

Two examples of comprehensive remote sensing instrumentations combining the different observation techniques are listed in Table 1 and further illustrated in Fig. 1. The Polar 5 aircraft (Wesche et al. 2016) was operated during the Arctic Cloud Observations Using airborne measurements during polar Day (ACLOUD) campaign in 2017 to investigate Arctic boundary-layer clouds (Wendisch et al. 2018). On the German High Altitude and Long Range Research Aircraft (HALO) a comparable suite of remote sensing instruments was employed during the research campaigns NARVAL (Next generation Advanced Remote sensing for VALidation Studies) in August 2016 (Stevens et al. 2018) and NAWDEX (North Atlantic Waveguide and Downstream Impact Experiment) in September and October 2016 (Schäfler et al. 2018). The application of the same package of remote sensing instrumentation on HALO is also planned for EUREC4A (Elucidating the role of clouds-circulation coupling in climate) in January 2020 (Bony et al. 2017) and HALO-$(AC)^3$ (ArctiC Amplification: Climate Relevant Atmospheric and SurfaCe Processes, and Feedback Mechanisms) in March 2021 (Pithan et al. 2018). On both aircraft (Polar 5 and HALO) the Spectral Modular Airborne Radiation measurement sysTem (SMART)-Albedometer is integrated measuring the spectral solar irradiance and nadir radiance reflected by clouds, the atmosphere, and the surface (Wendisch et al. 2001, 2016). Imaging spectrometers such as the AISA (Airborne Imaging Spectrometer for Applications) Eagle/Hawk (Bierwirth et al. 2013) and the Munich Aerosol Cloud Scanner (specMACS, Ewald et al. 2016) are applied to map the spectral radiance with a spatial resolution of less than 10 m in a field of view FOV of about 35° across track. For EUREC4A and HALO-$(AC)^3$ it is planned to map thermal infrared brightness temperatures with the two-dimensional thermal infrared imager VELOX that covers 6 spectral bands in the wavelength range of 7.7–12 μm. Directional solar radiation of the entire lower hemisphere is obtained by a 180° fish-eye camera on Polar 5 in three spectral channels (Ehrlich et al. 2012). Passive microwave radiometer are implemented in the HALO Microwave Package (HAMP) on HALO and in the airborne Microwave Radar/Radiometer for Arctic Clouds (MiRAC) on Polar 5 measuring brightness temperatures in different frequency channels (Mech et al. 2014). HAMP and MiRAC additionally include an active cloud radar systems operating at 36 GHz frequency (HAMP) and 94 GHz (MiRAC). In both configurations, active

Table 1 Remote sensing instruments installed on Polar 5 during ACLOUD (Wendisch et al. 2018) and HALO during NARVAL-II (Stevens et al. 2018), NAWDEX (Schäfler et al. 2018)

Names/acronyms	Technique	Measured/retrieved quantities	R: Range of measurement	Time resolution
Polar 5 (ACLOUD)				
SMART-Albedometer	Passive solar	Spectral irradiance (upward, downward)	R: $\lambda = 350-2200$ nm; $\Delta\lambda = 2-16$ nm	2 Hz
		Spectral radiance (upward, $FOV = 2.1°$)	R: $\lambda = 350-1000$ nm; $\Delta\lambda = 2-10$ nm	2 Hz
AISA Eagle/Hawk	Passive solar	Spectral radiance ($FOV = 36°$, 1028 px/348 px)	R: $\lambda = 400-2500$ nm; $\Delta\lambda = 1.5-10$ nm	20–30 Hz
180° fish-eye camera	Passive solar	Spectral radiance ($FOV = 180° \times 180°$, 3908 px × 2600 px)	R: $\lambda = 446, 530, 591$ nm; $\Delta\lambda = 76, 89, 83$ nm	6 s
AMALi	Active solar (Lidar)	Particle backscattering coefficient, cloud top height, particle depolarization	R: $\lambda = 335$ nm, 532 nm	1 Hz
MiRAC	Passive microwave	Brightness temperature	R: $\nu = 89, 183, 243, 340$ GHz	1–2 s
	Active microwave (Radar)	Radar reflectivity Factor, Doppler Velocity, Doppler Spectra Width	R: $\nu = 94$ GHz	1–2 s
Sun Photometer	Passive solar (direct sun)	Spectral aerosol optical depth (AOD)	R: $\lambda = 367-1024$ nm (10 channels)	1 Hz
HALO (HALO-(AC)^3, NARVAL-II, NAWDEX)				
SMART-Albedometer	Passive solar	Spectral irradiance (upward, downward)	R: $\lambda = 350-2200$ nm; $\Delta\lambda = 2-16$ nm	2 Hz
		Spectral radiance (upward, $FOV = 2.1°$)	R: $\lambda = 350-1000$ nm; $\Delta\lambda = 2-10$ nm	2 Hz
specMACS	Passive solar	Spectral radiance ($FOV = 34°$, 1300 px/320 px)	R: $\lambda = 400-2500$ nm; $\Delta\lambda = 2.5-12$ nm	20–30 Hz

(continued)

Table 1 (continued)

Names/acronyms	Technique	Measured/retrieved quantities	R: Range of measurement	Time resolution
WALES	Active solar (Lidar)	Particle backscattering coefficient, water vapour mixing ratio, cloud top height,	R: $\lambda = 532$ nm, 935 nm (4 times), 1064 nm	1 Hz
HAMP	Passive microwave	brightness temperature	R: $\nu = 22-183$ GHz (22 channels)	1–2 s
	Active microwave (Radar)	Radar reflectivity factor, doppler velocity, doppler spectra width, depolarization ratio	R: $\nu = 35.6$ GHz	1–2 s
VELOX[a]	Passive terrestrial	Brightness temperature ($FOV = 44 \times 35°$, 640 px $\times$ 512 px)	R: $\lambda = 7.7-12\,\mu$m (6 channels)	120 Hz

[a]Not flown during NARVAL-II and NAWDEX

Fig. 1 (top): Polar 5 research aircraft as equipped during ACLOUD. (bottom): HALO research aircraft as equipped for NARVAL-II and NAWDEX

lidar systems for cloud, aerosol, and water vapor observations are implemented. The Airborne Mobile Aerosol Lidar for Arctic research (AMALi) installed on Polar 5 in nadir viewing direction (zenith view optionally possible) is a backscatter lidar with polarization capabilities (Stachlewska et al. 2010). The Water Vapor Lidar Experiment in Space (WALES) demonstrator installed on HALO combines a dial and backscatter lidar at different wavelengths (Wirth et al. 2009). On Polar 5, a Sun photometer with an active tracking system (SPTA) is installed under a quartz dome of to derive the spectral aerosol optical depth (AOD).

The following sections will focus on passive solar radiation measurements to retrieve cloud optical and microphysical properties. Especially for this retrieval purpose, the Arctic environment with mixed-phase clouds and a high surface albedo is most challenging.

Solar remote sensing instruments such as the SMART-Albedometer, AISA Eagle/Hawk, and specMACS use measurements of the spectral radiance $I_\lambda^\uparrow(\lambda)$ as a function of wavelength λ, which is reflected by clouds and the surface into the optics of the instruments. Commonly, the radiance is normalized by the incident downward solar irradiance $F_\lambda^\downarrow(\lambda)$ to yield the dimensionless cloud reflectivity $\gamma_\lambda(\lambda)$,

$$\gamma_\lambda(\lambda) = \frac{\pi \cdot I_\lambda^\uparrow(\lambda)}{F_\lambda^\downarrow(\lambda)} \tag{1}$$

The spectral resolution of these instruments is in the range of 2–16 nm (full width of half maximum) which is sufficient to resolve the spectral absorption features of the cloud reflectivity, the surface albedo, and trace gases absorptivity such as that of water vapor and oxygen. These spectral differences of the absorptivity are, e.g., used by common bi-spectral cloud retrieval algorithms to derive cloud optical thickness τ and cloud particle effective radius $r_{\text{eff,C}}$. Therefore, measurements at a non-absorbing wavelengths (e.g., $\lambda = 645\,\text{nm}$) sensitive to τ and measurements at an absorbing wavelength (e.g., $\lambda = 1640\,\text{nm}$) sensitive to $r_{\text{eff,C}}$ are analyzed (e.g., Nakajima and King 1990). The observations are compared to forward radiative transfer simulations assuming a range of values of τ and $r_{\text{eff,C}}$ to identify the best match between simulated and measured reflectivities. This approach is identical to common satellite retrievals (Platnick et al. 2017).

3 Challenges for Remote Sensing of Arctic Clouds Using Solar Radiation

3.1 Mixed-Phase Clouds

Due to the low temperatures, stratiform clouds in the Arctic boundary layer are often of mixed-phase character (Shupe 2011; Mioche et al. 2015). The coexistence of liquid water droplets and solid ice crystals in these clouds adds another dimension to the inversion problem of cloud remote sensing. As mostly either the liquid or the ice phase dominates the cloud water content (Korolev et al. 2017), for some purposes already a rough phase classification into liquid and ice clouds is useful. However, even for typical liquid water dominated mixed-phase clouds, the ice crystals can have a significant influence on the cloud reflectivity.

Figure 2 shows γ_λ simulated for clouds of different ice fractions f_I defined as the ratio of the optical thickness of ice crystals and the total cloud optical thickness (ice plus liquid water). For the simulations a cloud optical thickness of $\tau = 20$, a

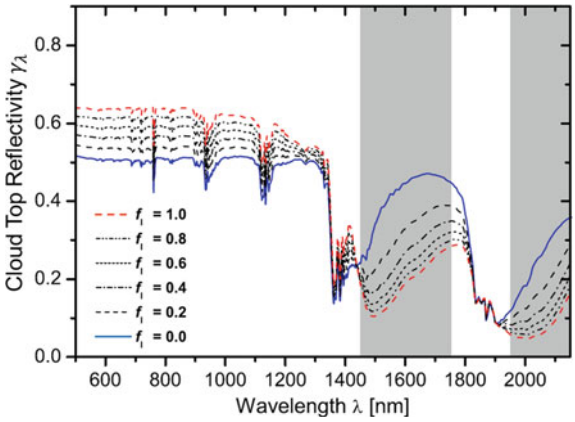

Fig. 2 **a** Cloud top reflectivity γ_λ simulated for clouds of various ice fraction f_I with fixed cloud optical thickness of $\tau = 20$, cloud droplet of $r_{eff,C} = 7.5$ μm, and ice crystal sizes of $r_{\text{eff,I}} = 90$ μm (columns). The wavelength ranges with enhanced liquid water and ice absorption are highlighted gray (adapted from Ehrlich 2009)

cloud droplet effective radius of $r_{\text{eff,C}} = 7.5\mu\text{m}$, and an ice crystal effective radius of $r_{\text{eff,I}} = 90$ μm (columns) were used. Figure 2 shows that γ_λ decreases with increasing ice fraction at wavelengths larger than 1400 nm because in this spectral range the absorption by ice crystals is stronger than that of liquid water droplets. At shorter wavelengths where scattering processes dominate, the cloud reflectivity increases with increasing values of f_I. Here the non-spherical shape of the ice crystals enhances the scattering into the viewing direction of the remote sensing instruments.

Additionally, the vertical distribution of ice crystals and liquid water droplets influences the cloud top reflectivity. In Arctic mixed-phase clouds, typically the liquid droplets dominate the cloud top layer, masking the ice crystals of the lower cloud layers (e.g., Shupe et al. 2006; McFarquhar et al. 2007). This vertical stratification limits the potential of solar remote sensing techniques to quantify the amount of ice in the clouds. Active remote sensing techniques by cloud radar, which are most sensitive to the larger ice crystals, can penetrate the liquid dominated cloud layers. Together with lidar observation, which are highly sensitive to the liquid droplets, the vertical structure of Arctic mixed-phase clouds can be characterized (Delanoë et al. 2013; Mech et al. 2014).

3.2 Surface Albedo

Large areas of the Arctic ocean and land surfaces are covered by sea ice or snow. The high surface albedo of snow and sea ice dramatically changes the lower boundary condition of radiative transfer in the atmosphere increasing the reflected radiation also in cloud-free areas. The spectral snow albedo α_λ for different effective snow grain sizes $r_{\text{eff,S}}$ is shown in Fig. 3a. At solar wavelengths less than 800 nm, typically used to retrieve cloud optical thickness, the spectral albedo of snow is close to unity (Wiscombe and Warren 1980). The high surface albedo significantly affects the cloud reflectivity observed above the clouds by remote sensing instruments. Spectral

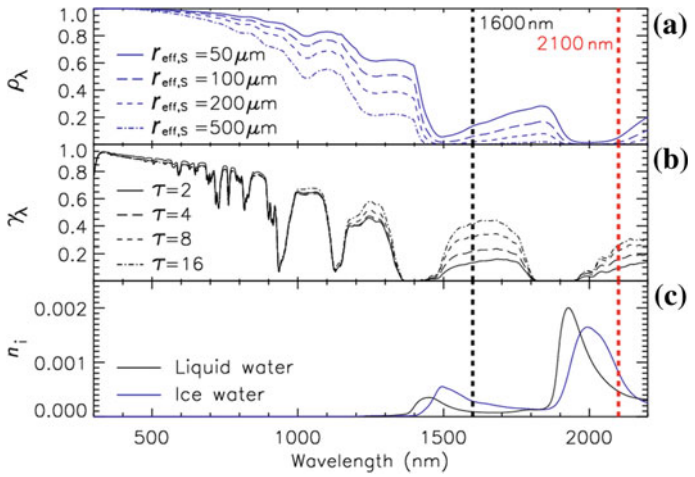

Fig. 3 **a** Spectral snow albedo for different $r_{\mathrm{eff,S}}$. **b** Cloud reflectivity γ_λ simulated for clouds with different τ and with fixed $r_{\mathrm{eff,C}} = 10$ μm and located above a snow surface with $r_{\mathrm{eff,S}} = 100$ μm. **c** The imaginary part of the refractive index of ice and liquid water (adapted from Ehrlich et al. 2017)

cloud top reflectivity γ_λ of clouds with different τ simulated above a snow surface assuming an effective snow grain size of $r_{\mathrm{eff,S}} = 100$ μm are shown in Fig. 3b. For wavelengths below 1200 nm the high snow albedo diminishes the contrast between cloud-free and cloudy conditions and erases the sensitivity of cloud reflectivity to cloud optical thickness. Therefore, in Arctic regions common cloud retrievals utilize observations at wavelengths larger than 1200 nm where the snow albedo is lower (e.g., Platnick et al. 2001). For example, the combination of the 1640 and 2130 nm wavelength bands is used for the Moderate Resolution Imaging Spectroradiometer (MODIS) to retrieve cloud optical thickness and droplet effective radius.

However, the snow albedo at larger wavelengths depends strongly on the size of the snow grains as illustrated in Fig. 3a (Wiscombe and Warren 1980). This variability overlaps with the spectral range where liquid droplets absorb solar radiation indicated by the imaginary part of the refractive index of liquid water and ice shown in Fig. 3c. The smaller the snow grains, the higher the surface albedo and the more radiation is reflected by the surface. Snow grain sizes vary temporally and spatially due to precipitation that decreases the snow grain size, and because of the snow metamorphism that slowly increases the snow grain size (e.g., Flanner and Zender 2006; Jacobi et al. 2010). In polar areas, the effective snow grain size typically ranges between 50 μm for freshly fallen snow and 1000 μm for aged snow (Wiebe et al. 2013). Therefore, the retrieval of cloud properties (optical thickness and droplet effective radius) over snow-covered surfaces requires a reasonable assumption of the effective snow grain size.

Figure 4a shows a bi-spectral retrieval grid ($\gamma_{1600\,\mathrm{nm}}$ vs. $\gamma_{2100\,\mathrm{nm}}$) obtained from the simulated cloud reflectivities for three effective snow grain sizes: 50, 100, and

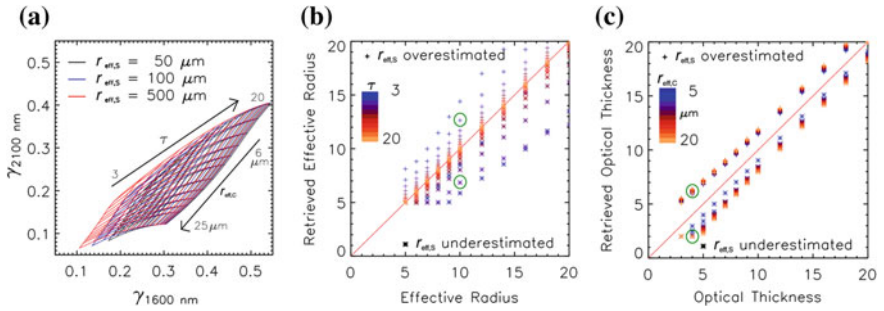

Fig. 4 **a** Bispectral retrieval grids of cloud top nadir reflectivity $\gamma_{1600\,nm}$ and $\gamma_{2100\,nm}$ assuming three different effective snow grain sizes $r_{eff,S}$ of 50, 100, and 500 μm. The simulated reflectivities cover cloud optical thickness τ between 3 and 20 and cloud droplet effective radius $r_{eff,C}$ between 6 and 25 μm. **b** and **c**: Comparison of synthetically retrieved τ b and $r_{eff,C}$ **c** with the original parameter value. Calculations in **b** and **c** are performed, assuming a larger effective snow grain size of $r_{eff,S}$ = 200 μm instead of the original $r_{eff,S}$ = 50 μm (crosses) and a smaller effective snow grain size of $r_{eff,S}$ = 50 μm instead of the original $r_{eff,S}$ = 200 μm (asterisks) (adapted from Ehrlich et al. 2017)

500 μm. The grids significantly differ and show a considerable snow grain size effect, especially for low values of $\gamma_{1600\,nm}$, while at higher reflectivities the grids tend to converge. The reflectivity $\gamma_{2100\,nm}$ is less affected by changes of $r_{eff,S}$ as the snow albedo is close to zero for $r_{eff,S} > 100$ μm (see Fig. 3a). As the retrieval of τ is strongly linked to γ_{1600nm}, the effect of the snow albedo on the retrieved τ is obvious. However, the non-rectangular shape of the grids indicates that both reflectivities are coupled to both cloud parameters and, thus, also the retrieved $r_{eff,C}$ are affected by changes in the effective snow grain size.

This snow grain size effect was estimated by Ehrlich et al. (2017) for the retrieval of typical Arctic low-level liquid water clouds and a fixed solar zenith angle of $\theta_0 = 63°$. Based on synthetic measurements obtained from the forward simulations, the uncertainty of the retrieval results was quantified. For each synthetic measurement defined by τ, $r_{eff,C}$, and $r_{eff,S}$, a set of retrievals assuming different values of effective snow grain sizes were performed. In Fig. 4b and c the retrieval results are compared to the original cloud properties for synthetic measurements calculated with an original effective snow grain size of 50 μm, but retrieved from forward simulations assuming an effective snow grain size of 200 μm (crosses). The asterisks in Fig. 4b, c indicate the opposite case: originally $r_{eff,S}$ = 200 μm is used to produce the synthetic measurement and then $r_{eff,S}$ = 50 μm is assumed in the retrieval of the cloud properties. While Fig. 4b shows retrieved values of τ for different values of $r_{eff,C}$ indicated by the color code, Fig. 4c presents retrieved $r_{eff,C}$ for clouds of different τ also indicated by a color code. For a typical low-level liquid water cloud ($\tau = 4$, $r_{eff,C} = 10$ μm), the retrieved cloud properties would differ by up to 50% if $r_{eff,S}$ is assumed to be 200 μm instead of the original effective snow grain size of 50 μm, or vice versa. Similar uncertainties caused by the assumption of surface albedo are reported for cirrus by Rolland and Liou (2001) and Fricke et al. (2014).

3.3 *Horizontal Inhomogeneities and Three-Dimensional Effects*

The Arctic sea ice cover often shows strong horizontal inhomogeneities. Due to ocean currents and the drag produced by the surface winds, the sea ice is typically broken into floes. Between the floes, cracks, leads, and polynias of open water may from and reduce the surface albedo locally. In the marginal sea ice zone (MIZ), where the size of the floes is smaller and the gaps in between larger (scattered ice floes), this horizontal inhomogeneity is most pronounced. The MIZ is characterized by a strong surface albedo contrast between the low albedo of open water (0.04 at 645 nm) and the high albedo of snow-covered sea ice (0.9 at 645 nm; Malinka et al. 2016), which affects the radiative transfer of solar radiation and retrieval of cloud properties (Schäfer et al. 2015). Airborne observations of spectral reflectivity $\gamma_{645\,\mathrm{nm}}$ are shown in Fig. 5 for three cases, a cloud-covered straight sea ice edge, cloud-covered ice floes, and cloud-free ice floes. The measurements have a horizontal resolution of about 4 m and were obtained by the imaging spectrometer AISA Eagle/Hawk during the international field campaign VERtical Distribution of Ice in Arctic clouds (VERDI) on 17 May 2012 (Schäfer et al. 2015). The left panels show the raw measurements, while a reflectivity threshold is applied to mask all sea ice covered pixel in the center images. Comparing the cloud-free case (Fig. 5b), where $\gamma_{645\mathrm{nm}}$ immediately changes at the sea ice edge, with the cloud-covered cases (Fig. 5d and f), an area of enhanced $\gamma_{645\,\mathrm{nm}}$ is visible around the sea ice edge when clouds are present. This smooth transition is caused by horizontal photon transport in the altitudes between surface and cloud top. To quantify this effect, the normalized frequency distribution

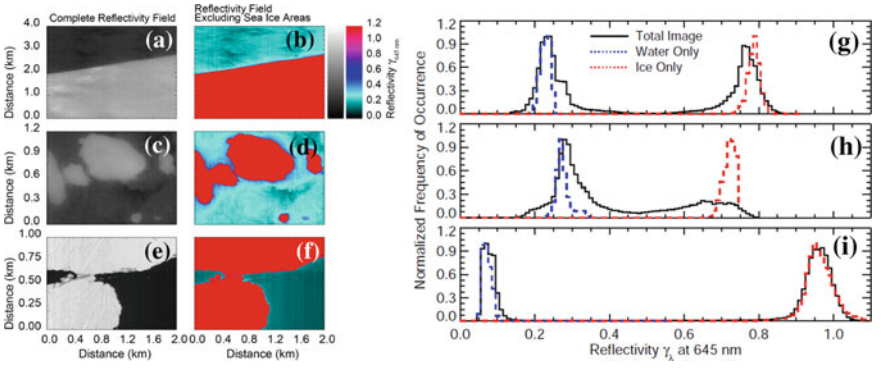

Fig. 5 Left panels: Fields of γ_λ at 645 nm, measured with the imaging spectrometer AISA Eagle/Hawk. The measurements were performed on 17 May 2012 during the international field campaign VERDI. Center panels: Same reflectivity fields as shown in (a), (b), and (c) but using a different color-scale and masking all pixel identified as sea ice by red shading. Right panels: Normalized distributions of the frequency of occurrence of $\gamma_{645\mathrm{nm}}$ measured for the three cases. Dashed lines illustrate the range of $\gamma_{645\,\mathrm{nm}}$ for pixel located over sea ice (red) and open ocean (blue) not effected by 3D radiative effects (adapted from Schäfer et al. 2015)

of occurrence of $\gamma_{645\,\mathrm{nm}}$ for the three cases are shown in Fig. 5g–i. Additionally, the range of $\gamma_{645\,\mathrm{nm}}$ for pixels located over sea ice (red) and open ocean (blue) not effected by three-dimensional (3D) radiative effects is indicated by dashed lines. For the cloud-free case, two separated modes, one for open ocean and one for sea ice, are observed. This separation weakens for the cloud-covered cases. Especially for the case with the ice floes, a significant amount if pixels show values of $\gamma_{645\,\mathrm{nm}}$ ranging between the two modes for pure sea ice and pure open ocean. This indicates, that large areas of the observed cloud field were effected by 3D radiative effects.

To quantify these effects, Schäfer et al. (2015) performed 3D radiative transfer simulations for an ideal straight sea ice edge covered by clouds of different cloud optical thickness, cloud base altitude and cloud geometric thickness. The simulated $\gamma_{645\,\mathrm{nm}}$ along a cross section perpendicular to the sea ice edge are shown in Fig. 6. A higher cloud optical thickness reduces the general contrast between pixel over sea ice and over open water. The transition of $\gamma_{645\,\mathrm{nm}}$ between high values over sea ice and low values over open water is smoothed for all simulated clouds. This 3D-radiative effect strongly depends on the cloud base altitude and cloud geometrical thickness, which both define the vertical distance between surface and cloud top. The higher the cloud base or the cloud thickness, the more horizontal distance the radiation can travel by horizontal photon transport after being reflected at the surface and subsequently being scattered by the cloud into the direction of the observer (nadir direction). Over open water $\gamma_{645\,\mathrm{nm}}$ is enhanced by more than 5% for distances up to 3 km depending on τ and cloud geometry.

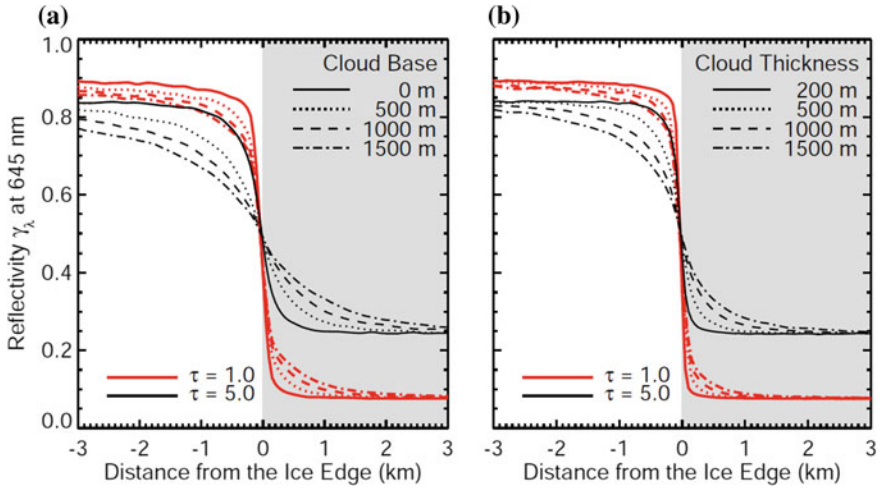

Fig. 6 Simulated $\gamma_{645\,\mathrm{nm}}$ for clouds of different cloud base altitudes (**a**) and with different geometrical thickness (**b**) for a cross section from a highly reflecting ice-covered region to a darker region of open water. The white area illustrates the ice covered area. In the simulations varying the cloud base altitude, the cloud geometrical thickness is fixed to 500 m. In the simulations varying the cloud geometrical thickness, the cloud base altitude is fixed to 0 m (adapted from Schäfer et al. 2015)

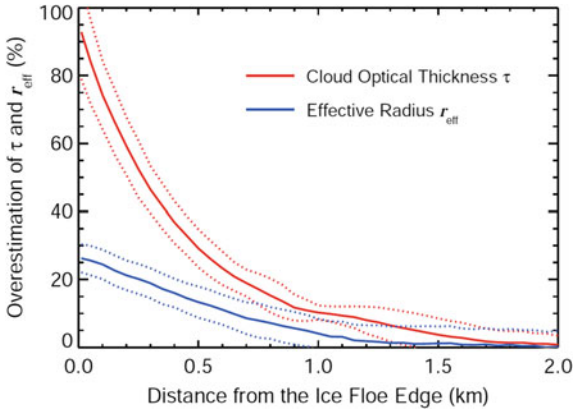

Fig. 7 Overestimation (average and standard deviation) of τ and $r_{\mathrm{eff,C}}$ as a function of the distance to the edge of an ice floe simulated for a cloud located in an altitude between 500 m to 1000 m and with $\tau = 10$ and $r_{\mathrm{eff,C}} = 15$ µm (adapted from Schäfer et al. 2015)

The enhancement of $\gamma_{645\,\mathrm{nm}}$ in the surrounding of sea ice can contaminate the retrieval of cloud properties over open water, which commonly do not consider 3D radiative effects. A higher $\gamma_{645\,\mathrm{nm}}$ will lead to an overestimation of cloud optical thickness and cloud particle size. For a typical sea ice field of the Arctic MIZ and a liquid cloud with $\tau = 10$ and $r_{\mathrm{eff,C}} = 15$ µm located in an altitude between 500 m to 1000 m, Schäfer et al. (2015) calculated the uncertainties caused by the 3D radiative effects. For this scenario, Fig. 7 shows the percentage difference between retrieved and assumed τ and $r_{\mathrm{eff,C}}$ as function of the distance to the ice floe edge. This study showed that τ is overestimated stronger than $r_{\mathrm{eff,C}}$. Right next to the ice floes, τ is retrieved almost 90% too high, while the overestimation of $r_{\mathrm{eff,C}}$ reaches 25%. In 1 km distance to the ice floes the differences are still significant with about 10% for τ and 5% for $r_{\mathrm{eff,C}}$. These effects need to be considered for airborne remote sensing of Arctic clouds where typically horizontal scales of less than 100 m are resolved. Similar effects may also affect the retrieval of aerosol properties as discussed by Lyapustin and Kaufman (2001).

4 Retrieval of Cloud Properties Based on Spectral Radiation Measurements

Airborne remote sensing using spectral solar radiation has the ability to measure cloud reflectivity with high spectral resolution. Spectral features can be resolved and analyzed. E.g. the maxima of the absorption bands of liquid water and ice are shifted by about 100 nm as illustrated by the imaginary part of refractive index shown in Fig. 3c. Separating this spectral information allows to retrieve the cloud thermodynamic phase of Arctic clouds (Sect. 4.1) and to simultaneously retrieve cloud and snow properties in case liquid water clouds are located above snow (Sect. 4.2.). These retrievals can be applied to airborne spectral imaging and provide maps of cloud properties that resolve the typical scales of cloud dynamic processes (Sect. 6).

4.1 Retrieval of Cloud Thermodynamic Phase

Figure 8 shows the spectral cloud top reflectivity γ_λ measured above an exemplary pure liquid and a pure ice cloud in the wavelength range 1400–1850 nm where absorption by liquid water and ice dominates. Compared to the liquid cloud, γ_λ of the ice cloud is significantly lower due to a lower cloud optical thickness and the stronger absorption by ice in the spectral range above 1500 nm. Additionally, the spectral slope between 1550 nm and 1700 nm, indicated by the dotted lines in Fig. 8, is steeper for the ice cloud than for the liquid cloud. These different spectral patterns are used to retrieve the cloud thermodynamic phase (e.g., Pilewskie and Twomey 1987; Ehrlich et al. 2008). Therefore, a spectral slope cloud phase index I_S is defined by,

$$I_S = 100 \cdot \frac{\lambda_b - \lambda_a}{\gamma_{1640\,\mathrm{nm}}} \cdot \left[\frac{\mathrm{d}\gamma_\lambda}{\mathrm{d}\lambda}\right]_{[\lambda_a,\lambda_b]} \tag{2}$$

Values of $I_S < 20$ indicate pure liquid clouds while higher values are observed for pure ice $I_S > 20$ and mixed-phase clouds. Alternatively, Ehrlich et al. (2008) apply a cloud phase index I_P, which uses the weighting coefficients resulting from a principle component analysis of radiative transfer simulations. This phase index improves the separation between pure liquid water ($I_P < 1$) and pure ice clouds ($I_P > 2$) as the complex spectral footprint of the absorption by ice crystals and liquid droplets is considered for all wavelengths in the spectral cloud reflectivity between 1500 and 1800 nm.

An example of a time series of the cloud phase indices I_S and I_P retrieved with the SMART-Albedometer along the flight track of the Polar 2 aircraft on 7 April 2007 during the Arctic Study of Tropospheric Aerosol, Clouds and Radiation (ASTAR, Ehrlich et al. 2008) campaign is shown in Fig. 9. During this flight, collocated satellite observations by the Cloud-Aerosol Lidar and Infrared Pathfinder Satellite

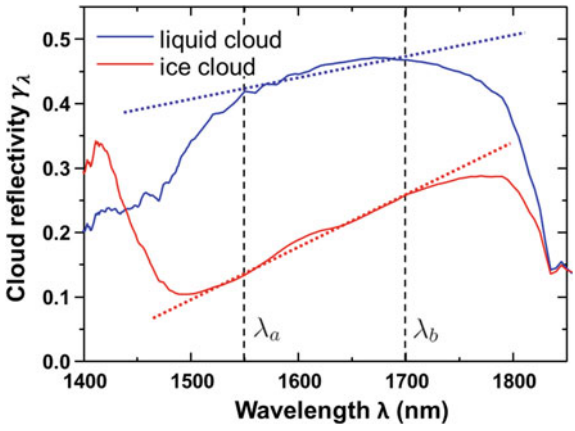

Fig. 8 Spectral cloud reflectivity γ_λ of a typical pure liquid phase and a typical pure ice cloud. The dotted lines illustrate the spectral slope between the two wavelengths λ_a and λ_b

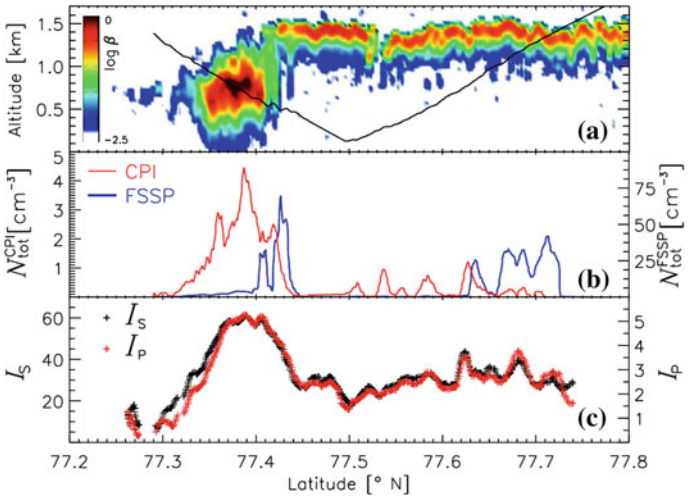

Fig. 9 Airborne and satellite observations along the flight track of the Polar 2 aircraft on 7 April 2007 during the ASTAR campaign. **a** Profile of total attenuated backscatter coefficient β in sr^{-1} km^{-1} measured by CALIPSO. The flight track of the in situ measurements is overlaid as a black line. **b** Ice and liquid water particle number concentrations N_{tot} measured by CPI and FSSP. (c): Cloud phase indices I_S and I_P (adapted from Ehrlich et al. 2008)

(CALIPSO) and concurrent in situ microphysical measurements are analysed. The total attenuated backscatter signal measured by CALIPSO and the particle number concentration measured by a cloud particle imager (CPI, Gayet et al. 2009) and a forward scattering spectrometer probe (FSSP) are shown in Fig. 9a and b.

The lidar could not completely penetrate the optically thick clouds with exception of the cloud edge (<77.4° N). Nevertheless, the lidar profiles reveal that in the southern part of the cloud deck ice particles are precipitating down to the surface. This is confirmed by the CPI in situ measurements, which is most sensitive to large ice crystals and shows a high particle number concentration up to $N_{\mathrm{tot}} = 3\ \mathrm{cm}^{-3}$ while the FSSP sampling small liquid water cloud droplets shows a low concentration. In this area of the cloud edge, both phase indices show high values. The maximum values of $I_{\mathrm{S}} = 60$ and $I_{\mathrm{P}} = 5$ indicate a pure ice cloud. The cloud parts north 77.4° N are characterized by lower values ($I_{\mathrm{S}} = 20 - 40$ and $I_{\mathrm{P}} = 2 - 4$) corresponding to mixed-phase clouds considering the range of cloud optical thickness and the cloud particle sizes observed for this cloud.

For Arctic mixed-phase clouds, the ice indices allow to qualitatively identify the mixed-phase nature of the clouds. A quantitative separation of liquid and ice water path is challenging as the spectral slope is affected by the size of ice crystals and liquid droplets and the vertical stratification of ice and liquid droplets in the cloud (Ehrlich et al. 2008). Assuming a homogeneous mixture of ice crystals and liquid water droplets, Thompson et al. (2016) tested a spectral fitting method to quantitatively separate the liquid and ice equivalent absorption and found a reasonable agreement

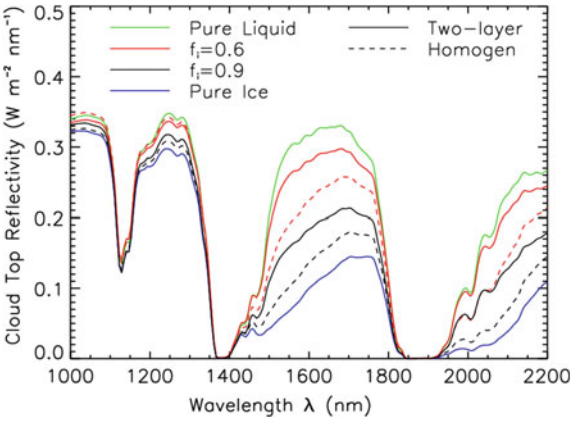

Fig. 10 Spectral cloud reflectivity γ_λ simulated for Arctic mixed-phase clouds of different ice mass fraction f_I^*. Two vertical structures of the mixing between liquid droplets and ice crystals are assumed; a homogeneous mixed cloud and a liquid-topped two-layer cloud

with in situ measurements of ice total mass fractions. However, the assumption of homogeneously mixed mixed-phase clouds does not hold for most Arctic clouds as shown by in situ cloud microphysical measurements (e.g., Gayet et al. 2009; Mioche et al. 2017). Typically, Arctic mixed-phase clouds are characterized by a liquid-dominated cloud top and higher ice water contents at cloud base. This vertical stratification influences the spectral cloud reflectivity and, therefore, can bias the separation of ice and liquid water content (Ehrlich et al. 2009). Figure 10 shows the spectral reflectivity of an Arctic mixed-phase cloud with different ice mass fractions f_I^* simulated for a vertically homogeneous mixture of ice and liquid particles (solid lines) and an inhomogeneous two-layer cloud (dashed lines). The two-layer cloud is assumed to have a pure liquid top layer and a pure ice layer at cloud bottom. For the two simulated ice fractions, the cloud reflectivity significantly differs depending on the cloud vertical structure. The homogeneous cloud always shows lower values of γ_λ in the wavelength range between 1400–1800 nm compared to the liquid-topped two-layer cloud. These differences are largest at $\lambda = 1500$ nm, which reduces both the spectral slope and the phase index in the simulations assuming a two-layer cloud. For the examples shown in Fig. 10, I_S decreases from $I_\mathrm{S} = 28$ to $I_\mathrm{S} = 18$ for $f_\mathrm{I}^* = 0.6$ and $I_\mathrm{S} = 49$ to $I_\mathrm{S} = 28$ for $f_\mathrm{I}^* = 0.9$ when switching from a homogeneous to a two-layer cloud structure. For typical Arctic mixed-phase clouds dominated by a liquid water cloud top layer, the phase index will be biased to values of pure liquid water clouds. Contrarily, for optically thin clouds located above sea ice the reflection at the snow surface might bias the phase index to higher values indicating the presence of ice particles.

4.2 Combined Retrieval of Cloud and Snow Properties

In case of pure liquid water clouds located over snow-covered sea ice, airborne spectral cloud reflectivity measurements can be used to retrieve the effective snow

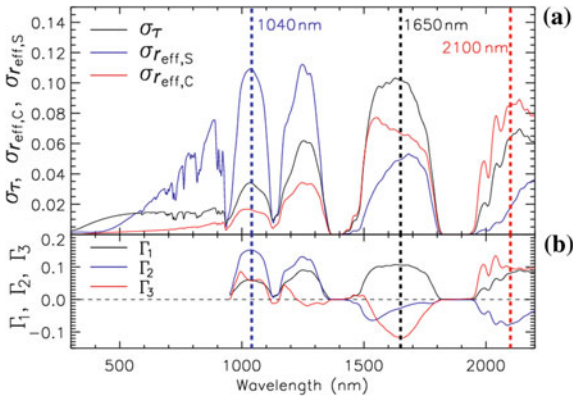

Fig. 11 Mean standard deviations of spectral cloud reflectivity σ_τ, $\sigma_{r_{\mathrm{eff,S}}}$, and $\sigma_{r_{\mathrm{eff,C}}}$ with respect to a single cloud or snow parameter τ, $r_{\mathrm{eff,S}}$, and $r_{\mathrm{eff,C}}$ calculated for a set of radiative transfer simulations (**a**). The first three spectral weights Γ_1, Γ_2, and Γ_3 of a principal component analysis are given in (**b**) (adapted from Ehrlich et al. 2017)

grain size $r_{\mathrm{eff,S}}$ of the snow surface by separating the spectral signature of the liquid cloud and the snow. Retrieving $r_{\mathrm{eff,S}}$ helps to overcome the uncertainties discussed in Sect. 3.2 and allows a more precise retrieval of cloud properties in the Arctic. As shown by Ehrlich et al. (2017), snow grains strongly absorb radiation at wavelengths of about 1000 nm where liquid clouds are non-absorbing. These spectral differences enable a separation of cloud and snow signature. Figure 11 shows the sensitivity of the spectral cloud reflectivity for three parameters, cloud optical thickness τ, droplet effective radius $r_{\mathrm{eff,C}}$ and effective snow grain size $r_{\mathrm{eff,S}}$. The sensitivities are quantified by (a) the standard deviation of a series of radiative transfer simulations where one of the three parameter is varied, and (b) the weighting coefficients of a principle component analysis. Three wavelength ranges are identified to be most sensitive to one of each parameter; 1000 nm for $r_{\mathrm{eff,S}}$, 1640 nm for τ and 2100 nm for $r_{\mathrm{eff,C}}$.

Based on airborne measurements at these three wavelengths obtained with the SMART-Albedometer during the VERDI campaign in 2012, a retrieval algorithm was developed to provide estimates of the three cloud and snow parameters τ, $r_{\mathrm{eff,S}}$, and $r_{\mathrm{eff,C}}$ (Ehrlich et al. 2017). Figure 12 shows an example of the retrieval applied to measurements of a stratiform Arctic boundary-layer cloud observed on 29 April 2012 over the Canadian Beaufort Sea. The retrieved τ, $r_{\mathrm{eff,S}}$, and $r_{\mathrm{eff,C}}$ are displayed along the flight track of the Polar 5 aircraft. They are compared to cloud and snow properties retrieved by MODIS (Platnick et al. 2017; Zege et al. 2011). For large areas of this cloud field the MODIS cloud product did not provide valid solutions due to the bright surface (Fig. 12a and b). In cloud-covered areas no values of $r_{\mathrm{eff,S}}$ could be retrieved (Fig. 12c). These gaps could be filled by the airborne observations which show reasonable agreement with the MODIS retrieval in areas where the retrieval did not fail.

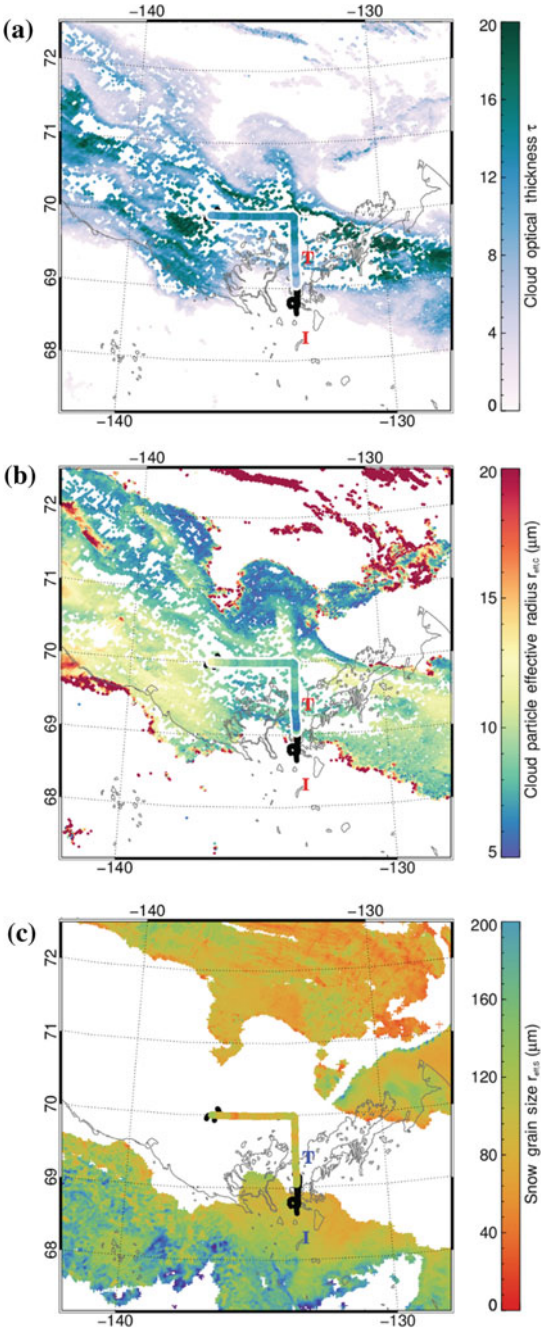

Fig. 12 Cloud optical thickness τ (**a**), cloud droplet effective radius $r_{\mathrm{eff,C}}$ (**b**) and effective snow grain size $r_{\mathrm{eff,S}}$ (**c**) retrieved by MODIS and the SMART-Albedometer for observations on 29 April 2012. The total flight track is indicated by a black line and overlaid by the retrieval results of the SMART-Albedometer. "I" and "T" mark the locations of Inuvik and Tuktoyaktuk (adapted from Ehrlich et al. 2017)

5 Retrieval of Cloud Properties Based on Directional Observations

A significant fraction of radiation reflected by clouds is from single scattering. This single-scattered portion is strongly influenced by the scattering phase function of the cloud particles. Examples if scattering phase functions of liquid droplets and non-spherical ice crystals of different shape are shown in Fig. 13. Non-spherical ice crystals typically show an enhanced sideward scattering in scattering angles around $\vartheta = 100°$ (grey shaded area). Liquid water cloud droplets show a cloud bow at about 140° (blue shaded area) and the backscatter glory at 180° scattering angle, which are sensitive to droplet size and the width of the droplet size distribution (Laven 2003; Mayer et al. 2004).

These features of the scattering phase function can be used to retrieve cloud phase and cloud droplet size at cloud top. This requires to measure the directional distribution of the radiation field above the clouds at scattering angles, which are sensitive to the particle shape. E.g., the presence of a glory can be used to identify liquid water clouds. Observations of a specular reflection of the Sun at the top of clouds suggest the presence of ice crystals. Figure 14 shows two representative measurements by a 180° fish-eye camera obtained during the ACLOUD campaign on 27 May 2017. The image taken on 15:00 UTC (left panel) shows a prominent backscatter glory and a cloud bow, which indicate that this low-level cloud is dominated by liquid water droplets at cloud top. At a different location on 16:00 UTC (right panel), a specular reflection is observed at cloud top indicating the presence of a thin layer of ice crystals.

By analysing the width and strength of the cloud bow, Ehrlich et al. (2012) retrieved the cloud droplet size. An example is shown in Fig. 15 for observations during the aircraft campaign SORPIC (Solar Radiation and Phase Discrimination of Arctic Clouds), conducted on 17 May 2010. A series of 50 camera images were averaged and converted into the hemispherical directional reflectance factor HDRF shown in Fig. 15a. In the polar plot the direction of the Sun is aligned from the left to

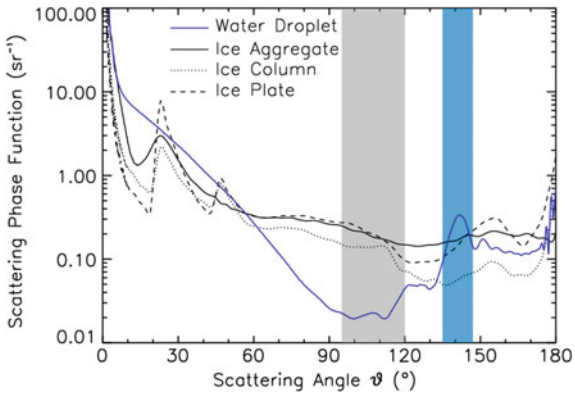

Fig. 13 Scattering phase function of liquid droplets and non-spherical ice crystals of different shapes. The grey shaded area indicates the range of scattering angles ϑ typically observed by nadir observations in the Arctic. The blue shaded area indicates the cloud bow

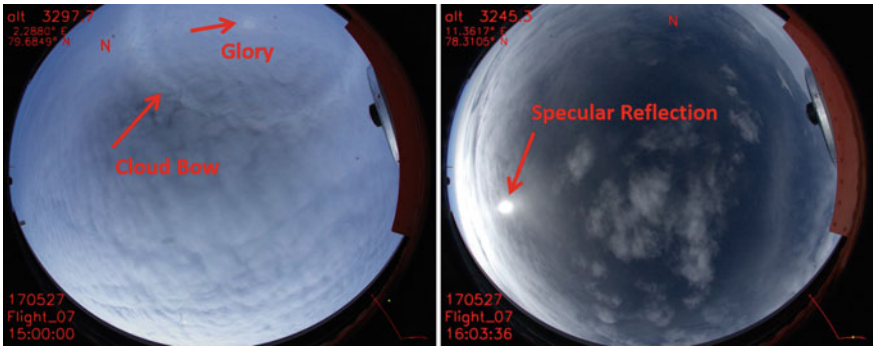

Fig. 14 Images of a 180° fish-eye camera operated on Polar 5 during ACLOUD. The observations are obtained on 27 May 2017, 15 and 16 UTC. The north direction of each image is labelled by "N". Cloud bow, backscatter glory and specular reflection are indicated by arrows

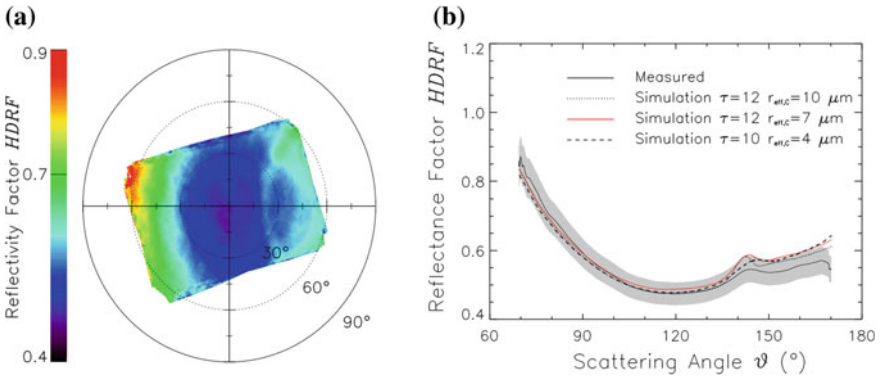

Fig. 15 Hemispherical directional reflectance factor HDRF measured during SORPIC with a wide-angle camera operated on Polar 5 over an Arctic stratocumulus. Panel **a** shows a polar plot of an average of 50 images. Panel **b** shows the measured HDRF as function of the scattering angle ϑ compared to the simulated HDRF for clouds with different optical thickness τ and effective diameter $r_{\mathrm{eff,C}}$. The uncertainty of the measurements is indicated by the gray area (adapted from Ehrlich et al. 2012)

the right. The averaging is required to eliminate the horizontal cloud inhomogeneities of the stratocumulus field. Enhanced values of the HDRF are observed in the forward scattering direction (left part of the polar plot) and in a large circle, the cloud bow, in the backscatter directions. In Fig. 15b the HDRF is analysed as function of the scattering angle and compared to radiative transfer simulations assuming different cloud droplet effective radii.

The enhancement of the cloud bow is superimposed to an increase of the HRDF to small and large scattering angles. In forward direction, this general increase is reproduced by the simulations. For ϑ at backscatter angles larger differences occur which likely are caused by three-dimensional radiative effects of the stratiform cloud.

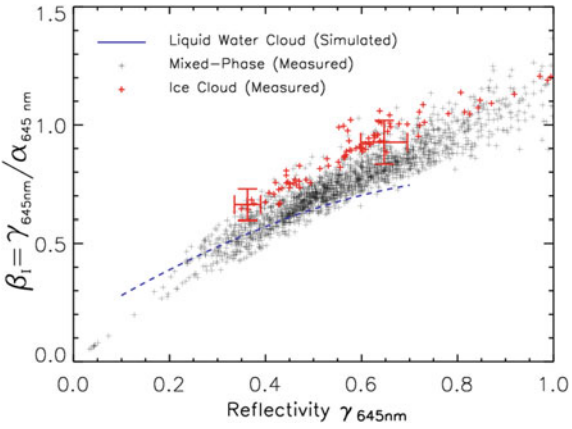

Fig. 16 Measured β_I as function of γ_{645nm} for different clouds observed with the SMART-Albedometer during ASTAR 2007, 2 April. Black crosses show measurements over mixed-phase clouds, red crosses over ice clouds. Simulations for pure liquid water clouds are shown as a blue line (adapted from Ehrlich et al. 2008)

The cloud bow is visible at about $\vartheta = 142°$. While simulations with $r_{\text{eff,C}} = 10\ \mu\text{m}$ show a narrow and strong cloud bow and the simulations with $r_{\text{eff,C}} = 4\ \mu\text{m}$ a broad and weak cloud bow, the best agreement between measurements and simulations is obtained for a cloud with $\tau = 12$ and $r_{\text{eff,C}} = 7\ \mu\text{m}$. A similar approach was followed by Mayer et al. (2004) retrieving the cloud droplet number size distribution from airborne imaging observation pointed into the direction of the backscatter glory.

For measurements in the Arctic with low Sun, the nadir cloud reflectivity refers to scattering angles of about 100° where sideward scattering can be used to identify the cloud phase. Ehrlich et al. (2008) analysed the ratio between the cloud reflectivity measured in nadir direction and the cloud albedo as a measure of the sideway scattering of the cloud. Figure 16 shows measurements of the SMART-Albedometer from the ASTAR 2007 campaign ($\theta_0 = 71°$) of the ratio β_I between nadir cloud top reflectivity γ_λ and cloud top albedo α_λ. The blue line represents values calculated by radiative transfer simulations of a pure liquid water cloud. The measured values of β_I significantly deviate from the theoretical curve simulated for pure liquid water clouds. This indicates the presence of ice crystals and therefore mixed-phase clouds. The highest values of β_I are observed when the spectral slope cloud phase index indicated pure ice clouds (red coloured measurements in Fig. 16).

The polarization state of solar radiation reflected in the cloud bow and backscatter glory is highly sensitive to cloud properties at cloud top and can increase the information content of airborne remote sensing. Multiangular polarimetric observations such as by the Airborne Multi-angle Spectro-Polarimetric Imager (Diner et al. 2013) or by the Research Scanning Polarimeter (Knobelspiesse et al. 2011) are applied to resolve the directional distribution of the degree of polarization in the back scatter glory or cloud bow. By use of parametric curve-fitting methods, the polarimetric retrievals are capable to estimate the cloud optical depth, droplet number size distribution, and above-cloud aerosol properties (Knobelspiesse et al. 2011; Xu et al. 2018).

6 High Resolution Cloud Spectral Imaging

Airborne spectral imaging is used to analyse the horizontal variability of Arctic boundary-layer clouds (e.g., Thompson et al. 2016; Schäfer et al. 2017). For a distance between cloud top and flight altitude of about 2000 m a spatial resolution of down to 5 m is obtained. Retrieval methods for cloud properties applied to airborne spectral imaging are almost identical to those used for airborne nadir observations of spectral solar radiances (Bierwirth et al. 2013). The retrievals provide maps of cloud optical thickness τ, particle effective radius $r_{\mathrm{eff,C}}$, and cloud phase index I_{S}. Examples of two-dimensional (2D) fields and probability distribution functions of $\gamma_{1240\mathrm{nm}}$, τ, $r_{\mathrm{eff,C}}$, and I_{S} observed above an Arctic stratocumulus during ACLOUD (2 June 2017) with the AISA Eagle/Hawk spectral imager are shown in Fig. 17. The retrieval of τ, $r_{\mathrm{eff,C}}$ was based on the assumption of pure liquid water clouds. The retrieved maps illustrate the variability of all three cloud parameters and show that dynamic processes within the stratocumulus determine the structure of the cloud field. The cloud optical thickness ranges between $15 < \tau < 40$, the effective cloud particle radius between $8\ \mu\mathrm{m} < r_{\mathrm{eff,C}} < 20\ \mu\mathrm{m}$. In areas of low $\gamma_{1240\,\mathrm{nm}}$ and low τ, the effective cloud particle size significantly increases with values exceeding $r_{\mathrm{eff,C}} > 20\ \mu\mathrm{m}$. This increase of cloud particle size may either result from evaporation of smaller cloud droplets by entrainment in the downdraft regions or the retrieval is affected by a higher concentration of ice crystals. The presence of an increased number of ice crystals is indicated by the enhanced values of $I_{\mathrm{S}} > 20$ found in these areas.

The 2D-fields allow to characterize the horizontal inhomogeneity of clouds with 2D-statistical analysis such as the 2D-autocorrelation to quantify the directional dependence of cloud structures. Schäfer et al. (2017) showed that standard one-dimensional (1D) inhomogeneity parameter such as the relative variability can be

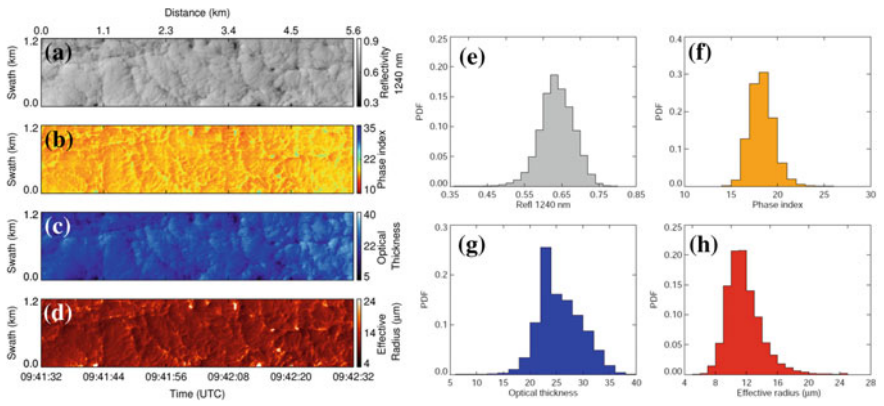

Fig. 17 Field of cloud top reflectivity $\gamma_{1240\,\mathrm{nm}}$ measured with AISA Eagle/Hawk during the ACLOUD campaign on 2 June 2017 (**a**). Retrieved cloud phase index I_S, optical thickness τ, and effective radius $r_{\mathrm{eff,C}}$ are given in panel (**b**)–(**d**). Probability distribution function of each quantity are presented in panel (**e**)–(**h**)

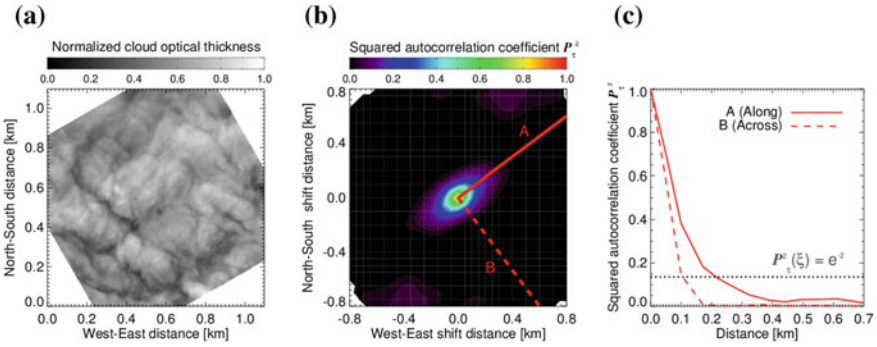

Fig. 18 Field of normalized cloud optical thickness retrieved from measurements with AISA Eagle/Hawk during the VERDI campaign on 16 May 2012 (**a**) and corresponding 2D (**b**) and 1D (**c**) autocorrelation function. The 1D autocorrelation functions refer to the directions A and B indicated in panel (**b**) by the solid and dashed red lines (adapted from Schäfer et al. 2018)

identical even when cloud fields appear different with respect to their directional structure. An example of a 2D-autocorrelation function of an Arctic stratocumulus observed on 16 May 2012 during the VERDI campaign with the spectral imager AISA Eagle/Hawk is shown in Fig. 18. The calculation of the autocorrelation function is based on the 2D-field of cloud optical thickness. For the calculation the field was shifted up to 800 m in both directions. The non-symmetric pattern of the autocorrelation function (Fig. 18b) suggests that a predominant direction of cloud inhomogeneities exists for this cloud case (dashed red line labelled with B). Along this direction the correlation decreases already for short distances indicating a frequent change of cloud properties. Perpendicular to this direction, the strongest autocorrelations are obtained indicating a weaker change of cloud properties (solid red line labelled with A). This approach to statistically analyse the 2D-fields of cloud properties can be adapted for simulated cloud fields. A comparison of the simulated cloud fields with observations allows to study how clouds are represented in cloud resolving models and to identify which parameters change the simulated cloud structure (Schäfer et al. 2018).

7 Concluding Remarks

Airborne remote sensing techniques based on spectral measurements of reflected solar radiation is a key component for observations of Arctic clouds. In particular, these methods provide a detailed view on cloud properties such as the cloud optical thickness, particle effective radius, and thermodynamic phase and their horizontal variability. Airborne imaging spectrometers can resolve cloud structures on scales below 10 m that cannot be observed by similar satellite instruments. However, the specialities of the Arctic, e.g., the bright surface and mixed-phase clouds challenge

retrieval techniques based on reflected solar radiation. Uncertainties of the assumed surface albedo and the assumed vertical stratification of ice and liquid water in Arctic clouds can bias the retrieved cloud properties. Additionally, these methods are not applicable during polar night. Active remote sensing techniques using radar and lidar present alternative approaches for cloud remote sensing. As a conclusion, the different methods need to be combined exploiting the individual advantages of each single approach to obtain a full picture of the Arctic atmosphere. Such comprehensive instrument packages are planned to be operated in Arctic field campaigns such as the airborne component of the Multidisciplinary drifting Observatory for the Study of Arctic Climate (MOSAiC) and the HALO-$(AC)^3$ campaign.

Acknowledgements We gratefully acknowledge the funding by the Deutsche Forschungsgemeinschaft (DFG, German Research Foundation)—Projektnummer 268020496—TRR 172, within the Transregional Collaborative Research Center "ArctiC Amplification: Climate Relevant Atmospheric and SurfaCe Processes, and Feedback Mechanisms $(AC)^3$".

References

Bierwirth E, Ehrlich A, Wendisch M, Gayet J-F, Gourbeyre C, Dupuy R, Herber A, Neuber R, Lampert A (2013) Optical thickness and effective radius of Arctic boundary-layer clouds retrieved from airborne nadir and imaging spectrometry. Atmos Meas Tech 6:1189–1200. https://doi.org/10.5194/amt-6-1189-2013

Bony S, Stevens B, Ament F, Bigorre S, Chazette P, Crewell S, Delanoë J, Emanuel K, Farrell D, Flamant C, Gross S, Hirsch L, Karstensen J, Mayer B, Nuijens L, Ruppert Jr JH, Sandu I, Siebesma P, Speich S, Szczap F, Totems J, Vogel R, Wendisch M, Wirth M (2017) EUREC4A: a field campaign to elucidate the couplings between clouds, convection and circulation. Surv Geophys 38:1529. https://doi.org/10.1007/s10712-017-9428-0

Carlsen T, Birnbaum G, Ehrlich A, Freitag J, Heygster G, Istomina L, Kipfstuhl S, Orsi A, Schäfer M, Wendisch M (2017) Comparison of different methods to retrieve optical-equivalent snow grain size in central Antarctica. Cryosphere 11:2727–2741. https://doi.org/10.5194/tc-11-2727-2017

Curry JA, Schramm JL, Rossow WB, Randall D (1996) Overview of arctic cloud and radiation characteristics. J Climate 9:1731–1764. https://doi.org/10.1175/1520-0442(1996)009%3c1731:OOACAR%3e2.0.CO;2

Delanoë J, Protat A, Jourdan O, Pelon J, Papazzoni M, Dupuy R, Gayet J, Jouan C (2013) Comparison of airborne in situ, airborne radar-lidar, and spaceborne radar-lidar retrievals of polar ice cloud properties sampled during the POLARCAT campaign. J Atmos Oceanic Technol 30:57–73. https://doi.org/10.1175/JTECH-D-11-00200.1

Diner DJ, Xu F, Garay MJ, Martonchik JV, Rheingans BE, Geier S, Davis A, Hancock BR, Jovanovic VM, Bull MA, Capraro K, Chipman RA, McClain SC (2013) The airborne multiangle spectropolarimetric imager (AirMSPI): a new tool for aerosol and cloud remote sensing. Atmos Meas Tech 6:2007–2025. https://doi.org/10.5194/amt-6-2007-2013

Ehrlich A (2009) The impact of ice crystals on radiative forcing and remote sensing of arctic boundary-layer mixed-phase clouds, Ph.D. thesis, Johannes Gutenberg University Mainz, Germany. http://nbn-resolving.org/urn:nbn:de:hebis:77-2014

Ehrlich A, Bierwirth E, Wendisch M, Gayet J-F, Mioche G, Lampert A, Heintzenberg J (2008) Cloud phase identification of Arctic boundary-layer clouds from airborne spectral reflection

measurements: test of three approaches. Atmos Chem Phys 8:7493–7505. https://doi.org/10.5194/acp-8-7493-2008
Ehrlich A, Wendisch M, Bierwirth E, Gayet J-F, Mioche G, Lampert A, Mayer B (2009) Evidence of ice crystals at cloud top of Arctic boundary-layer mixed-phase clouds derived from airborne remote sensing. Atmos Chem Phys 9:9401–9416. https://doi.org/10.5194/acp-9-9401-2009
Ehrlich A, Bierwirth E, Wendisch M, Herber A, Gayet J-F (2012) Airborne hyperspectral observations of surface and cloud directional reflectivity using a commercial digital camera. Atmos Chem Phys 12:3493–3510. https://doi.org/10.5194/acp-12-3493-2012
Ehrlich A, Bierwirth E, Istomina L, Wendisch M (2017) Combined retrieval of Arctic liquid water cloud and surface snow properties using airborne spectral solar remote sensing. Atmos Meas Tech 10:3215–3230. https://doi.org/10.5194/amt-10-3215-2017
Ewald F, Kölling T, Baumgartner A, Zinner T, Mayer B (2016) Design and characterization of specMACS, a multipurpose hyperspectral cloud and sky imager. Atmos Meas Tech 9:2015–2042. https://doi.org/10.5194/amt-9-2015-2016
Flanner MG, Zender CS (2006) Linking snowpack microphysics and albedo evolution. J Geophys Res 111:D12208. https://doi.org/10.1029/2005JD006834
Fricke C, Ehrlich A, Jäkel E, Bohn B, Wirth M, Wendisch M (2014) Influence of local surface albedo variability and ice crystal shape on passive remote sensing of thin cirrus. Atmos Chem Phys 14:1943–1958. https://doi.org/10.5194/acp-14-1943-2014
Gayet J-F, Mioche G, Dörnbrack A, Ehrlich A, Lampert A, Wendisch M (2009) Microphysical and optical properties of Arctic mixed-phase clouds. The 9 April 2007 case study. Atmos Chem Phys 9:6581–6595. https://doi.org/10.5194/acp-9-6581-2009
Haas C, Beckers J, King J, Silis A, Stroeve J, Wilkinson J, Notenboom B, Schweiger A, Hendricks S (2017) Ice and snow thickness variability and change in the high Arctic Ocean observed by in situ measurements. Geophys Res Lett 44:10462–10469. https://doi.org/10.1002/2017GL075434
Hüneke T, Aderhold O-A, Bounin J, Dorf M, Gentry E, Grossmann K, Grooß J-U, Hoor P, Jöckel P, Kenntner M, Knapp M, Knecht M, Lörks D, Ludmann S, Matthes S, Raecke R, Reichert M, Weimar J, Werner B, Zahn A, Ziereis H, Pfeilsticker K (2017) The novel HALO mini-DOAS instrument: inferring trace gas concentrations from airborne UV/visible limb spectroscopy under all skies using the scaling method. Atmos Meas Tech 10:4209–4234. https://doi.org/10.5194/amt-10-4209-2017
Jacobi H-W, Domine F, Simpson WR, Douglas TA, Sturm M (2010) Simulation of the specific surface area of snow using a one-dimensional physical snowpack model: implementation and evaluation for subarctic snow in Alaska. Cryosphere 4:35–51. https://doi.org/10.5194/tc-4-35-2010
Knobelspiesse K, Cairns B, Redemann J, Bergstrom RW, Stohl A (2011) Simultaneous retrieval of aerosol and cloud properties during the MILAGRO field campaign. Atmos Chem Phys 11:6245–6263. https://doi.org/10.5194/acp-11-6245-2011
Korolev A, McFarquhar G, Field P, Franklin C, Lawson P, Wang Z, Williams E, Abel S, Axisa D, Borrmann S, Crosier J, Fugal J, Krämer M, Lohmann U, Schlenczek O, Wendisch M (2017) Mixed-phase clouds: progress and challenges. In: Baumgardner D, McFarquhar G, Heymsfield A (eds) Chapter 5: Mixed-phase clouds: progress and challenges, AMS Meteorological Monographs 58, 5.1–5.50, ISSN: 0065-9401. https://doi.org/10.1175/AMSMONOGRAPHS-D-17-0001.1
Laven P (2003) Simulation of rainbows, coronas, and glories by use of Mie theory. Appl Opt 42:436–444. https://doi.org/10.1364/AO.42.000436
Lyapustin AI, Kaufman YJ (2001) Role of adjacency effect in the remote sensing of aerosol. J Geophys Res 106(D11):11909–11916. https://doi.org/10.1029/2000JD900647
Lyapustin A, Gatebe CK, Kahn R, Brandt R, Redemann J, Russell P, King MD, Pedersen CA, Gerland S, Poudyal R, Marshak A, Wang Y, Schaaf C, Hall D, Kokhanovsky A (2010) Analysis of snow bidirectional reflectance from ARCTAS spring-2008 campaign. Atmos Chem Phys 10:4359–4375. https://doi.org/10.5194/acp-10-4359-2010
Malinka A, Zege E, Heygster G, Istomina L (2016) Reflective properties of white sea ice and snow. Cryosphere 10:2541–2557. https://doi.org/10.5194/tc-10-2541-2016

Mayer B, Schröder M, Preusker R, Schüller L (2004) Remote sensing of water cloud droplet size distributions using the backscatter glory: a case study. Atmos Chem Phys 4:1255–1263. https://doi.org/10.5194/acp-4-1255-2004

McFarquhar GM, Zhang G, Poellot MR, Kok GL, Mccoy R, Tooman T, Fridlind A, Heymsfield AJ (2007) Ice properties of single-layer stratocumulus during the mixed-phase arctic cloud experiment: 1. Observations J Geophys Res 112:D24201

Mech M, Orlandi E, Crewell S, Ament F, Hirsch L, Hagen M, Peters G, Stevens B (2014) HAMP—the microwave package on the high altitude and long range research aircraft (HALO). Atmos Meas Tech 7:4539–4553. https://doi.org/10.5194/amt-7-4539-2014

Mioche G, Jourdan O, Ceccaldi M, Delanoe J (2015) Variability of mixed-phase clouds in the Arctic with a focus on the Svalbard region: a study based on spaceborne active remote sensing. Atmos Chem Phys 15:2445–2461. https://doi.org/10.5194/acp-15-2445-2015

Mioche G, Jourdan O, Delanoë J, Gourbeyre C, Febvre G, Dupuy R, Monier M, Szczap F, Schwarzenboeck A, Gayet J-F (2017) Vertical distribution of microphysical properties of Arctic springtime low-level mixed-phase clouds over the Greenland and Norwegian seas. Atmos Chem Phys 17:12845–12869. https://doi.org/10.5194/acp-17-12845-2017

Nakajima T, King M (1990) Determination of the optical thickness and effective particle radius of clouds from reflected solar radiation measurements. Part I: Theo J Atmos Sci 47:1878–1893

Nott GJ, Duck TJ (2011) Lidar studies of the polar troposphere. Met Apps 18:383–405. https://doi.org/10.1002/met.289

Pilewskie P, Twomey S (1987) Discrimination of ice from water in clouds by optical remote sensing. Atmos Res 21:113–122

Pithan F, Svensson G, Caballero R, Chechin D, Cronin TW, Ekman AML, Neggers R, Shupe MD, Solomon A, Tjernström M, Wendisch M (2018) Role of air-mass transformations in exchange between the Arctic and mid-latitudes. Nat Geosci 11:805–812. https://doi.org/10.1038/s41561-018-0234-1

Platnick S, Li JY, King MD, Gerber H, Hobbs PV (2001) A solar reflectance method for retrieving the optical thickness and droplet size of liquid water clouds over snow and ice surfaces. J Geophys Res 106(D14):15185–15199. https://doi.org/10.1029/2000JD900441

Platnick S, Meyer KG, King MD, Wind G, Amarasinghe N, Marchant B, Arnold GT, Zhang Z, Hubanks PA, Holz RE, Yang P, Ridgway WL, Riedi J (2017) The MODIS cloud optical and microphysical products: collection 6 updates and examples from Terra and Aqua. IEEE Trans Geosci Remote Sens 55:502–525. https://doi.org/10.1109/TGRS.2016.2610522

Riese M, Oelhaf H, Preusse P, Blank J, Ern M, Friedl-Vallon F, Fischer H, Guggenmoser T, Höpfner M, Hoor P, Kaufmann M, Orphal J, Plöger F, Spang R, Suminska-Ebersoldt O, Ungermann J, Vogel B, Woiwode W (2014) Gimballed limb observer for radiance imaging of the atmosphere (GLORIA) scientific objectives. Atmos Meas Tech 7:1915–1928. https://doi.org/10.5194/amt-7-1915-2014

Rolland P, Liou K (2001) Surface variability effects on the remote sensing of thin cirrus optical and microphysical properties. J Geophys Res 106:22965–22977. https://doi.org/10.1029/2001JD900160

Schäfer M, Bierwirth E, Ehrlich A, Jäkel E, Wendisch M (2015) Airborne observations and simulations of three-dimensional radiative interactions between Arctic boundary layer clouds and ice floes. Atmos Chem Phys 1:8147–8163. https://doi.org/10.5194/acp-15-8147-2015

Schäfer M, Bierwirth E, Ehrlich A, Jäkel E, Werner F, Wendisch M (2017) Directional, horizontal inhomogeneities of cloud optical thickness fields retrieved from ground-based and airborne spectral imaging. Atmos Chem Phys 17:2359–2372. https://doi.org/10.5194/acp-17-2359-2017

Schäfer M, Loewe K, Ehrlich A, Hoose C, Wendisch M (2018) Simulated and observed horizontal inhomogeneities of optical thickness of Arctic stratus. Atmos Chem Phys 18:13115–13133. https://doi.org/10.5194/acp-18-13115-2018

Schäfler A, Craig G, Wernli H, Arbogast P, Doyle JD, McTaggart-Cowan R, Methven J, Rivière G, Ament F, Boettcher M, Bramberger M, Cazenave Q, Cotton R, Crewell S, Delanoë J, Dörnbrack A, Ehrlich A, Ewald F, Fix A, Grams CM, Gray SL, Grob H, Groß S, Hagen M, Harvey B,

Hirsch L, Jacob M, Kölling T, Konow H, Lemmerz C, Lux O, Magnusson L, Mayer B, Mech M, Moore R, Pelon J, Quinting J, Rahm S, Rapp M, Rautenhaus M, Reitebuch O, Reynolds CA, Sodemann H, Spengler T, Vaughan G, Wendisch M, Wirth M, Witschas B, Wolf K, Zinner T (2018) The north atlantic waveguide and downstream impact experiment. Bull Amer Meteor Soc 99:1607–1637. https://doi.org/10.1175/BAMS-D-17-0003.1

Shupe MD (2011) Clouds at arctic atmospheric observatories. Part II: thermodynamic phase characteristics. J Appl Meteor Climatol 50:645–661. https://doi.org/10.1175/2010JAMC2468.1

Shupe MD, Matrosov SY, Uttal T (2006) Arctic mixed-phase cloud properties derived from surface-based sensors at SHEBA. J Atmos Sci 63:697–711

Stachlewska IS, Neuber R, Lampert A, Ritter C, Wehrle G (2010) AMALi—The airborne mobile aerosol lidar for Arctic research. Atmos Chem Phys 10:2947–2963. https://doi.org/10.5194/acp-10-2947-2010

Stevens B, Ament F, Bony S, Crewell S, Ewald F, Gross S, Hansen A, Hirsch L, Jacob M, Kölling T, Konow H, Mayer B, Wendisch M, Wirth M, Wolf K, Bakan S, Bauer-Pfundstein B, Brueck M, Delanoë J, Ehrlich A, Farrell D, Forde M, Gödde F, Grob H, Hagen M, Jäkel E, Jansen F, Klepp C, Klingebiel M, Mech M, Peters G, Rapp M, Wing AA, Zinner T, (2018) A high-altitude long-range aircraft configured as a cloud observatory—the NARVAL expeditions. Bull Am Meteorol Soc, in review

Stone RS, Sharma S, Herber A, Eleftheriadis K, Nelson DW (2014) A characterization of Arctic aerosols on the basis of aerosol optical depth and black carbon measurements. Elem Sci Anth 2:27. http://doi.org/10.12952/journal.elementa.000027

Thompson DR, McCubbin I, Gao BC, Green RO, Matthews AA, Mei F, Meyer KG, Platnick S, Schmid B, Tomlinson J, Wilcox E (2016) Measuring cloud thermodynamic phase with shortwave infrared imaging spectroscopy. J Geophys Res Atmos 121:9174–9190. https://doi.org/10.1002/2016JD024999

Tomasi C, Kokhanovsky AA, Lupi A, Ritter C, Smirnov A, O'Neill NT, Stone RS, Holben NN, Nyeki S, Wehrli C, Stohl A, Mazzola M, Lanconelli C, Vitale V, Stebel K, Aaltonen V, de Leeuw G, Rodriguez E, Herber A, Radionov VF, Zielinski T, Petelski T, Sakerin SM, Kabanov DM, Xue Y, Mei L, Istomina L, Wagener R, McArthur B, Sobolewski PS, Kivi R, Courcoux Y, Larouche P, Broccardo S, Piketh SJ (2015) Aerosol remote sensing in polar regions. Earth Sci Rev 140:108–157. https://doi.org/10.1016/j.earscirev.2014.11.001

Wendisch M, Brenguier J-L (2013) Airborne measurements for environmental research—methods and instruments, Wiley–VCH Verlag GmbH & Co. KGaA, Weinheim, Germany. ISBN: 978-3-527-40996-9. 655 pp. https://doi.org/10.1002/9783527653218

Wendisch M, Müller D, Schell D, Heintzenberg J (2001) An airborne spectral albedometer with active horizontal stabilization. J Atmos Oceanic Technol 18:1856–1866. https://doi.org/10.1175/1520-0426(2001)018%3c1856:AASAWA%3e2.0.CO;2

Wendisch M, Pöschl U, Andreae MO, Machado LAT, Albrecht R, Schlager H, Rosenfeld D, Martin ST, Abdelmonem A, Afchine A, Araujo A, Artaxo P, Aufmhoff H, Barbosa HMJ, Borrmann S, Braga R, Buchholz B, Cecchini MA, Costa A, Curtius J, Dollner M, Dorf M, Dreiling V, Ebert V, Ehrlich A, Ewald F, Fisch G, Fix A, Frank F, Fütterer D, Heckl C, Heidelberg F, Hüneke T, Jäkel E, Järvinen E, Jurkat T, Kanter S, Kästner U, Kenntner M, Kesselmeier J, Klimach T, Knecht M, Kohl R, Kölling T, Krämer M, Krüger M, Krisna TC, Lavric JV, Longo K, Mahnke C, Manzi AO, Mayer B, Mertes S, Minikin A, Molleker S, Münch S, Björn Nillius K, Pfeilsticker C, Pöhlker A-E, Roiger D, Rose D, Rosenow D, Sauer M, Schnaiter J, Schneider C, de Schulz RAF, Souza A, Spanu P, Stock D, Vila C, Voigt A, Walser D, Walter R, Weigel B, Weinzierl F, Werner MA, Yamasoe H, Ziereis T, Zinner M Zöger (2016) The ACRIDICON-CHUVA campaign: studying tropical deep convective clouds and precipitation over Amazonia using the new German research aircraft HALO. Bull Am Meteorol Soc 97(10):1885–1908. https://doi.org/10.1175/BAMS-D-14-00255.1

Wendisch M, Brückner M, Burrows JP, Crewell S, Dethloff K, Ebell K, Lüpkes Ch, Macke A, Notholt J, Quaas J, Rinke A, Tegen I (2017) ArctiC amplification: climate relevant atmospheric and SurfaCe processes, and feedback mechanisms: $(AC)^3$. Eos 98. https://doi.org/10.1029/2017EO064803

Wendisch M, Macke A, Ehrlich A, Lüpkes C, Mech M, Chechin D, Dethloff K, Barientos C, Bozem H, Brückner M, Clemen H-C, Crewell S, Donth T, Dupuy R, Dusny C, Ebell K, Egerer U, Engelmann R, Engler C, Eppers O, Gehrmann M, Gong X, ottschalk M, Gourbeyre C, Griesche H, Hartmann J, Hartmann M, Heinold B, Herber A, Herrmann H, Heygster G, Hoor P, Jafariserajehlou S, Jäkel E, Järvinen E, Jourdan O, Kästner U, Kecorius S, Knudsen EM, Köllner F, Kretzschmar J, Lelli L, Leroy D, Maturilli M, Mei L, Mertes S, Mioche G, Neuber R, Nicolaus M, Nomokonova T, Notholt J, Palm M, van Pinxteren M, Quaas J, Richter P, Ruiz-Donoso E, Schäfer M, Schmieder K, Schnaiter M, Schneider J, Schwarzenböck A, Seifert P, Shupe MD, Siebert H, Spreen G, Stapf J, Stratmann F, Vogl T, Welti A, Wex H, Wiedensohler A, Zanatta M, Zeppenfeld S (2018) The arctic cloud puzzle: using ACLOUD/PASCAL multi-platform observations to unravel the role of clouds and aerosol particles in arctic amplification. Accepted by Bull Amer Meteor Soc. https://doi.org/10.1175/BAMS-D-18-0072.1, in press

Wesche C, Steinhage D, Nixdorf U (2016) Polar aircraft polar 5 and polar 6 operated by the Alfred Wegener Institute. J Large-Scale Res Facilities 2:A87. https://doi.org/10.17815/jlsrf-2-153

Wiebe H, Heygster G, Zege E, Aoki T, Hori M (2013) Snow grain size retrieval SGSP from optical satellite data: Validation with ground measurements and detection of snow fall events. Remote Sens Environ 128:11–20. https://doi.org/10.1016/j.rse.2012.09.007

Wirth M, Fix A, Mahnke P, Schwarzer H, Schrandt F, Ehret G (2009) The airborne multi-wavelength water vapor differential absorption lidar WALES: system design and performance. Appl Phys 96B:201–213. https://doi.org/10.1007/s00340-009-3365-7

Wiscombe W, Warren S (1980) A model for the spectral albedo of snow I. Pure snow. J Atmos Sci 37:2712–2733

Xu F, van Harten G, Diner DJ, Davis AB, Seidel FC, Rheingans B, Tosca M, Alexandrov MD, Cairns B, Ferrare RA, Burton SP, Fenn MA, Hostetler CA, Wood R, Redemann J (2018) Coupled retrieval of liquid water cloud and above-cloud aerosol properties using the Airborne multiangle spectropolarimetric imager (AirMSPI). J Geophys Res: Atmos 123:3175–3204. https://doi.org/10.1002/2017JD027926

Zege EP, Katsev IL, Malinka AV, Prikhach AS, Heygster G, Wiebe H (2011) Algorithm for retrieval of the effective snow grain size and pollution amount from satellite measurements. Remote Sens Environ 115:2674–2685. https://doi.org/10.1016/j.rse.2011.06.001

Snow Albedo and Radiative Transfer: Theory, Modeling, and Parameterization

Cenlin He and Mark Flanner

Abstract Snow is a critical component of the Earth climate and water systems, affecting surface water and energy fluxes and balance. Due to its strong ability to reflect sunlight, surface snow has significant positive feedback to the atmosphere (snow albedo feedback), resulting in enhanced climate change over high mountains and polar regions. Thus, it is important to accurately compute snow albedo in the solar spectrum. In the past decades, many theoretical and modeling approaches have been developed for snow radiative transfer and albedo calculations, with many important scientific advances on this topic. This chapter firstly reviews several widely-used theories and models for snow radiative transfer problems and then summarizes computational methods and major features of snow single-scattering properties that are required for radiative transfer calculations. Furthermore, a number of commonly-used snow albedo parameterizations developed for application in climate and weather models are presented. Finally, current challenges and future research directions are discussed.

1 Introduction

Snow is a critically important element in the Earth climate and water systems, strongly altering surface water and energy fluxes via the positive albedo feedback (Qu and Hall 2006; Flanner et al. 2011). The radiative transfer process and albedo of snow in the solar spectrum affect surface radiative balance by changing the absorption of downward solar radiation and influence the water balance by changing snow melting and sublimation processes. Many important factors can impact snow albedo

C. He (✉)
Advanced Study Program and Research Applications Laboratory, National Center for Atmospheric Research (NCAR), Boulder, CO, USA
e-mail: cenlinhe@ucar.edu

M. Flanner
Department of Climate and Space Sciences and Engineering, University of Michigan, Ann Arbor, MI, USA

A. Kokhanovsky (ed.), *Springer Series in Light Scattering*,
Springer Series in Light Scattering,
https://doi.org/10.1007/978-3-030-38696-2_3

and radiative transfer, including snow grain size (e.g., Wiscombe and Warren 1980; Flanner et al. 2007; Picard et al. 2017), grain shape (e.g., Kokhanovsky 2013; Libois et al. 2013; Liou et al. 2014; Dang et al. 2016; Räisänen et al. 2017), grain aggregating (e.g., Kokhanovsky and Zege 2004; Peltoniemi 2007; He et al. 2017a), snow thickness and density (e.g., Warren 1982; Aoki et al. 2011), impurities in snow (e.g., Flanner et al. 2009; He et al. 2014; Lee et al. 2017; Tuzet et al. 2017; Pu et al. 2019; Yi et al. 2019), and environmental conditions such as diffuse/direct radiation and solar zenith angle (e.g., Warren 1982; Gardner and Sharp 2010). Thus, accurate estimates of snow albedo require a comprehensive integration of all these key factors in snow radiative transfer and albedo computations.

In the past few decades, enormous efforts have been made to explicitly compute snow albedo and associated radiative quantities by developing radiative transfer theories and models (e.g., Wiscombe and Warren 1980; Stamnes et al. 1988; Toon et al. 1989; Kokhanovsky and Zege 2004; Flanner et al. 2007; Liou et al. 2014), ranging from simplified approximations to detailed multi-stream treatments and sophisticated Monte Carlo methods. Along with the advances on snow radiative transfer theories and models, crucial improvements have also been achieved to more realistically treat snow grains and compute their single-scattering properties (e.g., Jin et al. 2008; Libois et al. 2013; Dang et al. 2016; He et al. 2017b; Kokhanovsky et al. 2018), which benefits from the development of particle-optics computational approaches. In addition, a number of empirical or physical parameterizations have been developed to represent snow albedo as a function of snow properties and environmental variables (e.g., Marshall 1989; Gardner and Sharp 2010; Dang et al. 2015; He et al. 2018a, 2019a; Saito et al. 2019), which provides efficient tools for application in weather and climate models. Based on these powerful computational and modeling tools, significant scientific advances have been made in understanding and quantifying the effects of key factors on snow optical properties and albedo. However, challenges still exist, and several important problems need to be tackled in future research.

Therefore, this chapter focuses on the current understanding and recent scientific advances on snow radiative transfer and albedo modeling and also sheds light on potential future studies on this topic. Figure 1 summarizes the key factors involved in snow albedo and radiative transfer computations, which are mostly covered in this chapter. Specifically, the widely-used theories and models for snow radiative transfer problems are firstly reviewed in Sect. 2, followed by a summary of snow single-scattering property computations in Sect. 3. Snow albedo parameterizations developed for climate and weather modeling are presented in Sect. 4. Finally, current challenges and future research directions are discussed in Sect. 5.

2 Snow Radiative Transfer Theory and Modeling

Snow radiative transfer processes in visible and near-infrared (NIR) wavelengths are governed by snow particle absorption and scattering, based on physical principles that are similar to those in atmospheric radiative transfer processes. In the past

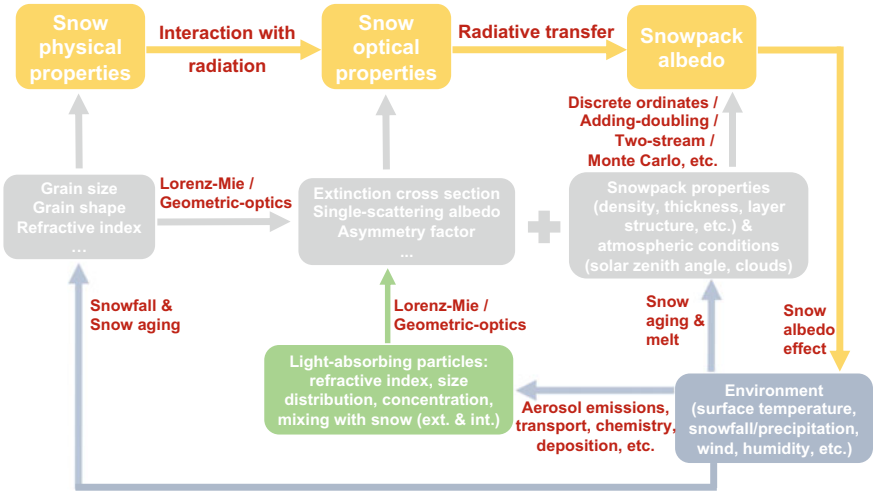

Fig. 1 A demonstration of key factors involved in the computation of snow single-scattering properties and albedo

decades, many advances on snow radiative transfer theories and models have been achieved, with different complexities ranging from early-stage exponential decay to simplified two-stream approximations to rigorous adding-doubling and discrete ordinate methods to detailed Monte Carlo photon tracing treatments. This section summarizes the essence and key mathematical equations for major radiative transfer approaches that are applied to snowpack. Note that these approaches have also been nicely presented in previous papers and books. More details of each theory/model can be found in the corresponding references provided in the following sub-sections.

The most common treatment of snowpack is as a medium of air containing a collection of ice particles. Thus, there exists a refractive boundary between porous snow and high-density ice (e.g., glacier ice or sea ice) but not for snow overlying land, leading to different radiative transfer treatments for snow on ice (non-uniformly refractive layered media) and snow on land (uniformly refractive layered media). Thus, these two types of snow radiative transfer processes are discussed separately here, with a focus on plane-parallel snowpack conditions. Figure 2 illustrates the key processes accounted for in contemporary snow and ice radiative transfer theories and models.

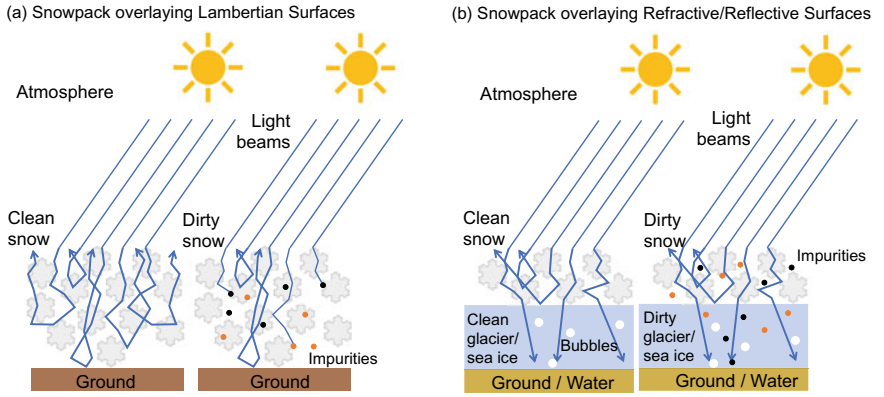

Fig. 2 An illustration of key processes accounted for in contemporary snow and ice radiative transfer models: **a** in the case of snowpack overlaying Lambertian surfaces, multiple scattering and directional distributions of scattering by snow grains for clean snow as well as absorption and albedo reduction by impurities such as black carbon (black circles) and dust (orange circles) for dirty snow; **b** in the case of snowpack overlaying refractive/reflective surfaces, refraction and Fresnel reflection at interfaces of layers with different refractive indices, such as clean or dirty porous snow overlying high-density ice with bubbles (white circles) and/or impurities. Note that atmospheric radiative transfer processes are not demonstrated in detail here

2.1 Basic Radiative Transfer Formulation

The general mathematical equations of snowpack radiative transfer are similar to those of atmospheric radiative transfer (Liou 2002), but with different optical properties and boundary conditions applied in solving the equations. Assuming time-independent elastic scattering (i.e., no conversion from one radiation wavelength to another) and sufficiently rare media where each particle is in the far-field of the scattered radiation from other particles (i.e., no interparticle shadowing), the basic equation describing the transfer of monochromatic radiation in a plane-parallel homogeneous medium (e.g., atmosphere or snowpack) can be written as (Chandrasekhar 1960):

$$\mu \frac{dI(\tau, \mu, \phi)}{d\tau} = I(\tau, \mu, \phi) - S(\tau, \mu, \phi) \tag{2.1.1}$$

where $I(\tau, \mu, \phi)$ is the total (diffuse + direct) intensity at optical depth τ within unit solid angle measured downward from the upper boundary in the direction of μ (the cosine of polar/zenith angle, which is positive with respect to the upward normal) and ϕ (the azimuthal angle). $S(\tau, \mu, \phi)$ is the source function given by

$$S(\tau,\mu,\phi)=\frac{\tilde{\omega}}{4\pi}\int_0^{2\pi}\int_{-1}^{1}p\left(\mu,\phi;\mu',\phi'\right)\times I\left(\tau,\mu',\phi'\right)d\mu' d\phi'+Q(\tau,\mu,\phi) \tag{2.1.2}$$

where the first term on the right-hand side represents multiple scattering and $Q(\tau,\mu,\phi)$ represents additional sources (e.g., thermal emission and/or direct incident flux). $p\left(\mu,\phi;\mu',\phi'\right)$ is the phase function for radiation scattered from the direction (μ',ϕ') to the direction (μ,ϕ), and $\tilde{\omega}$ is the single-scattering albedo (i.e., the ratio of scattering coefficient to extinction coefficient). When the usual distinction between direct and diffuse radiation is made, $I(\tau,\mu,\phi)$ in Eqs. (2.1.1) and (2.1.2) indicates the diffuse intensity only, along with the $Q(\tau,\mu,\phi)$ term expressed as:

$$Q(\tau,\mu,\phi)=\frac{\tilde{\omega}F_0}{4\pi}p(\mu,\phi;-\mu_0,\phi_0)e^{-\tau/\mu_0} \tag{2.1.3}$$

for a parallel direct beam incident from the direction (μ_0,ϕ_0) on a non-emitting medium. μ_0 (positive) is the cosine of solar zenith angle, and $\mu_0 F_0$ is the direct-beam solar flux. Note that the internal thermal emission of the medium is not considered here in the solar spectrum, which however is important at longer wavelengths (e.g., >3 μm). Thus, the general radiative transfer equation to be solved for a plane-parallel homogeneous medium is (see also Fig. 3):

$$\mu\frac{dI(\tau,\mu,\phi)}{d\tau}=I(\tau,\mu,\phi)-\frac{\tilde{\omega}}{4\pi}\int_0^{2\pi}\int_{-1}^{1}p\left(\mu,\phi;\mu',\phi'\right)\times I\left(\tau,\mu',\phi'\right)d\mu' d\phi' - \frac{\tilde{\omega}F_0}{4\pi}p(\mu,\phi;-\mu_0,\phi_0)e^{-\tau/\mu_0} \tag{2.1.4}$$

Furthermore, vertically inhomogeneous media can be approximated by multiple layered homogeneous media with proper treatments of boundary conditions between adjacent layers (see Sect. 2.2). For non-uniformly refractive layered media (e.g., snow on glacier/sea ice), special considerations of the direct-beam source term ($Q(\tau,\mu,\phi)$) and the refractive boundary/interface between two adjacent media should be taken (see Sect. 2.3). Here, we summarize the widely-used approaches for solving snow radiative transfer equations under different conditions.

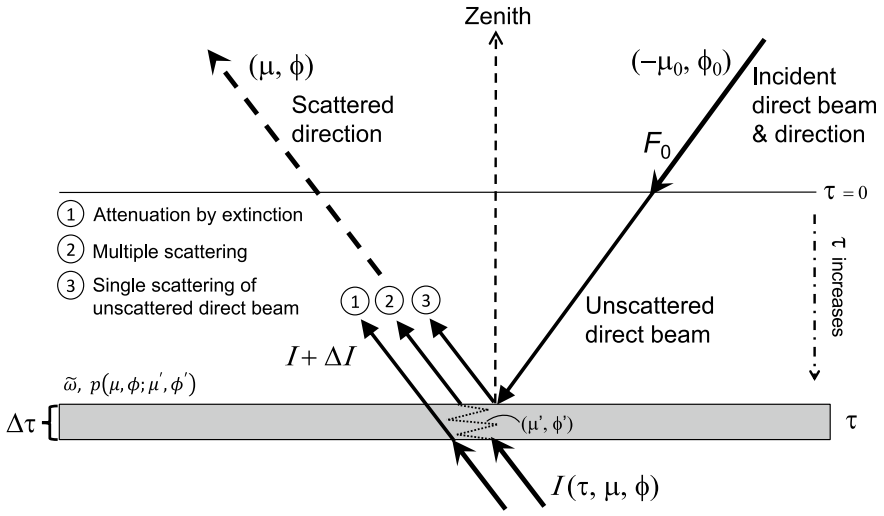

Fig. 3 An illustration of the general radiative transfer equation (Eq. 2.1.4) for a plane-parallel homogeneous medium with phase function ($p(\mu, \phi; \mu', \phi')$) and single-scattering albedo ($\tilde{\omega}$). Three major components contributing to diffuse intensity changes are (1) attenuation by extinction, (2) multiple scattering, and (3) single scattering of unscattered direct beam, which correspond to the three terms on the right-hand side of Eq. (2.1.4). Note that internal thermal emission of the medium is not considered here in the solar spectrum. The notations and symbols are defined in the text

2.2 Snow on Land (Uniformly Refractive Layered Media)

2.2.1 The Discrete-Ordinate-Method Radiative Transfer (DISORT) Theory

The discrete ordinate radiative transfer (DISORT) method is one of the most rigorous approaches to solve radiative transfer problems, and was firstly introduced by Chandrasekhar (1960). The DISORT computation is often used as a benchmark when evaluating other radiative transfer model results (Dang et al. 2019). The major advantage of the DISORT method is reducing the integral-differential radiative transfer equation (Eq. 2.1.4) to a cluster of ordinary differential equations. However, the original formulation and solution described by Chandrasekhar suffer from some mathematical and numerical difficulties in finding eigenvectors and eigenvalues (Liou 1973). Throughout the years, many efforts have been made to improve the DISORT method (e.g., Liou 1973, 1975; Asano 1975; Liou et al. 1978; Stamnes and Swanson 1981; Stamnes et al. 1988). Among them, the most commonly-used one is the numerically stable algorithm based on matrix formulation proposed by Stamnes et al. (1988). This algorithm has been applied to many snow and snow-atmosphere radiative transfer models (e.g., Glendinning and Morris 1999; Green et al. 2002; Lee-Taylor and Madronich 2002; Namazi et al. 2015).

According to Chandrasekhar (1960), the phase function $p(\mu, \phi; \mu', \phi')$ and intensity $I(\tau, \mu, \phi)$ can be numerically expanded in a series of Legendre polynomials and a Fourier cosine series, respectively, as follows:

$$I(\tau, \mu, \phi) = \sum_{m=0}^{2N-1} I^m(\tau, \mu) \cos\left(m(\phi_0 - \phi)\right) \tag{2.2.1}$$

$$p(\mu, \phi; \mu', \phi') \equiv p(\cos\ \Theta) = \sum_{l=0}^{2N-1} (2l+1) g_l P_l(\cos\ \Theta) \tag{2.2.2a}$$

$$g_l = \frac{1}{2} \int_{-1}^{1} P_l(\cos\ \Theta) p(\cos\ \Theta) d\cos\ \Theta \tag{2.2.2b}$$

where $2N$ is the number of expanded Legendre polynomials and Fourier components, Θ is the scattering angle (i.e., the angle between the direction vectors before and after scattering), $P_l(\cos\ \Theta)$ is the Legendre polynomial, and g_l is the expansion coefficient. Substituting these expansion equations into Eq. (2.1.4), we have $2N$ independent equations corresponding to $2N$ Fourier components as follows:

$$\mu \frac{dI^m(\tau, \mu)}{d\tau} = I^m(\tau, \mu) - \int_{-1}^{1} D^m(\mu, \mu') \times I^m(\tau, \mu') d\mu' - Q^m(\tau, \mu)$$
$$[m = 0, 1, \ldots, 2N-1] \tag{2.2.3a}$$

$$D^m(\mu, \mu') = \frac{\tilde{\omega}}{2} \sum_{l=m}^{2N-1} (2l+1) \frac{(l-m)!}{(l+m)!} g_l P_l^m(\mu) P_l^m(\mu') \tag{2.2.3b}$$

$$Q^m(\tau, \mu) = X_0^m(\tau, \mu) e^{-\tau/\mu_0} \tag{2.2.3c}$$

$$X_0^m(\tau, \mu) = \frac{\tilde{\omega} F_0}{4\pi} (2 - \delta_{0,m}) \sum_{l=0}^{2N-1} (-1)^{l+m} (2l+1) \frac{(l-m)!}{(l+m)!} g_l P_l^m(\mu) P_l^m(\mu_0) \tag{2.2.3d}$$

$$\delta_{0,m} = \begin{cases} 1\ if\ m = 0 \\ 0\ otherwise \end{cases} \tag{2.2.3e}$$

where $P_l^m(\mu)$ is the associated Legendre polynomial, and $Q^m(\tau, \mu)$ is the mth Fourier component of the direct-beam source. As a result, $I^m(\tau, \mu)$ can be determined by solving these $2N$ independent equations, followed by $I(\tau, \mu, \phi)$ computed using Eq. (2.2.1).

Using the Gaussian quadrature (Skyes 1951), Eq. (2.2.3a) can be further written as (for each mth component):

$$\mu_i \frac{dI^m(\tau,\mu_i)}{d\tau} = I^m(\tau,\mu_i) - \sum_{\substack{j=-N' \\ j\neq 0}}^{N'} w_j D^m(\mu_i,\mu_j) \times I^m(\tau,\mu_j) - Q^m(\tau,\mu_i)$$
$$\left[i = \pm 1, \pm 2, \ldots, \pm N'\right] \tag{2.2.4a}$$

$$\sum_{\substack{j=-N' \\ j\neq 0}}^{N'} w_j D^0(\mu_i,\mu_j) = \sum_{\substack{i=-N' \\ i\neq 0}}^{N'} w_i D^0(\mu_i,\mu_j) = \tilde{\omega} \tag{2.2.4b}$$

where μ_i and w_i are quadrature points (streams) and weights of the double-Gauss scheme, satisfying that $\mu_{-j} = -\mu_j$ and $w_{-j} = w_j$. Equation (2.2.4b) implies that the re-normalization of phase function is unnecessary, and energy is conserved in the calculations.

If considering a single homogeneous layer in which the single-scattering albedo and phase function do not vary, Eq. (2.2.4a) can be written in a matrix form (for each mth component):

$$\begin{vmatrix} \frac{d\mathbf{I}^+}{d\tau} \\ \frac{d\mathbf{I}^-}{d\tau} \end{vmatrix} = \begin{vmatrix} -\alpha & -\beta \\ \beta & \alpha \end{vmatrix} \begin{vmatrix} \mathbf{I}^+ \\ \mathbf{I}^- \end{vmatrix} + \begin{vmatrix} \mathbf{M}^{-1}\mathbf{Q}^+ \\ \mathbf{M}^{-1}\mathbf{Q}^- \end{vmatrix} \tag{2.2.5a}$$

$$\alpha = \mathbf{M}^{-1}\left(\mathbf{D}^+\mathbf{W} - \mathbf{I}\right) \tag{2.2.5b}$$

$$\beta = \mathbf{M}^{-1}\mathbf{D}^-\mathbf{W} \tag{2.2.5c}$$

where

$$\mathbf{I}^{\pm} = \left[I^m(\tau,\pm\mu_i)\right], \quad i = 1,2,\ldots,N'$$

$$\mathbf{Q}^{\pm} = \left[Q^m(\tau,\pm\mu_i)\right], \quad i = 1,2,\ldots,N'$$

$$\mathbf{M} = \left[\mu_i\delta_{i,j}\right], \quad i,j = 1,2,\ldots,N'$$

$$\mathbf{W} = \left[w_i\delta_{i,j}\right], \quad i,j = 1,2,\ldots,N'$$

$$\mathbf{D}^{\pm} = \left[D^m(\pm\mu_i,\mu_j)\right] = \left[D^m(\mp\mu_i,-\mu_j)\right], \quad i,j = 1,2,\ldots,N'$$

Equation (2.2.5a, b, c) is a system of $2N'$ coupled linear ordinary differential equations with constant coefficients. Based on linear algebra and eigenvector theory, the general solution to Eq. (2.2.4a) for each mth component can be found as (omitting the superscript m):

$$I(\tau, \mu_i) = \sum_{\substack{j=-N' \\ j\neq 0}}^{N'} C_j G_j(\mu_i) e^{-k_j \tau} + Z_0(\mu_i) e^{-\tau/\mu_0} \tag{2.2.6a}$$

where $G_j(\mu_i)$ and k_j are the eigenvectors and eigenvalues of the homogeneous version ($\mathbf{Q}^{\pm} = \mathbf{0}$) of Eq. (2.2.5a), C_j is the coefficient to be determined by boundary conditions (Eq. 2.2.7a, b), and $Z_0(\mu_i)$ is the coefficient for the particular solution of the direct-beam source term, which is determined by solving the following linear equation system (omitting the superscript m):

$$\sum_{\substack{j=-N' \\ j\neq 0}}^{N'} \left[\left(1 + \frac{\mu_j}{\mu_0}\right) \delta_{i,j} - w_j D(\mu_i, \mu_j) \right] Z_0(\mu_j) = X_0(\mu_i) \tag{2.2.6b}$$

where $X_0(\mu_i)$ is defined by Eq. (2.2.3d).

To solve these equations, the general boundary conditions at the top and bottom boundaries of one homogeneous layer are

$$I(\tau = 0, -\mu, \phi) = I_{top}(-\mu, \phi) \tag{2.2.7a}$$

$$I(\tau = \tau_L, \mu, \phi) = I_{bot}(\mu, \phi) \tag{2.2.7b}$$

where τ_L is the total optical depth of the homogeneous snow layer. I_{top} and I_{bot} are the light intensities incident at the top and bottom boundaries, respectively. For snowpack in the solar spectrum specifically, the intensity incident at the top snow boundary can be direct and/or diffuse solar radiation after going through the atmosphere, while the intensity incident at the bottom snow boundary can be radiation reflected by the underlying ground, expressed as:

$$\begin{aligned} I_{bot}(\mu, \phi) = I(\tau = \tau_L, \mu, \phi) = & \frac{1}{\pi} \int_0^{2\pi} \int_0^1 R_g(\mu, \phi; -\mu', \phi') \times I(\tau_L, -\mu', \phi') \mu' d\mu' d\phi' \\ & + \frac{\mu_0 F_0}{\pi} R_g(\mu, \phi; -\mu_0, \phi_0) e^{-\tau_L/\mu_0} \end{aligned} \tag{2.2.7c}$$

where $R_g(\mu, \phi; -\mu', \phi')$ is the bidirectional reflectivity of the underlying ground.

Furthermore, the inhomogeneous snowpack could be approximated by multiple adjacent homogeneous snow layers through solving the preceding radiative transfer equations with additional continuity requirements across layer interfaces. Assuming a snowpack consisting of L homogeneous snow layers, then the following continuity and boundary conditions should be satisfied:

$$I_1^m(\tau = 0, -\mu_i) = I_{top}^m(-\mu_i), \quad i = 1, 2, \ldots, N' \tag{2.2.8a}$$

$$I_p^m(\tau=\tau_p,\mu_i)=I_{p+1}^m(\tau=\tau_p,\mu_i),\quad i=\pm1,\pm2,\ldots,\pm N',\ p=1,\ldots,L-1 \tag{2.2.8b}$$

$$I_L^m(\tau=\tau_L,\mu_i)=I_{bot}^m(\mu_i),\quad i=1,2,\ldots,N' \tag{2.2.8c}$$

where $I_{bot}^m(\mu_i)$ is the mth Fourier component derived from the Fourier and Legendre expansions of $I_{bot}(\mu,\phi)$ and $R_g(\mu,\phi;-\mu',\phi')$ in Eq. (2.2.7c), respectively. Therefore, based on the boundary and continuity conditions, the preceding snow radiative transfer problem can be solved. Interested readers can refer to Stamnes et al. (1988) for detailed numerical implementations of the DISORT algorithm, with the corresponding computer program available at http://lllab.phy.stevens.edu/disort/.

Many studies have used the DISORT method in snow albedo modeling. For example, Glendinning and Morris (1999) incorporated DISORT into a physically-based snow energy budget model (SNTHERM) to improve simulations of snow albedo and heating, which showed a better comparison with measurements. Green et al. (2002) employed the DISORT snow radiative transfer model to investigate how the spectral snow reflectance is affected by snow grain size and liquid water fraction. Lee-Taylor and Madronich (2002) developed a coupled atmosphere-snow radiative transfer model based on the DISORT algorithm to quantify the in-snow nitrate photolysis rate. Recently, Dang et al. (2015) applied the DISORT model to snow albedo modeling and developed a set of snow albedo parameterizations. Namazi et al. (2015) used the DISORT model for snow simulations to generate a lookup table of snow albedo and transmission as a function of snow water equivalent, underlying surface albedo, solar zenith angle, snow grain size, and impurity content, which was further implemented into the Canadian Atmospheric Global Climate Model (CanAM4.2).

2.2.2 The Adding-Doubling Method

Another rigorous approach to solve radiative transfer equations is the adding method. The basic radiative transfer principle of the adding method was described by Stokes (1862), with further development for different radiative transfer applications since then (e.g., Peebles and Plesset 1951; Hansen 1971; Takano and Liou 1989). One commonly-used formulation is the one proposed by van de Hulst (1980). The adding method has been widely used in solving snowpack and snow-atmosphere radiative transfer systems (e.g., Aoki 1992; Aoki et al. 2000; Liou et al. 2014; Saito et al. 2019).

Based on the adding theory, two important physical parameters, transmission function (T) and reflection function (R), for a light beam incident downward on the top of a homogeneous medium layer are firstly defined using the following equations:

$$I_{out,top}(\mu,\phi)=\frac{1}{\pi}\int_0^{2\pi}\int_0^1 R(\mu,\phi;\mu',\phi')\times I_{in,top}(\mu',\phi')\mu' d\mu' d\phi' \tag{2.2.9a}$$

$$I_{out,bottom}(\mu,\phi)=\frac{1}{\pi}\int_0^{2\pi}\int_0^1 T\left(\mu,\phi;\mu',\phi'\right)\times I_{in,top}\left(\mu',\phi'\right)\mu' d\mu' d\phi' \quad (2.2.9b)$$

Similarly, for a light beam incident upward on the bottom of the medium layer, we have:

$$I_{out,bottom}(\mu,\phi)=\frac{1}{\pi}\int_0^{2\pi}\int_0^1 R^*\left(\mu,\phi;\mu',\phi'\right)\times I_{in,bottom}\left(\mu',\phi'\right)\mu' d\mu' d\phi' \quad (2.2.9c)$$

$$I_{out,top}(\mu,\phi)=\frac{1}{\pi}\int_0^{2\pi}\int_0^1 T^*\left(\mu,\phi;\mu',\phi'\right)\times I_{in,bottom}\left(\mu',\phi'\right)\mu' d\mu' d\phi' \quad (2.2.9d)$$

where R (R^*) and T (T^*) denote functions for the light beam coming from above (below). For a thin homogeneous layer, the reflection and transmission functions are the same ($R=R^*$ and $T=T^*$) when illuminated from above or below under the same angular distribution of incident light. However, when accounting for the adding of layers (see below), the reflection and transmission functions for combined layers will rely on the incident direction of light beams (i.e., coming from above or below).

For a homogeneous layer with an optical depth of $\Delta\tau$ that is sufficiently small to adopt the single-scattering approximation under direct beam (no diffuse light input), the source function in Eq. (2.1.2) can be written as:

$$S(\tau,\mu,\phi)=\frac{\tilde{\omega}F_0}{4\pi}p(\mu,\phi;-\mu_0,\phi_0)e^{-\tau/\mu_0} \quad (2.2.10a)$$

$$I_{in,top}(\mu,\phi)=0 \quad (2.2.10b)$$

$$I_{in,bottom}(\mu,\phi)=0 \quad (2.2.10c)$$

Substituting these equations into the basic radiative transfer equation (Eq. 2.1.1), the reflection and transmission functions can be solved as (Liou 2002):

$$R(\mu,\phi;\mu_0,\phi_0)=\frac{\tilde{\omega}}{4(\mu+\mu_0)}p(\mu,\phi;-\mu_0,\phi_0)\left(1-e^{-\Delta\tau\left(\frac{1}{\mu}+\frac{1}{\mu_0}\right)}\right) \quad (2.2.11a)$$

$$T(\mu,\phi;\mu_0,\phi_0)=\begin{cases}\frac{\tilde{\omega}}{4(\mu-\mu_0)}p(-\mu,\phi;-\mu_0,\phi_0)\left(e^{-\Delta\tau/\mu}-e^{-\Delta\tau/\mu_0}\right), & \mu\neq\mu_0\\ \frac{\tilde{\omega}\Delta\tau}{4\mu_0^2}p(-\mu,\phi;-\mu_0,\phi_0)e^{-\Delta\tau/\mu_0}, & \mu=\mu_0\end{cases} \quad (2.2.11b)$$

For an infinitesimal layer with a very small $\Delta\tau$ (e.g., 10^{-8}), it is reasonable to assume that only single scattering occurs within the layer. As a result, Eq. (2.2.11a, b) can be further simplified as ($\Delta\tau \to 0$):

$$R(\mu, \phi; \mu_0, \phi_0) = \frac{\tilde{\omega}\Delta\tau}{4\mu\mu_0} p(\mu, \phi; -\mu_0, \phi_0) \tag{2.2.12a}$$

$$T(\mu, \phi; \mu_0, \phi_0) = \frac{\tilde{\omega}\Delta\tau}{4\mu\mu_0} p(-\mu, \phi; -\mu_0, \phi_0) \tag{2.2.12b}$$

$$R^*(\mu, \phi; \mu_0, \phi_0) = \frac{\tilde{\omega}\Delta\tau}{4\mu\mu_0} p(-\mu, \phi; \mu_0, \phi_0) \tag{2.2.12c}$$

$$T^*(\mu, \phi; \mu_0, \phi_0) = \frac{\tilde{\omega}\Delta\tau}{4\mu\mu_0} p(\mu, \phi; \mu_0, \phi_0) \tag{2.2.12d}$$

For two adjacent layers with optical depth τ_1 and τ_2, we denote the reflection and total (direct and diffuse) transmission functions for the first and second layers by R_1, $\widetilde{T}_1$, and R_2, $\widetilde{T}_2$, respectively. Considering numerous light reflections within the two layers, the combined reflection (R_{12}) at the top of the first layer ($\tau = 0$) and the combined transmission ($\widetilde{T}_{12}$) at the bottom of the second layer ($\tau = \tau_1 + \tau_2$) can be derived as (Liou 2002):

$$\begin{aligned} R_{12} &= R_1 + \widetilde{T}_1^* R_2 \widetilde{T}_1 + \widetilde{T}_1^* R_2 R_1^* R_2 \widetilde{T}_1 + \widetilde{T}_1^* R_2 R_1^* R_2 R_1^* R_2 \widetilde{T}_1 + \cdots \\ &= R_1 + \widetilde{T}_1^* R_2 \left(1 - R_1^* R_2\right)^{-1} \widetilde{T}_1 \end{aligned} \tag{2.2.13a}$$

$$\begin{aligned} \widetilde{T}_{12} &= \widetilde{T}_2 \widetilde{T}_1 + \widetilde{T}_2^* R_1^* R_2 \widetilde{T}_1 + \widetilde{T}_2^* R_1^* R_2 R_1^* R_2 \widetilde{T}_1 + \cdots \\ &= \widetilde{T}_2 \left(1 - R_1^* R_2\right)^{-1} \widetilde{T}_1 \end{aligned} \tag{2.2.13b}$$

Similarly, the combined total transmission ($\widetilde{D}$) and reflection (U) functions between the two layers can be expressed as:

$$\widetilde{D} = \widetilde{T}_1 + R_1^* R_2 \widetilde{T}_1 + R_1^* R_2 R_1^* R_2 \widetilde{T}_1 + \cdots = \left(1 - R_1^* R_2\right)^{-1} \widetilde{T}_1 \tag{2.2.13c}$$

$$U = R_2 \widetilde{T}_1 + R_2 R_1^* R_2 \widetilde{T}_1 + R_2 R_1^* R_2 R_1^* R_2 \widetilde{T}_1 + \cdots = R_2 \left(1 - R_1^* R_2\right)^{-1} \widetilde{T}_1 \tag{2.2.13d}$$

To further separate direct and diffuse components of the total transmission function, we can use

$$\widetilde{T} = T + e^{-\tau/\mu_0} \tag{2.2.14}$$

Substituting Eq. (2.2.14) into Eq. (2.2.13a, b, c, d), the diffuse and direct components can then be explicitly expressed.

Thus, the preceding analysis indicates a set of iterative equations (i.e., the adding equations) to compute the diffuse reflection and transmission in two layers, which can be summarized by:

$$Q = R_1^* R_2 \tag{2.2.15a}$$

$$S = Q(1-Q)^{-1} \tag{2.2.15b}$$

$$D = T_1 + ST_1 + Se^{-\tau_1/\mu_0} \tag{2.2.15c}$$

$$U = R_2 D + R_2 e^{-\tau_1/\mu_0} \tag{2.2.15d}$$

$$R_{12} = R_1 + e^{-\tau_1/\mu} U + T_1^* U \tag{2.2.15e}$$

$$T_{12} = e^{-\tau_2/\mu} U + T_2 e^{-\tau_1/\mu_0} + T_2 D \tag{2.2.15f}$$

$$T_{direct-beam} = e^{-(\tau_1+\tau_2)/\mu_0} \tag{2.2.15g}$$

where the product of the two functions denotes an integration over an appropriate solid angle to account for all possible multiple scattering contributions, which is defined as:

$$R_1^* R_2 = \frac{1}{\pi} \int_0^{2\pi} \int_0^1 R_1^*(\mu, \phi; \mu', \phi') \times R_2(\mu', \phi'; \mu_0, \phi_0) \mu' d\mu' d\phi' \tag{2.2.16}$$

Practically, it is often assumed that $\tau_1 = \tau_2$ in numerical computations, which is referred to as the adding-doubling method. Specifically, for a snowpack with an optical depth of τ_s, one can start with a very small $\Delta\tau$ and use Eqs. (2.2.12a, b, c, d)–(2.2.16) to calculate the light reflection and transmission for two adjacent homogeneous layers with a total optical depth of $2\Delta\tau$. Subsequently, the computations of these equations are repeated by adding more layers until the desired snowpack optical depth (τ_s) is obtained. For practical considerations, if $\Delta\tau$ is too small, the computational burden can be rather heavy. Thus, an appropriate $\Delta\tau$ should be selected to balance computational accuracy and efficiency, which may vary from case to case. Typically, a thin snow layer with a thickness of 1 mm, a density of 150 kg m^{-3}, and a grain radius of 100 μm has an optical depth of about 2.5.

One important issue associated with the adding-doubling method is the calculation of the phase function $p(\mu, \phi; \mu', \phi')$ in Eq. (2.2.12a, b, c, d). For particles with a sharp diffraction peak in the phase function (e.g., ice crystals), it requires thousands of Fourier components in the phase function expansion to achieve accurate results. To improve the numerical efficiency, special treatments (e.g., truncation and approximation) are usually used (Joseph et al. 1976; Liou 2002), leading

to necessary adjustments (e.g., delta-transform/scaling) of particle single-scattering properties (see Sect. 2.2.3). The preceding adding equations can be further applied to cases that account for polarization, where the light beam is characterized by the Stokes parameters and the scalar phase function should be replaced by a phase matrix (Takano and Liou 1989).

Based on the adding-doubling method, a number of snow radiative transfer models have been developed. For example, Aoki (1992) developed a multiple scattering model for the coupled atmosphere-snow system using the adding-doubling theory. Leroux et al. (1999) proposed a snow bidirectional reflectance model based on the adding-doubling method, which also includes polarization information and was used to investigate snow grain shape effects on the reflectance. Liou et al. (2014) innovated a stochastic aerosol-snow albedo model using the adding-doubling method for radiative transfer computations and the geometric-optics surface-wave (GOS) approach for single-scattering property calculations (see Sect. 3.1.3). Recently, Saito et al. (2019) constructed a multi-layer snow albedo model based on the adding-doubling and improved geometric-optics methods to account for the effects of various ice crystal shapes. Besides, Briegleb and Light (2007) also developed a delta-Eddington adding-doubling method to treat radiative transfer for snow on sea ice (see Sect. 2.3.2). More detailed descriptions of the adding method have been presented by Liou (2002).

2.2.3 The Two-Stream Approximation

The two-stream approximation is one of the most widely-used methods for modeling radiative transfer in snowpack and the atmosphere, due to its high computational efficiency and adequate accuracy, which is particularly suitable for application in climate models. The first application of the two-stream approximation to snow radiative transfer calculations was conducted by Dunkle and Bevans (1956), followed by other studies (e.g., Barkstrom 1972; Bohren and Barkstrom 1974; Choudhury and Chang 1979). Warren (1982) gave a thorough review of these early-stage two-stream snow models, while Meador and Weaver (1980) provided a more general summary of the two-stream approximation. The first modern and accurate snow albedo model with a two-stream radiative transfer framework may be that developed by Wiscombe and Warren (1980) for homogeneous multiple-scattering snow layers, while Toon et al. (1989) further generalized the two-stream approximation to radiative transfer in vertically inhomogeneous media. These two studies are the basis of the commonly-used Snow, Ice, and Aerosol Radiation (SNICAR) model (Flanner and Zender 2006; Flanner et al. 2007), which has been implemented in a number of global land and climate models. Here, we briefly review the early-stage two-stream models and then focus on introducing the framework of Wiscombe and Warren (1980) and formulations developed by Toon et al. (1989).

The early two-stream snow models proposed by Dunkle and Bevans (1956) and Giddings and LaChapelle (1961) are applicable under diffuse light and high snow albedo. Their models require two input variables, which can be loosely linked to snow

grain size and absorption coefficient and are usually derived by fitting albedo and flux measurements, instead of explicitly calculating scattering by individual snow grains. Bohren and Barkstrom (1974) is the first study to apply the modern radiative transfer theory that computes the single-scattering properties of snow grains and to further relate them to observable quantities based on a series of approximations. This model, however, can only be applied to visible wavelengths. Adapting the Bohren and Barkstrom (1974) theory, Berger (1979) investigated snow absorption and emissivity in the thermal IR wavelengths. Furthermore, Choudhury and Chang (1979) used the Sagan-Pollack two-stream model (Sagan and Pollack 1967) for snow radiative transfer computation, which is applicable at wider wavelength ranges and is more accurate than the earlier models (e.g., Dunkle and Bevans 1956; Bohren and Barkstrom 1974). Their follow-up study (Choudhury and Chang 1981) introduced a special "surface reflection" term to account for the Fresnel reflection from a flat ice sheet at the snowpack surface, which, however, is unnecessary and incorrect for snowpack in the solar spectrum (Warren 1982). At the same time, Wiscombe and Warren (1980) developed an accurate and analytic snow albedo model for homogeneous snowpack that can compute snow albedo at any wavelength as a function of snow grain size, snowpack thickness, the ratio of diffuse-to-direct radiation, solar zenith angle, and underlying ground albedo. Nevertheless, it only calculates fluxes instead of intensities and bidirectional reflectance functions and neglects effects of snow grain packing and nonsphericity. Their companion study (Warren and Wiscombe 1980) further included the impurity effect in the model. Toon et al. (1989) extended the two-stream theory to vertically inhomogeneous media and formulated a numerically-stable and computationally-efficient algorithm, which becomes one common two-stream algorithm used for snow radiative transfer calculations (e.g., Flanner et al. 2007; Libois et al. 2013).

Specifically, based on the general radiative transfer Eq. (2.1.4), the integration over both azimuth and zenith angle for a single homogeneous layer gives (Toon et al. 1989):

$$\frac{dF^{\pm}}{d\tau} = \pm \int_0^1 I^{\pm}(\tau,\mu)d\mu \mp \frac{1}{2}\int_0^1\int_{-1}^1 p\left(\mu,\mu'\right) \times I^{\pm}\left(\tau,\mu'\right)d\mu' d\mu \mp F_0\tilde{\omega}\beta_0 e^{-\tau/\mu_0} \tag{2.2.17a}$$

$$F^{\pm} = \int_0^1 \mu I^{\pm}(\tau,\mu)d\mu \tag{2.2.17b}$$

$$I^{\pm}(\tau,\mu) = \int_0^{2\pi} I(\tau,\pm\mu,\phi)d\phi \tag{2.2.17c}$$

$$\beta_0 = \frac{1}{2}\int_0^1 p(\mu_0, -\mu')d\mu' \tag{2.2.17d}$$

$$p(\mu, \mu') = \frac{1}{2\pi}\int_0^{2\pi} p(\mu, \phi; \mu', \phi')d\phi' \tag{2.2.17e}$$

where $F^{\pm}$ is the diffuse flux in the upward (downward) direction, and $I^{\pm}(\tau, \mu)$ is the azimuthally integrated intensity.

One important piece of the two-stream solution is to approximate $I(\tau, \mu)$ in Eq. (2.2.17a) so that it is related to F. In general, all types of the two-stream equations for multiple layers can be expressed as (Meador and Weaver 1980):

$$\frac{dF_n^+}{d\tau_n} = \gamma_{1n}F_n^+ - \gamma_{2n}F_n^- - \gamma_{3n}F_0\tilde{\omega}e^{-(\tau_c+\tau)/\mu_0} \tag{2.2.18a}$$

$$\frac{dF_n^-}{d\tau_n} = \gamma_{2n}F_n^+ - \gamma_{1n}F_n^- + \gamma_{4n}F_0\tilde{\omega}e^{-(\tau_c+\tau)/\mu_0} \tag{2.2.18b}$$

where γ_1, γ_2, γ_3, and γ_4 are the coefficients depending on the particular form of the two-stream approximations but are independent of τ. n is the layer number, and τ_c is the cumulative optical depth of layers above the nth layer. The conservation of energy requires $\gamma_4 = 1 - \gamma_3$ (Meador and Weaver 1980). Table 1 summarizes the values of these coefficients (γ_i) for different types of two-stream approximations. Detailed derivations and discussions can be found in Meador and Weaver (1980).

To solve the coefficients and hence the radiative transfer Eq. (2.2.18), a key step is to compute the phase function. However, simple approximations such as the Eddington approximation often have difficulties in handling highly asymmetric phase functions (e.g., ice crystal). One common solution is to approximate the phase function by using a Dirac delta function for the strong forward scattering peak and a two-stream expansion of the phase function, which leads to the widely-used "delta-transform" method. The delta-transform/scaling is formulated as (Joseph et al. 1976):

$$g^* = \frac{g}{1+g} \tag{2.2.19a}$$

$$\tilde{\omega}^* = \frac{(1-g^2)\tilde{\omega}}{1-\tilde{\omega}g^2} \tag{2.2.19b}$$

$$\tau^* = (1-\tilde{\omega}g^2)\tau \tag{2.2.19c}$$

where g, $\tilde{\omega}$, and τ are the original asymmetry factor, single-scattering albedo, and optical depth of particles (e.g., snow grains) computed based on single-scattering principles (Sect. 3), which are required input parameters for solving the radiative transfer equations. g^*, $\tilde{\omega}^*$, and τ^* are the delta-transformed parameters used to

Table 1 Coefficients (γ_i) in Eq. (2.2.18a, b) for common two-stream approximations. In the following expressions, $\tilde{\omega}$ is the single scattering albedo, g is the asymmetry factor, $\gamma_4 = 1 - \gamma_3$, β_0 is defined in Eq. (2.2.17d), and $\mu_1 = (1 - \tilde{\omega})/(\gamma_1 - \gamma_2)$

Approximation	γ_1	γ_2	γ_3	μ_1
Eddington	$\left[7 - \tilde{\omega}(4 + 3g)\right]/4$	$-\left[1 - \tilde{\omega}(4 - 3g)\right]/4$	$(2 - 3\mu_0 g)/4$	1/2
Modified eddington	$\left[7 - \tilde{\omega}(4 + 3g)\right]/4$	$-\left[1 - \tilde{\omega}(4 - 3g)\right]/4$	β_0	1/2
Quadrature	$\sqrt{3}\left[2 - \tilde{\omega}(1 + g)\right]/2$	$\tilde{\omega}\sqrt{3}(1 - g)/2$	$\left(1 - \sqrt{3}\mu_0 g\right)/2$	$1/\sqrt{3}$
Modified quadrature	$\sqrt{3}\left[1 - \tilde{\omega}(1 - \mu_1)\right]$	$\sqrt{3}\mu_1\tilde{\omega}$	β_0	$1/\sqrt{3}$
Hemispheric mean	$2 - \tilde{\omega}(1 + g)$	$\tilde{\omega}(1 - g)$		1/2
Hemispheric constant[a]	$2\left[1 - \tilde{\omega}(1 - \beta)\right]$	$2\tilde{\omega}\beta$	β_0	1/2
Delta function	$\left[1 - \tilde{\omega}(1 - \beta_0)\right]/\mu_0$	$\tilde{\omega}\beta_0/\mu_0$	β_0	μ_0
Delta-eddington[2]	$\left[7 - \tilde{\omega}^*(4 + 3g^*)\right]/4$	$-\left[1 - \tilde{\omega}^*(4 - 3g^*)\right]/4$	$(2 - 3\mu_0 g^*)/4$	1/2
Delta-quadrature[b]	$\sqrt{3}\left[2 - \tilde{\omega}^*(1 + g^*)\right]/2$	$\tilde{\omega}^*\sqrt{3}(1 - g^*)/2$	$\left(1 - \sqrt{3}\mu_0 g^*\right)/2$	$1/\sqrt{3}$
Delta-hemispheric mean[b]	$2 - \tilde{\omega}^*(1 + g^*)$	$\tilde{\omega}^*(1 - g^*)$		1/2

[a] $\beta = \frac{1}{2} \times \int_0^1 \int_0^1 p(\mu, -\mu')d\mu d\mu'$

[b] delta-transform (Joseph 1976): $g^* = g/(1 + g)$, $\tilde{\omega}^* = \left(1 - g^2\right)\tilde{\omega}/\left(1 - \tilde{\omega}g^2\right)$, $\tau^* = \left(1 - \tilde{\omega}g^2\right)\tau$

replace the original ones (i.e., g, $\tilde{\omega}$, and τ) in the radiative transfer equations and solutions (see below). Applying the delta-transform technique improves the accuracy of different two-stream approximations for cases with highly asymmetric phase functions (Joseph et al. 1976), resulting in several important variants of the two-stream approximations such as the delta-Eddington, delta-Quadrature, and delta-Hemispheric mean approximations (see Table 1). Among them, the delta-Eddington and delta-Quadrature schemes show reasonably accurate results in the solar spectrum but have undesirable properties when accounting for internal isotropic sources such as thermal emissions, in which case the delta-Hemispheric mean scheme is preferable (Toon et al. 1989). Besides, several other delta-type approximations have also been developed to improve the accuracy and applicability, including the delta-M (Wiscombe 1977) and delta-fit (Hu et al. 2000) approximations. In addition, Katsev et al. (2010) presented an alternative truncation approximation for a not very elongated phase function with optical properties transformed as follows:

$$p^*(\Theta) = \frac{\mathrm{p}(\Theta)}{1 - \eta} \tag{2.2.19d}$$

$$\tilde{\omega}^* = \frac{(1 - \eta)\tilde{\omega}}{1 - \tilde{\omega}\eta} \tag{2.2.19e}$$

$$\tau^* = (1 - \tilde{\omega}\eta)\tau \tag{2.2.19f}$$

$$\eta = \frac{1}{2}\int_0^{\Theta^*} p(\Theta)\sin\Theta d\Theta \tag{2.2.19g}$$

$$\frac{1}{2}\int_0^{\pi} p(\Theta)\sin\Theta d\Theta = 1 \tag{2.2.19h}$$

where $p(\Theta)$ is the phase function with the scattering angle Θ, $p^*(\Theta)$ is the transformed phase function, and η is the truncated part of the phase function with the truncation angle Θ^*.

The general solution to the two-stream problem (Eq. 2.2.18a, b) for multiple (n) layers can be written as (Toon et al. 1989):

$$F_n^+(\tau) = k_{1n}e^{\Lambda_n\tau} + \Gamma_n k_{2n}e^{-\Lambda_n\tau} + C_n^+(\tau) \tag{2.2.20a}$$

$$F_n^-(\tau) = \Gamma_n k_{1n}e^{\Lambda_n\tau} + k_{2n}e^{-\Lambda_n\tau} + C_n^-(\tau) \tag{2.2.20b}$$

where k_1 and k_2 are solved by using boundary conditions, while Λ and Γ are determined by the specific form of the two-stream approximations as follows:

$$\Lambda = \sqrt{\gamma_1^2 - \gamma_2^2} \tag{2.2.20c}$$

$$\Gamma = \frac{\gamma_2}{\gamma_1 + \Lambda} = \frac{\gamma_1 - \Lambda}{\gamma_2} \tag{2.2.20d}$$

For solar radiation, we have:

$$C^+(\tau) = \frac{\tilde{\omega}F_0\left[(\gamma_1 - 1/\mu_0)\gamma_3 + \gamma_2\gamma_4\right]e^{-(\tau_c+\tau)/\mu_0}}{\Lambda^2 - 1/\mu_0^2} \tag{2.2.21a}$$

$$C^-(\tau) = \frac{\tilde{\omega}F_0\left[(\gamma_1 + 1/\mu_0)\gamma_4 + \gamma_2\gamma_3\right]e^{-(\tau_c+\tau)/\mu_0}}{\Lambda^2 - 1/\mu_0^2}$$

The $C^{\pm}(\tau)$ functions are zero when there is no direct-beam solar flux, and are indeterminate when $\Lambda = 1/\mu_0$. This problem can be solved by choosing a slightly different value of μ_0 in practice. Thus, for a vertically inhomogeneous medium (e.g., snowpack) consisting of multiple homogeneous layers, the radiative transfer problem can be solved using the preceding equations with proper boundary and continuity conditions as follows:

$$F_1^-(\tau = 0) = F_0^-(\tau = 0) \tag{2.2.22a}$$

$$F_N^+(\tau = \tau_N) = R_g F_N^-(\tau = \tau_N) + R_g \mu_0 F_0 e^{-\tau_c/\mu_0} \quad (2.2.22b)$$

$$F_n^+(\tau = \tau_n) = F_{n+1}^+(\tau = 0) \quad (2.2.22c)$$

$$F_n^-(\tau = \tau_n) = F_{n+1}^-(\tau = 0) \quad (2.2.22d)$$

where N is the total number of layers, n denotes the nth layer, R_g is the reflectivity of the underlying ground. The detailed expressions of the final solution under these boundary conditions are provided by Toon et al. (1989) for numerical implementation. The accuracy of this algorithm is generally high, with errors less than 10% (Toon et al. 1989).

Recently, Flanner et al. (2007) have applied the two-stream radiative algorithm from Toon et al. (1989) to develop a multi-layer snow albedo model, SNICAR, which has been widely-used and implemented into global climate models. The SNICAR model uses the delta-Eddington and delta-Hemispheric mean approximations in the visible and NIR wavelengths, respectively. The model also accounts for the impurity effect (Flanner et al. 2009; He et al. 2018c). Dang et al. (2019) showed that the errors of the two-stream models in snow visible albedo under direct-beam solar radiation are small (<0.005) and increase as snowpack becomes thinner (particularly for aged snow), while the albedo errors at NIR wavelengths are small for solar zenith angle less than 75° but increase as the angle increases. For diffuse radiation, SNICAR tends to underestimate visible snow albedo and substantially overestimate NIR albedo (Dang et al. 2019). Besides, Yasunari et al. (2011) implemented a two-stream approximation snow albedo scheme developed by Yamazaki et al. (1993) into the GEOS-5 land surface model and upgraded it with the effect of impurities in snow, resulting in good agreement with SNICAR calculations. The Two-stream Analytical Radiative TransfEr in Snow (TARTES) model also employs the two-stream (Eddington) approximation. This model has been implemented in the CROCUS snow model and used to study the impact of snow grain properties and impurities on albedo (Libois et al. 2013, 2015; Tuzet et al. 2017).

2.2.4 The Approximate Asymptotic Radiative Transfer (AART) Theory

In addition to the aforementioned sophisticated numerical radiative transfer methods, a recent study (Kokhanovsky and Zege 2004) developed a simplified analytical snow radiative transfer theory, Approximate Asymptotic Radiative Transfer (AART), which is particularly useful for application in remote sensing retrievals of snow grain size and impurity content in snow. So far, the AART theory has been used in several snow satellite retrieval and modeling studies (e.g., Zege et al. 2008, 2015; Kokhanovsky 2013; Libois et al. 2013; Kokhanovsky et al. 2018). However, this theory is designed specifically for vertically and horizontally homogeneous and optically thick snowpack, which may limit its application to some extent. The basic

ideas of this theory include (1) snow grains modeled as fractal close-packed ice crystals rather than non-interactive spheres, (2) snow local optical properties computed by the simple geometric-optics method instead of Mie theory, and (3) snow global optical properties approximated by special analytical, exponential, asymptotic solutions of radiative transfer principles instead of numerical computations from rigorous radiative transfer codes. Kokhanovsky and Zege (2004) provided a comprehensive description of the AART theory, while Kokhanovsky (2013) further extended the theory by including the impurity effect. Here, we summarize the essence of this theory.

Following the approximate analytical solution of the radiative transfer equation for a semi-infinite homogeneous snow layer (Kokhanovsky and Zege 2004), which is valid for weak absorption, the snow reflectance function (or bidirectional reflectance; R) can be expressed as (see Kokhanovsky 2013 for detailed derivations of the following exponential approximation):

$$R(\mu, \mu_0, \phi) = R_0(\mu, \mu_0, \phi) r_s^{f(\mu,\mu_0,\phi)} \tag{2.2.23a}$$

$$f(\mu, \mu_0, \phi) = \frac{K(\mu)K(\mu_0)}{R_0(\mu, \mu_0, \phi)} \tag{2.2.23b}$$

$$r_s = \exp\left(-4\sqrt{\frac{1-\tilde{\omega}}{3(1-g)}}\right) \tag{2.2.23c}$$

where R_0 is the reflectance of a semi-infinite non-absorbing homogeneous snow layer, r_s is the snow spherical albedo, $\tilde{\omega}$ is the snow single-scattering albedo,g is the snow asymmetry factor, μ_0 is the cosine of solar zenith angle, and μ is the cosine of viewing zenith angle. $K(\mu_0)$ is the escape function in radiative transfer theory, which determines the angular distribution of light escaping from the semi-infinite non-absorbing medium (Kokhanovsky and Zege 2004) and can be approximated as (for all types of scattering particles):

$$K(\mu_0) = \frac{3}{7}(1 + 2\mu_0) \quad , if\ \mu_0 \geq 0.2 \tag{2.2.23d}$$

Equation (2.2.23a, b, c, d) has been recently extended for application to finite (but optically thick) layers in Zege et al. (2015). The snow spherical (i.e., white-sky or diffuse) albedo (r_s) and plane (i.e., black-sky or direct) albedo (r_p) are defined as:

$$r_p(\mu_0) = \frac{1}{\pi} \int_0^1 \int_0^{2\pi} R(\mu, \mu_0, \phi) \mu d\mu d\phi \tag{2.2.24a}$$

$$r_s = 2 \int_0^1 r_p(\mu_0) \mu_0 d\mu_0 \tag{2.2.24b}$$

Furthermore, the parameter (β_a) represents the probability of photon absorption, defined as follows (Kokhanovsky 2013):

$$\beta_a = \frac{\kappa_{abs}}{\kappa_{ext}} = 1 - \tilde{\omega} \tag{2.2.25a}$$

$$\kappa_{abs} = \kappa_{abs}^{ice} + \kappa_{abs}^{imp} \tag{2.2.25b}$$

where κ_{abs} and κ_{ext} are the snow absorption and extinction coefficients, while κ_{abs}^{ice} and κ_{abs}^{imp} are the absorption coefficients of pure ice and impurities (e.g., soot, dust, brown carbon, and algae). Since the light scattering and extinction of the snow-impurity system are still dominated by those of ice crystals, based on the geometric-optics theory (which is reasonable for snow grains in the solar spectrum), we have:

$$\kappa_{ext} = \frac{3C_v}{D_e} \tag{2.2.26a}$$

$$D_e = \frac{3\overline{V}}{2\overline{S}} \tag{2.2.26b}$$

$$C_v = N_{sno}\overline{V} \tag{2.2.26c}$$

where C_v is the volumetric concentration of snow grains, N_{sno} is the number of snow grains in unit volume, D_e is the effective snow grain diameter, $\overline{V}$ is the mean snow grain volume, and $\overline{S}$ is the corresponding projected area averaged over all directions (see He et al. 2017b and Saito et al. 2019 for conversion among different snow effective sizes).

Moreover, based on the particle-optics theory, when the product of the effective snow diameter (D_e) and the bulk ice absorption coefficient (α as defined below) is very small (close to zero), it follows that (Kokhanovsky and Zege 2004):

$$\kappa_{abs}^{ice} = B\alpha C_v \tag{2.2.27a}$$

$$\alpha = \frac{4\pi m_{im}}{\lambda} \tag{2.2.27b}$$

where B is the absorption enhancement parameter depending on snow grain shape, and m_{im} is the imaginary part of ice refractive indices at the wavelength λ. To account for the impurity effect in snow, κ_{abs}^{imp} can be expressed as:

$$\kappa_{abs}^{imp}(\lambda) = \kappa_{abs}^{imp}(\lambda_0)\left[\frac{\lambda}{\lambda_0}\right]^{-m_a} \tag{2.2.27c}$$

where λ_0 is a reference wavelength (e.g., 1 μm) and m_a is the absorption Angstrom coefficient. Based on Eqs. (2.2.25a, b)–(2.2.27a, b, c) we have:

$$\beta_a = \frac{B\alpha D_e}{3} + \beta_a^{imp} \tag{2.2.28a}$$

$$\beta_a^{imp} = \frac{\kappa_{abs}^{imp}(\lambda_0)[\lambda/\lambda_0]^{-m_a} D_e}{3C_v} \tag{2.2.28b}$$

Therefore, it follows Eq. (2.2.23a, b, c, d) that

$$r_s = \exp\left(-\sqrt{[\alpha + p_0(\lambda/\lambda_0)^{-m_a}]}l_a\right) \tag{2.2.29a}$$

$$R(\mu, \mu_0, \phi) = R_0(\mu, \mu_0, \phi) \times \exp\left(-f(\mu, \mu_0, \phi)\sqrt{[\alpha + p_0(\lambda/\lambda_0)^{-m_a}]}l_a\right) \tag{2.2.29b}$$

$$p_0 = \frac{\kappa_{abs}^{imp}(\lambda_0)}{C_v B} \tag{2.2.29c}$$

$$l_a = \xi_a D_e \tag{2.2.29d}$$

$$\xi_a = \frac{16B}{9(1-g)} \tag{2.2.29e}$$

where l_a is the effective absorption length depending on both snow grain size and shape, while ξ_a is a parameter affected by snow grain shape but independent of grain size. The parameter l_a can be obtained from albedo or reflectance measurements, which could be further used to determine snow grain diameter by Eq. (2.2.29d) assuming a specific grain shape. Previous experiments (Libois et al. 2014) showed that the mean value of the parameter B is about 1.6. Using a typical visible asymmetry factor (g) of 0.75 for crystalline clouds (Kokhanovsky and Zege 2004), we have $\xi_a \approx 11.4$. Kokhanovsky et al. (2019) proposed another set of values for g (0.83) and ξ_a (16.7). It should be noted that the ξ_a value can vary according to different g values under various snow conditions. In addition, based on the definition of snow plane/direct albedo (Eq. 2.2.24a), it follows that

$$r_p = \exp\left(-K(\mu_0)\sqrt{[\alpha + p_0(\lambda/\lambda_0)^{-m_a}]}l_a\right) \tag{2.2.29f}$$

Comparisons between the AART theory and observations demonstrated high accuracy for snow reflection under a solar zenith angle less than 60°, whereas the accuracy reduces as the angle becomes greater than 60° (Kokhanovsky et al. 2005). Overall, the spectral reflectance and albedo of clean/polluted semi-infinite homogeneous snow are determined by four a priori parameters (i.e., l_a, R_0, p_0, and m_a), which can be estimated from multi-wavelength reflectance or albedo measurements. This enables further determination of snow grain size and impurity content from measurements and investigation of grain shape and pollution effects on snow albedo.

Zege et al. (2008, 2011) have designed an AART-based snow model/algorithm (SGSP) to retrieve effective snow grain size and pollutant amount in snow from satellite measurements, which currently works routinely in the Moderate Resolution Imaging Spectroradiometer (MODIS) processing chain to provide snow retrieval products for selected polar regions. Lyapustin et al. (2009) also developed a different AART-based snow model/algorithm and applied it to retrieve snow grain size over Greenland from MODIS observations. Recently, based on the AART theory, Kokhanovsky et al. (2018) have proposed an advanced system to retrieve snow grain size and absorption coefficient of snow impurities from snow reflectance and/or albedo measurements in the visible and NIR wavelengths. Their further study (Kokhanovsky et al. 2019) applied the AART theory and snow retrieval algorithm to retrieve snow properties from the Sentinel-3 satellite observations and showed a relatively high retrieval accuracy (e.g., <3% errors for spectral clean snow albedo with increasing errors for polluted snow albedo). In addition to the applications in snow remote sensing, the AART theory has also been incorporated into several snow models. For example, a recent Spectral Albedo Model for Dirty Snow (SAMDS) model was developed based on the AART algorithm to compute spectral snow albedo influenced by snow grain size, shape, and impurity content (Wang et al. 2017). The CROCUS-TARTES snow model also adopts the AART theory to account for snow grain shape effects and combines it with a two-stream approximation scheme (Libois et al. 2013, 2015).

2.3 Snow on Ice (Non-uniformly Refractive Layered Media)

The radiative transfer problem for snow on ice (e.g., glacier/sea ice) is different from that for snow on land but similar to that for the coupled atmosphere-sea ice/ocean system. This is because the real part of the refractive index of air medium ($m_{re} = 1.0$) is different from that of pure ice ($m_{re} = 1.31$), leading to a discontinuous refractive interface/boundary between the porous low-density snow and high-density ice. The Fresnel reflection and refraction occur at this interface and affect the form of the applicable radiative transfer equations and solutions. Thus, special treatments of the refractive boundary/interface between two adjacent media (e.g., snow and ice) should be used. In general, three important processes at a flat refractive interface should be accounted for, including the reflection and refraction of downward solar radiation (direct and diffuse) at the interface as well as the reflection and transmission of multiple-scattered upward radiation from below the interface.

For a coupled snow-ice system, the basic radiative transfer formulations (Eqs. 2.1.1 and 2.1.2) are still applicable, whereas the solar-beam source term $Q(\tau, \mu, \phi)$ should be modified to (Jin and Stamnes 1994):

$$Q_s(\tau, \mu, \phi) = \frac{\tilde{\omega} F_0}{4\pi} p(\mu, \phi; -\mu_0, \phi_0) e^{-\tau/\mu_0}$$

$$+\frac{\tilde{\omega}F_0}{4\pi}R(-\mu_0,n)p(\mu,\phi;\mu_0,\phi_0)e^{-(2\tau_s-\tau)/\mu_0} \tag{2.3.1a}$$

where Q_s is the solar-beam source in snow, n is the refractive index of ice relative to snow (air), τ_s is the total snow optical depth, and $R(-\mu_0, n)$ is the ice surface reflectance for solar radiation. The first term on the right-hand side of Eq. (2.3.1a) is the contribution from the downward incident solar beam, while the second term is the contribution from the upward beam reflected at the snow-ice interface (Fresnel reflection). Similarly, the solar-beam source in ice (Q_i) becomes:

$$Q_i(\tau,\mu,\phi)=\frac{\tilde{\omega}F_0}{4\pi}\frac{\mu_0}{\mu_{0n}(\mu_0,n)}T(-\mu_0,n)p(\mu,\phi;-\mu_{0n},\phi_0)e^{-\tau_s/\mu_0}e^{-(\tau-\tau_s)/\mu_{0n}} \tag{2.3.1b}$$

$$\mu_{0n}(\mu_0,n)=\sqrt{1-\left(1-\mu_0^2\right)/n^2} \tag{2.3.1c}$$

where μ_{0n} is the cosine of solar zenith angle in the ice (e.g., glacier/sea ice), which is related to μ_0 by Snell's law (Eq. 2.3.1c), and $T(-\mu_0, n)$ is the transmittance through the interface.

Thus, based on these modified solar-beam source terms in snow and glacier/sea ice as well as proper boundary and continuity conditions, the radiative transfer problems for a coupled snow-ice system can be solved using the aforementioned methods (Sect. 2.2). Here, we summarize the common methods that have been extended and applied to deal with non-uniformly refractive layered media. Since within each individual uniformly refractive media, the radiative transfer treatments are the same as those presented in Sect. 2.2, we will not repeat this part but focus on special treatments of the refractive interface/boundary.

2.3.1 The Extended DISORT Theory

Grenfell (1983, 1991) and Jin and Stamnes (1994) have extended the DISORT model/algorithm to handle radiative transfer in non-uniformly refractive layered media, which can be applied to a coupled snow-ice system. As shown in Sect. 2.2.1, the intensity and phase function in snow can be expanded as 2 N Fourier cosine series (Eq. 2.2.1) and 2N series of Legendre polynomials (Eq. 2.2.2a, b). Substituting the expanded series into the basic radiative transfer equation (Eq. 2.1.1), we have 2 N independent equations (one for each Fourier component; Eq. 2.2.3a, b, c, d, e). The only difference is the Fourier component of the solar-beam source term in snow (Q_s^m), which should be modified to (based on Eq. 2.3.1a):

$$Q_s^m(\tau,\mu)=X_0^m(\tau,\mu)e^{-\tau/\mu_0}+X_{01}^m(\tau,\mu)e^{\tau/\mu_0} \tag{2.3.2a}$$

$$X_0^m(\tau,\mu)=\frac{\tilde{\omega}F_0}{4\pi}\left(2-\delta_{0,m}\right)\sum_{l=0}^{2N-1}(-1)^{l+m}(2l+1)\frac{(l-m)!}{(l+m)!}g_l P_l^m(\mu)P_l^m(\mu_0) \tag{2.3.2b}$$

$$X_{01}^m(\tau,\mu)=\frac{\tilde{\omega}F_0}{4\pi}R(-\mu_0,n)e^{-2\tau_s/\mu_0}\left(2-\delta_{0,m}\right)\sum_{l=0}^{2N-1}(2l+1)\frac{(l-m)!}{(l+m)!}g_l P_l^m(\mu)P_l^m(\mu_0) \tag{2.3.2c}$$

The solar-beam source term in ice (Q_i^m) can be expressed as (Jin and Stamnes 1994):

$$Q_i^m(\tau,\mu)=X_{02}^m(\tau,\mu)e^{-\tau/\mu_{0n}} \tag{2.3.3a}$$

$$\begin{aligned}X_{02}^m(\tau,\mu)=&\frac{\tilde{\omega}F_0}{4\pi}\frac{\mu_0}{\mu_{0n}(\mu_0,n)}T(-\mu_0,n)e^{-(\tau_s/\mu_0-\tau_s/\mu_{0n})}\\&\times\left(2-\delta_{0,m}\right)\sum_{l=0}^{2N-1}(-1)^{l+m}(2l+1)\frac{(l-m)!}{(l+m)!}g_l P_l^m(\mu)P_l^m(\mu_{0n})\end{aligned} \tag{2.3.3b}$$

Based on the Gaussian quadrature, we can obtain similar equations as Eq. (2.2.4a, b) for each layer in snow or ice, but by replacing the original $Q^m(\tau,\mu_i)$ with $Q_s^m\left(\tau,\mu_{i,sno}\right)$ or $Q_i^m\left(\tau,\mu_{i,ice}\right)$. Note that the numbers and values of quadrature points and weights can be different in snow and ice. Jin and Stamnes (1994) provided some discussions on the choice of quadrature. Particularly, for the quadrature points and weights in the Fresnel cone of ice (i.e., refracting downward streams in snow into ice), we have:

$$\mu_{i,ice}=S\left(\mu_{i,sno}\right)=\sqrt{1-\left(1-\mu_{i,sno}^2\right)/n^2}\quad i=1,2,\ldots,N_1 \tag{2.3.4a}$$

$$w_{i,ice}=\frac{\mu_{i,sno}}{n^2 S\left(\mu_{i,sno}\right)}w_{i,sno}\quad i=1,2,\ldots,N_1 \tag{2.3.4b}$$

where $2N_1$ is the number of quadrature points in snow. $\mu_{i,sno}$ and $w_{i,sno}$ are the quadrature points and weights in snow, while $\mu_{i,ice}$ and $w_{i,ice}$ are those in ice.

Thus, using the matrix-formulation procedure presented in Sect. 2.2.1, we can have a general solution to the intensity in snow or ice that is similar to Eq. (2.2.6a). But the particular solution (the second term on the right-hand side of Eq. 2.2.6a) for snow (U_s) and ice (U_i) should be modified to (omitting the superscript m):

$$U_s\left(\mu_{i,sno}\right)=Z_0\left(\mu_{i,sno}\right)e^{-\tau/\mu_0}+Z_{01}\left(\mu_{i,sno}\right)e^{\tau/\mu_0}\quad i=\pm1,\pm2,\ldots,\pm N_1 \tag{2.3.5a}$$

$$U_i\left(\mu_{i,ice}\right)=Z_{02}\left(\mu_{i,ice}\right)e^{-\tau/\mu_{0n}(\mu_0,n)}\quad i=\pm1,\pm2,\ldots,\pm N_2 \tag{2.3.5b}$$

where the coefficients Z_0, Z_{01}, and Z_{02} can be determined by the following linear equation systems (omitting the superscript m):

$$\sum_{\substack{j=-N_1 \\ j\neq 0}}^{N_1} \left[\left(1+\frac{\mu_{j,sno}}{\mu_0}\right)\delta_{i,j} - w_{j,sno}D\left(\mu_{i,sno},\mu_{j,sno}\right)\right]Z_0\left(\mu_{j,sno}\right) = X_0\left(\tau,\mu_{i,sno}\right) \tag{2.3.6a}$$

$$\sum_{\substack{j=-N_1 \\ j\neq 0}}^{N_1} \left[\left(1+\frac{\mu_{j,sno}}{\mu_0}\right)\delta_{i,j} - w_{j,sno}D\left(\mu_{i,sno},\mu_{j,sno}\right)\right]Z_{01}\left(\mu_{j,sno}\right) = X_{01}\left(\tau,\mu_{i,sno}\right) \tag{2.3.6b}$$

$$\sum_{\substack{j=-N_2 \\ j\neq 0}}^{N_2} \left[\left(1+\frac{\mu_{j,ice}}{\mu_{0n}}\right)\delta_{i,j} - w_{j,ice}D\left(\mu_{i,ice},\mu_{j,ice}\right)\right]Z_{02}\left(\mu_{j,ice}\right) = X_{02}\left(\tau,\mu_{i,ice}\right) \tag{2.3.6c}$$

To completely solve the preceding radiative transfer equations for multiple layers of snow (L_1) and ice (L_2), the following boundary and continuity conditions are required (omitting the superscript m):

At the top of snowpack:

$$I_1\left(0,-\mu_{i,sno}\right) = I_{top}\left(-\mu_{i,sno}\right), \quad i=1,2,\ldots,N_1 \tag{2.3.7a}$$

At the interface between snow layers:

$$I_p\left(\tau_p,\mu_{i,sno}\right) = I_{p+1}\left(\tau_p,\mu_{i,sno}\right), \quad i=\pm 1,\pm 2,\ldots,\pm N_1,\ p=1,\ldots,L_1-1 \tag{2.3.7b}$$

At the interface between snow and ice:

$$I_{L_1}\left(\tau_s,\mu_{i,sno}\right) = I_{L_1}\left(\tau_s,-\mu_{i,sno}\right)R\left(-\mu_{i,sno},n\right) + \left[I_{L_1+1}\left(\tau_s,\mu_{i,ice}\right)/n^2\right]T\left(\mu_{i,ice},n\right) \quad i=1,2,\ldots,N_1 \tag{2.3.7c}$$

$$I_{L_1+1}\left(\tau_s,-\mu_{i,ice}\right)/n^2 = \left[I_{L_1+1}\left(\tau_s,\mu_{i,ice}\right)/n^2\right]R\left(\mu_{i,ice},n\right) + I_{L_1}\left(\tau_s,-\mu_{i,sno}\right)T\left(-\mu_{i,sno},n\right) \quad i=1,2,\ldots,N_1 \tag{2.3.7d}$$

$$I_{L_1+1}\left(\tau_s,-\mu_{i,ice}\right) = I_{L_1+1}\left(\tau_s,\mu_{i,ice}\right), \quad i=N_1+1,\ldots,N_2 \tag{2.3.7e}$$

At the interface between ice layers:

$$I_p(\tau_p, \mu_{i,ice}) = I_{p+1}(\tau_p, \mu_{i,ice}), \quad i = \pm 1, \pm 2, \ldots, \pm N_2, \\ p = L_1 + 1, \ldots, L_1 + L_2 - 1 \tag{2.3.7f}$$

At the bottom boundary, if the substrate is non-transmissive ground (e.g., rock or soil beneath the ice in places like the Tibetan glaciers),

$$I_{L_1+L_2}(\tau_{all}, \mu_{i,ice}) = I_{bot}(\mu_{i,ice}), \quad i = 1, 2, \ldots, N_2 \tag{2.3.7g}$$

where I_{bot} is determined by the bidirectional reflectance of the bottom ground. If the bottom is ocean water (e.g., Arctic sea ice), we need to repeat the preceding radiative transfer procedures using the boundary and continuity conditions between sea ice and water. Another simplified treatment is to use a constant spectral/broadband ocean water albedo/reflectance as the bottom boundary of sea ice, which may be valid when very little light transmits through the sea ice.

Jin and Stamnes (1994) gave a detailed description of the extended DISORT model for application to non-uniformly refractive layered media. Marks and King (2013) used the DISORT model in a coupled atmosphere-snow-sea ice system to quantify the black carbon (BC) effects on albedos of snow and sea ice over the Arctic. Recently, Pirazzini et al. (2015) modeled snow albedo on an Antarctic melting ice sheet using the DISORT model and observed snow grain size, which showed good agreement with observed albedo when there was fresh or drifted snow at the surface.

2.3.2 The Delta-Eddington Adding-Doubling Method

Briegleb and Light (2007) developed a multi-layer snow-sea ice solar radiative transfer model by combining the two-stream (delta-Eddington) approximation and the adding-doubling method. This model has been implemented into two community sea ice models, including the Los Almos Sea Ice Model (CICE) and the Model for Prediction Across Scales (MPAS)-seaice. The basic idea is (1) using the two-stream delta-Eddington solutions (see Sect. 2.2.3) to compute the single snow or sea ice layer reflectance and transmittance, which accounts for multiple light scattering within each layer, and then (2) combining the derived single-layer reflectance and transmittance to compute the radiative transfer throughout the snow-sea ice system based on the adding-doubling method (see Sect. 2.2.2), including a modification of the adding formula at the refractive boundary. This scheme overcomes the inapplicability of the conventional two-stream approximation in non-uniformly refractive media. In principle, this delta-Eddington adding-doubling scheme can be applied to both uniformly and non-uniformly layered media.

Specifically, the delta-Eddington two-stream radiative transfer solution is evaluated for each individual snow or sea ice layer using the procedure and solution presented in Sect. 2.2.3. Thus, the reflection (R) and transmission (T) functions within a single (Lth) layer for diffuse ($\overline{R}$ and $\overline{T}$) and direct ($R(\mu_{0,L})$ and $T(\mu_{0,L})$) radiation can be expressed as (Briegleb and Light, 2007):

$$R(\mu_{0,L}) = A_L e^{-\tau/\mu_{0,L}} + B_L\left(e^{k_L\tau} - e^{-k_L\tau}\right) + D_L \tag{2.3.8a}$$

$$T(\mu_{0,L}) = E_L e^{-\tau/\mu_{0,L}} + H_L\left(e^{k_L\tau} - e^{-k_L\tau}\right)e^{-\tau/\mu_{0,L}} + M_L \tag{2.3.8b}$$

$$\overline{R} = 2\int_0^1 \mu R(\mu)d\mu \tag{2.3.8c}$$

$$\overline{T} = 2\int_0^1 \mu T(\mu)d\mu \tag{2.3.8d}$$

where A_L, B_L, k_L, D_L, E_L, H_L, and M_L are the coefficients determined by snow or sea ice optical properties (Sect. 3) based on the delta-Eddington solution. The reflection and transmission functions for diffuse radiation ($\overline{R}$ and $\overline{T}$) are computed as integrations of those for direct radiation over the incident hemisphere assuming isotropic incidence following Wiscombe and Warren (1980).

Furthermore, the multiple scattering between adjacent layers (except for the refractive boundary) is accounted for by combining the preceding reflection and transmission functions of each individual layer (Eq. 2.3.8a, b, c, d) using the adding method (Sect. 2.2.2). Thus, the combination equations for direct and diffuse radiation incident on two adjacent homogeneous layers from above can be expressed as (Briegleb and Light 2007):

$$R_{12}(\mu) = R_1(\mu) + \frac{\left[\left(T_1(\mu) - e^{-\tau_1/\mu}\right)\overline{R}_2 + R_2(\mu)e^{-\tau_1/\mu}\right]\overline{T}_1}{1 - \overline{R}_1\overline{R}_2} \tag{2.3.9a}$$

$$T_{12}(\mu) = T_2(\mu)e^{-\tau_1/\mu} + \frac{\left[\left(T_1(\mu) - e^{-\tau_1/\mu}\right) + R_2(\mu)\overline{R}_1 e^{-\tau_1/\mu}\right]\overline{T}_2}{1 - \overline{R}_1\overline{R}_2} \tag{2.3.9b}$$

$$\overline{R}_{12} = \overline{R}_1 + \frac{\overline{T}_1\overline{R}_2\overline{T}_1}{1 - \overline{R}_1\overline{R}_2} \tag{2.3.9c}$$

$$\overline{T}_{12} = \frac{\overline{T}_1\overline{T}_2}{1 - \overline{R}_1\overline{R}_2} \tag{2.3.9d}$$

where the cosines of solar zenith angle (μ) are different in snow and sea ice, depending on the refraction process occurring in the refractive boundary/interface (Eq. 2.3.1c). Here, the transmission functions for each layer ($T_1(\mu)$ and $T_2(\mu)$) and combined layers $T_{12}(\mu)$ represent total transmission that includes direct and diffuse components. Based on the preceding layer combination procedure, the reflectance and transmittance at every layer interface and thus the entire column can be derived, with special treatments of the snow-sea ice refractive interface.

In the refractive snow-sea ice boundary layer, based on the Fresnel formula, the reflection (R_f) and transmission (T_f) functions for unpolarized radiation from above

can be written as (Liou 2002):

$$R_f(\mu) = \frac{1}{2}\left(R_1^2 + R_2^2\right) \tag{2.3.10a}$$

$$T_f(\mu) = \frac{1}{2}\left(T_1^2 + T_2^2\right)\frac{n\mu_n}{\mu} \tag{2.3.10b}$$

$$R_1 = \frac{\mu - n\mu_n}{\mu + n\mu_n} \tag{2.3.11a}$$

$$R_2 = \frac{n\mu - \mu_n}{n\mu + \mu_n} \tag{2.3.11b}$$

$$T_1 = \frac{2\mu}{\mu + n\mu_n} \tag{2.3.11c}$$

$$T_2 = \frac{2\mu}{n\mu + \mu_n} \tag{2.3.11d}$$

$$\mu_n = \sqrt{1 - \left(1 - \mu^2\right)/n^2} \tag{2.3.12}$$

where μ and μ_n are the cosine zenith angles of the incident and refracted radiation, respectively. n is the refractive index of sea ice relative to snow (air). R_1, R_2, and T_1, T_2 are the reflection and transmission amplitude factors for polarizations perpendicular (1) and parallel (2) to the plane, respectively. Thus, the reflection ($\overline{R}_{fa}$) and transmission ($\overline{T}_{fa}$) functions of diffuse radiation from above can be derived by:

$$\overline{R}_{fa}(\mu) = \left[\int_0^1 \mu R_f(\mu) d\mu\right] / \int_0^1 \mu d\mu \tag{2.3.13a}$$

$$\overline{T}_{fa}(\mu) = 1 - \overline{R}_{fa}(\mu) \tag{2.3.13b}$$

where the non-absorbing nature of the refractive boundary is used to compute $\overline{T}_{fa}$. Similarly, for the reflection ($\overline{R}_{fb}$) and transmission ($\overline{T}_{fb}$) functions of diffuse radiation from below, we have:

$$\overline{R}_{fb}(\mu) = \left[\int_{-1}^{-\mu_c} \mu_n R_f(\mu_n) d\mu_n + \int_{-\mu_c}^{0} \mu_n d\mu_n\right] \Bigg/ \int_{-1}^{0} \mu_n d\mu_n \tag{2.3.14a}$$

$$\overline{T}_{fb}(\mu) = 1 - \overline{R}_{fb}(\mu) \tag{2.3.14b}$$

$$\mu_c = \sqrt{1 - 1/n^2} \tag{2.3.14c}$$

where μ_c is the cosine of critical zenith angle for complete internal reflection based on Snell's law. Using typical values for the refractive indices of air and ice, we obtain $\overline{R}_{fa} = 0.063$, $\overline{R}_{fb} = 0.455$, $\overline{T}_{fa} = 0.937$, $\overline{T}_{fb} = 0.545$ (Briegleb and Light 2007). This indicates that the refractive snow-sea ice boundary is much less transmissive to the upward diffuse radiation from below than it is to downward diffuse radiation from above. Practically, the Fresnel-reflecting bare sea ice is almost never seen in reality, and thus Briegleb and Light (2007) included a thin, coarse-grained, snow-like "surface scattering layer" at the top of sea ice when there is no overlying snow in the model.

Therefore, based on the derived reflectance and transmittance for every layer (including the refractive boundary), the associated downward/upward direct/diffuse radiative fluxes at these interfaces and hence the entire column can eventually be computed. More detailed descriptions and derivations are provided by Briegleb and Light (2007).

2.3.3 The Delta-Four-Stream Approximation

Lee and Liou (2007) developed a coupled radiative transfer model for non-uniformly refractive layered media based on the analytic delta-four-stream approximation (Liou 1974; Liou et al. 1988). The model was originally designed for an atmosphere-ocean system but could be potentially applied to a snow-ice system. This model gives an analytical solution for radiative flux calculations with sufficient accuracy and compares well with DISORT model results.

The goal of this model is to solve the basic radiative transfer equations (Eq. 2.3.1a, b, c) for non-uniformly layered media. The four-stream scheme adopts a similar procedure as used in the extended DISORT model (Sect. 2.3.1) to solve the equations. It firstly expands the intensity and phase function into Fourier and Legendre series (Eqs. 2.3.2a, b, c and 2.3.3a, b), and then applies the double-Gauss quadrature method to solve each Fourier component of the expanded intensity, with solution equations similar to those in the DISORT algorithm (Eqs. 2.2.6a and 2.3.5a, b). The difference between the four-stream approximation and the DISORT algorithm is that only four quadrature points (streams) and weights (Eq. 2.2.4a, b) are used in the four-stream scheme, which could be treated as a special/simplified case of the DISORT algorithm. Moreover, the delta-function scaling/adjustment (Sect. 2.2.3) is also applied when solving the radiative transfer equation in the Lee and Liou (2007) model. The boundary and continuity conditions are generally the same as those used in the DISORT algorithm (Eq. 2.3.7a, b, c, d, e), except that only four streams ($i = \pm 1, \pm 2$) are considered in this case. More details can be found in Lee and Liou (2007).

2.3.4 The Backward Monte Carlo Method

Light et al. (2003) developed a two-dimensional axisymmetric backward Monte Carlo model to solve radiative transfer equations in media with multiple refractive

layers, which was originally designed for sea ice but has the potential for application to a coupled snow-ice system. The basic idea is that, in the forward model, a large number of photons generated from an incident source enter the model domain with traveling trajectories determined by the probabilities of scattering and absorption events. If a scattering event occurs, the scattering angle is computed by sampling the phase function to update the direction of the photon trajectory. This process is continued until the photon is absorbed, exits the domain, or reaches a simulated detector (Light et al. 2003). However, this forward model can be very inefficient if only very few of the incident photons reach the detector. Thus, the backward Monte Carlo method is used instead, based on the principle of reciprocity in the radiative transfer theory, which requires solutions to the adjoint/time-reversed problem. As such, in the backward model, photons are generated at the detector with their trajectories traced back to the original source. The backward Monte Carlo method has also been applied for radiative transfer problems in clouds (Evans 1993) and the ocean (Mobley and Sundman 2003).

The basic radiative transfer equation is similar to Eq. (2.1.4), and can be expressed by (the 3D version of Eq. 2.1.4 in a vector coordinate system; Light et al. 2003):

$$(\boldsymbol{\xi}\nabla)L(\boldsymbol{r},\boldsymbol{\xi})+\kappa_{ext}(\boldsymbol{r})L(\boldsymbol{r},\boldsymbol{\xi})=\kappa_{sca}(\boldsymbol{r})\int p\left(\boldsymbol{r},\boldsymbol{\xi}'\to\boldsymbol{\xi}\right)L\left(\boldsymbol{r},\boldsymbol{\xi}'\right)\cdot d\Omega\left(\boldsymbol{\xi}'\right)+Q(\boldsymbol{r},\boldsymbol{\xi}) \tag{2.3.15}$$

where $L(\boldsymbol{r},\boldsymbol{\xi})$ is the radiance at vector location $\boldsymbol{r}$ in the direction of unit vector $\boldsymbol{\xi}$ (positive for downward direction). $\kappa_{sca}(\boldsymbol{r})$ and $\kappa_{ext}(\boldsymbol{r})$ are the scattering and extinction coefficients, respectively. $p\left(\boldsymbol{r},\boldsymbol{\xi}'\to\boldsymbol{\xi}\right)$ is the scattering phase function from direction $\boldsymbol{\xi}'$ to direction $\boldsymbol{\xi}$. Ω is the solid angle integrated over 4π steradians. $Q(\boldsymbol{r},\boldsymbol{\xi})$ is the intensity of all sources at location $\boldsymbol{r}$ in direction $\boldsymbol{\xi}$. Denoting the radiance at the detector location $(\boldsymbol{r}_d)$ as $L_1(\boldsymbol{r}_d,\boldsymbol{\xi})$, the downward irradiance at the bottom detector $(E_d(\boldsymbol{r}_d))$ normalized by the incident downward irradiance $(E_d(\boldsymbol{r}_0))$ at the top surface $(\boldsymbol{r}_0)$ can be written as (Light et al. 2003):

$$\frac{E_d(\boldsymbol{r}_d)}{E_d(\boldsymbol{r}_0)}=\frac{-\int_{\boldsymbol{\xi}\cdot\boldsymbol{u}<0}L_1(\boldsymbol{r}_d,\boldsymbol{\xi})\boldsymbol{\xi}\cdot\boldsymbol{u}d\Omega}{-\int_{\boldsymbol{\xi}\cdot\boldsymbol{u}<0}L_1(\boldsymbol{r}_0,\boldsymbol{\xi})\boldsymbol{\xi}\cdot\boldsymbol{u}d\Omega} \tag{2.3.16}$$

where the two integrations are carried out only for downward directions ($\boldsymbol{\xi}\cdot\boldsymbol{u}<\boldsymbol{0}$). Based on the reciprocity principle, if the phase function is time-reversal invariant (i.e., $p\left(\boldsymbol{r},\boldsymbol{\xi}'\to\boldsymbol{\xi}\right)=p\left(\boldsymbol{r},-\boldsymbol{\xi}\to-\boldsymbol{\xi}'\right)$), then the adjoint (backward) problem can be related to the preceding forward problem by:

$$\int_{\boldsymbol{\xi}\cdot\boldsymbol{u}<0}d\Omega\int_S d\mathrm{S}|\boldsymbol{\xi}\cdot\boldsymbol{u}|L_1(\boldsymbol{r}_0,\boldsymbol{\xi})L_2(\boldsymbol{r}_0,-\boldsymbol{\xi})=\int_{4\pi}d\Omega\int_V dV\left[L_1(\boldsymbol{r},-\boldsymbol{\xi})Q_2(\boldsymbol{r},\boldsymbol{\xi})\right] \tag{2.3.17}$$

where S and V are the surface and volume for a closed convex model domain, L_2 is the radiance for the adjoint problem, and Q_2 is the function governing the angular distribution for photons released at the detector location in the adjoint problem. Thus, the normalized transmitted irradiance in Eq. (2.3.16) can be derived from Eq. (2.3.17) by choosing a proper $Q_2(\boldsymbol{r}, \boldsymbol{\xi})$ value.

Further assuming the incident radiance (L_0) is isotropic, the corresponding irradiance ($E_d(\boldsymbol{r}_0)$) is πL_0. Using the following $Q_2(\boldsymbol{r}, \boldsymbol{\xi})$ value for a transmitted irradiance detector:

$$Q_2(\boldsymbol{r}, \boldsymbol{\xi}) = \begin{cases} (\boldsymbol{\xi} \cdot \boldsymbol{u})\delta(\boldsymbol{r} - \boldsymbol{r}_d) J_0 & \boldsymbol{\xi} \cdot \boldsymbol{u} > \mathbf{0} \\ 0 & \boldsymbol{\xi} \cdot \boldsymbol{u} \leq \mathbf{0} \end{cases} \tag{2.3.18}$$

where J_0 is the total number of photons released, then Eq. (2.3.16) can be expressed as (for the upward-looking hemisphere):

$$\frac{E_d(\boldsymbol{r}_d)}{E_d(\boldsymbol{r}_0)} = \frac{\int_S dS \int_{\boldsymbol{\xi} \cdot \boldsymbol{u} > 0} d\Omega |\boldsymbol{\xi} \cdot \boldsymbol{u}| L_2(\boldsymbol{r}_0, -\boldsymbol{\xi})}{\pi J_0} \tag{2.3.19}$$

This equation can be further computed using the Monte Carlo simulation by releasing photons that simulate Q_2 at $\boldsymbol{r}_d$ and tracking through the domain until they exit the top surface as $L_2(\boldsymbol{r}_0, -\boldsymbol{\xi})$. All photons passing through $\boldsymbol{r}_0$ constitute the radiance $L_2(\boldsymbol{r}_0, -\boldsymbol{\xi})$ and contribute to the solution integral. When the incident radiation is angle-dependent, $C(\boldsymbol{\xi})$, exiting photons must be weighted by $C(\boldsymbol{\xi})$ as they contribute to $L_2(\boldsymbol{r}_0, -\boldsymbol{\xi})$. More details for the numerical implementation of the backward Monte Carlo model are discussed by Light et al. (2003).

2.4 Other Theories and Models

In addition to the aforementioned common radiative transfer theories and models that are applied to either snow on land or snow on ice, some other snow albedo models have also been developed with special foci and treatments of radiative transfer problems.

2.4.1 The Physically-Based Snow Albedo Model (PBSAM)

Aoki et al. (2011) developed a physically-based snow albedo model (PBSAM), particularly designed for implementation in global climate models, which is applicable to any snowpack layer structure and depth. The model computes snowpack broadband (visible and NIR) albedos and associated solar heating profile as a function of snow and solar illumination properties.

Specifically, the model requires several key input parameters, including snow grain radius, impurity (BC/dust) mass concentration, and snow water equivalent in each snow layer as well as the underlying surface albedo and illumination variables (i.e.,

solar zenith angle, spectral diffuse fraction, and relative fraction of solar radiation in visible and NIR bands). Then, the model uses a look-up table for albedo and transmittance computations for a homogeneous snow layer. The look-up table is generated offline for a wide range of snow parameter values and solar illumination conditions based on a spectrally detailed radiative transfer model (Aoki et al. 2000). To more accurately account for changes in the spectral distribution of solar radiation within snowpack, the visible and NIR broadbands are both divided into five sub-bands with the sub-band information also included in the look-up table. The effect of light-absorbing snow impurities (BC and dust) is taken into consideration using a snow impurity factor (SIF), which represents the total mass absorption cross-sections of impurities per unit snow mass. Moreover, the model accounts for an inhomogeneous snow layer by combining several homogeneous layers based on a simplified adding method, where the reflection and transmission functions of each homogeneous layer are used. Finally, the computed sub-band albedo and transmittance are integrated into broadband values using downward solar fluxes as spectral weights. The diffuse-to-direct ratio of solar illumination is further used to calculate the broadband albedo and transmittance under different sky conditions.

Model assessments showed that PBSAM can produce broadband albedos and solar heating profiles with reasonable accuracy for one and two snow layers compared with a spectrally detailed radiative transfer model (Aoki et al. 2011). Evaluation against in situ measurements suggested that different numbers of snow layers and sub-bands are required to achieve high model accuracy.

2.4.2 The Microstructure-Based Photon-Tracking Model

Kaempfer et al. (2007) proposed a three-dimensional microstructure-based photon-tracking radiative transfer model for snow, which explicitly resolves snow grain structures and their interactions with solar radiation. Basically, the model uses a geometric-optics-based Monte Carlo method to track numerous photons through a porous network of ice and air as well as their interactions (refraction, Fresnel reflection, and absorption) with snow microstructures, which are generated by either a discrete element model or an X-ray microtomography image. The porous ice-air network is an ensemble of sintered snow grains and the air filling pore spaces. The interactions between photons and snowpack are determined by the fundamental optics principle at the ice-air interfaces and within snow grains. However, the model neglects diffraction that could be important for snow radiative transfer (Bohren and Huffman 1983). Thus, the model is particularly useful in examining the sensitivity of snow radiative transfer to snow grain geometries and detailed layer structures.

Specifically, the Cold Regions Research and Engineering Laboratory (CRREL) microstructural snow model based on the discrete element model (Johnson and Hopkins 2005) is used to simulate snow structure characteristics and the interactions of photons with snow grains within an ice matrix by defining appropriate particle collision and contact rules. The snow grains are created as spherical or cylindrical with hemispherical ends and random orientation. The light reflection, refraction, and

absorption problems within the snow are solved by applying the geometric-optics principle (Liou 2002) due to the large snow grain size relative to the visible and NIR wavelengths. During model simulations, thousands of individual photons are released sequentially with a specified direction and angle at certain incident location and are tracked until they exit the top (reflected) or bottom (transmitted) of the samples or are absorbed and hence terminated within snow grains. When a photon collides with a snow grain, it is either reflected or transmitted at the ice-air interface depending on the geometric-optics principle. When a photon travels through the interior of a snow grain, it may be absorbed with a probability depending on the photon wavelength and traveling distance. More detailed derivations and descriptions of the algorithm can be found in Kaempfer et al. (2007).

Compared with the results from a four-stream DISORT radiative transfer model, this photon-tracking model showed good agreement in the spectral shape of snow albedo, but with a higher albedo and lower transmittance by ~10%, particularly at shorter wavelengths (Kaempfer et al. 2007). This is probably due to the omission of external diffraction in the model. This model has been applied to quantify changes in light scattering and absorption in snow caused by variations in snow depth, density, and grain size, and could be potentially valuable in snow photochemistry studies. New capabilities of treating snow metamorphism are also being implemented into the model, with the envisaged inclusion of impurity effects.

2.4.3 The Transport-Approximation Model

Recently, Dombrovsky et al. (2019) developed a new approach to compute the solar radiation transfer and associated heating in snow based on the transport approximation for the scattering phase function and the two-flux (Schwarzschild-Schuster) method. Their further study (Dombrovsky and Kokhanovsky 2019) includes the snow impurity effect in the model. This model is particularly designed to solve the vertical profile of solar heating in snowpack.

Specifically, the model calculates snow optical properties based on the geometric-optics solution obtained by Kokhanovsky and Zege (1995) and employs the transport approximation for scattering phase function (Dombrovsky 1996, 2012). On this basis, the model only needs to compute two dimensionless characteristics of snow absorption and scattering, including the absorption efficiency factor (Q_{abs}) and the so-called transport efficiency factor of scattering $\left(Q_{sca}^{tr} = Q_{sca}(1-g)\right)$, where g is the asymmetry factor. The transport efficiency factor of extinction $\left(Q_{ext}^{tr}\right)$ and transport single-scattering albedo $\left(\tilde{\omega}^{tr}\right)$ are thus expressed as $Q_{ext}^{tr} = Q_{abs} + Q_{sca}^{tr}$ and $\tilde{\omega}^{tr} = Q_{sca}^{tr}/Q_{ext}^{tr}$, respectively. These optical parameters are obtained as a function of snow size parameter and refractive index using the geometric-optics solution (Kokhanovsky and Zege 1995). The inclusion of impurities in snow further increases the snow absorption coefficient. According to the transport approximation, the scattering phase function in the radiative transfer equation can be approximated by a sum of the isotropic component and the other component representing the peak of forward scattering. Thus, the radiative transfer equation can be written in the same way as that

for the conventional one (e.g., Eq. 2.1.4) but by replacing the conventional scattering and extinction coefficients in the equation with the transport scattering and extinction coefficients. Finally, the solution to the radiative transfer equation is obtained by using the two-flux (Schwarzschild-Schuster) approach. Detailed derivations and solutions of this transport-approximation snow radiative transfer model are provided by Dombrovsky et al. (2019) and Dombrovsky and Kokhanovsky (2019). This model shows good accuracy in simulating absorbed radiation in snowpack compared with the direct Monte Carlo simulation.

2.4.4 The Bidirectional-Reflectance Model

Snow bidirectional reflectance, defined as the ratio of the reflected intensity along a direction toward the detector to the incident intensity, is an important parameter for snow remote sensing retrieval. A number of snow models and theories focusing on computing bidirectional reflectance have been developed. One widely-used method is the accurate and efficient radiative transfer algorithm proposed by Mishchenko et al. (1999) for a semi-infinite homogeneous snowpack with randomly oriented and distributed snow grains. The basic idea is to obtain a bidirectional reflection function by an iterative solution of the Ambartsumian's nonlinear integral equation (Dlugach and Yanovitskij 1974), without computing the internal radiation field. This method neglects the packing density and coherent backscattering.

Specifically, the bidirectional reflection function ($R(\mu, \mu_0, \phi)$) can be expanded in a Fourier series as follows

$$R(\mu, \mu_0, \phi) = R^0(\mu, \mu_0) + 2\sum_{m=1}^{m_{\max}} R^m(\mu, \mu_0)\cos(m\phi) \tag{2.4.1}$$

The coefficients $R^m(\mu, \mu_0)$ can thus be determined by numerically solving the Ambartsumian's nonlinear integral equation via a quadrature method with n division points and weights, which converts the integral equation into a system of $n \times n$ nonlinear algebraic equations. This system is then solved by simple iterations along with a procedure similar to that developed by Dlugach and Yanovitskij (1974) to accelerate convergence. The separation of the first-order-scattering procedure is also used to reduce the required n and improve computational accuracy. The bidirectional reflection function can be further used to calculate the reflected intensity and hence the plane albedo $\left(r_p(\mu_0)\right)$ and spherical albedo (r_s) as follows

$$r_p(\mu_0) = \frac{1}{\pi}\int_0^1 \mu d\mu \int_0^{2\pi} R(\mu, \mu_0, \phi)d\phi = 2\int_0^1 R^0(\mu, \mu_0)\mu d\mu \tag{2.4.2a}$$

$$r_s = 2\int_0^1 r_p(\mu_0)\mu_0 d\mu_0 \tag{2.4.2b}$$

Mishchenko et al. (1999) provided a comprehensive description of the numerical implementation of this algorithm, including the Legendre expansion and Fourier components of the phase function, iterative solution of the Ambartsumian's equation, and numerical integration. Xie et al. (2006) compared the Mishchenko et al. (1999) technique with the DISORT and adding-doubling methods, and they found that all three approaches combined with the delta-fit/delta-M treatment can simulate the bidirectional reflectance of a semi-infinite snow layer with reasonably good accuracy. The Mishchenko et al. (1999) model is applicable to a wide range of snow remote sensing problems.

3 Snow Single-Scattering Property Computation

In Sect. 2, we describe and discuss a number of widely-used snow radiative transfer theories and models. As the required inputs to these radiative transfer calculations, snow single-scattering/optical properties should be obtained beforehand, at least including single-scattering albedo, extinction cross-section (or efficiency), and asymmetry factor (or phase function). The snow single-scattering properties are generally affected by snow grain size, shape, packing/aggregating, ice refractive indices, the inclusion of impurities, and radiation wavelength, which show important interactive effects. Thus, in this section, we summarize the computation of snow single-scattering properties that are used for snowpack radiative transfer and albedo modeling.

3.1 Computational Methods

3.1.1 Mie Theory

One common and accurate approach used to compute optical properties for spherical particles is Lorenz–Mie–Debye theory (hereafter Mie theory), which calculates particle single-scattering quantities by solving the fundamental Maxwell equations for the incident electromagnetic field interacting with particles. Several books and review papers have nicely described the mathematical details of Mie theory (van de Hulst 1957; Bohren and Huffman 1983; Liou 2002). Here we briefly introduce the essence of this theory.

Assuming homogeneous spheres, Mie theory derives the complex scattering (Mie) coefficients from the particle refractive index, angular functions that depend on scattering angles, and size parameters (X) defined as:

$$X = \frac{2\pi R_e}{\lambda} \tag{3.1.1}$$

where R_e is the particle effective radius and λ is the wavelength. Based on the scattering (Mie) coefficients and angular functions, the scattering amplitude functions and hence the scattering (Müeller) matrix are further computed. Subsequently, other particle single-scattering properties are derived, including efficiency factors of scattering, extinction, backscattering, and radiation pressure. Finally, the single-scattering albedo, absorption (or extinction) efficiency, and asymmetry factor are calculated as a function of the preceding efficiency factors. The Mie calculations are also extended to treat concentric core-shell (coated spherical) particles (e.g., snow grains coated by liquid water or single aerosol particle mixed in the center of a snow grain) with similar formulations (Bohren and Huffman 1983). For spherical particles containing other small components (e.g., small impurity particles mixed inside snow grains), the Mie theory can still be applied by using an effective refractive index for the entire particle based on certain mixing rules (Bohren and Huffman 1983), including volume mixing of refractive indices and volumetric weighting of other particle properties (e.g., dielectric constant, Lorentz-Lorenz quantity, and mean dielectric function obtained from the Bruggeman or Maxwell Garnett effective medium theory). Note that different mixing rules may result in nontrivial differences in the calculated particle single-scattering properties (Bond et al. 2006). For impurities externally mixed with (i.e., outside) snow grains, a linear combination of snow and impurity single-scattering properties weighted by their optical depths are used to compute the single-scattering properties of impurity-snow external mixtures.

Due to its high computational accuracy, Mie theory has been widely used to compute snow single-scattering properties (e.g., Wiscombe and Warren 1980; Flanner et al. 2007), particularly the single-scattering albedo, extinction efficiency, and asymmetry factor required for snow radiative transfer calculations. To account for BC aerosols mixed internally with (i.e., inside) snow grains, Jacobson (2004) assumed each snow grain containing one single BC particle in the center using the concentric core-shell structure based on the core-shell Mie theory. But in reality, multiple BC particles are often randomly mixed inside one snow grains, where the single inclusion core-shell assumption may be invalid. Flanner et al. (2012) employed Mie calculations together with the dynamic effective medium approximation (Chýlek and Srivastava 1983) to produce the effective refractive indices of snow grains containing many small BC particles. However, the effective medium approximation can only be applied to very small aerosols (e.g., BC rather than dust) mixed inside snow grains (Bohren 1986). Besides, Mie calculations are limited to spherical particles only, whereas snow grains are typically nonspherical in the real snowpack (Dominé et al. 2003). To circumvent this limitation, some studies (Grenfell and Warren 1999; Neshyba et al. 2003) have proposed using the "equivalent" spheres that have the same volume-to-area ratio as the nonspherical ice particles in Mie calculations to approximately represent the single-scattering properties of nonspherical grains. Nevertheless, this "equivalent"-sphere approximation may work well in the computation of snow extinction efficiency and single-scattering albedo but is much less accurate for snow asymmetry factor (Dang et al. 2016). Thus, some other methods have been developed to deal with inhomogeneous nonspherical particles (see the following sub-sections).

3.1.2 The Geometric-Optics (Ray-Tracing) Theory

Since snow grains typically have large size parameters (>~50) in the solar spectrum, the laws of conventional geometric optics (ray-tracing) can be applied with acceptable accuracy to compute snow single-scattering properties. The geometric-optics calculation is an asymptotic method that becomes more accurate with increasing particle size parameters. The basic geometric optics processes include light reflection by particles and refraction into particles followed by absorption or internal reflection. Particles with large size parameters also scatter light through diffraction, which is concentrated in a narrow lobe in the forward direction. In the far-field, the diffracted component of the scattered light can be approximated by the Fraunhofer diffraction theory (Born and Wolf 1975). In general, the total particle scattering and absorption contain the energy equal to that incident on the particle cross-section, while diffraction contributes to approximately the same amount of energy. Liou (2002) provided a detailed mathematical description of the geometric-optics theory and associated derivation.

Briefly, the light diffraction by particles can be quantified according to Babinet's principle, which states that the far-field diffraction pattern (Fraunhofer diffraction) from a circular aperture is the same as that from an opaque disk or sphere of the same radius. On this basis, the angular intensity function for diffraction analogous to Mie theory can be derived as a function of particle size parameter but independent of refractive index. The geometric reflection, refraction, and transmission processes are solved based on Fresnel theory and Snell's law, with the amplitude coefficients as a function of relative refractive indices of the two media and light-beam incident angles. As a result, the scattered intensities due to reflection and refraction can be further derived. The light absorption inside particles is also accounted for during this process (van de Hulst 1980; Liou 2002). Following this, the particle extinction efficiency, single-scattering albedo, and asymmetry factor are thus obtained. The geometric-optics calculations can be applied to both spheres and nonspherical particles such as hexagonal ice crystals (Takano and Liou 1989). The conventional geometric-optics theory has been used in the AART snow albedo theory (Sect. 2.2.4) to simplify radiative transfer computations and account for nonspherical snow grains (Kokhanovsky and Zege 2004). Macke et al. (1996) also applied the geometric-optics theory (including far-field diffraction approximation) to investigate the effect of ice crystal shape on single-scattering properties. Räisänen et al. (2015) further used the Macke et al. (1996) geometric-optics model to develop parameterizations for snow single-scattering properties affected by snow grain size and shape. Recently, Malinka (2014) combined the geometric optics and stereological (geometric statistics) approaches for application to porous materials (e.g., snowpack) by assuming stochastic mixtures of solid materials and air.

The conventional geometric-optics theory has several limitations and shortcomings (Liou 2002), including (1) the requirement of the ray localization principle, (2) the assumption of equal energy extinction from diffraction and Fresnel rays, (3) the neglect of the electromagnetic field's vector property in Fraunhofer diffraction formulations, and (4) the discontinuous distribution of the scattered energy caused

by direct calculations of the far-field. Thus, to overcome these shortcomings and limitations, Yang and Liou (1995, 1996a) developed an improved geometric-optics approach. The basic idea is that the energy determined from geometric ray-tracing at the particle surface is collected and mapped to the far-field according to the exact internal geometric ray-tracing. The conventional geometric-optics method, however, collects the energy produced by geometric refractions and reflections directly at the far-field through a prescribed solid angle. In practice, the mapping of the near-field solution to the far-field can be done in its entirety for the electric field of the illuminated side, while for the shadowed side, the mapping is conducted ray by ray and the results include the diffraction pattern. This mapping process fully accounts for phase interferences in the determination of the phase function. Based on the mapping process and the energy conservation principle, other single-scattering properties can be subsequently derived from electromagnetic integral equations. This improved geometric-optics approach has been widely used to quantify single-scattering properties of ice crystals with various shapes (e.g., Fu 1996; Bi et al. 2011; Yang et al. 2013; Saito et al. 2019).

3.1.3 The Monte Carlo Photon-Tracing Approach

Wendling et al. (1979) first developed a Monte Carlo method along with the geometric ray-tracing for hexagonal ice plates and columns. Later, Takano and Liou (1995) proposed a hit-and-miss Monte Carlo method to trace photons interacting with ice crystals of complex shapes. Following this work, Liou et al. (2010, 2011) recently innovated a geometric-optics surface-wave (GOS) approach to deal with inhomogeneous particles with irregular shapes, which has been further improved through several studies (Takano et al. 2013; Liou et al. 2014; He et al. 2015, 2016). This approach accounts for geometric reflection and refraction, diffraction, and surface wave components of light processes by explicitly simulating particle structures. Liou and Yang (2016) gave a detailed summary of the GOS approach and its application.

Briefly, a stochastic procedure is firstly used to construct particle shapes in a 3-D coordinate system (Liou et al. 2011). Then, the geometric refraction and reflection are carried out using the hit-and-miss Monte Carlo photon tracing technique (Takano and Liou 1995), followed by a ray-by-ray integration approach (Yang and Liou 1997). As a result, optical (extinction, absorption, and radiation pressure) cross-sections and efficiencies of the particle can be determined. Subsequently, the optical efficiencies of randomly oriented particles are calculated based on effective geometric cross-sections (i.e., photon-number weighted shadowing area on a plane perpendicular to the incident light). Diffraction by randomly oriented particles is further computed based on Babinet's principle and effective geometric cross-sections. The surface-wave component in GOS accounts for the interaction of incident light at grazing angles near the particle edge and propagating along the particle surface into shadow areas. Following the complex angular momentum theory (Nussenzveig and Wiscombe 1980), a surface-wave adjustment factor depending on particle shapes is derived for the computation of optical efficiencies. Finally, the single-scattering

albedo and asymmetry factor are calculated from the optical efficiencies and the phase function.

The accuracy of GOS calculations has been evaluated for various particle sizes and shapes by comparing with laboratory measurements and other numerical approaches, showing reasonably good results (Liou et al. 2010, 2011; Takano et al. 2013; He et al. 2015, 2016; He 2019b). The GOS approach, which has also been coupled with the Rayleigh–Gans–Debye approximation for small (<~2) size parameters (Takano et al. 2013), is applicable to a wide range of particle shapes and sizes (size parameters of 0.1–1000) with high computational efficiency. Recently, based on the GOS approach, Liou et al. (2014) developed a stochastic aerosol-snow albedo model (SASAM), which explicitly resolves snow grain shape, aerosol-snow mixing state (internal/external), and aerosol size distribution. The GOS method along with the SASAM model has been successfully used to quantify the impacts of snow impurities (He et al. 2018b, 2019a), snow grain size and shape (He et al. 2017b, 2018a), and grain packing (He et al. 2017a) on snow single-scattering properties and albedo.

3.1.4 Other Methods

In addition to the preceding methods, several other useful approaches have been developed to compute single-scattering properties of inhomogeneous particles with complex structures, including the Finite Difference Time Domain (FDTD) method (Yang and Liou 1995, 1996b), the Discrete Dipole Approximation (DDA) method (Draine and Flatau 1994), and the *T*-matrix method (Mishchenko et al. 1996; Mackowski 2014). These methods have been applied to relatively small particles such as aerosols and ice clouds (Yang et al. 2015 and references therein). However, they are not computationally efficient and/or accurate for application to large particles (e.g., snow grains) and hence have not been widely used in the snow community. For example, Liou (2002) showed that the FDTD method can obtain reliable results with adequate accuracy for particle size parameters less than ~20, while the DDA method can efficiently compute particle optical properties for size parameters less than ~20, however, with substantial increases in computational resources for larger size parameters. Note that the typical size parameter for snow grains in the solar spectrum is larger than 50–100.

3.2 Snow Single-Scattering Properties

3.2.1 Ice Refractive Index

The refractive index ($m(\lambda) = m_{re}(\lambda) - i \cdot m_{im}(\lambda)$) is a fundamental physical property of ice, which determines snow/ice scattering and absorption abilities and is required to produce snow single-scattering property calculations. The real part (m_{re}) of the ice refractive index is related to scattering, while the imaginary part (m_{im})

determines absorption ($\alpha = 4\pi m_{im}/\lambda$), where α is the pure ice absorption coefficient. Several early studies have compiled and updated the spectral ice refractive indices (e.g., Irvine and Pollack 1968; Ray 1972; Wiscombe and Warren 1980; Warren 1984), as more accurate measurements became available. Currently, the most complete, updated, and widely-used compilation of spectral ice refractive indices based on measurements is from Warren and Brandt (2008) and Picard et al. (2016). Here we summarize the main features of ice refractive indices in the solar spectrum based on the Warren and Brandt (2008) database along with the updates from Picard et al. (2016).

Figure 4 shows the imaginary part (m_{im}) of the spectral ice refractive indices compiled by Warren and Brandt (2008). The ice absorption is very strong (i.e., large m_{im} values) at 100–160 nm wavelengths, while there is a steep decrease in m_{im} from 160 nm to 200 nm. The minimum m_{im} ($\leq 2 \times 10^{-11}$) and hence absorption is in the range of 200–390 nm, followed by a quick increase in absorption from visible to NIR wavelengths (~1.4 μm). The weak absorption in the visible band determines the high snow scattering and visible albedo. In the NIR wavelengths, m_{im} and ice absorption generally tend to increase from 0.7–5.0 μm with some fluctuations. The three peaks corresponding to strong absorption are around 1.5, 2.0, and 3.0 μm wavelengths, followed by a small peak at ~4.5 μm. This spectral pattern of m_{im} largely determines the spectral pattern of snow single-scattering albedo (Sect. 3.2.3) and asymmetry factor (Sect. 3.2.4). The real part (m_{re}, Fig. 4) of spectral ice refractive indices is related to and can be derived from m_{im} based on the Kramers-Kronig relation, which is further forced to match measurements at some wavelengths. In general, m_{re} has a near-constant value of ~1.33 in the solar spectrum, expect for extremely strong peak (up to 1.65) and dip (down to 0.95) values around 3 μm.

However, there are still uncertainties associated with ice refractive indices, particularly for the imaginary part (m_{im}). For example, the ice absorption is rather weak at 200–600 nm, the measurement of which is easily affected by factors like impurity and

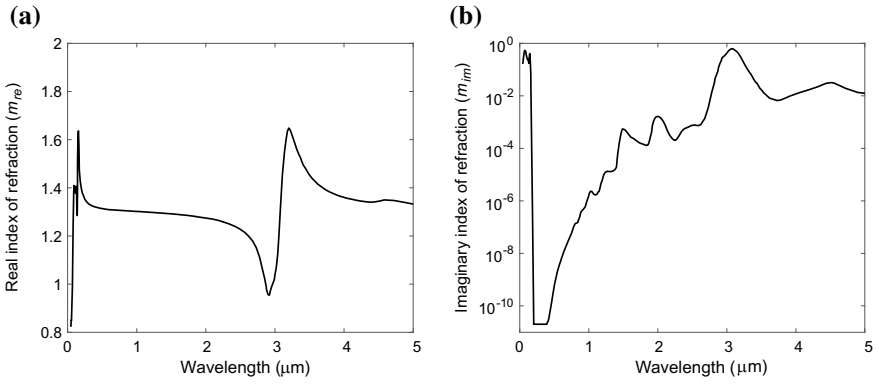

Fig. 4 Real and imaginary parts of spectral ice refractive indices in the solar spectrum based on the Warren and Brandt (2008) database

bubble contents. Thus, the uncertainty of m_{im} in the UV and visible wavelengths are up to ~100% (Warren and Brandt 2008). Moreover, a recent study (He et al. 2018c) found that using the Warren and Brandt (2008) database leads to a slight but consistent snow albedo overestimation at wavelengths less than ~400 nm, which suggests that the ice refractive indices and hence absorption may be too low. Recent measurements in the Antarctic snow (Picard et al. 2016) showed a much higher ice absorption coefficient at these wavelengths than that from Warren and Brandt (2008), indicating that the uncertainty in ice visible absorption is probably larger than generally appreciated. The uncertainty of m_{im} at NIR wavelengths (0.7–5.0 μm) is generally small (<~10%). For the real part (m_{re}), the uncertainty is rather small in the solar spectrum (Warren and Brandt 2008).

3.2.2 Extinction Efficiency

The extinction efficiency (Q_{ext}) is the ratio of extinction cross-section to geometric cross-section. This quantity is required in radiative transfer computation only when the snow layer is not optically semi-infinite. For large particles such as snow grains in the solar spectrum (size parameters larger than ~50), Q_{ext} has a value of approximately 2 (i.e., geometric-optics limit). However, this geometric-optics limit is not always accurate, especially for small snow grains at NIR wavelengths, in which case Mie calculations are preferable. Figure 5 shows the extinction efficiency of snow spheres with different grain sizes based on Mie calculations. Q_{ext} is generally a weak function of wavelength, which is closer to the value of 2 as the grain size increases. Although Q_{ext} departs increasingly from its geometric-optics limit as the wavelength increases, the difference is still very small (e.g., <6% for snow radii of >50 μm). The sharp dips of Q_{ext} at ~3 μm wavelength are due to the sharp decrease of m_{re} to ~1.0 (Fig. 4), where the Fresnel reflectance at the surface of snow spheres largely vanishes, eliminating the contribution of reflection to Q_{ext}. For nonspherical snow grains, the use of optically

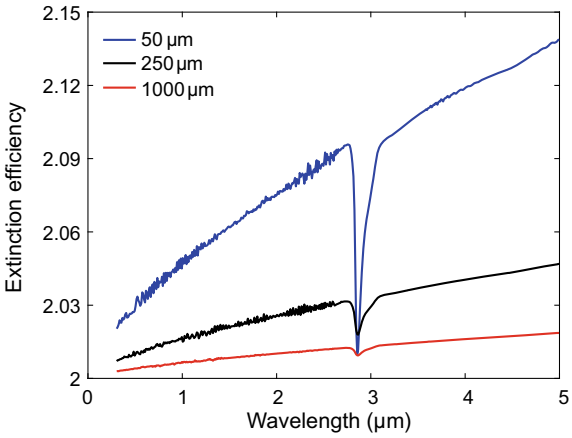

Fig. 5 Spectral extinction efficiencies for spherical snow grains with radii of 50, 250, and 1000 μm based on Mie calculations from Flanner et al. (2007)

equivalent (i.e., effective) spheres with the same volume-to-area as their nonspherical counterparts produces relatively accurate Q_{ext} values (e.g., Grenfell and Warren 1999; Neshyba et al. 2003). He et al. (2017b, 2018b) further found that both snow grain shapes and impurities in snow have negligible (<3%) effects on Q_{ext} based on explicit simulations of various grain shapes internally mixed with BC.

Moreover, if assuming spherical snow grains, the optical depth (τ) of a homogeneous snowpack can be calculated based on extinction efficiency as follows

$$\tau = NC_{ext}z = \frac{3\rho_s z Q_{ext}}{4\rho_{ice} R_e} \tag{3.2.1}$$

where z is the snow layer thickness, N is the number density of snow grains, R_e is the snow grain radius, and C_{ext} is the extinction cross-section. ρ_s and ρ_{ice} are the densities of snow and ice.

3.2.3 Single-Scattering Albedo/Coalbedo

The single-scattering albedo ($\tilde{\omega}$, within values of 0–1) is the ratio of scattering efficiency to extinction efficiency, representing the probability that photons intercepted by the particle will be scattered rather than absorbed. For snow grains, another related parameter, single-scattering coalbedo ($1 - \tilde{\omega}$), is also often used to represent snow absorption ability. The spectral variation of snow single-scattering albedo (or coalbedo) largely determines the spectral feature of snow albedo (Wiscombe and Warren 1980), and can be affected by snow grain size, shape, and impurity content (Warren 1982; Liou et al. 2014; Räisänen et al. 2015; Dang et al. 2016).

Figure 6 shows the snow single-scattering coalbedo ($1 - \tilde{\omega}$) for various grain sizes and shapes and their relative differences based on the GOS calculations (He et al. 2017b). In general, the coalbedo increases monotonically from very small values (<~10^{-5}) at visible wavelengths to values of up to ~0.5 at wavelengths greater than 1.5 μm, with some fluctuations. This primarily follows the spectral pattern of the ice imaginary index of refraction (Sect. 3.2.1). The fluctuations at wavelengths greater than 1.5 μm become smaller for larger snow grain sizes. The upper limit of coalbedo is about 0.5 instead of 1.0 (Hansen and Travis 1974), suggesting that scattering will always occur and snow albedo will never be strictly zero. The snow single-scattering coalbedo tends to increase substantially (by up to one order of magnitude) as the grain size increases (note the log-scale y-axis in Fig. 6), indicating much stronger absorption for larger snow grains. This feature has been confirmed by many studies (Wiscombe and Warren 1980; Flanner et al. 2007). In contrast, nonspherical grain shapes have relatively small (<20%) effects on snow single-scattering coalbedo (Fig. 6), which implies that $1 - \tilde{\omega}$ is predominantly impacted by snow grain size instead of grain shape (Jin et al. 2008; Räisänen et al. 2015). Previous studies (Grenfell and Warren 1999; Neshyba et al. 2003; Dang et al. 2016) also showed that the equal-volume-to-area representation of different snow grain shapes works reasonably well for single-scattering albedo.

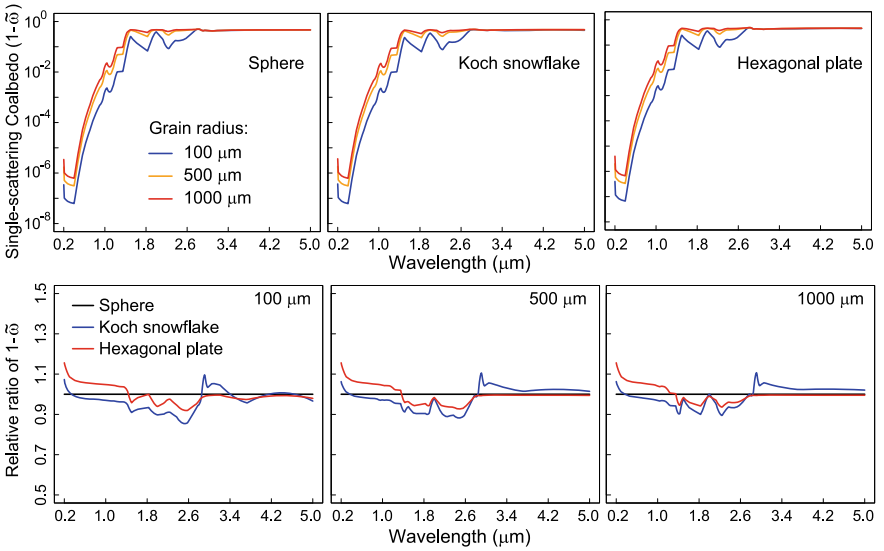

Fig. 6 Top row: Spectral single-scattering coalbedos $(1 - \tilde{\omega})$ for snow sphere, Koch snowflake, and hexagonal plate with volume-equivalent sphere radii of 100, 500, and 1000 μm. Bottom row: The spectral relative ratio of $(1 - \tilde{\omega})$ for different snow grain shapes to that for sphere, and hence sphere (black lines) has a value of 1. Data are obtained from computations by He et al. (2017b)

In addition to grain size and shape, snow single-scattering coalbedo $(1 - \tilde{\omega})$ is also significantly affected by impurities in snow. Figure 7 demonstrates $1 - \tilde{\omega}$ for snow grains internally mixed with BC aerosols. BC in snow strongly enhances snow single-scattering coalbedo at wavelengths less than 1.0 μm, with stronger enhancement ratios for higher BC concentrations, whereas the impact is negligible at wavelengths greater than 1.0 μm due to the spectral characteristics of BC and snow optical properties. The enhancement ratio (i.e., the ratio of $1 - \tilde{\omega}$ for contaminated snow to that for pure snow) is a function of BC concentration and is mostly independent of

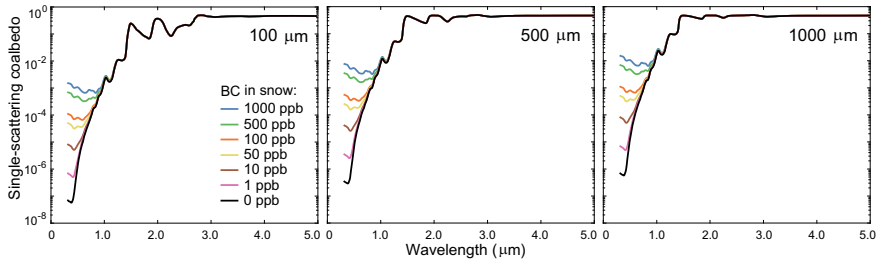

Fig. 7 Spectral single-scattering coalbedos for snow spheres internally mixed with different BC concentrations for snow effective radii of 100, 500, and 1000 μm. Data are obtained from computations by He et al. (2018c)

snow grain size and shape (He et al. 2017b). Note that snow grain size and shape still influence the single-scattering coalbedo of pure snow, and thus BC effects on the absolute value of the single-scattering coalbedo of contaminated snow can vary with snow size and shape. As a result, compared to smaller snow grains, larger grains with a higher $1-\tilde{\omega}$ will have a stronger increase in the absolute values of $1-\tilde{\omega}$ when mixed with the same BC concentrations, causing a stronger reduction in snow albedo (Liou et al. 2014).

For convenient application in snow and climate modeling, Räisänen et al. (2015) parameterized snow single-scattering coalbedo as a function of snow effective (volume-to-projected-area-equivalent) radius (including nonspherical grains) and refractive indices based on the conventional geometric-optics calculations. Recently, He et al. (2017b, 2018b) further used the GOS method to develop new parameterizations for snow single-scattering coalbedo by accounting for the effects of both snow effective grain size and impurities (concentration and size distribution).

3.2.4 Asymmetry Factor and Phase Function

The phase function ($p(\cos\ \Theta)$), when multiplied by single-scattering albedo, represents the probability for photons to be scattered from one incident angle to a certain scattering angle, which is a function of only the scattering phase angle (Θ) for spherical particles. The complete phase function is required for radiative transfer computations of intensity, whereas only the asymmetry factor (g) is required for computing fluxes. The asymmetry factor is defined as:

$$g = \frac{1}{2}\int_{-1}^{1} p(\cos\ \Theta)\cos\ \Theta d\cos\ \Theta \tag{3.2.2}$$

Figure 8 shows an example of snow asymmetry factors for different grain sizes and shapes. The asymmetry factor is fairly constant at visible wavelengths but larger

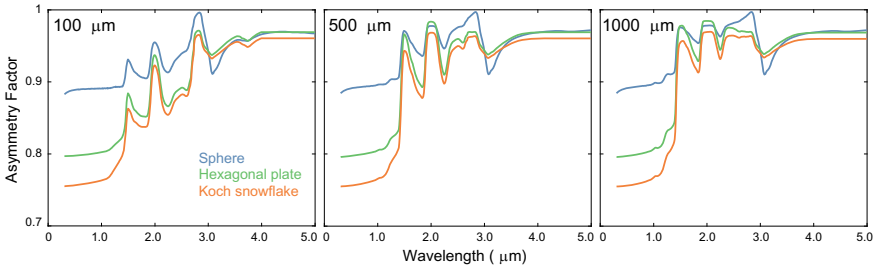

Fig. 8 Spectral asymmetry factors for snow sphere, hexagonal plate, and Koch snowflake with grain effective radii of 100, 500, and 1000 μm. Data are obtained from computations by He et al. (2018c)

and more variable at NIR wavelengths. It increases to ~1.0 around 3 μm wavelength due to the vanishing of Fresnel reflection contributions to Q_{ext} (Sect. 3.2.2). The sharp peaks around 1.5 and 2.0 μm correspond to the spectral feature of the ice imaginary index of refraction (Sect. 3.2.1). In general, larger snow grains tend to have larger asymmetry factors, particularly at wavelengths greater than 1.0 μm (Dang et al. 2016; He et al. 2017b). For nonspherical snow grains, the use of the equal-volume-to-area representation is not accurate for asymmetry factor (Dang et al. 2016), in contrast to the cases of extinction efficiency and single-scattering albedo. He et al. (2017b) found that nonspherical snow grains tend to have smaller (up to ~20%) asymmetry factors and hence weaker forward scattering than spherical grains, particularly at wavelengths less than 3.0 μm, which eventually results in higher albedo for nonspherical snow grains. Moreover, impurities in snow have negligible effects on snow asymmetry factors (Liou et al. 2014). The perturbation of light-absorbing impurities on snow albedo, however, is reduced with lower asymmetry factors, as impurities deeper in the snow column are exposed to less radiation.

To account for the snow shape effect in radiative transfer and climate models, Räisänen et al. (2015) developed nonlinear parameterizations for snow asymmetry factor and phase function depending on effective grain size and refractive index. He et al. (2017b) further proposed a parameterization to relate snow asymmetry factor to grain size and shape by extending the Fu (2007) formulation for ice clouds. The He et al. (2017b) parameterizations for both snow asymmetry factor and single-scattering coalbedo have been successfully implemented into the widely-used SNICAR model to account for effects of snow nonsphericity and impurity contamination (He et al. 2018c), which compares well with observations.

4 Snow Albedo Parameterizations

Based on snow radiative transfer schemes (Sect. 2) and single-scattering properties (Sect. 3), snow albedo can be computed on a physical basis. However, the sophisticated snow radiative transfer calculations sometimes may not be computationally efficient for intensive climate modeling tasks. Thus, enormous efforts have been made to develop efficient and accurate parameterizations for snow albedo based on either rigorous physically-based radiative transfer computations or empirical derivation from measurements. Here we briefly review several widely-used snow albedo parameterizations developed in the past few decades for application in various land and/or climate models. Note that each of these parameterizations has its own limitations and uncertainties.

4.1 Accounting for Snow Grain Properties

Since snow single-scattering properties are directly related to snow grain properties, including size, shape, packing structure, density, and refractive index, it is straightforward to parameterize snow albedo as a function of snow properties. In early years, based on the two-stream approximation, Bergen (1975) attempted to formulate a parameterization of spectral snow albedo $\left(r_{s,\lambda}\right)$ for an optically semi-infinite snowpack under diffuse radiation, which can be expressed as:

$$r_{s,\lambda} = R_i + \beta(1 - R_i)^2(1 - R_i\beta)^{-1} \tag{4.1.1a}$$

$$\beta = \left[k_\lambda + R_i - \left(k_\lambda^2 + 2k_\lambda R_i\right)^{0.5}\right]/R_i$$

where k_λ is a wavelength-dependent parameter determined by the ice absorption coefficient, and R_i is related to snow grain size and snow density. This scheme was later improved for application to multiple snow layers by Yamazaki et al. (1993) using a similar method based on the two-stream approximation, and was further implemented in the NASA GEOS-5 snow model (Yasunari et al. 2011).

On the other hand, Bohren and Barktrom (1974) applied the geometric-optics theory in the limit of small absorption to the analysis of snow single-scattering properties, and further simplified the radiative transfer solution by assuming a semi-infinite snowpack and using some other approximations. They finally derived the following simple spectral snow albedo equation for diffuse radiation at visible wavelengths:

$$r_{s,\lambda} = 1 - 5.96\left(\kappa_{i,\lambda} D_e\right)^{0.5} \tag{4.1.2}$$

where $\kappa_{i,\lambda}$ is the wavelength-dependent absorption coefficient for pure ice, and D_e is the mean snow grain diameter. Later, based on the two-stream approximation for a semi-infinite homogeneous snowpack, Choudhury and Chang (1981) gave the following simplified equation for diffuse snow albedo (r_s):

$$r_s = 1 - \frac{2(1 - \tilde{\omega})^{0.5}}{(1 - \tilde{\omega}g)^{0.5} + (1 - \tilde{\omega})^{0.5}} \tag{4.1.3a}$$

$$\tilde{\omega} = 0.5 + 0.5e^{-1.67\kappa_i R_e} \tag{4.1.3b}$$

$$g = 0.87e^{-2\kappa_i R_e} + 0.97\left[1 - e^{-2\kappa_i R_e}\right] \tag{4.1.3c}$$

where$g$ and $\tilde{\omega}$ are the asymmetry factor and single-scattering albedo, respectively, which are both related to the ice absorption coefficient (κ_i) and snow grain radius (R_e). They further derived the following approximate relation between diffuse snow albedo and grain size following the Bohren and Barktrom (1974) formulation, based on a coupled atmosphere-snowpack model simulation:

$$r_{s,\lambda} \approx 0.9517 - 0.1335(R_e)^{0.5} \tag{4.1.3d}$$

A number of snow albedo parameterizations have also been proposed particularly for application in weather and climate models. For example, Brun et al. (1992) developed a sophisticated snow model (CROCUS) for avalanche forecasting with up to 50 snow layers, which has been coupled with the French ARPEGE climate model. In the model, snow albedo (r_s) is empirically parameterized based on effective grain diameter (D_e; unit: m) as follows:

$$r_s = \begin{cases} 1 - 1.58D_e^{0.5} - 0.2\chi/60 & 0.3 - 0.8\ \mu\text{m} \\ 1 - 15.4D_e^{0.5} & 0.8 - 1.5\ \mu\text{m} \\ 346.3D_e - 32.31D_e^{0.5} & 1.5 - 2.8\ \mu\text{m} \end{cases} \tag{4.1.4}$$

where χ is the snow-surface age (days), and the snow grain size depends on snow type. This parameterization has been further updated in CROCUS as follows (Vionnet et al. 2012):

$$r_s = \begin{pmatrix} \max\left(0.6,\ r_{s,m} - \Delta r_{s,age}\right) & 0.3 - 0.8\ \mu\text{m} \\ \max\left(0.3,\ 0.9 - 15.4D_e^{0.5}\right) & 0.8 - 1.5\ \mu\text{m} \\ 346.3D_{e,s} - 32.31D_{e,s}^{0.5} + 0.88 & 1.5 - 2.8\ \mu\text{m} \end{pmatrix} \tag{4.1.5a}$$

$$r_{s,m} = \min\left(0.92,\ 0.96 - 1.58D_e^{0.5}\right) \tag{4.1.5b}$$

$$\Delta r_{s,age} = \min(1,\ \max(P/P_0,\ 0.5)) \times 0.2\chi/60 \tag{4.1.5c}$$

$$D_{e,s} = \min(D_e,\ 0.0023) \tag{4.1.5d}$$

where P is the mean pressure, and P_0 is the reference pressure (870 hPa).

Greuell and Konzelmann (1994) proposed a density-dependent snow albedo parameterization in the SOMARS snow/ice model, which represents the albedo (r_s) as follows

$$r_s = r_{s,i} - (\rho_{ss} - \rho_i)\left(\frac{r_{s,fs} - r_{s,i}}{\rho_{fs} - \rho_i}\right) \tag{4.1.6}$$

where $r_{s,i}$ and $r_{s,fs}$ are the albedos of ice and fresh snow, respectively, while ρ_i, ρ_{ss}, and ρ_{fs} are the densities of ice, surface snow, and fresh snow, respectively. This scheme has also been used in other snowmelt and glacier mass balance models (e.g., Wright et al. 2007).

More recently, based on the accurate DISORT snow radiative transfer calculations, Dang et al. (2015) developed a broadband snow albedo (r_s) parameterization as a function of snow radius under both clear sky and overcast-cloud sky by assuming spherical grains and a semi-infinite homogeneous snowpack:

$$r_s(R_e) = m_0 + m_1 R_n + m_2 R_n^2 \tag{4.1.7a}$$

$$R_n = \log_{10}\left(R_e / R_{e,0}\right) \tag{4.1.7b}$$

where $R_{e,0}$ (= 100 μm) is the reference radius, and m_i is the parameterization coefficient depending on wavelength bands. Their further study (Dang et al. 2016) proposed a scaling factor (f_{rs}) for correcting albedo of snow spheres in order to match that of nonspherical grains, which is a function of snow effective size and aspect ratio (AR):

$$f_{rs} = c_1(AR)R_n^2 + c_2(AR)R_n + c_3(AR) \tag{4.1.8}$$

where $c_i(AR)$ is the coefficient depending on AR. Their study was mainly based on the asymmetry factor parameterization formulated by Fu (2007) for nonspherical ice clouds, which was then used as input to the DISORT model simulation to generate the database for parameterization development. Following these two studies, He et al. (2018a) improved the Dang et al. (2015) parameterization using the same formulation (Eq. 4.1.7a, b) but explicitly resolving nonspherical snow shapes based on the stochastic aerosol-snow albedo model simulations. Thus, a set of updated coefficient values (m_i) for different snow grain shapes in wavelength bands of several widely-used land/climate models have been provided by He et al. (2018a). Furthermore, a recent study (Saito et al. 2019) also extended the same parameterization (Eq. 4.1.7a, b) by using the similar methodology of He et al. (2018a) but including an ensemble of observed snow shapes and size distributions as well as an adjustment for two-layer snowpack structures. This provides updated coefficients for more realistic snow properties.

In addition to grain size and shape, He et al. (2017a) also attempted to account for snow grain close packing/aggregating and resolved a simplified grain packing structure in the radiative transfer computation. They found that snow grain packing can be treated equivalently as an increase of snow effective sizes, and the snow albedo with close packing $\left(r_{s,cp}\right)$ can be linearly related to that without packing $\left(r_{s,ncp}\right)$ in a first-order approximation as follows:

$$r_{s,cp} = b_1 r_{s,ncp} - b_2 \tag{4.1.9}$$

where b_i is the parameterization coefficient depending on the strength of grain packing. Thus, the grain packing (or a denser snowpack) tends to reduce snow albedo (Peltoniemi 2007).

4.2 Accounting for Snow Impurities

Impurities such as BC, dust, and brown carbon can significantly reduce snow albedo. In addition to conducting rigorous radiative transfer calculations with snow single-scattering properties modified by the inclusion of impurities (Sect. 3.2), a number of simplified snow albedo parameterizations have also been developed to account for impurity effects. For example, Hadley et al. (2010) derived an empirical relationship between snow albedo reduction $\left(\Delta r_{s,BC}\right)$ and BC mass concentration (C_{BC}, ppb) by fitting previous measurements and radiative transfer model results, which is expressed as:

$$\Delta r_{s,BC} = 0.17 \times (C_{BC})^{0.83} \tag{4.2.1}$$

This parameterization, however, may have large uncertainty since the data points used for fitting were obtained under quite different snow and atmospheric conditions.

Dang et al. (2015) further proposed the following physically-based parameterization derived from DISORT simulations by combining externally-mixed BC mass concentration (C_{BC}) and spherical snow grain radius (R_e):

$$\Delta r_{s,BC} = 10^{k_1 p^2 + k_2 p + k_3} \tag{4.2.2a}$$

$$p = \log_{10}\left([C_{BC}/C_0]\left[R_e/R_{e,0}\right]^s\right) \tag{4.2.2b}$$

where C_0 and $R_{e,0}$ are the reference values, and k_i and s are the parameterization coefficients. They also suggested converting dust mass concentration (C_{dst}, <100 ppm) to the equivalent BC mass concentration $\left(C_{BC}^{eq}\right)$ using the following relation:

$$C_{BC}^{eq} = C_{dst}/\left(v_0 + v_1 x + v_1 x^2\right) \tag{4.2.3a}$$

$$x = \log_{10}(C_{dst}) \tag{4.2.3b}$$

where v_i are the parameterization coefficients.

Recently, He et al. (2018a) developed a set of new parameterizations by simultaneously accounting for BC-snow internal mixing and nonspherical snow grains, based on the rigorous stochastic aerosol-snow model simulations. Their formulation follows an empirical relation derived from laboratory measurements by Hadley and Kirchstetter (2012) and is expressed as:

$$\Delta r_{s,BC} = d_0 \times (C_{BC})^k \tag{4.2.4a}$$

$$k = d_1 \times \left(R_e/R_{e,0}\right)^{d_2} \tag{4.2.4b}$$

where $\Delta r_{s,BC}$ is the BC-induced snow albedo reduction, C_{BC} is the BC mass concentration (ppb), $R_{e,0}$ and R_e are the effective radii of reference and target snow grains, and d_i is a coefficient depending on snow shape and wavelengths. This parameterization works for a semi-infinite homogeneous snowpack. On this basis, Saito et al. (2019) further extended the parameterization (Eq. 4.2.4a, b) to account for an ensemble of observed snow shapes and size distributions as well as two-layer snowpack structures, which provides updated coefficients.

Moreover, He et al. (2018b) found that BC size distribution has significant impacts on the BC-induced snow albedo reduction. Thus, they developed a set of parameterizations that include BC size effects for internal mixing with nonspherical snow grains in a semi-infinite snowpack, which are expressed as:

$$\Delta r_{s,R_{BC}} = \left(\frac{R_{BC}}{0.05}\right)^{p_\lambda} \times \Delta r_{s,R_{BC}=0.05} \tag{4.2.5a}$$

$$\Delta r_{s,poly} = c_\lambda \times \Delta r_{s,mono} \tag{4.2.5b}$$

where $\Delta r_{s,R_{BC}}$ and $\Delta r_{s,R_{BC}=0.05}$ are the BC-induced snow albedo reductions for a certain BC effective radii (R_{BC}) and a reference R_{BC} ($= 0.05$ μm), respectively, with the other conditions unchanged. $\Delta r_{s,poly}$ and $\Delta r_{s,mono}$ are the snow albedo reductions for polydisperse and monodisperse BC with the same effective radius, respectively, when the other conditions are the same. p_λ and c_λ are the wavelength-dependent coefficients. These relationships are applicable to different snow grain sizes and shapes as a first-order approximation.

4.3 Accounting for Atmospheric Variables

The environmental conditions (e.g., temperature, surface condition, and solar illumination) could exert external forcing on snowpack properties and albedo evolution. Thus, many snow albedo parameterizations have been developed to include atmospheric variables. For example, to account for the effect of solar zenith angle, Dickinson et al. (1986) proposed an early version of snow albedo parameterization that accounts for the change of solar zenith angle (θ_z), which has been implemented in the Biosphere-Atmosphere Transfer Scheme (BATS). The snow albedo is parameterized as:

$$r_{s,vis/NIR} = r_{s,d,vis/NIR} + \max\left[0,\ 0.4\left(\frac{1 - r_{s,d,vis/NIR}}{b}\right)\left(\frac{b+1}{1+2b\cos\ \theta_z} - 1\right)\right] \tag{4.3.1a}$$

$$r_{s,d,vis/NIR} = \left(1 - C_{vis/NIR} F_{age}\right) r_{s,0,vis/NIR} \tag{4.3.1b}$$

where $r_{s,d,vis/NIR}$ is the diffuse snow albedo for $\theta_z < 60°$ at visible or NIR bands, and $r_{s,0,vis/NIR}$ is the prescribed fresh snow albedo for $\theta_z < 60°$ at visible (0.95) or NIR (0.65) bands. b is a tunable parameter (often set to 2), and F_{age} is a tunable factor for snow aging effects due to grain growth, snow melting, and impurities. This albedo scheme was also used in the NCAR Community Land Model (CLM) version 3 (Oleson et al. 2004).

Later, Marshall (1989) found that the effect of solar zenith angle on snow albedo can be equivalently represented by altering snow grain size. Thus, based on the piecewise curve fitting of theoretical snow model results (Wiscombe and Warren 1980), they developed the following equation to adjust snow grain radius (R_e) based on solar zenith angle (θ_z):

$$R'_e = R_e\left[1 + a(\cos\ \theta_z - 0.65)\right]^2 \tag{4.3.2}$$

where a is a wavelength-dependent coefficient (0.781 for visible, 0.791 for NIR, and 0.786 for the whole solar wavelengths). They further proposed parameterizations to include the impacts of impurities and finite snow depth, which, however, rely heavily on look-up tables. Following the Marshall (1989) work, Marks and Dozier (1992) proposed a more direct relation between snow albedo (r_s) and solar zenith angle (θ_z) as follows

$$r_{s,vis} = r_{s,\max,vis} - k_{vis,1}R_e^{0.5} + k_{vis,2}R_e^{0.5}(1 - \cos\ \theta_z) \tag{4.3.3a}$$

$$r_{s,NIR} = r_{s,\max,NIR}\exp\left(k_{NIR,1}R_e^{0.5}\right) + \left(k_{NIR,2}R_e^{0.5} + k_{NIR,3}\right)(1 - \cos\ \theta_z) \tag{4.3.3b}$$

where k is a coefficient for visible or NIR bands, R_e is the snow grain radius, and $r_{s,\max}$ is the snow albedo at $\theta_z = 0°$. This parameterization has been implemented in the SNTHERM.ver4 snow model. This albedo scheme was further used by Melloh et al. (2002) for snowpack under canopy, with improvements through an albedo correction for thin snow layers achieved by matching with two-stream model results. Yasunari et al. (2011) also used this scheme to include solar zenith angle effects in the GEOS-5 snow model.

Recently, Saito et al. (2019) proposed a parameterization to correct snow albedo based on solar zenith angle (θ_z). They empirically fitted the snow albedo results from rigorous radiative transfer modeling, and found the following relation:

$$\Delta r_{s,\theta} = \left(s_1 + s_2 \cdot r_{s,0}^{s_3}\right)\left(\frac{1 - \cos\ \theta_z}{1 + \cos\ \theta_z}\right)^{s_0} \tag{4.3.4}$$

where $\Delta r_{s,\theta}$ is the change of direct-beam snow albedo due to non-zero θ_z compared to the snow albedo $\left(r_{s,0}\right)$ with $\theta_z = 0$. $r_{s,0}$ also includes impurity effects. s_i is the wavelength-dependent coefficient for one- or two-layer snowpack.

In addition, several useful parameterizations have been proposed to account for the effects of surface temperature and/or snow aging (time) on albedo. In the UK Meteorological Office (UKMO) climate model, a snow-free albedo $(r_{s,0})$ and a cold deep snow albedo $(r_{s,cds})$ are specified, with the effective snow albedo (r_s) parameterized as (Essery et al. 1999):

$$r_s = \begin{cases} r_{s,cds} & T_s \le -2\ ^\circ\mathrm{C} \\ r_{s,cds} - 0.15\left(r_{s,cds} - r_{s,0}\right)(T_s + 2) & T_s > -2\ ^\circ\mathrm{C} \end{cases} \tag{4.3.5}$$

where T_s is the surface temperature. Similar parameterizations with the linear temperature dependence are also used in the ECHAM5 climate model (Roeckner et al. 2003).

In the Interaction between Soil, Biosphere and Atmosphere (ISBA) land surface model (Douville et al. 1995) and the Instituto Nacional de Meteorologia (INM) model (Fernandez 1998), the snow albedo (r_s) is parameterized as a function of snow age (χ) that is prescribed according to different snow conditions. For cold (non-melting) snow, it is a linear time-decay relation:

$$r_s(t + \Delta t) = r_s(t) - \Delta t/\chi_1 \tag{4.3.6a}$$

For melting snow, it is an exponential time-decay relation:

$$r_s(t + \Delta t) = \left[r_s(t) - r_{s,\min}\right]e^{-\Delta t/\chi_2} + r_{s,\min} \tag{4.3.6b}$$

where χ_1 and χ_2 are tunable decay time scales (snow age), and $r_{s,\min}$ is 0.5. The fresh snow albedo is prescribed as 0.85, and the snow albedo is refreshed to fresh albedo with 10 mm snow water equivalent of snowfall. The same treatment was also included in the ECMWF model (Pirazzini 2009). Similar time-dependent snow albedo parameterizations have also been used in the Canadian Land Surface Scheme (CLASS) (Verseghy 1991), where the albedo (r_s) is expressed as

$$r_s(t + \Delta t) = \left[r_s(t) - r_{s,\min}\right]e^{-k\Delta t} + r_{s,\min} \tag{4.3.7}$$

where k is a decay coefficient (0.01 h^{-1}). For snowpack with >0.5 cm fresh snowfall, $r_s(t)$ is reset to 0.84 (fresh snow albedo), while $r_{s,\min}$ is set to 0.70 and 0.50 for dry and melting snow, respectively. Sun et al. (1999) further combined these formulations for snow albedo calculations in a simple snow-atmosphere-soil transfer (SAST) model, with the exponential albedo decay relation (Eq. 4.3.6b) for deep snow cover and the linear albedo decay (Eq. 4.3.6a) for shallow melting and dry snow. The preceding empirical time/temperature-dependent parameterizations are intended to include the combined effects of many snow aging processes, including metamorphism and evolution of grain size, snow depth, impurity content, and atmospheric conditions.

To account for cloud cover effects that change the ratio of diffuse-to-direct radiation, Greuell and Konzelmann (1994) proposed a linear relationship between clear-sky and cloudy-sky snow albedos as follows:

$$r_{s,cloud} = r_{s,clear} + 0.05(n_c - 0.5) \tag{4.3.8}$$

where n_c is the cloud cover.

Moreover, Gardner and Sharp (2010) recently developed a physically-based parameterization to relate broadband snow albedo to many snowpack and atmospheric variables, including specific surface area of snow spheres, snow depth, BC concentration (external mixing), solar zenith angle, and cloud optical depth, based on a coupled DISORT atmosphere-snow radiative transfer model. For pure snow, the albedo $\left(r_{s,0}\right)$ is a function of snow grain specific surface area (S; within 0.07–1300 $\text{cm}^2\ \text{g}^{-1}$) as follows:

$$r_{s,0} = 1.48 - S^{-0.07} \tag{4.3.9}$$

Further accounting for impurities, the change $\left(\Delta r_{s,c}\right)$ in snow albedo is affected by BC mass concentration (C_{BC}; within 0–2 ppmw) as follows:

$$\Delta r_{s,c} = \max\left(0.04 - r_{s,0},\ \frac{-C_{BC}^{0.55}}{0.16 + 0.6S^{0.5} + 1.8C_{BC}^{0.6}S^{-0.25}}\right) \tag{4.3.10a}$$

Further accounting for solar zenith angle (θ_z), the change $\left(\Delta r_{s,\theta}\right)$ in snow albedo is expressed as:

$$\Delta r_{s,\theta} = 0.53 r_{s,0}\left(1 - r_{s,0} - \Delta r_{s,c}\right)(1 - \cos\ \theta_z)^{1.2} \tag{4.3.10b}$$

Further accounting for cloud cover, the change $\left(\Delta r_{s,\tau}\right)$ in snow albedo can be expressed as a function of cloud optical depth (τ; within 0–30) as follows:

$$\Delta r_{s,\tau} = \frac{0.1\tau\left(r_{s,0} + \Delta r_{s,c}\right)^{1.3}}{(1 + 1.5\tau)^{r_{s,0}}} \tag{4.3.10c}$$

The resulting broadband albedo (r_s) for a homogeneous semi-infinite snowpack by accounting for all the preceding factors is:

$$r_s = r_{s,0} + \Delta r_{s,c} + \Delta r_{s,\theta} + \Delta r_{s,\tau} \tag{4.3.10d}$$

When considering a finite snow layer with depth z (m), a further correction can be made by replacing the $\Delta r_{s,c}$ in Eq. (4.3.10a–d) with the new $\Delta r'_{s,c}$ in the following:

$$\Delta r'_{s,c} = \left(r_{s,c}^{btm} - r_{s,0}^{top}\right) + A\left(r_{s,c}^{top} - r_{s,c}^{btm}\right) \tag{4.3.11a}$$

$$r_{s,c} = r_{s,0} + \Delta r_{s,c} \tag{4.3.11b}$$

$$A = \min\left(1,\ 2.1z^{1.35\left(1-r_{s,0}^{top}\right)-0.1C_{BC}^{top}-0.13}\right) \tag{4.3.11c}$$

This comprehensive snow albedo parameterization was designed for climate modeling applications.

5 Summary, Challenges, and Future Directions

This chapter gave a critical review of the commonly-used snow radiative transfer and albedo theories, models, and parameterizations in the solar spectrum. Overall, there have been significant advances in both scientific understanding and technical methods/theories for solving snow albedo and radiative transfer problems in the past decades, with much progress in model developments with different applications.

For snow radiative transfer (Sect. 2), we firstly introduced the basic formulation of the problem (Sect. 2.1), followed by several important radiative transfer theories that have been used to solve the problems for snow on land (uniformly refractive layered media) (Sect. 2.2), including the discrete ordinate radiative transfer (DISORT) theory, the adding-doubling method, the two-stream approximation, and the approximate asymptotic radiative transfer (AART) theory. We also summarized the methods applied to snow on ice (non-uniformly refractive layered media) (Sect. 2.3) and particularly emphasized their differences from those used for snow on land, including the extended DISORT theory, the delta-Eddington adding-doubling method, the delta-four-stream approximation, and the backward Monte Carlo method. There are also many other theories and models such as the physically-based snow albedo model (PBSAM), microstructure-based photon-tracking radiative transfer model, the transport-approximation model, and the bidirectional-reflectance model, which were briefly reviewed too (Sect. 2.4). As the necessary inputs for snow radiative transfer modeling, snow single-scattering properties (Sect. 3) and associated computational methods (Sect. 3.1) were also summarized in this chapter, including Mie theory, the geometric-optics method, and the Monte Carlo photon-tracing approach. The major spectral features of snow single-scattering properties, such as ice refractive index, extinction efficiency, asymmetry factor, and single-scattering albedo/coalbedo, were discussed (Sect. 3.2) particularly focusing on the effects of snow grain size, grain shape, and impurity. Finally, we briefly reviewed the commonly-used snow albedo parameterizations developed for application in weather and climate modeling (Sect. 4), which account for the effects of snow grain properties (Sect. 4.1), snow impurities (Sect. 4.2), and atmospheric conditions (Sect. 4.3).

However, there are still a number of challenges and scientific questions associated with snow radiative transfer and albedo computations, hindering accurate estimates of snowpack evolution and hence its interactions with land, atmosphere, and ocean components in weather and climate models as well as snow remote sensing retrievals. To facilitate future studies, the following important topics and directions are worth exploring.

(1) Snow aging/metamorphism plays a key role in changing snowpack properties (e.g., grain size, grain shape, density/compaction, and depth) and hence snow albedo through vapor diffusion and melting/refreezing processes (Flanner and Zender 2006). Nevertheless, some models still treat snow radiative transfer and/or albedo calculations separately from the evolution of snow properties (e.g., snow aging/metamorphism), including the widely-used BATS and CLASS schemes embedded in the WRF/Noah-MP model, leading to an inconsistent treatment of snowpack evolution. A full and self-consistent coupling of the two components is necessary to precisely simulate snowpack mass and energy changes. Besides, during snow aging/metamorphism processes, snowpack becomes more compact, resulting in closely-packed snow grain aggregates (i.e., densely-packed particle media), which may alter the snow optical properties and radiative transfer processes (Kokhanovsky and Zege 2004). Recently, He et al. (2017a) gave an attempt to explicitly resolve the closely-packed snow structure by constructing a packed cubic aggregate consisting of many snow grains based on the stochastic aerosol-snow albedo model (Liou et al. 2014). More realistic treatments of close-packing snow structures and future investigation of its radiative effects will be beneficial.

(2) The interactions between snow and canopy, such as snow interception by canopy and canopy shading effects on surface snow albedo, are critical to surface temperature and subsequent hydrological predictions as well as responses to regional climate (Melloh et al. 2002; Thackeray et al. 2014). Improved model treatments of the coupled snow-canopy-radiation system may largely remove the surface albedo biases in current climate models (Thackeray et al. 2015). Recent studies (Seyednasrollah et al. 2013; Seyednasrollah and Kumar 2014) have developed a physically-based forest radiation model to quantify solar radiation on the snow-covered forest ground, which is a valuable attempt to better resolve the canopy shading effect on snowpack solar radiation.

(3) The large-scale topographic effect of snow surface (e.g., snow-covered mountains) could play a critical role in determining snow radiative energy balance. Previous radiative transfer calculations only assumed parallel planes in models, which may not be applicable over mountains. Due to the intricacy of spatial orientation and inhomogeneous features of mountain topography and the complex interaction of direct and diffuse radiation with mountain surfaces, it is challenging to quantify topography-radiation interactions and effects, which has not been accounted for in most snow and land models. Recent studies (Lee et al. 2013, 2015) have developed a 3D radiative parameterization to quantify the

snow-topography-radiation interactions for application in weather and climate models, which provides the basis for future model improvements.

(4) In addition to the large-scale topography, the small-scale roughness of a snowpack surface is also important (e.g., Warren et al. 1998; Zhuravleva and Kokhanovsky 2011; Lhermitte et al. 2014). Compared to a flat/smooth surface, a rough surface can lead to additional multiple surface scattering and hence higher probabilities for snow absorption (i.e., "trapping" effect of photons), which further reduces snow albedo. However, the majority of snow models do not include or well represent the snowpack surface roughness/irregularity effect. More measurements and physical understanding are required for developing realistic parameterizations in models to account for this effect.

(5) Moreover, the micro-scale structure of each individual snow grain can also change the snow single-scattering properties and hence snow albedo calculations. For example, the rough surface of individual ice crystal can alter its interaction with light beams and therefore its optical properties (e.g., Yang and Liou 1998; Fu 2007), though particle roughness has not been accounted for in most snow radiative transfer and albedo models. Furthermore, snow grains may also contain air bubbles (more common in glacier/sea ice), which can affect scattering within snow grains via air-ice interfaces. But only very few studies (e.g., Gardner and Sharp 2010) included this factor in snow albedo calculations. An assessment of this factor's impact is needed in future research. Another potentially important micro-scale factor is liquid water in snowpack during snow melting, which could change snow optical properties and/or radiative transfer treatments by covering snow grain surfaces and/or filling in voids between snow grains (Gardner and Sharp 2010). Green et al. (2002) assumed liquid water either to be separate spheres interspersed with snow grains or to be coatings on snow grains, and found significant impacts of liquid water on reflectance spectra of melting snow. Nevertheless, this effect is not considered in the majority of snow radiative transfer models and requires more attention.

(6) For snow impurity effects, there are many advances in the past decade in simulating aerosol-snow-radiation interactions, for example, from aerosols externally mixed with snow spheres (e.g., Warren and Wiscombe 1980; Flanner et al. 2007) to aerosols internally mixed with nonspherical snow grains (e.g., Flanner et al. 2012; Dang et al. 2016; He et al. 2017b, 2018a). However, this progress has largely focused on BC aerosols. A further quantification of dust-snow internal mixing is needed, since dust aerosols are efficient ice nuclei and could be mixed inside snow grains. He et al. (2019a) recently made the first attempt to simulate and parameterize the effects of dust internally mixed with nonspherical snow grains. Besides, large uncertainties still exist in simulating snow albedo reduction by brown carbon (Zhou et al. 2019) and algae (Cook et al. 2017), because of the large uncertainties in single-scattering properties of brown carbon and algae, which are significantly affected by their composition. More measurements are required to produce a reliable optical property database for these light-absorbing impurities, while an efficient way to properly incorporate these properties in snow models needs to be developed.

(7) Finally, there are limitations and uncertainties in every snow albedo parameterization. Due to the strong snow albedo feedback (Qu and Hall 2006; Flanner et al. 2011), it is imperative to assess the uncertainties associated with snow albedo schemes in different models and their contributions to biases of other variables/phenomena (e.g., snowmelt, glacier retreat, runoff, surface temperature, polar amplification, and regional/global warming) in weather forecasts and climate model projection.

Acknowledgements The authors thank the editor, Dr. Alexander Kokhanovsky, for the opportunity to contribute to this book chapter. Cenlin He was supported by the NCAR Advanced Study Program Fellowship. The National Center for Atmospheric Research is sponsored by the National Science Foundation.

Appendix

See Table 2.

Table 2 Key parameters and their physical meanings used in this chapter

Parameter	Physical meaning
I	Radiation intensity
F_0	Direct-beam solar flux
F	Diffuse flux
μ	Cosine of zenith angle
θ_z	Solar zenith angle
ϕ	Azimuthal angle
Θ	scattering angle
$p(\cdot)$	Phase function
τ	Optical depth
$\tilde{\omega}$	Single-scattering albedo
g	Asymmetry factor
P_l	Legendre polynomials
g_l	Legendre expansion coefficient
R	Reflection/reflectance function
T	Transmission function
r_s	Spherical/white-sky/diffuse albedo
r_p	Plane/black-sky/direct albedo
κ_{abs}	Absorption coefficient
κ_{ext}	Extinction coefficient
κ_{sca}	Scattering coefficient
Q_{sca}	Scattering efficiency
Q_{abs}	Absorption efficiency
Q_{ext}	Extinction efficiency
C_{ext}	Extinction cross-section
λ	Wavelength
B	Absorption enhancement parameter
α	ice absorption coefficient/absorptivity
β_a	Single-scattering coalbedo (i.e., one minus single-scattering albedo)
X	Size parameter
R_e	Particle effective radius
D_e	Particle effective diameter
ρ	Density
χ	Snow age
m_{im}	Imaginary part of refractive indices
m_{re}	Real part of refractive indices

References

Aoki T (1992) A multiple scattering model for the atmosphere-snow system. Proc NIPR Symp Polar Meteor Glaciol 6:77–83

Aoki T, Aoki T, Fukabori M, Hachikubo A, Tachibana Y, Nishio F (2000) Effects of snow physical parameters on spectral albedo and bidirectional reflectance of snow surface. J Geophys Res 105:10219–10236

Aoki T, Kuchiki K, Niwano M, Kodama Y, Hosaka M, Tanaka T (2011) Physically based snow albedo model for calculating broadband albedos and the solar heating profile in snowpack for general circulation models. J Geophys Res 116:D11114

Asano S (1975) On the discrete-ordinates method for the radiative transfer. J Meteorol Soc Jpn 53:92–95

Barkstrom BR (1972) Some effects of multiple scattering on the distribution of solar radiation in snow and ice. J Glaciol 11(63):357–368

Bergen JD (1975) A possible relation of albedo to the density and grain size of natural snow cover. Water Resour Res 11(5):745–746

Berger RH (1979) Snowpack optical properties in the infrared. CRREL Rep., 79–11, U.S. Army Cold Reg Res Eng Lab, Hanover, N.H., pp 1–9

Bi L, Yang P, Kattawar GW, Hu Y, Baum BA (2011) Scattering and absorption of light by ice particles: solution by a new physical-geometric optics hybrid method. J Quant Spectrosc Radiat Transfer 112(9):1492–1508

Bohren CF (1986) Applicability of effective-medium theories to problems of scattering and absorption by nonhomogeneous atmospheric particles. J Atmos Sci 43(5):468–475

Bohren CF, Barkstrom BR (1974) Theory of the optical properties of snow. J Geophys Res 79(30):4527–4535

Bohren CF, Huffman DR (1983) Absorption and scattering of light by small particles. Wiley, Hoboken, N. J., p 530

Bond TC, Habib G, Bergstrom RW (2006) Limitations in the enhancement of visible light absorption due to mixing state. J Geophys Res 111:D20211

Born M, Wolf E (1975) Principles of optics. Pergamon, Oxford

Briegleb BP, Light B (2007) A delta-eddington multiple scattering parameterization for solar radiation in the sea ice component of the community climate system Model. NCAR Tech. Note 472 1 STR, 100 pp

Brun E, David P, Sudul M, Brunot G (1992) A numerical model to simulate snow-cover stratigraphy for operational avalanche forecasting. J Glaciol 38(128):13–22

Chandrasekhar S (1960) Radiative transfer. Dover, New York, p 393

Choudhury BJ, Chang ATC (1979) The solar reflectance of a snow field. Cold Reg Sci Technol 1(2):121–128

Choudhury BJ, Chang ATC (1981) On the angular variation of solar reflectance of snow. J Geophys Res-Oceans 86(C1):465–472

Chýlek P, Srivastava V (1983) Dielectric constant of a composite inhomogeneous medium. Phys Rev B 27(8):5098

Cook JM, Hodson AJ, Taggart AJ, Mernild SH, Tranter M (2017) A predictive model for the spectral "bioalbedo" of snow. J Geophys Res-Earth Surface 122(1):434–454

Dang C, Brandt RE, Warren SG (2015) Parameterizations for narrowband and broadband albedo of pure snow and snow containing mineral dust and black carbon. J Geophys Res-Atmos 120:5446–5468

Dang C, Fu Q, Warren SG (2016) Effect of snow grain shape on snow albedo. J Atmos Sci 73(9):3573–3583

Dang C, Zender CS, Flanner MG (2019) Inter-comparison and improvement of 2-stream shortwave radiative transfer models for unified treatment of cryospheric surfaces in ESMs. The Cryosphere, in press

Dickinson RE, Henderson-Sellers A, Kennedy PJ, Wilson MF (1986) Biosphere–atmosphere transfer scheme (BATS) for the NCAR Community Climate Model. NCAR Tech Note TN-275 + STR 69

Dlugach JM, Yanovitskij EG (1974) The optical properties of Venus and the Jovian planets. II. Methods and results of calculations of the intensity of radiation diffusely reflected from semi-infinite homogeneous atmospheres. Icarus 22(1):66–81

Dombrovskii LA (1996) Approximate methods for calculating radiation heat transfer in dispersed systems. Therm Eng 43(3):235–243

Dombrovskii LA (2012) The use of the transport approximation and diffusion-based models in radiative transfer calculations. Comput Therm Sci 4:297–315

Dombrovsky LA, Kokhanovsky AA (2019) The influence of pollution on solar heating and melting of a snowpack. J Quant Spectrosc Radiat Transfer 233:42–51

Dombrovsky LA, Kokhanovsky AA, Randrianalisoa JH (2019) On snowpack heating by solar radiation: a computational model. J Quant Spectrosc Radiat Transfer 227:72–85

Dominé F, Lauzier T, Cabanes A, Legagneux L, Kuhs WF, Techmer K, Heinrichs T (2003) Snow metamorphism as revealed by scanning electron microscopy. Microsc Res Tech 62(1):33–48

Douville H, Royer JF, Mahfouf JF (1995) A new snow parameterization for the Meteo-France climate model. Clim Dyn 12(1):21–35

Draine BT, Flatau PJ (1994) Discrete dipole approximation for scattering calculations. J Opt Soc Am A 11:1491–1499

Dunkle RV, Bevans JT (1956) An approximate analysis of the solar reflectance and transmittance of a snow cover. J Meteorol 13(2):212–216

Essery R, Martin E, Douville H, Fernandez A, Brun E (1999) A comparison of four snow models using observations from an alpine site. Clim Dyn 15(8):583–593

Evans KF (1993) A general solution for stochastic radiative transfer. Geophys Res Lett 20(19):2075–2078

Fernández A (1998) An energy balance model of seasonal snow evolution. Phys Chem Earth 23(5–6):661–666

Flanner MG, Zender CS (2006) Linking snowpack microphysics and albedo evolution. J Geophys Res-Atmos 111(D12)

Flanner MG, Zender CS, Randerson JT, Rasch PJ (2007) Present-day climate forcing and response from black carbon in snow. J Geophys Res-Atmos 112:D11202

Flanner MG, Zender CS, Hess PG, Mahowald NM, Painter TH, Ramanathan V, Rasch PJ (2009) Springtime warming and reduced snow cover from carbonaceous particles. Atmos Chem Phys 9:2481–2497

Flanner MG, Shell KM, Barlage M, Perovich DK, Tschudi MA (2011) Radiative forcing and albedo feedback from the Northern Hemisphere cryosphere between 1979 and 2008. Nat Geosci 4(3):151–155

Flanner MG, Liu X, Zhou C, Penner JE, Jiao C (2012) Enhanced solar energy absorption by internally-mixed black carbon in snow grains. Atmos Chem Phys 12:4699–4721

Fu Q (1996) An accurate parameterization of the solar radiative properties of cirrus clouds for climate models. J Climate 9(9):2058–2082

Fu Q (2007) A new parameterization of an asymmetry factor of cirrus clouds for climate models. J Atmos Sci 64(11):4140–4150

Gardner AS, Sharp MJ (2010) A review of snow and ice albedo and the development of a new physically based broadband albedo parameterization. J Geophys Res 115:F01009

Giddings JC, LaChapelle E (1961) Diffusion theory applied to radiant energy distribution and albedo of snow. J Geophys Res 66(1):181–189

Glendinning JHG, Morris EM (1999) Incorporation of spectral and directional radiative transfer in a snow model. Hydrol Process 13(12–13):1761–1772

Green RO, Dozier J, Roberts D, Painter T (2002) Spectral snow-reflectance models for grain-size and liquid-water fraction in melting snow for the solar-reflected spectrum. Ann Glaciol 34:71–73

Grenfell TC (1983) A theoretical model of the optical properties of sea ice in the visible and near infrared. J Geophys Res-Oceans 88(C14):9723–9735
Grenfell TC (1991) A radiative transfer model for sea ice with vertical structure variations. J Geophys Res-Oceans 96(C9):16991–17001
Grenfell TC, Warren SG (1999) Representation of a nonspherical ice particle by a collection of independent spheres for scattering and absorption of radiation. J Geophys Res-Atmos 104(D24):31697–31709
Greuell W, Konzelmann T (1994) Numerical modelling of the energy balance and the englacial temperature of the Greenland Ice Sheet. Calculations for the ETH-Camp location (West Greenland, 1155 m asl). Glob Planet Chang 9(1–2):91–114
Hadley OL, Kirchstetter TW (2012) Black-carbon reduction of snow albedo. Nature Climate Change 2(6):437
Hadley OL, Corrigan CE, Kirchstetter TW, Cliff SS, Ramanathan V (2010) Measured black carbon deposition on the Sierra Nevada snow pack and implication for snow pack retreat. Atmos Chem Phys 10(15):7505–7513
Hansen JE (1971) Multiple scattering of polarized light in planetary atmospheres. Part II. Sunlight reflected by terrestrial water clouds. J Atmos Sci 28:1400–1426
Hansen JE, Travis LD (1974) Light scattering in planetary atmospheres. Space Sci Rev 16(4):527–610
He C (2019b) Radiative properties of atmospheric black carbon (soot) particles with complex structures. In: Kokhanovsky A (eds) Springer series in light scattering, vol 4. Springer, Cham. https://doi.org/10.1007/978-3-030-20587-4_5
He C, Li Q, Liou KN et al (2014) Black carbon radiative forcing over the Tibetan Plateau. Geophys Res Lett 41(22):7806–7813
He C, Liou KN, Takano Y, Zhang R, Levy Zamora M, Yang P, Li Q, Leung LR (2015) Variation of the radiative properties during black carbon aging: theoretical and experimental intercomparison. Atmos Chem Phys 15:11967–11980
He C, Takano Y, Liou KN, Yang P, Li Q, Mackowski DW (2016) Intercomparison of the GOS approach, superposition T-matrix method, and laboratory measurements for black carbon optical properties during aging. J Quant Spectrosc Radiat Transfer 184:287–296
He C, Takano Y, Liou KN (2017a) Close packing effects on clean and dirty snow albedo and associated climatic implications. Geophys Res Lett 44:3719–3727
He C, Takano Y, Liou KN, Yang P, Li Q, Chen F (2017b) Impact of snow grain shape and black carbon-snow internal mixing on snow optical properties: parameterizations for climate models. J Clim 30(24):10019–10036
He C, Liou KN, Takano Y, Yang P, Qi L, Chen F (2018a) Impact of grain shape and multiple black carbon internal mixing on snow albedo: parameterization and radiative effect analysis. J Geophys Res-Atmos 123:1253–1268
He C, Liou KN, Takano Y (2018b) Resolving size distribution of black carbon internally mixed with snow: Impact on snow optical properties and albedo. Geophys Res Lett 45:2697–2705
He C, Flanner MG, Chen F, Barlage M, Liou KN, Kang S, Ming J, Qian Y (2018c) Black carbon-induced snow albedo reduction over the Tibetan Plateau: uncertainties from snow grain shape and aerosol–snow mixing state based on an updated SNICAR model. Atmos Chem Phys 18:11507–11527
He C, Liou KN, Takano Y, Chen F, Barlage M (2019a) Enhanced snow absorption and albedo reduction by dust-snow internal mixing: modeling and parameterization. J Adv Model Earth Syst 11:3755–3776
Hu YX, Wielicki B, Lin B, Gibson G, Tsay SC, Stamnes K, Wong T (2000) δ-Fit: a fast and accurate treatment of particle scattering phase functions with weighted singular-value decomposition least-squares fitting. J Quant Spectrosc Radiat Transfer 65(4):681–690
Irvine WM, Pollack JB (1968) Infrared optical properties of water and ice spheres. Icarus 8(1–3):324–360

Jacobson MZ (2004) Climate response of fossil fuel and biofuel soot, accounting for soot's feedback to snow and sea ice albedo and emissivity. J Geophys Res Atmos 109(D21)
Jin Z, Stamnes K (1994) Radiative transfer in nonuniformly refracting layered media: atmosphere–ocean system. Appl Opt 33(3):431–442
Jin Z, Charlock TP, Yang P, Xie Y, Miller W (2008) Snow optical properties for different particle shapes with application to snow grain size retrieval and MODIS/CERES radiance comparison over Antarctic. Remote Sens Environ 112:3563–3581
Johnson JB, Hopkins MA (2005) Identifying microstructural deformation mechanisms in snow using discrete-element modeling. J Glaciol 51:432–442
Joseph JH, Wiscombe WJ, Weinman JA (1976) The delta-Eddington approximation for radiative flux transfer. J Atmos Sci 33(12):2452–2459
Kaempfer TU, Hopkins MA, Perovich DK (2007) A three-dimensional microstructure-based photon-tracking model of radiative transfer in snow. J Geophys Res Atmos 112(D24)
Katsev IL, Prikhach AS, Zege EP, Grudo JO, Kokhanovsky AA (2010) Speeding up the aerosol optical thickness retrieval using analytical solutions of radiative transfer theory. Atmos Meas Tech 3(5):1403–1422
Kokhanovsky A (2013) Spectral reflectance of solar light from dirty snow: a simple theoretical model and its validation. Cryosphere 7(4):1325–1331
Kokhanovsky AA, Zege EP (1995) Local optical parameters of spherical polydispersions: simple approximations. Appl Opt 34(24):5513–5519
Kokhanovsky AA, Zege EP (2004) Scattering optics of snow. Appl Opt 43(7):1589–1602
Kokhanovsky AA, Aoki T, Hachikubo A, Hori M, Zege EP (2005) Reflective properties of natural snow: approximate asymptotic theory versus in situ measurements. IEEE Trans Geosci Remote Sens 43(7):1529–1535
Kokhanovsky A, Lamare M, Mauro BD et al (2018) On the reflectance spectroscopy of snow. The Cryosphere 12(7):2371–2382
Kokhanovsky A, Lamare M, Danne O et al (2019) Retrieval of snow properties from the Sentinel-3 Ocean and Land Colour Instrument. Remote Sens, in review
Lee WL, Liou KN (2007) A coupled atmosphere–ocean radiative transfer system using the analytic four-stream approximation. J Atmos Sci 64(10):3681–3694
Lee WL, Liou KN, Wang CC (2013) Impact of 3-D topography on surface radiation budget over the Tibetan Plateau. Theoret Appl Climatol 113(1–2):95–103
Lee WL, Gu Y, Liou KN, Leung LR, Hsu HH (2015) A global model simulation for 3-D radiative transfer impact on surface hydrology over the Sierra Nevada and Rocky Mountains. Atmos Chem Phys 15(10):5405–5413
Lee WL, Liou KN, He C et al (2017) Impact of absorbing aerosol deposition on snow albedo reduction over the southern Tibetan plateau based on satellite observations. Theoret Appl Climatol 129(3–4):1373–1382
Lee-Taylor J, Madronich S (2002) Calculation of actinic fluxes with a coupled atmosphere–snow radiative transfer model. J Geophys Res Atmos 107(D24):4796
Leroux C, Lenoble J, Brogniez G, Hovenier JW, De Haan JF (1999) A model for the bidirectional polarized reflectance of snow. J Quant Spectrosc Radiat Transfer 61(3):273–285
Lhermitte S, Abermann J, Kinnard C (2014) Albedo over rough snow and ice surfaces. Cryosphere 8(3):1069–1086
Libois Q, Picard G, France JL et al (2013) Influence of grain shape on light penetration in snow. Cryosphere 7(6):1803–1818
Libois Q, Picard G, Dumont M et al (2014) Experimental determination of the absorption enhancement parameter of snow. J Glaciol 60(222):714–724
Libois Q, Picard G, Arnaud L et al (2015) Summertime evolution of snow specific surface area close to the surface on the Antarctic Plateau. Cryosphere 9(6):2383–2398
Light B, Maykut GA, Grenfell TC (2003) A two-dimensional monte carlo model of radiative transfer in sea ice. J Geophys Res Oceans 108(C7):3219

Liou KN (1973) A numerical experiment on Chandrasekhar's discrete-ordinate method for radiative transfer: applications to cloudy and hazy atmospheres. J Atmos Sci 30(7):1303–1326
Liou KN (1974) Analytic two-stream and four-stream solutions for radiative transfer. J Atmos Sci 31:1473–1475
Liou KN (1975) Applications of the discrete-ordinates method for radiative transfer to inhomogeneous aerosol atmospheres. J Geophys Res 80:3434–3440
Liou KN (2002) An Introduction to atmospheric radiation. Academic Press, 583 pp
Liou KN, Yang P (2016) Light scattering by ice crystals: fundamentals and applications, 168–173. Cambridge Univ. Press, Cambridge, UK
Liou KN, Freeman KP, Sasamori T (1978) Cloud and aerosol effects on the solar heating rate of the atmosphere. Tellus 30(1):62–70
Liou KN, Fu Q, Ackerman TP (1988) A simple formulation of the delta-four-stream approximation for radiative transfer parameterizations. J Atmos Sci 45(13):1940–1948
Liou KN, Takano Y, Yang P (2010) On geometric optics and surface waves for light scattering by spheres. J Quant Spectrosc Radiat Transfer 111:1980–1989
Liou KN, Takano Y, Yang P (2011) Light absorption and scattering by aggregates: application to black carbon and snow grains. J Quant Spectrosc Radiat Transfer 112:1581–1594
Liou KN, Takano Y, He C, Yang P, Leung LR, Gu Y, Lee WL (2014) Stochastic parameterization for light absorption by internally mixed BC/dust in snow grains for application to climate models. J Geophys Res-Atmos 119:7616–7632
Lyapustin A, Tedesco M, Wang Y, Aoki T, Hori M, Kokhanovsky A (2009) Retrieval of snow grain size over Greenland from MODIS. Remote Sens Environ 113(9):1976–1987
Macke A, Mueller J, Raschke E (1996) Single scattering properties of atmospheric ice crystals. J Atmos Sci 53(19):2813–2825
Mackowski DW (2014) A general superposition solution for electromagnetic scattering by multiple spherical domains of optically active media. J Quant Spectrosc Radiat Transfer 133:264–270
Malinka AV (2014) Light scattering in porous materials: geometrical optics and stereological approach. J Quant Spectrosc Radiat Transfer 141:14–23
Marks D, Dozier J (1992) Climate and energy exchange at the snow surface in the alpine region of the Sierra Nevada: 2. Snow cover energy balance. Water Resour Res 28(11):3043–3054
Marks AA, King MD (2013) The effects of additional black carbon on the albedo of Arctic sea ice: variation with sea ice type and snow cover. Cryosphere 7(4):1193–1204
Marshall SE (1989) A physical parameterization of snow albedo for use in climate models. NCAR Cooperative Thesis 123. National Center for Atmospheric Research, Boulder, CO, 175 pp.
Meador WE, Weaver WR (1980) Two-stream approximations to radiative transfer in planetary atmospheres: a unified description of existing methods and a new improvement. J Atmos Sci 37(3):630–643
Melloh RA, Hardy JP, Bailey RN, Hall TJ (2002) An efficient snow albedo model for the open and sub-canopy. Hydrol Process 16(18):3571–3584
Mishchenko MI, Travis LD, Mackowski DW (1996) T-matrix computations of light scattering by nonspherical particles: a review. J Quant Spectrosc Radiat Transfer 55:535–575
Mishchenko MI, Dlugach JM, Yanovitskij EG, Zakharova NT (1999) Bidirectional reflectance of flat, optically thick particulate layers: an efficient radiative transfer solution and applications to snow and soil surfaces. J Quant Spectrosc Radiat Transfer 63(2–6):409–432
Mobley CD, Sundman LK (2003) Effects of optically shallow bottoms on upwelling radiances: inhomogeneous and sloping bottoms. Limnol Oceanogr 48:329–336
Namazi M, Salzen KV, Cole JN (2015) Simulation of black carbon in snow and its climate impact in the canadian global climate model. Atmos Chem Phys 15(18):10887–10904
Neshyba SP, Grenfell TC, Warren SG (2003) Representation of a nonspherical ice particle by a collection of independent spheres for scattering and absorption of radiation: 2. Hexagonal columns and plates. J Geophys Res-Atmos 108(D15)
Nussenzveig HM, Wiscombe WJ (1980) Efficiency factor in Mie scattering. Phys Rev Lett 45:1490–1494

Oleson K, Dai Y, Bonan B, et al (2004) Technical description of the community land model (CLM). NCAR Tech. Note NCAR/TN-4611STR, 173 pp
Peebles GH, Plesset MS (1951) Transmission of gamma rays through large thicknesses of heavy materials. Phys Rev 81:430–439
Peltoniemi JI (2007) Spectropolarised ray-tracing simulations in densely packed particulate medium. J Quant Spectrosc Radiat Transfer 108(2):180–196
Picard G, Libois Q, Arnaud L (2016) Refinement of the ice absorption spectrum in the visible using radiance profile measurements in Antarctic snow. Cryosphere 10(6):2655–2672
Picard G, Arnaud L, Dumont M (2017) Time-series of snow spectral albedo and superficial snow specific surface area and impurity content at Col de Porte, French Alps, 2014. PANGAEA
Pirazzini R (2009) Challenges in snow and ice albedo parameterizations. Geophysica 45(1–2):41–62
Pirazzini R, Räisänen P, Vihma T, Johansson M, Tastula EM (2015) Measurements and modelling of snow particle size and shortwave infrared albedo over a melting Antarctic ice sheet. Cryosphere 9(6):2357–2381
Pu W, Cui J, Shi T, Zhang X, He C, Wang X (2019) The remote sensing of radiative forcing by light-absorbing particles (LAPs) in seasonal snow over northeastern China. Atmos Chem Phys 19:9949–9968
Qu X, Hall A (2006) Assessing snow albedo feedback in simulated climate change. J Clim 19(11):2617–2630
Räisänen P, Kokhanovsky A, Guyot G, Jourdan O, Nousiainen T (2015) Parameterization of single-scattering properties of snow. Cryosphere 9(3):1277–1301
Räisänen P, Makkonen R, Kirkevåg A, Debernard JB (2017) Effects of snow grain shape on climate simulations: sensitivity tests with the Norwegian Earth System Model. Cryosphere 11:2919–2942
Ray PS (1972) Broadband complex refractive indices of ice and water. Appl Opt 11(8):1836–1844
Roeckner E, Bauml G, Bonaventura L et al (2003) The atmospheric general circulation model ECHAM5. Part I: model description. Max Planck Institute for Meteorology, Rep 349, 127 pp
Sagan C, Pollack JB (1967) Anisotropic nonconservative scattering and the clouds of Venus. J Geophys Res 72(2):469–477
Saito M, Yang P, Loeb NG, Kato S (2019) A novel parameterization of snow albedo based on a two-layer snow model with a mixture of grain habits. J Atmos Sci 76(5):1419–1436
Seyednasrollah B, Kumar M (2014) Net radiation in a snow-covered discontinuous forest gap for a range of gap sizes and topographic configurations. J Geophys Res-Atmos 119(17):10–323
Seyednasrollah B, Kumar M, Link TE (2013) On the role of vegetation density on net snow cover radiation at the forest floor. J Geophys Res-Atmos 118(15):8359–8374
Stamnes K, Swanson RA (1981) A new look at the discrete ordinate method for radiative transfer calculations in anisotropically scattering atmospheres. J Atmos Sci 38(2):387–399
Stamnes K, Tsay SC, Wiscombe W, Jayaweera K (1988) Numerically stable algorithm for discrete-ordinate-method radiative transfer in multiple scattering and emitting layered media. Appl Opt 27(12):2502–2509
Stokes GG (1862) On the intensity of the light reflected from or transmitted through a pile of plates. Proc Roy Soc London 11:545–556
Sun S, Jin J, Xue Y (1999) A simple snow-atmosphere-soil transfer model. J Geophys Res-Atmos 104(D16):19587–19597
Sykes JB (1951) Approximate integration of the equation of transger. Mon Not R Astron Soc 111(4):377–386
Takano Y, Liou KN (1989) Solar radiative transfer in cirrus clouds. II. Theory and computation of multiple scattering in an anisotropic medium. J Atmos Sci 46:20–36
Takano Y, Liou KN (1995) Radiative transfer in cirrus clouds. Part III: Light scattering by irregular ice crystals. J Atmos Sci 52(7):818–837
Takano Y, Liou KN, Kahnert M, Yang P (2013) The single- scattering properties of black carbon aggregates determined from the geometric-optics surface-wave approach and the T- matrix method. J Quant Spectrosc Radiat Transfer 125:51–56

Thackeray CW, Fletcher CG, Derksen C (2014) The influence of canopy snow parameterizations on snow albedo feedback in boreal forest regions. J Geophys Res-Atmos 119(16):9810–9821
Thackeray CW, Fletcher CG, Derksen C (2015) Quantifying the skill of CMIP5 models in simulating seasonal albedo and snow cover evolution. J Geophys Res-Atmos 120(12):5831–5849
Toon OB, McKay CP, Ackerman TP, Santhanam K (1989) Rapid calculation of radiative heating rates and photodissociation rates in inhomogeneous multiple scattering atmospheres. J Geophys Res-Atmos 94(D13):16287–16301
Tuzet F, Dumont M, Lafaysse M et al (2017) A multilayer physically based snowpack model simulating direct and indirect radiative impacts of light-absorbing impurities in snow. Cryosphere 11(6):2633–2653
van de Hulst HC (1957) Light scattering by small particles. Wiley, 470 pp
van de Hulst HC (1980) Multiple light scattering. Tables, formulas, and applications, vols. 1 and 2. Academic Press, New York
Verseghy DL (1991) CLASS–A Canadian land surface scheme for GCMs. I. Soil model. Int J Climatol 11(2):111–133
Vionnet V, Brun E, Morin S et al (2012) The detailed snowpack scheme Crocus and its implementation in SURFEX v7. 2. Geosci Model Dev 5:773–791
Wang X, Pu W, Ren Y et al (2017) Observations and model simulations of snow albedo reduction in seasonal snow due to insoluble light-absorbing particles during 2014 Chinese survey. Atmos Chem Phys 17(3):2279
Warren SG (1982) Optical properties of snow. Rev Geophys 20(1):67–89
Warren SG (1984) Optical constants of ice from the ultraviolet to the microwave. Appl Opt 23(8):1206–1225
Warren SG, Brandt RE (2008) Optical constants of ice from the ultraviolet to the microwave: a revised compilation. J Geophys Res-Atmos 113(D14)
Warren SG, Wiscombe WJ (1980) A model for the spectral albedo of snow. II: Snow containing atmospheric aerosols. J Atmos Sci 37(12):2734–2745
Warren SG, Brandt RE, O'Rawe Hinton P (1998) Effect of surface roughness on bidirectional reflectance of Antarctic snow. J Geophys Res-Planets 103(E11):25789–25807
Wendling P, Wendling R, Weickmann HK (1979) Scattering of solar radiation by hexagonal ice crystals. Appl Opt 18(15):2663–2671
Wiscombe WJ (1977) The delta–M method: rapid yet accurate radiative flux calculations for strongly asymmetric phase functions. J Atmos Sci 34(9):1408–1422
Wiscombe WJ, Warren SG (1980) A model for the spectral albedo of snow. I: pure snow. J Atmos Sci 37(12):2712–2733
Wright AP, Wadham JL, Siegert MJ, Luckman A, Kohler J, Nuttall AM (2007) Modeling the refreezing of meltwater as superimposed ice on a high arctic glacier: a comparison of approaches. J Geophys Res-Earth Surface 112(F4)
Xie Y, Yang P, Gao GC, Kattawar GW, Mishchenko MI (2006) Effect of ice crystal shape and effective size on snow bidirectional reflectance. J Quant Spectrosc Radiat Transfer 100(1–3):457–469
Yamazaki T, Kondo J, Sakuraoka T, Nakamura T (1993) A one dimensional model of the evolution of snow-cover characteristics. Ann Glaciol 18:22–26
Yang P, Liou KN (1995) Light scattering by hexagonal ice crystals: comparison of finite-difference time domain and geometric optics models. J Opt Soc Amer A 12(1):162–176
Yang P, Liou KN (1996a) Geometric-optics–integral-equation method for light scattering by nonspherical ice crystals. Appl Opt 35(33):6568–6584
Yang P, Liou KN (1996b) Finite-difference time domain method for light scattering by small ice crystals in three-dimensional space. J Opt Soc Amer A 13(10):2072–2085
Yang P, Liou KN (1997) Light scattering by hexagonal ice crystals: solution by a ray-by-ray integration algorithm. J Opt Soc Amer A 14:2278–2288
Yang P, Liou KN (1998) Single-scattering properties of complex ice crystals in terrestrial atmosphere. Contrib. Atmos. Phys. 71(2):223–248

Yang P, Bi L, Baum BA et al (2013) Spectrally consistent scattering, absorption, and polarization properties of atmospheric ice crystals at wavelengths from 0.2 to 100 μ m. J Atmos Sci 70(1):330–347

Yang P, Liou KN, Bi L, Liu C, Yi BQ, Baum BA (2015) On the radiative properties of ice clouds: light scattering, remote sensing, and radiation parameterization. Adv Atmos Sci 32(1):32–63

Yasunari TJ, Koster RD, Lau KM et al (2011) Influence of dust and black carbon on the snow albedo in the NASA Goddard Earth Observing System version 5 land surface model. J Geophys Res-Atmos 116(D2)

Yi K, Meng J, Yang H, He C, Henze D, Liu J, Guan D, Liu Z, Zhang L, Zhu X, Cheng Y, Tao S (2019) The cascade of global trade to large climate forcing over the Tibetan Plateau glaciers. Nat Commun 10:3281

Zege E, Katsev I, Malinka A, Prikhach A, Polonsky I (2008) New algorithm to retrieve the effective snow grain size and pollution amount from satellite data. Ann Glaciol 49:139–144

Zege E, Katsev I, Malinka A, Prikhach A, Heygster G, Wiebe H (2011) Algorithm for retrieval of the effective snow grain size and pollution amount from satellite measurements. Remote Sens Environ 115(10):2674–2685

Zege E, Malinka A, Katsev I et al (2015) Algorithm to retrieve the melt pond fraction and the spectral albedo of Arctic summer ice from satellite optical data. Remote Sens Environ 163:153–164

Zhou Y, Wen H, Liu J, Pu W, Chen Q, Wang X (2019) The optical characteristics and sources of chromophoric dissolved organic matter (CDOM) in seasonal snow of northwestern China. Cryosphere 13(1):157–175

Zhuravleva TB, Kokhanovsky AA (2011) Influence of surface roughness on the reflective properties of snow. J Quant Spectrosc Radiat Transfer 112(8):1353–1368

Spectral Reflectance of Soil

Jerzy Cierniewski

1 Introduction

The reflectance spectra of soils in the visible and near infrared (VNIR) and shortwave infrared (SWIR) contain information on mineral groups, organic matter and soil texture. The spectra collected by airborne hyperspectral scanners were corrected for the influence of the atmosphere and the non-Lambertian behavior of soil surfaces whose real roughness formed is by agricultural tools; this made it possible to determine the content of soil organic carbon, calcium carbonate and textural clay with an accuracy expressed by a coefficient of determination (R^2) of 60–75% (Schwanghart and Jarmer 2011; Gomez et al. 2008a, b; Selige et al. 2006). The same soils' spectra obtained in the laboratory on air-dried, smooth soil samples using a spectroradiometer with a contact-probe sensor show a higher overall reflectance (mainly due to the effect of their roughness having been minimized) and this allowed the contents of the above mentioned components to be determined with an R^2 of about 10–20% higher. Quantitative soil properties in both of the above situations were obtained by multivariate linear regression analysis of the reflectance spectra with respect to such chemical and physical data, using, for example, partial-square regression, spline signal regression and support vector machine (Selige et al. 2006; Stevens et al. 2010). As part of a research project aimed at quantifying the annual dynamics of shortwave radiation reflected from arable lands on a global scale taking into account their roughness, the soil spectra obtained in the laboratory were also used to predict the variation of the diurnal broadband blue-sky albedo of soils (α) in clear-sky conditions. This variation allows for more precise calculation of the average diurnal α values of soils and, on this basis, also of their average α values over longer periods of several days, a month, a season or a year. It can be useful for modeling the climate on a global

J. Cierniewski (✉)
Department of Soil Science and Remote Sensing of Soils, Adam Mickiewicz University, Bogumiła Krygowskiego 10, 61-680 Poznań, Poland
e-mail: ciernje@amu.edu.pl

A. Kokhanovsky (ed.), *Springer Series in Light Scattering*,
Springer Series in Light Scattering,
https://doi.org/10.1007/978-3-030-38696-2_4

scale, which in light of the statement of Sellers et al. (1995) require α values with an accuracy of better than $\pm 2\%$. The laboratory reflectance spectra of geo-referenced topsoil samples, which are stored together with the chemical and physical attributes of these samples in soil spectral libraries (SSL) on national and continental scales, were used in this project. The example of this project shows that information coded in the soil spectra collected in the Global SSL not only "can be associated to land cover and its global geographic distribution, which may acting as a surrogate for global climate variability" (Viscarra Rossel et al. 2016), but can also be directly used for quantification dynamics of shortwave radiation reflected from one of the Earth's land surface components—bare arable lands. Although bare arable soils occur in relatively short periods on these conventionally cultivated lands (Cierniewski et al. 2018c; Cierniewski and Ceglarek 2018), due to their large total surface they can significantly affect the energy transfer between them and the atmosphere (expressed by their α), depending on their spectral reflectance properties, including their roughness formed by agricultural tools. Smoothing rough arable lands that have previously been deeply plowed with, for example, a smoothing harrow increases their α, resulting in a lower amount of shortwave radiation being absorbed by their surface layer. Those surfaces emit less long-wave radiation, leading to a reduction in their temperature, which can modify the Earth's climate (Desjardins 2009; Farmer and Cook 2013).

2 Reflectance Spectra

The proportions between amounts of radiant flux of electromagnetic radiation in specific wavelength (λ) incident on an object that are reflected from its surface (ρ_λ), absorbed by the surface and transmitted by the surface vary relative to the wavelength in a way that is particular to each of Earth object (Lillesand et al. 2004). The reflectance has a directional character and as such depends on the direction of surface illumination and of its observation by a sensor. The reflectance spectrum of an object in the optical domain (0.35–2.5 μm) is the collection of the $\rho_{\Omega,\lambda}$ values describing the ratio of the reflected radiant flux from its surface (L) into solid angle (Ω) to the radiant flux incident on its surface (E) into Ω for a specific λ (Palmer 1982):

$$\rho_{\Omega,\lambda} = \frac{L_{\Omega,\lambda}}{E_{\Omega,\lambda}} \tag{1}$$

Each object has a specific spectrum, which can distinguish the object from others, identify it and determine its properties. The higher the number of spectral bands and the narrower the ranges that are taken into account, the more accurate this identification will be. The significant technological advances that have occurred over the past 30 years in the construction of spectrometers and radiometers working in visible and near infrared (VNIR: 0.35–1.1 μm) and shortwave infrared (SWIR: 1.1–2.5 μm),

enabled the development of remote sensing methods for identification of Earth's objects and their properties using the spectra measured by these instruments.

2.1 Factors Affecting Soil Reflectance Spectra

Soil is the medium for plant growth, and a habitat for many insects and other organisms. It provides us food, fuel and fibers. It acts as a system for carbon storage and filtration of surface water and regulates the emissions of greenhouse gases, and thus affects the Earth's climate. Soil degradation and increasing urbanization disturb the agro-ecological balance (Viscarra Rossel et al. 2016). In order to manage soils in a sustainable manner (UN Sustainable Development Knowledge 2015) and thus preserve them for future generations, it is important to have a deeper understanding of the processes and function they perform. As a natural body of Earth material, soil consists of minerals and organic substances. These constituents have an influence on the soil's spectral reflectance pattern. Nearly all optical shortwave radiation incident on soil surfaces is either absorbed or reflected, and only a little part is transmitted. Strong absorption of the radiation is mainly caused by the solid phase of soils consisting of opaque mineral particles covered with soil organic matter (SOM) in its various stages of decomposition, as well as the soil liquid phase that consists of water and dissolved ions in various amounts. Soil pores not filled with the liquid phase are filled with soil air, constituting the gas phase, i.e. soil air of similar composition to that of atmospheric air but with varying concentrations of oxygen and carbon dioxide depending on the biochemical activity at the root zone. The pores filled with soil air can act as specific optical fibers, having their origin on soil surfaces and ending at a depth of 1–10 mm (Mikhajlova and Orlov 1986). Shortwave radiation is mostly absorbed in such a thin layer of soils, usually in the horizon of SOM accumulation.

The shape and overall level of soil spectra in the solar reflective radiation range is the result of the physical process of light scattering in the VNIR region, depending on the size of soil particles, and their shape and distribution in soil materials (Ben-Dor et al. 1999). Soil components such as iron oxides or organic matter determine the slope of the spectra at the wide wavelength range lower than 1.0 μm. The chemical processes associated with the absorption of light by soil components are revealed in the narrow ranges of the SWIR region of soil spectra. The presence of water molecules contained in the soil in the form of hygroscopic water is clearly visible around 1.4 and 1.9 m, and for example, clay minerals and calcite around 2.2 and 2.3 m (Ben-Dor 2002).

2.1.1 Soil Organic Matter

The spectral reflectance level of soils in the VNIR region decreases as their SOM content increases. If the SOM content is lower than 2%, a small increase results in a strong decrease in the reflectance of such soils (Al-Abbas et al. 1972; Fedchenko

1982). More and more fragments of usually bright mineral particles in such soils are covered by dark SOM; hence the reflectance of these soils is less and less similar to that of their parent material. A growth in the amount of SOM from 2 to 4% results in a further increase in the surrounding of the parent material particles by SOM. If the last of these particles are completely surrounded by SOM, and this occurs at an SOM content of about 5–6%, a further increase in its content very slightly decreases the reflectance of soils. The minimum of this reflectance is observed for soils with SOM content of about 10–12% (Swain 1978; Latz et al. 1984). Vinogradov (1981), Orlov and Sukhanova (1983) and Baumgardner et al. (1986) described the relation between the SOM of soils and their reflectance in the VNIR using an exponential function. The reflectance level of bare soils also depends on the quality of SOM, resulting from the proportion of the two main fractions of humus compounds, humic and fulvic acids (Obukhov and Orlov 1964; Białousz and Girard 1978; Bauer et al. 1981; Vinogradov 1981; Mikhajlova and Orlov 1986). Humic acids absorb more visible radiation than do fulvic acids: the latter reflect from 1.5 to 2 times more radiation in the range of blue waves and from 3 to 4 times more in the range of green and red waves (Obukhov and Orlov 1964). The differentiation in the reflectance of these fractions of humus compounds is explained by the difference in their molecular structure. Molecules of humic acids have a spatially more complicated structure than fulvic acids, so that they are optically denser and thus absorb more shortwave radiation (Kononova 1956, 1963). The higher the proportion of humic acid to fulvic acid in SOM (expressing the SOM quality) and the higher the SOM content, the lower the spectral reflectance of bare soils. The relations between the spectral reflectance of soils and their SOM content were determined on the basis of soil samples of various SOM qualities. Thus, the wavelength ranges for which these relations were closest were found in different wavelength ranges. Al-Abbas et al. (1972), Vinogradov (1981), Mikhajlova and Orlov (1986) defined this range for orange and red waves (between 0.6 and 0.75 μm), while Henderson et al. (1992) defined it for the wider range from blue to red wavelength (0.43–0.69 μm). Close relations between SOM and soil reflectance level was also found in the SWIR region. Dalal and Henry (1986) determined it between 1.7 and 2.05 μm, and Morra et al. (1991) between 1.73 and 2.43 μm.

Another course of the relationship between the spectral reflectance level of soils and their SOM content has been observed in peat soils with different levels of organic matter decomposition. With the progress of decomposition of peat materials from fibric through hemic to sapric, a pronounced decrease in the spectral reflectance of such materials was observed (Baumgardner et al. 1986). Mikhajlova and Orlov (1986) reported a minimum of this reflectance for peat material with an SOM content of 60–80%, which corresponds to sapric material.

2.1.2 Iron Oxides

Among the iron compounds, iron oxides in the form of non-aluminosilicate minerals such as goethite and hematite, as well as poorly crystallized and amorphous forms that surround the mineral soil particles, have the strongest effects on spectral reflectance

of soils in VNIR (Karmanova 1981; Mikhajlova and Orlov 1986). The content of iron oxides in soils reduces their spectral reflectance mainly in the yellow and red waves range from 0.52 to 0.62 μm (Obukhov and Orlov 1964; Krishna Murti and Satyanarayana 1971; White 1971). However, this reduction has a selective character (Cipra et al. 1971). It is observed in the yellow waves for strongly hydrated oxides, among which goethite dominates, and in the red waves for less hydrated oxides, where hematite has the largest share. Other absorption bands occur around 0.7 and 0.87 μm (Stoner et al. 1980), and there is additional absorption in the middle infrared wavelengths (Hunt and Salisbury 1970; Mulders 1987).

2.1.3 Calcium Carbonates

Clark et al. (2003) found that calcium carbonate ($CaCO_3$) most strongly absorbs shortwave radiation at wavelengths of 2.21 and 2.35 μm (2008). $CaCO_3$ differently affects the spectral reflectance of soils in laboratory conditions than in field conditions. In the laboratory, the higher the $CaCO_3$ content in the soil samples with disturbed aggregates, the higher their reflectance (Lagacherie et al. 2008). Cierniewski and Kuśnierek (2010) reported that this relationship in laboratory conditions is almost directly proportional in the spectral region above 1 μm. Bialousz (1978) found that the relation in field conditions becomes directly proportional if the $CaCO_3$ content is higher than 20%. If the content is lower than this value, this relation is inversely proportional and indirect. This author explained that $CaCO_3$ is conducive to the formation of soil aggregates. These aggregates increase the surface roughness of the soil, thus reducing of soil reflectance despite the high spectral reflectance of this substance. $CaCO_3$ promotes the formation and accumulation of permanent connections between humus compounds, iron oxides and clay fraction.

2.1.4 Moisture of Soil Surface

Generally, a decrease in the moisture of the soil surface causes an increase in the overall level of their reflectance spectra (Idso et al. 1975; Baumgardner et al. 1986; Music and Pelletier 1986). The darkening of a moist soil in VNIR, where water absorption is minimal, is mainly due to the increased probability of the light scattering forward, deeper into the depth, which increases multiply scattering, increases the probability of absorption and decreases the reflectance of the soil (Twomey et al. 1986; Lekner and Dorf 1988; Philpot 2010). The tendency for increased scattering of such soil is further increased by the presence of air–water boundaries in the soil pore spaces. If the soil water content (SWC) decreases from the state of full saturation (FS) to the state of field capacity (FC), the level of soil spectral reflectance does not change (Tolchelnikov 1974; Vinogradov 1983) or decreases slightly (Cierniewski 1988, 1993). The increase in the level of the soil spectra is most pronounced if SWC decreases from FC to the state of maximum hygroscopicity (MH) (Bowers and Smith 1972; Tolchelnikov 1974). If SWC continues to decline to the absolutely

dry state (AD), the reflectance level increases slightly (Vinogradov 1976, 1983) or is unnoticeable (Tolchelnikov 1974; Cierniewski 1985, 1988; Cierniewski et al. 1988). The aforementioned soil moisture states, depending on their texture, correspond to different SMC values expressed as the proportion mass of water to mass of dry soil. For example, sand and clay get MH at SMC of about 1%, and 6%, respectively (Vinogradov 1983). However, the same materials obtain FC at SMC of around 5 and 22%. Such different courses of dependence between the spectral reflectance level of soils and their moisture in these three SWC ranges are explained by the dissimilarity between the water forms that occur there. In the SWC range from FS to FC there is gravitational water. In the range from FC to MH there is capillary water in fine pores, and in the range from MH to AD there is only chemically combined water, water in the form of vapor and hygroscopic water.

Moisture of the soil surface is the most dynamically changing factor determining the overall level of reflectance spectra of soils in field conditions (Milfred and Kiefer 2010). It is observed especially in the summer when the surface layer of soils quickly achieves a state of air-dried soil (Andronikov 1979). The increase in soil spectral reflectance is more noticeable for light-colored soils with a lower SOM content than for dark-colored soils with a higher such content (Białousz and Girard 1978; Evans 1979; Mikhajlova and Orlov 1986).

2.1.5 Soil Surface Roughness

Soil Surface Roughness in the Laboratory

The property of soils that is unchanged over time is the particle size of their mineral fraction. Investigation of the effect of this size on the level of spectral reflectance in the laboratory on samples with natural structure having been destroyed shows clearly that their reflectance decreases with the increase in the diameter of soil particles. Bowers and Hanks (1965) analyzed fractionated soil material with particle diameters from 0.02 mm to 2.65 mm and determined that this relationship could be described using the exponential function, which represents the sharpest decline in the reflectance in the range of the diameters from 0.02 mm to 0.4 mm. This regularity was also confirmed by studies conducted by Piech and Walker (1974), who analyzed it in the VNIR range on seven loamy soil fractions separated on sieves with mesh diameters from 0.62 to 2 mm. Gerbermann and Weber (1979), investigated the spectral reflectance of soil samples prepared as mixtures from the clay and sandy fractions, and found that it is directly proportional to the content of their sandy fraction.

Soil samples with destroyed aggregates sieved through a 2-mm sieve are prepared to measure soil reflectance spectra in laboratory conditions in order to determine the soil texture and the content of such soil components as soil organic carbon (SOC), iron oxides and calcium carbonates (Ben-Dor et al. 2015). In order to minimize the impact of surface irregularities in these samples, receptors recording diffusion reflectance are most commonly used, such as for example a High-Brite Muglight receptor. Quantitative data on the properties of the investigated soils are extracted

from their reflectance spectra using multivariate linear regression analysis of the spectra against the chemical and physical data through several methods, such as for example partial squares regression (PLSR), spline signal regressions (PSR) and support vector machine (SVM) (Selige et al. 2006; Stevens et al. 2013). The proportion of sand and clay and the content of $CaCO_3$ and SOC can be determined in this way with the correctness expressed by coefficient of determination (R^2) reaching 0.85–0.95 (Selige et al. 2006; Gomez et al. 2008a, b; Schwanghart and Jarmer 2011). The correctness of these components in field conditions with a much greater natural roughness using airborne hyperspectral scanners shows a lower correctness of about 20% due to the influence of the atmosphere and the position of the sun and the direction of observation of studied soil surfaces.

Soil Surface Roughness in the Field

The influence of soil particle size on the spectral reflectance level of soils is usually almost imperceptible compared to the considerably stronger impact of their surface roughness caused by the existence of soil aggregates, clods and stones of various sizes under field conditions. In general, in these conditions, coarse texture (sandy) soils form smaller aggregates than those developed from fine texture (for example loamy), which form larger aggregates and clods. Smaller soil aggregates have a more compact, spherical shape than larger ones that have an irregular shape and are often cracked. As a result, the surfaces of these first soils appear smoother, with a higher spectral reflectance than especially those with a high density of large clods, which causes a clearly lower soil reflectance (Orlov 1969; Orlov et al. 1976). Thus, the particle size in the field indirectly and inversely affects the level of soil reflectance in contrast to its effect in the laboratory. Al-Abbas et al. (1972) noticed that a higher proportion of the sandy fraction significantly reduces the roughness of the soil surfaces, which increases their spectral reflectance. The reflectance from the soil surfaces with aggregates with a diameter from 2 to 10 mm is almost invariable, while with smaller aggregates it shows a clear differentiation (Orlov 1969; Curran et al. 1990). Generally, as the size of soil aggregates decreases, there is a clear increase in its spectral reflectance (Bowers and Hanks 1965; Piech and Walker 1974). The decrease in spectral reflectance of soils as a result of their roughness increasing is explained by the phenomenon of multiple reflections of the radiation that illuminates them. Most of the direct sunlight falling on the soil surfaces is absorbed by them and reflected from them, scattering it in all directions. This scattered radiation falling on them again is absorbed once again and reflected from them in a much smaller proportion than the original incident (Linden 1979; Cruse et al. 1980). The deep spaces between the large aggregates and clods are mostly "traps" for the sunlight directly falling on them (Orlov 1966; Coulson and Reynolds 1971).

Girard and Białousz (1989) presented the results of field studies showing how the effect of SOM content and soil surface moisture on the spectral reflectance of soils as their roughness changed. Epiphanio and Vitorello (1984) state that the correct

separation of dried soil surfaces from wet ones using remote sensing depends largely on their roughness.

Measurements of Soil Surface Roughness

In some climatic zones, the rain strongly changes the physical properties of the soil surface, reducing the infiltration of rainwater and increases the effects of water erosion through increased surface runoff (Collinet and Valentin 1985; Morgan 1985; Ghishi and Morgan 1986; Römkens and Wang 1986; Zobeck and Onstad 1987; Moreno et al. 2008; Thomsen et al. 2015). To effectively counteract these processes, the interdependencies between the state of roughness of selected soil surfaces and the possibilities of absorbing and storing water in their surface levels were investigated (Mitchell and Jones 1978; Onstad 1984). Decades ago, the variation of soil surface shape was measured along a direction using a profile meter with needles or a chain set (King 1979; Boiffin and Monnier 1986; Gilley and Kottwitz 1995). Desmet et al. (1988) suggested recording irregularities in soil surfaces using a paint sprayer on a vertically positioned piece of paper. Huang et al. (1988) and Bertuzzi et al. (1990) propose replacing or supplementing these simple tools with laser scanners constructed by them to measure the height of soil aggregates and clods in two-dimensional space along a single line with resolution of approximately 1 mm. Cierniewski et al. (2004), investigating the bidirectional reflectance of stony, sandy and silty surfaces in the Negev desert, measured their irregularities in three-dimensional space in a 1×1 cm grid with resolution of 1.5 mm using a laser device constructed at Ben Gurion University of the Negev. Some years later, Cierniewski et al. (2013) used a laser scanner camera, which measured the shape of desert and cultivated soil surfaces also in three-dimensional space with horizontal and vertical spatial resolutions of 1 mm. Currently, roughness of a soil surface is often examined by close-range digital photogrammetry using its images in three-dimensional space taken from over a dozen directions by a hand-held digital camera moving around the surface (Rieke-Zapp and Nearing 2005; Peter Heng et al. 2010; Gilliot et al. 2017). This photogrammetric method makes it possible to register soil surface irregularities with a similar spatial resolution of approximately 1 mm. Data obtained in this way allow digital elevation models (DEM) of the examined surfaces to be created, and these then become the basis for calculating soil surface roughness indices.

Soil Roughness Indices

The roughness of soil surfaces was described using quantitative indices. The standard deviation of the surface height (*HSD*) is the most common index for describing the soil surface roughness (Ulaby et al. 1982). The turtle index, representing the ratio of the actual length of the soil surface profile to the projected horizontal length of this profile, was proposed by Boiffin (1986). Later, Taconet and Ciarletti (2007) modified this index to describe the irregularities of a surface in two-dimensional space (T_{3D}),

defining it as the ratio of the real surface area within its basic DEM unit to its flat horizontal area. Other indices used to describe changes in soil surfaces roughness due to rainfall or sprinkler irrigation (caused by the breakdown of soil aggregates and the formation of soil crust) use a semivariogram analysis (Rosa et al. 2012; Croft et al. 2013; Vermang et al. 2013).

2.2 Bidirectional Reflectance Quantities

It is not only differences in the scale of soil surface irregularities between those measured under field conditions (with naturally formed aggregates and clods) and samples of the same soils measured in the laboratory (where the influence of their roughness is minimized by the destruction of soil aggregates) that cause distinctly different values of their bidirectional reflectance. Surfaces in the field are illuminated by direct sunbeams and diffuse light from the sky, while the samples in the laboratory are usually illuminated by a single collimated light source. The latter case can be described using the bidirectional reflectance distribution function (BRDF) that expressed the scattering of parallel (collimated) beams incident on a surface from one direction in the hemisphere into another direction in the hemisphere (Schaepman-Strub et al. 2006):

$$\mathrm{BRDF} = f_r(\Omega_i, \Omega_r) = f_r(\theta_i, \phi_i; \theta_r, \phi_r) = \frac{dL_r(\theta_i, \phi_i; \theta_r, \phi_r)}{dE_i(\theta_i, \phi_i)} \left[\mathrm{sr}^{-1}\right] \quad (2)$$

However, it should be remembered that, in proposing BRDF as the fundamental quantity characterizing the reflecting properties of a surface, Nicodemus et al. (1977) formulated that the surface must be horizontally homogeneous, and that a uniform irradiance flux coming from a single direction covers a large enough area that radiation leaving the surface does not vary with horizontal position. Therefore, BRDF defines only the point of such a surface (Di Girolamo 2003) (Fig. 1). The two radiation environments are defined by two angles, depending on the direction of incidence of radiation of the light source Ω_i and the direction of reflected radiance coming to the sensor Ω_r. One of them refers to the zenith and symbolizes the light source zenith angle as θ_i and the view zenith angle as θ_r. The second is horizontal, and is called the azimuth angle, and indicates the light source azimuth angle as ϕ_i and the view azimuth angle as ϕ_r. By measuring the reflectance (ρ) of a sample surface such as, for example, soil, illuminating it with parallel beams from a single light source (as is usual in laboratory measurements), the bidirectional reflectance factor (BRF) is used. This unitless quantity is defined as the ratio of the reflected radiant flux (Φ_r) from the surface area dA to the radiant flux (Φ_r^{id}) reflected from an ideal lossless and diffuse (Lambertian) standard panel, illuminated and observed at the same directions as the sample surface being tested (Schaepman-Strub et al. 2006):

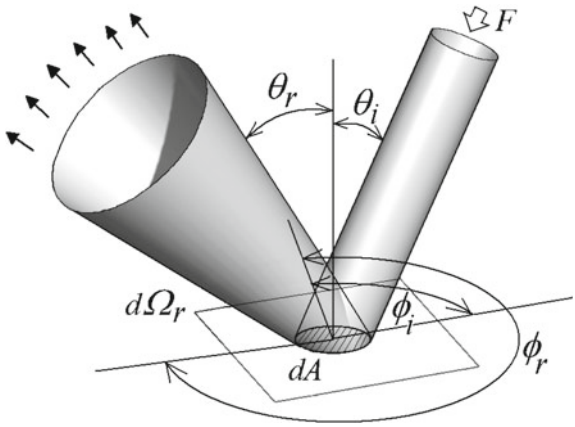

Fig. 1 Geometric relations between radiation of a collimated beam of flux density F incident at the zenith angle θ_i and the azimuth angle ϕ_i on an area dA, which is then scattered into solid angle dΩ_r in the direction, described by the zenith θ_r and azimuth ϕ_r angles

$$\mathrm{BRF} = \rho(\theta_i, \phi_i; \theta_r, \phi_r) = \frac{d\Phi_r(\theta_i, \phi_i; \theta_r, \phi_r)}{d\Phi_r^{id}(\theta_i, \phi_i)}. \tag{3}$$

Because there is no angular dependence on the ideal Lambertian surface (Palmer 1982; Jackson et al. 1987), the θ_r, ϕ_r angles for Φ_r^{id} were omitted. For surfaces illuminated by irradiation from the entire hemisphere, as in field conditions, Schaepman-Strub et al. (2006) suggest the use of hemispherical reflectance (HDRF):

$$\mathrm{HDRF} = \rho(\theta_i, \phi_i; 2\pi; \theta_r, \phi_r) = \frac{d\Phi_r(\theta_i, \phi_i; 2\pi; \theta_r, \phi_r)}{d\Phi_r^{id}(\theta_i, \phi_i; 2\pi)} \tag{4}$$

to describe the reflectance of such a surface. This quantity is similarly defined as the BRF, but it takes into account both the direct and the diffuse irradiance.

2.3 *Non-lambertian Behavior of Soil Surfaces*

Bare soil surfaces, like many natural and man-made objects, reveal their non-Lambertian behavior. Such surfaces show variation in their radiance due to the direction of their irradiation and the direction along which the reflected radiation is viewed by ground, air-borne and satellite sensors. Irregularities in soil surfaces caused by soil mineral particles, and especially by large aggregates and clods formed with the high participation of SOM, produce shadow areas where the solar beams do not directly reach the surface (Graetz and Gentle 1982; Norman et al. 1985; Otterman 1985; Cooper and Smith 1985; Jon Ranson et al. 1985; Cierniewski 1987, 1989; Milton and Webb 1987; Huete 1987; Pinty et al. 1989; Deering et al. 1989, 1990; Jackson et al. 1990; Irons et al. 1992) The spaces between the smaller aggregates are usually less intensely shaded than those between larger aggregates. Radiation leaving the shaded areas is many orders of magnitude smaller than radiation reflected

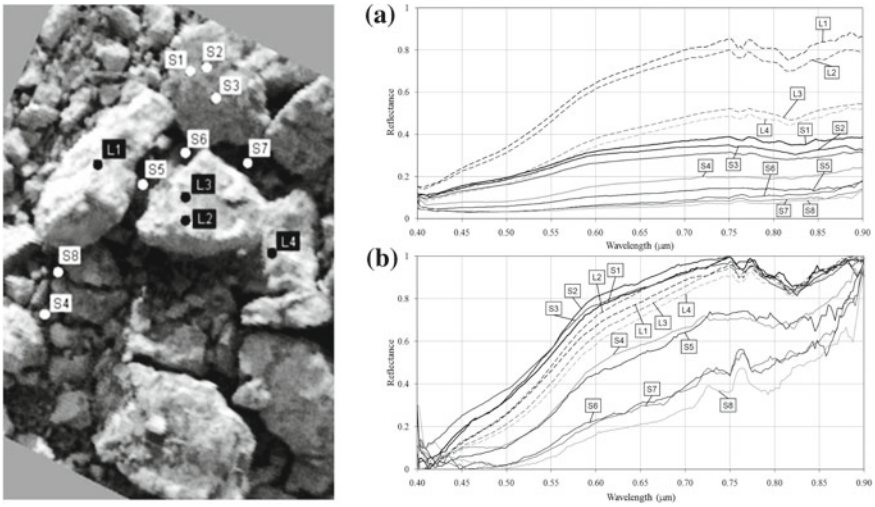

Fig. 2 Reflectance spectra of a soil surface at its sunlit [L] and shaded [S] fragments (**a**) and the same spectra normalized by the min–max method (**b**)

from sunlit soil fragments. A hyperspectral camera suspended over the ploughed soil observed this phenomenon (Cierniewski et al. 2010). Spectra related to the shaded soil fragments (marked 'S') show lower reflectance than the sunlit fragments (marked 'L'). The shape of these two categories of these spectra became similar to each other, if they were normalized by the min–max method (Fig. 2). Bare arable lands with dominant diffuse features usually appear brightest from the direction that gives the lowest proportion of shaded fragments. Those soil surfaces show a strong backscattering character with a reflectance peak towards the Sun position (the 'hot spot' direction) and decreasing reflectance in the direction away from the peak (Brennan and Bandeen 1970; Kriebel 1976; Milton and Webb 1987; Foody 1988). The non-Lambertian behavior of two soils, one uncultivated and smooth and another cultivated and moderate rough, is presented in Fig. 3 Irregularities in both their surfaces are spread non-directionally. Their reflectance distributions normalized to the nadir viewing in all possible directions for the chosen wavelength of 0.85 μm under clear-sky conditions at various solar zenith (θ_s) and azimuth (ϕ_s) angles were predicted by a hemispherical-directional reflectance model (Cierniewski et al. 2004). The larger the soil surface irregularities and the higher the θ_s, the higher the variation of the soil directional reflectance. The variation is greatest along the solar principal plane. Croft et al. (2012) presented a similar non-Lambertian behavior of soils in relation to almost the same roughness ranges as in the above examples, but their samples were subjected to artificial rainfall in laboratory conditions. Wang et al. (2012) showed examples of soil surface anisotropy analyzed in the laboratory on samples with undamaged surface structure as in field conditions in a much wider range of roughness. The result of a laboratory measurement experiment simulating

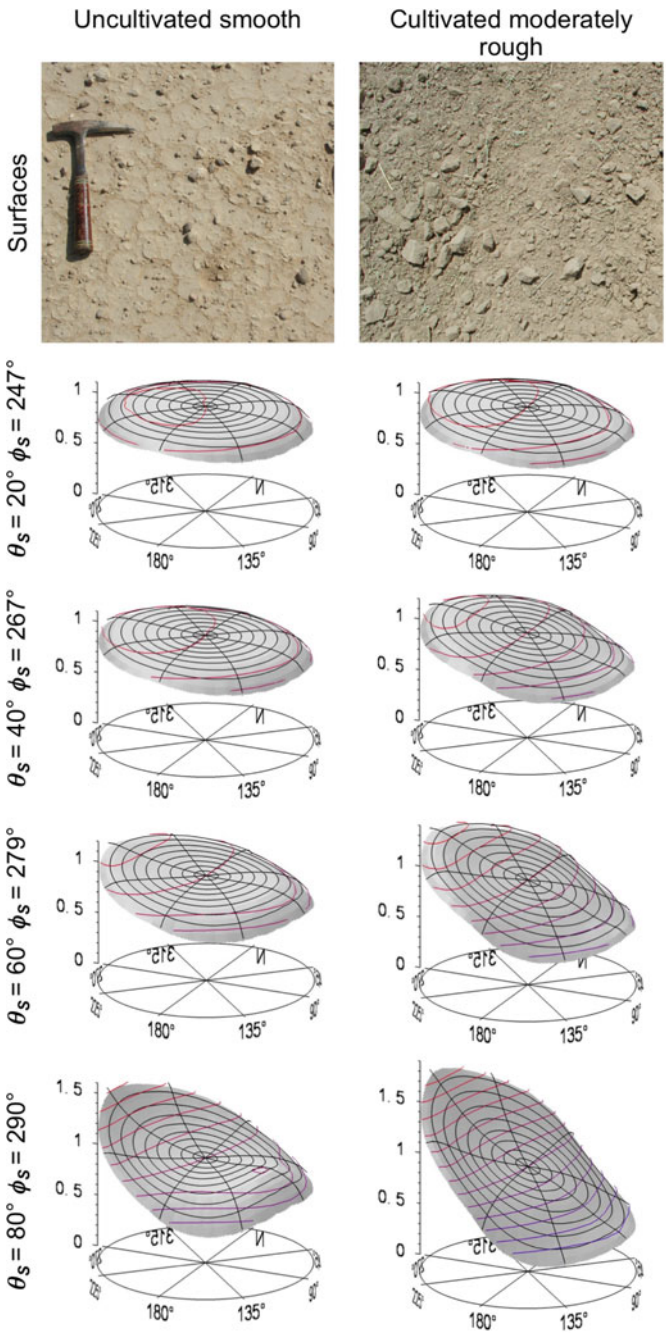

Fig. 3 Normalized directional reflectance distributions of soils for chosen wavelength of 0.85 μm under clear sky conditions at various solar zenith (θ_s) and azimuth (ϕ_s) angle predicted by a hemispherical-directional reflectance model (Cierniewski et al. 2004)

the behavior of the spectral reflectance of sandy soils with furrows treated by a harrow or a seeder show that a directional microrelief of those surfaces can additionally complicate the reflectance of those soils (Cierniewski and Guliński 2009). The level of the spectrum of such surfaces viewed at the nadir and illuminated by sunbeams coming along the furrows can be about 5–10% higher than for the same surface illuminated by sunbeams perpendicular to the furrows.

Spectral reflectance of desert soil surfaces can have both a backscattering and forward scattering character (Deering et al. 1990). The surfaces show maximum reflectance in the extreme forward scatter direction near the horizon if they are relatively smooth with strong specular features. Shoshany (1993) reported that different types of stony pavements and rocky surfaces investigated in various lighting conditions revealed an anisotropic reflection with a clear backscattering component.

Soil surface roughness is a particularly dynamically changing factor within arable land formed by agricultural tools. They create a specific micro-relief configuration, sometimes with a clear directional distribution of furrows. Cierniewski (2001) analyzed spectral reflectance of soils developed from loamy materials formed by a plow and different harrows (spike-tooth, rotary and disc). Matthias et al. (2000) found that the albedo of dried soil surfaces developed from fine sandy loam treated by a plow, a disk and a seedbed decreased its albedo by about 27%, 18% and 8%, respectively, in relation to the albedo of its smoothed surface. Surfaces of soils with a low cation-exchange capacity have an unstable structure, contributing easily to their roughness being reduced by rain or ling irrigation, even in the case of their early tillage (Pratt 1961). Potter et al. (1987) reported that, conversely, the reflectance of plowed sandy soils increased by about 25% after rain and subsequent drying of their surface.

Obukhov and Orlov (1964) reported that dried unstructured soil surfaces reflected 15–20% more solar reflective radiation than similar dried soils with a well-developed structure. Van der Heide and Koolen (1980) noticed that changes in the surface structure of such soils do not modify the shape of their reflectance spectra. The reflectance level of plowed soils clearly increases after rainfall and the drying of their surface (Cierniewski 1999, 2001). Cipra et al. (1971), in analyzing spectral reflectance of *Alfisols* developed from fine loamy textures, found that wetting and drying of those soils created a thin crust on their surfaces, significantly smoothing them and increasing their reflectance. Kondratyev and Fedchenko (1980) reported that the crust created on soils with aggregates and clods with a diameter of 5 to 15 cm increased the reflectance of the soils by 10–15%. The authors also explained that the lightening of surface of these soils could be the effect of washing out the clay and humus fractions from the surface of the aggregates and clods, which could significantly increase the share of bright quartz particles on their surface. Other authors—Ben-Dor et al. (2003), Eshel et al. (2004), Goldshleger et al. (2004), and de Jong et al. (2011)—estimated that this increase in the spectral reflectance caused by the crust ranged from 10 to 40%.

2.4 Measurements of Soil Bidirectional Reflectance

Most of the goniometric devices for testing the bidirectional reflectance of soil samples in the laboratory are equipped with one collimated halogen light source that can change its zenith angle being invariably aimed at the center of these samples and not changing distance from them. Devices of a similar purpose working in field conditions use the natural illumination of direct sunbeams (reaching the tested surfaces under the changing zenith and azimuth angles) with different share of the diffuse skylight. In both cases, the bidirectional reflectance of soil surfaces, such as others, is measured from many directions, and expressed using BRF or HDRF, where measurements of the radiant flux reaching the tested surfaces are determined by measuring the radiant flux reflected from the ideal lossless Lambertian panel. The majority of goniometric devices operating in the laboratory are those whose sensors are always aimed at the center of the samples and the panel, regardless of the direction of their observation. Examples of such devices are: a compact laboratory spectrogoniometer (CLabSpeG) developed at the Katholieke Universiteit Leuven, Belgium (Biliouris et al. 2007), University of Lethbridge Goniometer System 2.0 (ULGS-2.0) constructed in Canada (Coburn and Peddle 2006), Goniometer of Rochester Institute of Technology (GRIT) made in USA (Bachmann et al. 2017; Harms et al. 2017). Some of the goniometers specially designated for field measurements observe the tested surfaces in the same way as those mentioned above. The most well-known are the Field Goniometer System (FIGOS) developed by the Remote Sensing Laboratory of the University of Zurich and the Sandmeier Field Goniometer (SFG) by the NASA Ames Research Center (Sandmeier 2000). NASA has also constructed a field Portable Apparatus for Rapid Acquisition of Land and Atmosphere (PARABOLA) that observes studied surfaces differently (Deering et al. 1990). The goniometer's boom-mounted rotating head, which changes the view zenith angle (θ_v) of the surfaces along a direction expressed by the azimuth angle, aims its sensor at other adjacent surface fragments.

2.5 Modeling of Soil Bidirectional Reflectance

The influence of soil surface roughness, illumination and viewing conditions of soils on the soil bidirectional reflectance pattern that are discussed on the above examples is better understood if it is modeled mathematically.

Walthall et al. (1985) express bidirectional reflectance of a bare soil surface as a three-parameter function of view direction to the solar direction. These parameters of an empirical character are not explicitly related to soil surface properties.

The model by Norman et al. (1985) was worked out on the assumption that the shadowing of larger soil particles or aggregates, which are simulated by cuboids, has a greater influence on the soil reflectance distribution than the scattering properties of basic soil particles of silt and clay. The cuboids and horizontal surface on which

they lie have Lambertian scattering properties. Soil surfaces simulated in this way show a backscatter regime. The bidirectional reflectance distribution function for the simulated soil surface shows a clear backscatter regime. It manifests higher reflectance if the Sun is at the 'back' of the sensor. The reflectance peak increases with the increase in the solar zenith angle. For nearly smooth soils, the distribution is almost quite 'flat', and the soil surface behaves as a perfect Lambertian reflector.

The Monte Carlo soil surface reflectance model created by Cooper and Smith (1985) was developed to study the effects that bare soil surface irregularities much larger than the wavelength of incident radiation had on soil reflectance. It assumes that the soil is a perfectly diffuse reflector at a microscopic level. So, the probability that a photon will be scattered at a given angle only depends on the orientation of the soil surface irregularities. They are described by two microrelief forms whose heights vary periodically with cosine in one or two directions for 'row' and 'clump' soils respectively. The diffuse character of the model causes rough soil surfaces to show the backscattering regime.

Models Hapke's (1981, 1984, 1986, 1993, 2002, 2008) models developed for interpreting the reflectance properties of planetary surfaces produce bidirectional signatures similar to those of a medium composed of particles characterized by a single scattering albedo and a phase function. The models take into account a parameter that depends upon regolith porosity and particle size distribution. They are applicable to macroscopically rough surfaces, i.e., those with irregularities at scales larger than the wavelength of the radiation interacting with them. The macroscopic roughness causes shadowing at large phase angles and interparticle shadow hiding at small phase angles. The models have input parameters related to a single scattering coefficient, hot spot phenomenon, and the scattering phase function. Jacquemoud et al. (1992) added a specular contribution and separated those parameters that depend on the wavelength (the single-scattering albedo) from those that were not wavelength-dependent.

The model by Irons et al. (1992) describes the soil surface as being made of uniform opaque spheres regularly spaced on a horizontal surface. The geometry of the structure (roughness) is defined as the area of a single sphere in the horizontal projection in a circle of unit area of the horizontal surface. Both direct and isotropically diffuse light illuminate the soil surface. The spheres and background are Lambertian. Soil reflectance is expressed as a function of the horizontal area shaded by the spheres, the sunlit fraction, and the proportion of diffuse illumination, which depends on wavelength. These terms depend on the solar and view directions and on the characteristics of the simulated surface. The model uses an empirical function describing the relation between the fractional area of the plane in which shadow area overlaps the area obscured from view by the sphere, and the angle between the directions of solar illumination and viewing. The model was fit to soil bidirectional reflectance data for bare loamy soil of varying surface roughness.

Otterman's model (Otterman 1981, 1985; Deering et al. 1990) treats bare soil as thin vertical cylinders of variable heights with facet-reflectance and transmittance located randomly on a horizontal plane with Lambertian reflectance. The architecture of the soil protrusions is described by a parameter, which is the sum of the

height times diameter of these cylinders per unit horizontal area. The model assumes that the facet-reflectance largely controls the backscatter while facet transmittance is responsible for determining forward scattering. This was the first model simulating both backscattering and forward scattering. It predicted a clear forward scattering character of reflectance for a surface with nearly pure gypsum crystals of high transmittance.

The first model of Cierniewski (1987, 1988, 1989) describes soil aggregates by regularly spaced equal-sized opaque spheres of a given diameter. This first model takes into account a freely sloping plane at a specified angle on which the aggregates are lying. The roughness of the geometrical structure is expressed as the proportion of the areas of aggregates (in the plane parallel to the soil sloping plane) in a given unit area of soil surface. Sunbeams illuminate this structure at θ_s. A part of it is shaded. It is assumed that the reflectance level of a rough soil surface in relation to a soil that is the same but for having a smooth surface decreases with an increase in the share of shaded fragments of this structure according to the exponential function. Successively improved versions of the model simulate soil aggregates by spheroids with a specific ratio of their vertical to horizontal radii (Cierniewski and Verbrugghe 1993), the structure of simulated soil surface being illuminated both by direct sunbeams and by diffuse light expressed by a specified factor (Cierniewski and Verbrugghe 1994), and the radiation leaving the fragments directly illuminated by sunbeams having a specular-diffuse character (Cierniewski et al. 1996; Cierniewski and Verbrugghe 1997a, 1997b). This reflected radiance in these versions of the geometrical model is expressed by the relative reflectance factor defined as the proportion of the total radiance viewed from the off-nadir direction to the radiance viewed from the nadir.

The next model also predicts the distributions of shortwave radiation reflected from soil surfaces, the irregularities of which are caused by soil particles and aggregates dispersed regularly in all directions (Cierniewski 1999). The model calculates the directional reflectance of such soil surfaces along the solar principal plane (SPP), where the variation of the reflectance in θ_v is the highest. Using the fact that the reflectance variation at the orthogonal plane (OP) is minimum near zero, the model also approximates this reflectance distribution at any measure plane outside of the SPP, interpolating it between the SPP and OP planes. Soil aggregates in this model have a more realistic shape than the model discussed above. The soil surface is simulated by equal-sized opaque spheroids with horizontal (a) and vertical (b) radii lying on a freely sloping plane at angle β (Fig. 4). They are absorbed into the ground of the slope plane, having their tops at height t above the ground. The spheroids are regularly arranged on the slope plane so their centers are in a net of squares of the side d. The model was tested in outdoor conditions on soil samples formed by: dune sand (with particles of 0.05 cm diameter) and loamy sand to sandy loam materials with aggregates of diameter from 1.5 cm to 4 cm, as well as stones with diameter of 5–6 cm and loamy clods simulating their general shape. Figure 5 shows photography of the dune sand, and its synthetic surface that enables the generation of its normalized reflectance (NR) distribution along the SPP for 0.65 μm. The distribution reveals the impact of specular features of the sand in the forward scattering direction particularly at high θ_s angles. The next figures show analogous data for cultivated rough

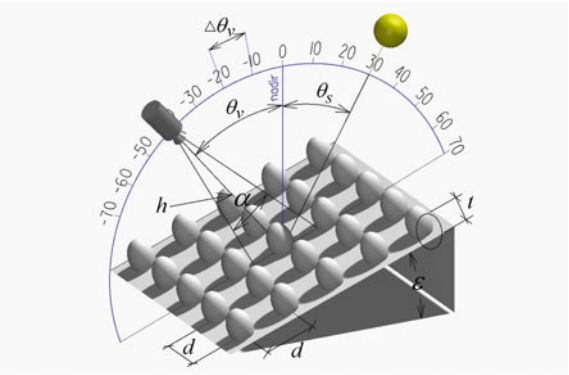

Fig. 4 Illumination and viewing geometry of the soil surface representation in the model of Cierniewski (1999)

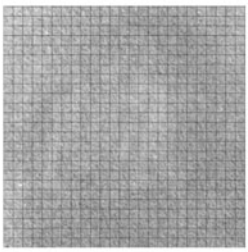

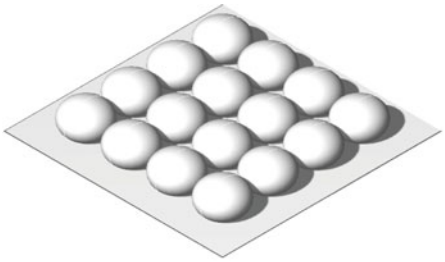

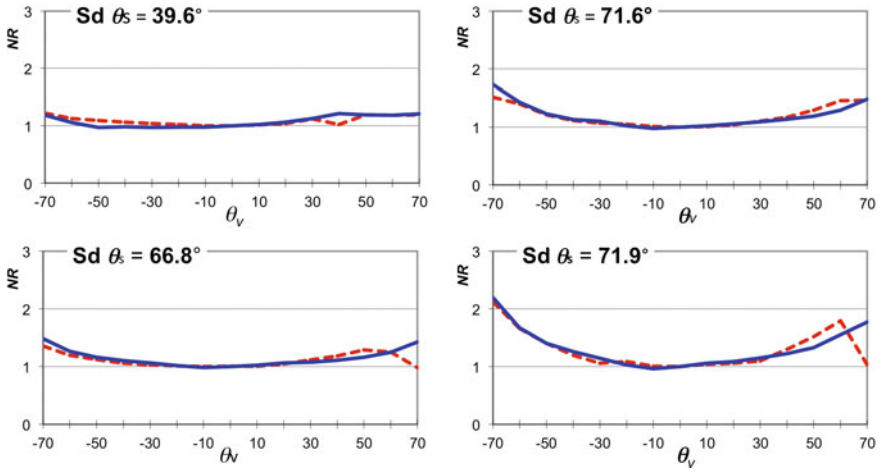

Fig. 5 Photography of the dune sand (Sd), its synthetic surface and normalized reflectance (*NR*), measured (red dashed line) and predicted (blue solid line) along the solar principal plane illuminated at different solar zenith angles (θ_s) for the wavelengths of 0.65 μm

and smoothed soils developed from loamy sand (Fig. 6) and sandy loam (Fig. 7). The higher the θ_s, the greater the *NR* variation of these surfaces along the SPP, regardless

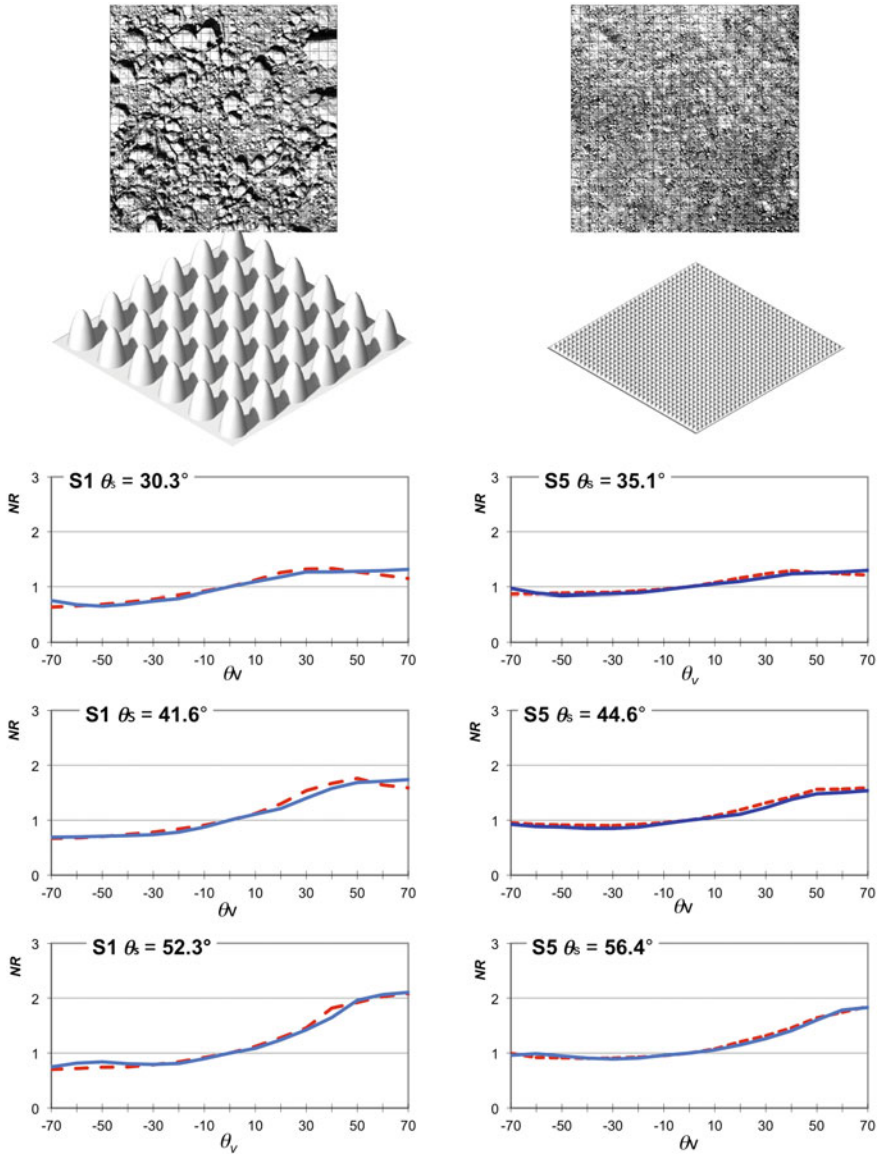

Fig. 6 Photographs of cultivated rough (S1) and smoothed (S5) loamy sands and their synthetic surfaces with their normalized reflectance (*NR*), measured (red dashed line) and predicted (blue solid line) along the solar principal plane illuminated at different solar zenith angles (θ_s) for the wavelengths of 0.65 μm

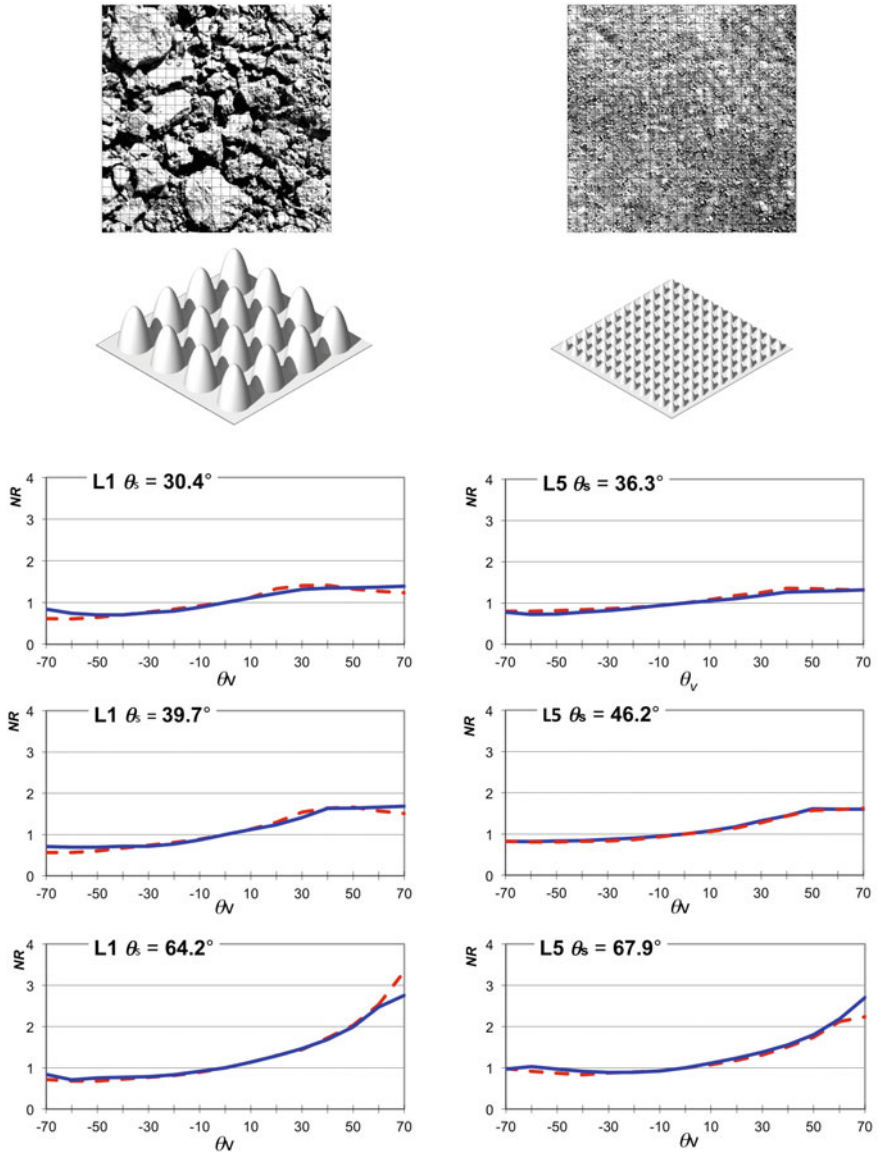

Fig. 7 Photographs of cultivated rough (L1) and smoothed (L5) sandy loams and their synthetic surfaces with their normalized reflectance (*NR*), measured (red dashed line) and predicted (blue solid line) along the solar principal plane illuminated at different solar zenith angles (θ_s) for the wavelengths of 0.65 μm

of their roughness. The effect of the specular component in the *NR* data of both cultivated soils is almost invisible. In contrast, the increasing variation of their *NR* along the SPP as a result of their smoothing is clearly visible. The data presented in Fig. 8, which show surfaces of a similar general shape made of stones and loamy clods, prove that their spectral reflectance is determined more by this shape than by their texture.

The model published two years later (Cierniewski 2001) describes the spectral reflectance from soil surfaces subjected to directional agricultural treatments (Fig. 9). Simulated soil aggregates are spread on such surfaces in a row, creating furrows of a kind along the direction of these treatments. The spheroids are situated on planes described by the vertical angle β_{d} related to the plane of the horizon and the horizontal angle $\phi_{\mathrm{d\text{-}s}}$ determined in relation to the direction of the sun's rays. The slope represents two parallel planes: the lower one, which is defined by the lines running in the bottom of the hollows between the furrows, and the above-laid plane constituting the base of the ridge of these furrows. The horizontal angle between these lines and the direction of sunlight $\phi_{\mathrm{c-s}}$ determines the direction of the agricultural treatments. The spheroids are pressed into the upper plane, so that their tops protrude above it to a height of t_{r}. With regard to this, t_{p} specifies the irregularities of the simulated surface in the direction perpendicular to the direction of furrows. Irregularities in this surface along the direction of furrows are smaller, which is expressed by the smaller height of protruding parts of the ellipsoid t_{r} above the plane of the furrow ridge. The geometrical structures of the two above models are illuminated by direct sunbeams coming to it at θ_s, and by diffuse light described by the factor f_{di}. The f_{di} approximates a reflectance effect from soil surfaces illuminated only by the diffuse light component. The factor is defined as the part of the direct solar beams' radiation. A sensor is suspended over the simulated soil surfaces. It observes them along the SPP at zenith angles θ_v, at the $\Delta\theta_v$ increments in forward scattering and backscattering directions, which are described by negative and positive values of the θ_v, respectively. The sensor aims at the same point of the analyzed surfaces, being at distance h from it. The sensor field of view defines the angle ξ.

The reflectance of the main solar plane is calculated twice, assuming that the SPP runs along the furrows and perpendicular to this direction. The amounts of energy reaching the directly illuminated fragments of the simulated soil structure are calculated using the factor $Ei^{\downarrow}_{vfa}$:

$$Ei^{\downarrow}_{vfa} = \cos\theta_s \cos\beta_{fa} + \sin\beta_{fa} + \sin\theta_s + \cos(\phi_d - \phi_s), \tag{5}$$

where: β_{fa} is the angle of inclination of the elementary fragment of this structure, and ϕ_d and ϕ_s are the horizontal angles describing, respectively, the location of the soil slope and the Sun. The factor $Ei^{\downarrow}_{vfa}$ expresses the cosine of the angle of incidence of the rays' γ relative to the normal one for the elementary fragment *fa*. Radiation falling on the fragment is reflected in both a diffusive and a specular way, and its vectors in the two-dimensional plane create the shape of a circle and an elongated ellipse, respectively (Fig. 10). The length of the vectors of the specular component, treated as non-polarized light, is calculated using the Fresnel equations:

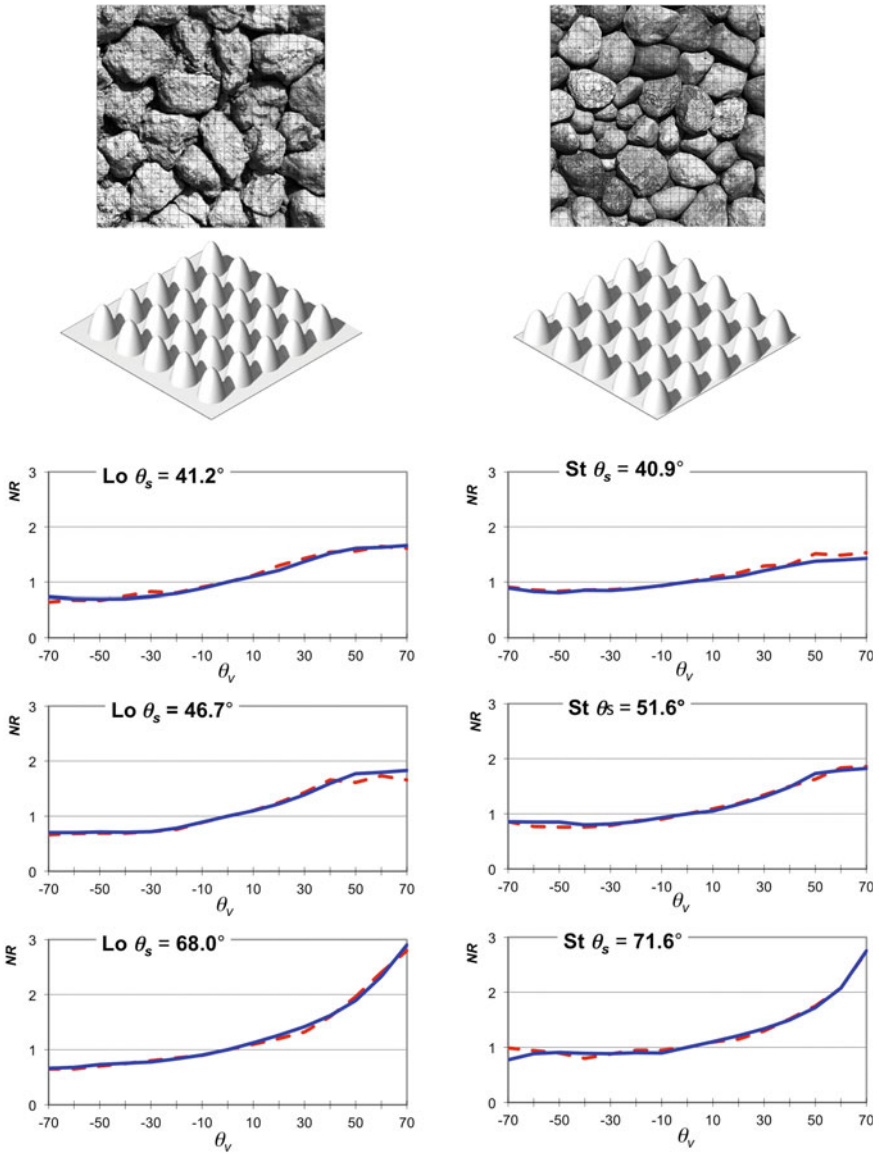

Fig. 8 Surfaces of a similar general shape made of loamy clods (Lo) and stones (St) and their synthetic surfaces with their normalized reflectance (*NR*), measured (red dashed line) and predicted (blue solid line) along the solar principal plane illuminated at different solar zenith angles (θ_s) for the wavelengths of 0.65 μm

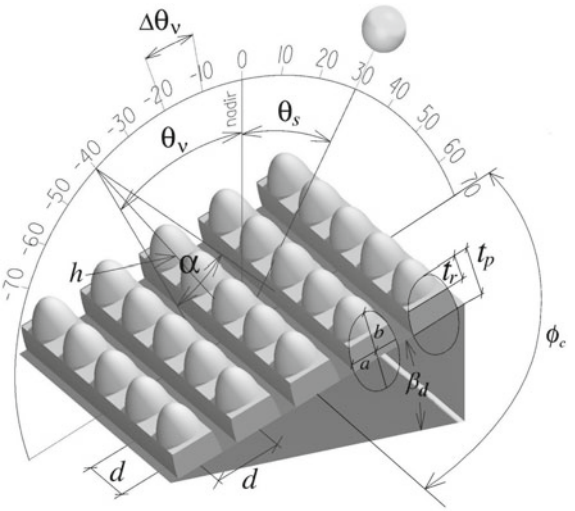

Fig. 9 Illumination and viewing geometry of a simulated soil surface with furrowed microrelief in the model of Cierniewski (2001)

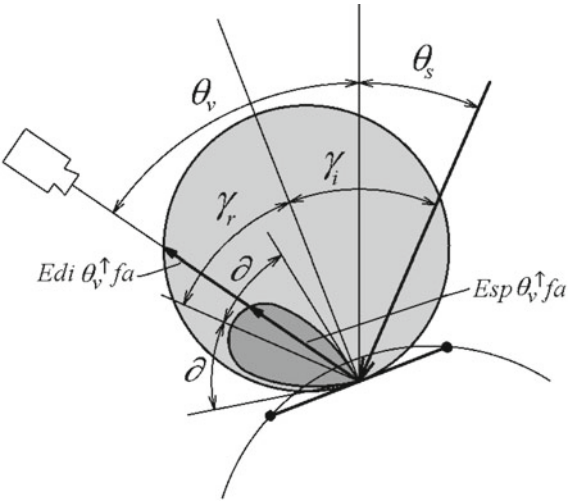

Fig. 10 Distribution of the energy leaving a facet of the simulated soil surface in the specular Esp_{vfa} and the diffuse way Edi_{vfa}

$$Esp^{\uparrow}_{\theta_v fa} = Ei^{\downarrow}_{vfa} Fp_{(\gamma_i)} \quad Fp_{(\gamma_i)} = \frac{r_{\perp}^2 + r_{=}^2}{2} \tag{6}$$

where $r_{\perp}$ and $r_{=}$ are respectively the perpendicular and parallel Fresnel reflection coefficient. The vector of reflected energy $Esp^{\uparrow}_{\theta_v fa}$ is oriented in such a way that the angle of incidence γ_{i} equals the reflection angle γ_{r}. Specular effects are perceived by the sensor only to a limited extent defined by the angle 2∂ around the direction γ_{r}. The length of the $Esp^{\uparrow}_{\theta_v fa}$ vector at a distance $\pm\partial$ from γ_{r} falls linearly to zero.

The length of the vector $Ei^{\downarrow}_{vfa}$ completes the diffuse component $Edi^{\uparrow}_{\theta v\ fa}$ is defined as:

$$Edi^{\uparrow}_{\theta_v fa} = \left(1 - Fp_{(\gamma_i)}\right) Ei^{\downarrow}_{vfa} \cos\theta_v. \tag{7}$$

Finally, the total radiation $Eis^{\uparrow}_{\theta_v fa}$ reaching to the sensor at θ_v, reflected from the directly illuminated elemental part *fa* of simulated soils is calculated by dividing $Ei^{\downarrow}_{vfa}$ by $\cos\theta_v$. The amount of diffuse sky-light ($E^{\downarrow}_{sk\,\mathrm{fa}}$) that reaches to the sunlit and shaded fragments of the simulated soil surface is reduced by the presence of neighbouring ellipsoids (Fig. 11):

$$Esk^{\downarrow}_{fa} = f_{di}\frac{\delta}{180^{\circ}}, \tag{8}$$

where δ is a plane angle in the analyzed plane limiting the sky light input to the analyzed fragment of the simulated soil surface. The luminance factor of the simulated soil surface, including sunlit and shaded elementary fragments, viewed at θ_v along a specific profile is defined as:

$$L^{\uparrow}_{\theta_v} pr = \sum_{i=1}^{j}\left[\left(Eis^{\uparrow}_{\theta_v fa} + Esk^{\downarrow}_{fa_{(i)}}\right)\xi i_{fa_{(i)}}\right] + \sum_{i=1}^{j}\left(Esk^{\downarrow}_{fa} + \xi s_{fa_{(i)}}\right), \tag{9}$$

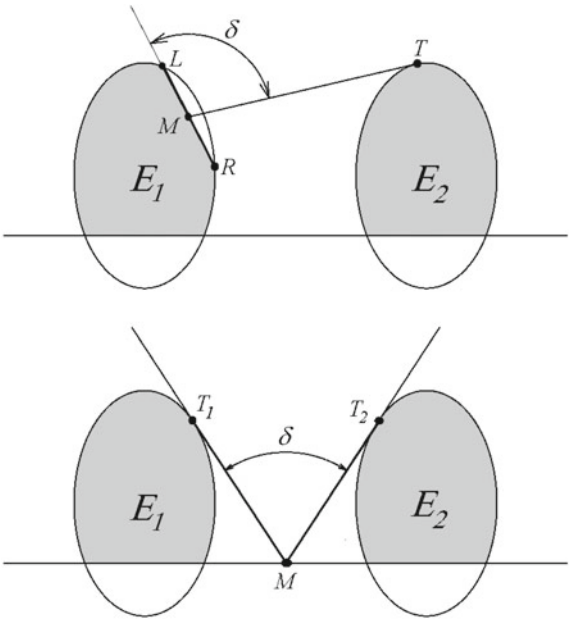

Fig. 11 Limitation in illumination by skylight of the facet segment (*LR*) on the ellipse E_1 ark and the slope plane between ellipses E_1 and E_2, expressed by the angle δ. *M* is the middle point of the segments *LR* and T_1 and T_2 are the tangent points of the angle δ sides to the adjoining ellipses

where i is the fragment of the analyzed structure, ξ_{ifa} and ξ_{sfa} are respectively elementary viewing angles of illuminated and shaded fragments. Luminance received by the sensor from its entire field of view, $L^{\uparrow}_{\theta_v FOV}$ is the average value of luminance from individual cross-sections $L^{\uparrow}_{\theta_v} pr$ and the space between ellipsoids $L^{\uparrow}_{\theta_v} sm$, weighted according to the equation:

$$L^{\uparrow}_{\theta_v FOV} = L^{\uparrow}_{\theta_v} pr_{(1)} \frac{a}{2\mathrm{m}-1} + \sum_{i=2}^{m} L^{\uparrow}_{\theta_v} pr_{(i)} \frac{a}{m-0.5} + L^{\uparrow}_{\theta_v} sm\left(\frac{d}{2} - a\right), \quad (10)$$

where m is the number o the profiles. If modeling directional spectral reflection is to refer to a situation where the main solar plane does not run either parallel or perpendicular to the direction of fissures, then the luminance $L^{\uparrow}_{(\phi_r,\theta_v)FOV}$ of the illuminated surface is calculated according to the equation:

$$L^{\uparrow}_{(\phi_r,\theta_v)FOV} = Lr^{\uparrow}_{\theta_v, FOV}\left(1 - \frac{\psi}{90^{\circ}}\right) + Lp^{\uparrow}_{\theta_v, FOV}\frac{\psi}{90^{\circ}}, \quad (11)$$

where $Lr^{\uparrow}_{\theta_v, FOV}$ and $Lp^{\uparrow}_{\theta_v, FOV}$ are luminance values calculated respectively along and perpendicular to the direction of furrows, and ψ is the horizontal angle measured between the SPP and the direction of the furrow course. Finally, reflectance from the rough surface of the soil along the SPP is described by means of the normalized indicator $NR_{(\theta_v=\mathrm{SPP},\theta_v)}$, defined as the ratio of total luminance $L^{\uparrow}_{\theta_v FOV}$ of the soil surface measured obliquely to its luminance measured in the nadir direction. Assuming that the NR index in the OP for each angle θ_v takes the value 1, the distribution of $NR_{(\phi_v,\theta_v)}$ in the function of the azimuthal angle ϕ_v between SPP and OP has a straight line and its value for any oriented plane can be defined as:

$$NR_{(\phi_v,\theta_v)} = NR_{(\theta_v=\mathrm{SPP},\theta_v)} + \left(1 - \frac{\phi_v}{90^{\circ}}\right) + \frac{\phi_v}{90^{\circ}}, \quad (12)$$

where ϕ_v is the relative horizontal angle determining the angular distance from the SPP. The model was tested in field conditions on plots with loamy sand and sandy loam soils freshly formed by a plow and harrows and then modified by rainfalls in Poland (Cierniewski 2001), on fields in France with a loamy soil that had been plowed, harrowed and rolled, and prepared for sowing colza (Cierniewski et al. 2002). The irregularities in the plots tested in Poland were recorded on stereoscopic images. The maximum difference in height of the presented fragment of the freshly plowed field was 35 cm (Fig. 12) and, after a total of 92 mm rainfall, was only 26 cm (Fig. 13). The larger height differences were observed transversely, rather than along the furrows. The standard deviation of the height crosswise and parallel to the furrows were 4.6 and 4.4 cm, respectively, in the first case, and 1.9 and 1.5 cm in the second. In the freshly plowed surface, larger aggregates that had previously had sharp edges changed their shape to round after this rainfall, and the smaller soil aggregates were mostly eliminated. The height difference in the same surface developed from the

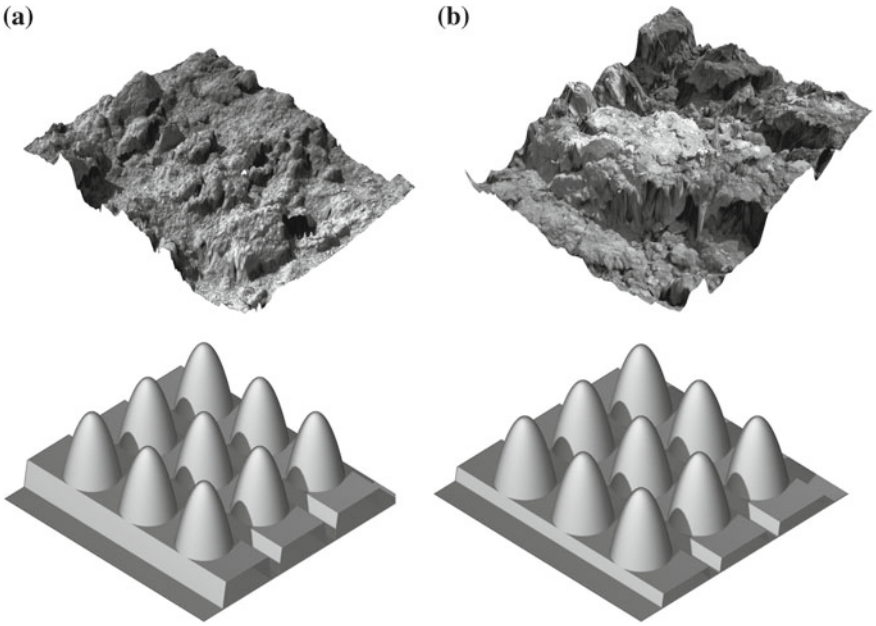

Fig. 12 View of soil surfaces 50 × 50 cm size, freshly plowed (**a**) and after 92 mm (**b**) with their diagrams of digital elevation model in the form of a triangular net covered by the real image and below their virtual equivalents

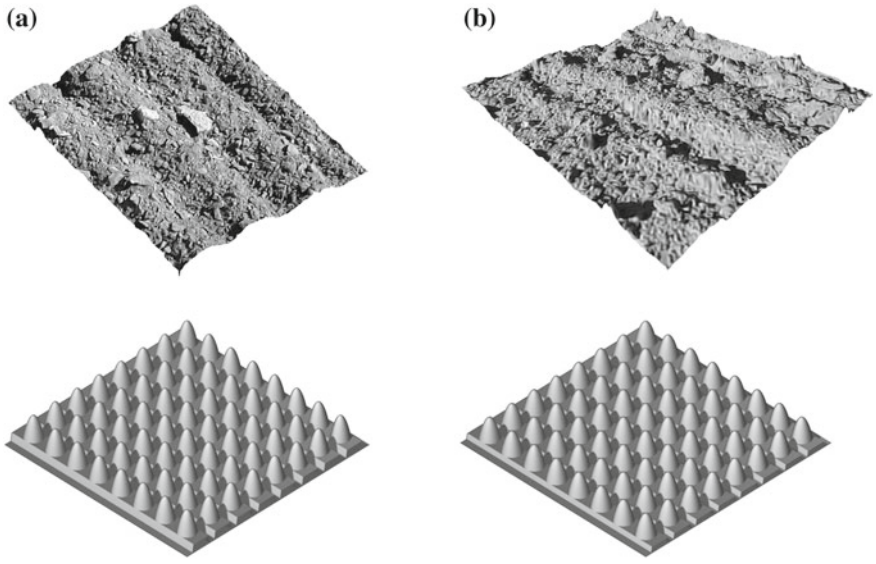

Fig. 13 View of soil surfaces 50 × 50 cm size, freshly harrowed and after 25 mm rain **a** with their diagrams of digital elevation model in the form of a triangular net covered by the real image and below their virtual equivalents

loamy sand reached 10 cm, and 7 cm after a total of 25 mm rainfall. The standard deviation of its height both crosswise and parallel to its furrows was 1.3 cm for the freshly formed surface and 1.2 cm after the rainfall. The measured and predicted data using this model show that the *NR* variation of these plots increased along the SPP due not only to the increase in θ_s, but also to the increase in ϕ_{c-s} angle describing the illumination of their furrows. This variation is the greater, the deeper their furrows. This is particularly evident in the case of plots illuminated at almost the same θ_s angles. Thus, the impact of this ϕ_{c-s} is more pronounced for freshly plowed plot (Fig. 14) than harrowed plots (Fig. 15) and it becomes less visible due to the gradual smoothing of the surface of larger soil aggregates by rain (Fig. 16) and complete elimination of smaller aggregates (Fig. 17). It should also be noted that the measured reflectance of the soils (in the diagrams expressed by its *BRF* and marked with the '*R*' symbol) are clearly lower for plots with greater roughness, i.e. with deeper freshly formed furrows than those with lower roughness, especially with those modified after rainfall. The reflectance of soils used to test this model was measured in Poland by a six-channel field luminancemeter in the following wavelength bands: 0.45, 0.55, 0.65, 0.85 and 1.65 μm, and in France by three channel bands: 0.55, 0.65, 0.85 μm. The soil reflectance data collected in France show that rougher soil surfaces do not always have a higher variation in *NR* distribution along the SPP than do smooth

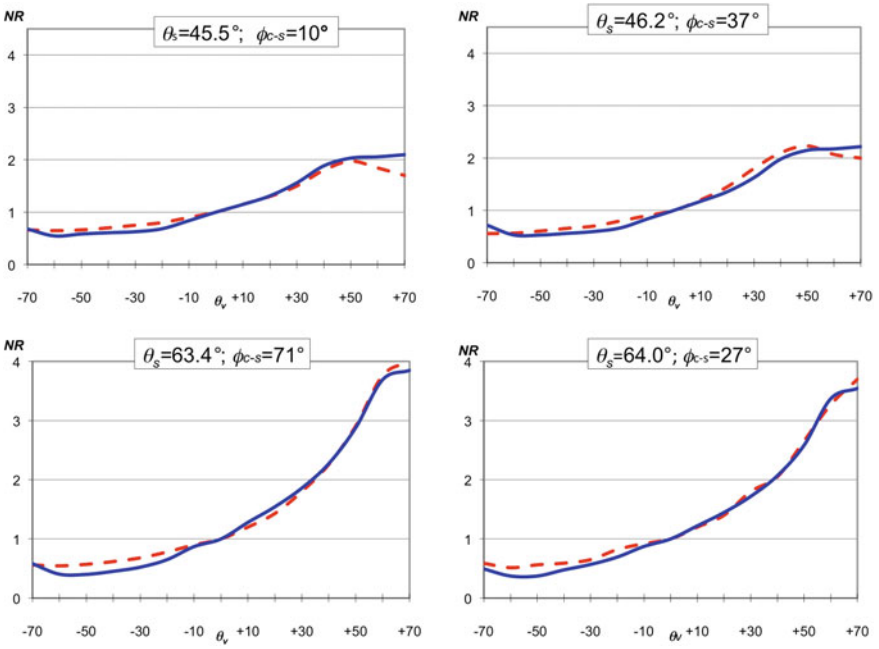

Fig. 14 Normalized reflectance (*NR*), measured (red dashed line) and predicted (blue solid line) of freshly plowed plots illuminated at almost the same θ_s and different ϕ_{c-s} angles along the solar principal plane, for the wavelengths of 0.85 μm

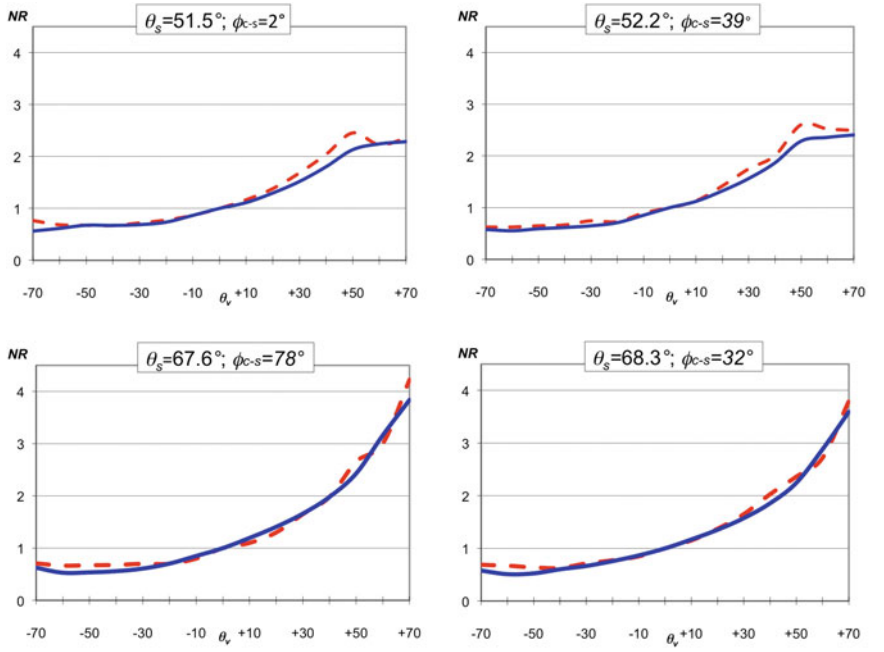

Fig. 15 Normalized reflectance (*NR*), measured (red dashed line) and predicted (blue solid line) of freshly harrowed plots illuminated at almost the same θ_s and different ϕ_{c-s} angles along the solar principal plane, for the wavelengths of 0.85 μm

ones. Soil surfaces smoothed by rolling can display an *NR* distribution quite similar to those of more rough surfaces that have been ploughed or furrowed by a seeder (Fig. 18).

The distribution of hemispherical-directional reflectance of cultivated and uncultivated soils was also modeled by surfaces with irregularities constructed by a set of n points k_i of coordinates (x_i, y_i, z_i) of $i = 1, \ldots, n$ and the positive real numbers r_1, r_2, r_3, …, r_n related to them, respectively (Cierniewski et al. 2004). A pair (k_i, r_i) is interpreted as the opaque sphere of radius r_i with the center k_i. The shape of those surfaces is the solution of the following equation:

$$\sum_{i=1}^{n}\left(2d_i^3 - 3d_i^2 + 1\right) - \frac{1}{2} = 0 \quad d_i = \frac{\min\left(r_i\sqrt{(x - x_i)^2 + (y - y_i)^2 + +(z - z_i)^2}\right)}{r_i} \tag{13}$$

The centers k_i are dispersed regularly in a net of squares with a side of $1/\sqrt{n}$ in the perpendicular projection to the XY plane. The height z_i of the k_i center is expressed by the equation:

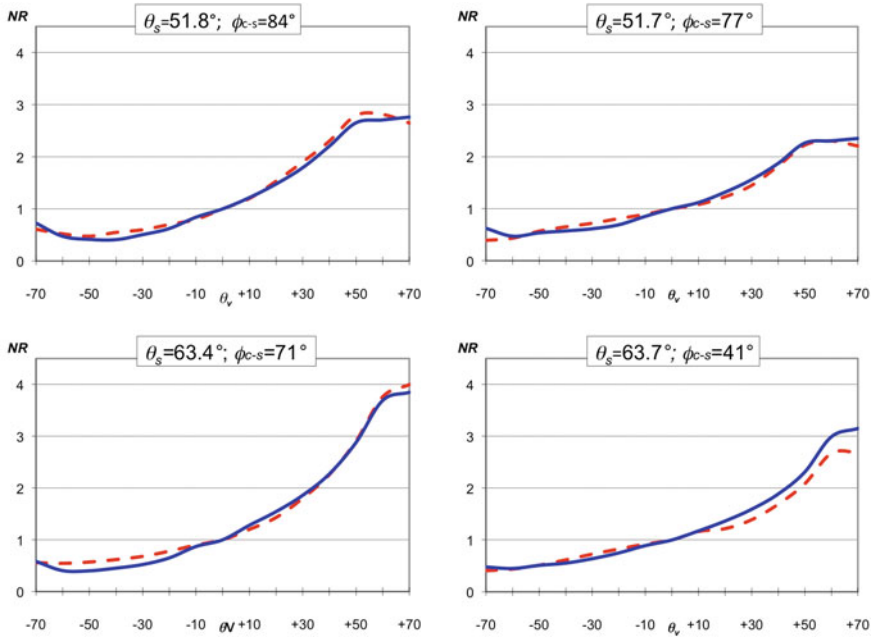

Fig. 16 Normalized reflectance (*NR*), measured (red dashed line) and predicted (blue solid line) of plowed plots after smoothing them by 92 mm rainfall illuminated at almost the same θ_s and different ϕ_{c-s} angles along the solar principal plane, for the wavelengths of 0.85 μm

$$z_i = a \cdot |\sin(\pi \cdot x_i)| \cdot \langle 1 - b \cdot [1 - |\sin(\pi \cdot y_i)|] \rangle + c \cdot f_{dis}(i), \tag{14}$$

where a expresses the amplitude of sin function along the x-axis, and b along the y-axis to a. The final z_i position of ith sphere is an effect of a disturbance approximated by the sequence $f_{dis}(i) \in [0.1)$ with uniform distribution. The c describes the maximum deviation from the z_i value, as determined by only these a and b parameters (Fig. 19). The shape of the surface is characterized by the directivity factor D_R, expressing the differences between the maximum and the minimum deviations of its height, calculated along all possible directions (Fig. 20).

The surface is illuminated by a hemisphere light source created by m point sources $s_1, s_2, s_3, \ldots, s_m$ of the intensity $e_1, e_2, e_3, \ldots, e_m$, respectively, equally spread on the hemisphere. It is assumed that in outdoor conditions the ratio of the direct solar irradiance to the global irradiance δ in clear-sky conditions changes with the sun's position $S = [\theta_s, \phi_s]$ and normal optical thickness τ (Fraser 1975). The distribution of the hemispherical light for the non-absorbing Rayleigh atmosphere dependent on θ_s and τ attributed to the wavelength λ is shown in Fig. 21. The intensity of the direct solar irradiance at point S reaches 1 independently of both τ and λ. The light is scattered from the simulated surface in accordance the quasi-Lambertian function (Fig. 22). The shape of the surface R described by Eq. 13 allows definition of the vectors of the normal to any points on this surface. These vectors make it possible

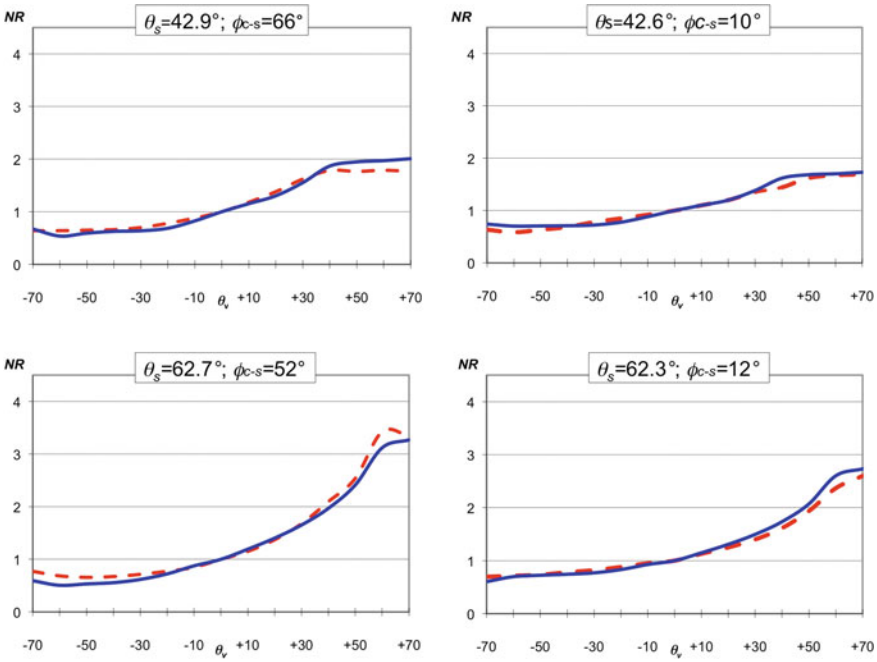

Fig. 17 Normalized reflectance (*NR*), measured (red dashed line) and predicted (blue solid line) of harrowed plots and after smoothing them 25 mmm rainfall illuminated at almost the same θ_s and different ϕ_{c-s} angles along the solar principal plane, for the wavelengths of 0.85 μm

to determine the amount and direction of the light reflected from the total area of the surface. The light $e_{f_R}\left(i, \vec{k}\right)$ reflected only once from the fragment f_R along the direction $\vec{k}$, due to illumination from the unblocked point source, s_i, is calculated as:

$$e_{f_R}\left(i, \vec{k}\right) = e_i \cdot f\left(\vec{s_i}, \vec{n}, \vec{k}\right), \tag{15}$$

where $\vec{n}$ is the normal to the fragment f_R. A cloud of all the vectors $\vec{k} \cdot e_{f_R}\left(i, \vec{k}\right)$ characterizes the scattering properties of the R surface in its f_R fragment. The total light energy $E\left(f_R, \vec{v}, H\right)$ reflected from the f_R fragment in the direction $\vec{k}$ and viewed along a direction $\vec{v} = [\theta_v, \phi_v]$ is expressed by:

$$E\left(f_R, \vec{v}, H\right) = \sum_{i=1}^{m} e_{f_R}\left(i, \vec{v}\right), \tag{16}$$

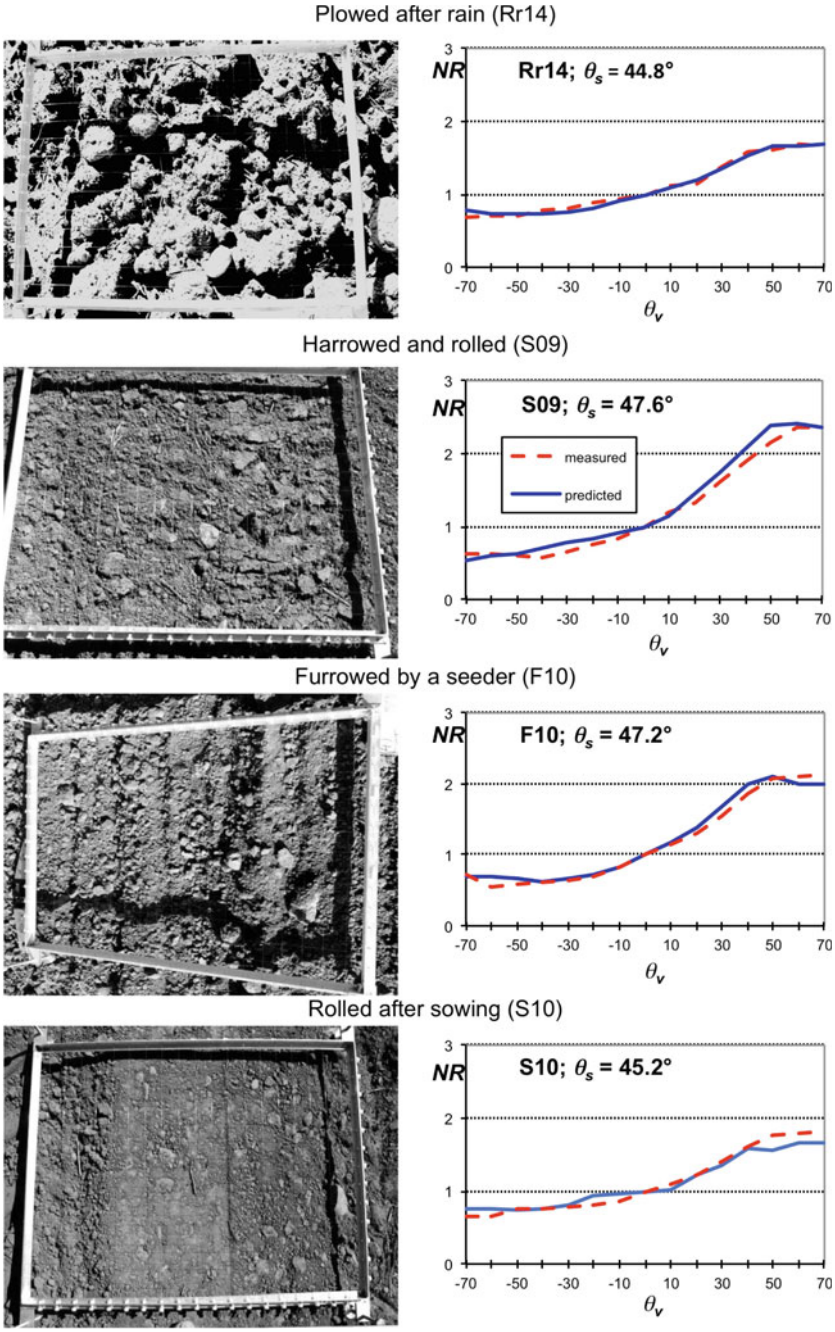

Fig. 18 View of selected soil surfaces treated by different agricultural tools with the normalized reflectance (*NR*) of the surfaces, measured and predicted by the model of Cierniewski (2001), illuminated at similar θ_s angles along the solar principal plane for the wavelength of 0.65 μm

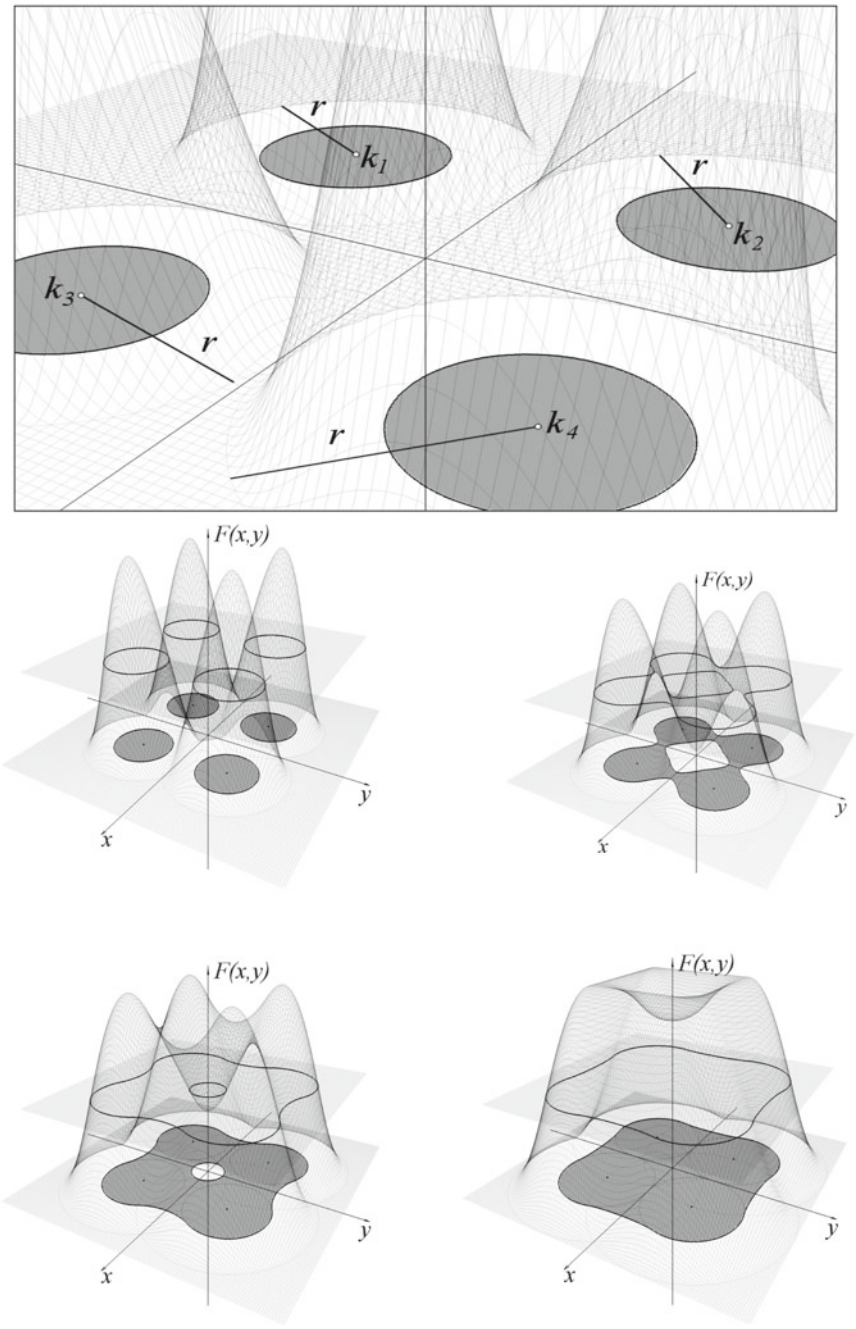
r
k1
r
k2
k3
r
r
k4
F(x,y)
y
x
F(x,y)
y
x
F(x,y)
y
x
F(x,y)
y
x

◀**Fig. 19** Influence of the radius r_i on the shape of the R surface described by Eqs. 13–14 in two dimensional space. The marked fragments on the plane OXY expresses the solutions of the equations. The higher r_i values around the points of k_i with their invariable position, the larger merging of the R shape with simultaneous reduction or elimination of gaps in it. Below—segments of soil surfaces generated by different values of the a, b, and c parameters and their directivity factors D_R

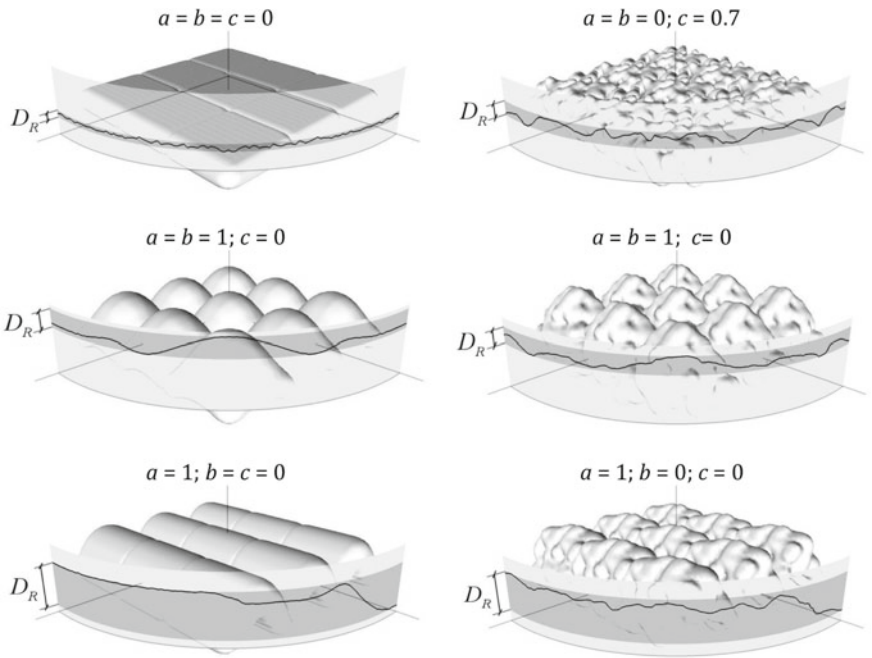

Fig. 20 Segments of soil surfaces generated by different values of the a, b, and c parameters and their directivity factors D_R

where the sum is only limited for unblock light source s_i. The function HDRDF $\left(R, \vec{v}, H\right)$:

$$\text{HDRDF}\left(R, \vec{v}, H\right) = \frac{1}{|\Omega|} \int_{\Omega} E\left(f_R, \vec{v}, H\right) d\Omega \tag{17}$$

describes the hemispherical–directional reflectance of the whole surface R, where Ω is the FOV of a sensor suspended over the surface. This model was tested on directional reflectance data collected on a bare arable soil with furrows and desert loess and rocky surfaces in Israel. They were obtained by the same six-channel luminancemeter as mentioned above. The *NR* distribution of the cultivated soil was predicted by a virtual surface with furrows as in reality. The measured *NR* values of

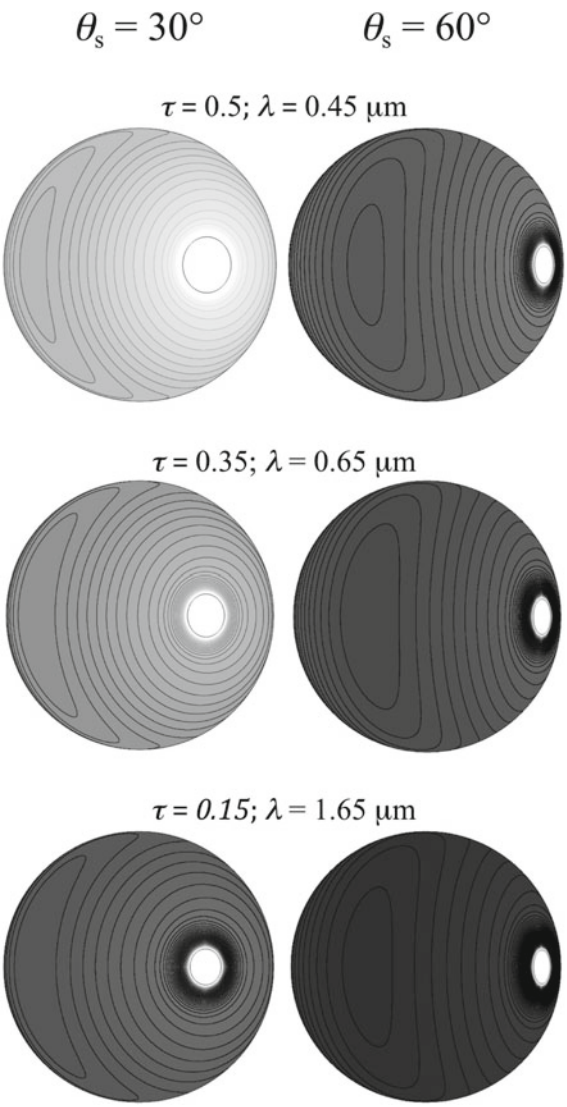

Fig. 21 Distributions of the hemispherical light for the non-absorbing Rayleigh atmosphere depending on the solar zenith angle θ_s and the normal optical thickness τ attributed to the wavelength λ

the cultivated soil, unlike its modeled values, clearly showed asymmetry in their *NR* distribution. These desert surfaces did not reveal this asymmetry either in the data measured or in the data calculated using this model (Fig. 23).

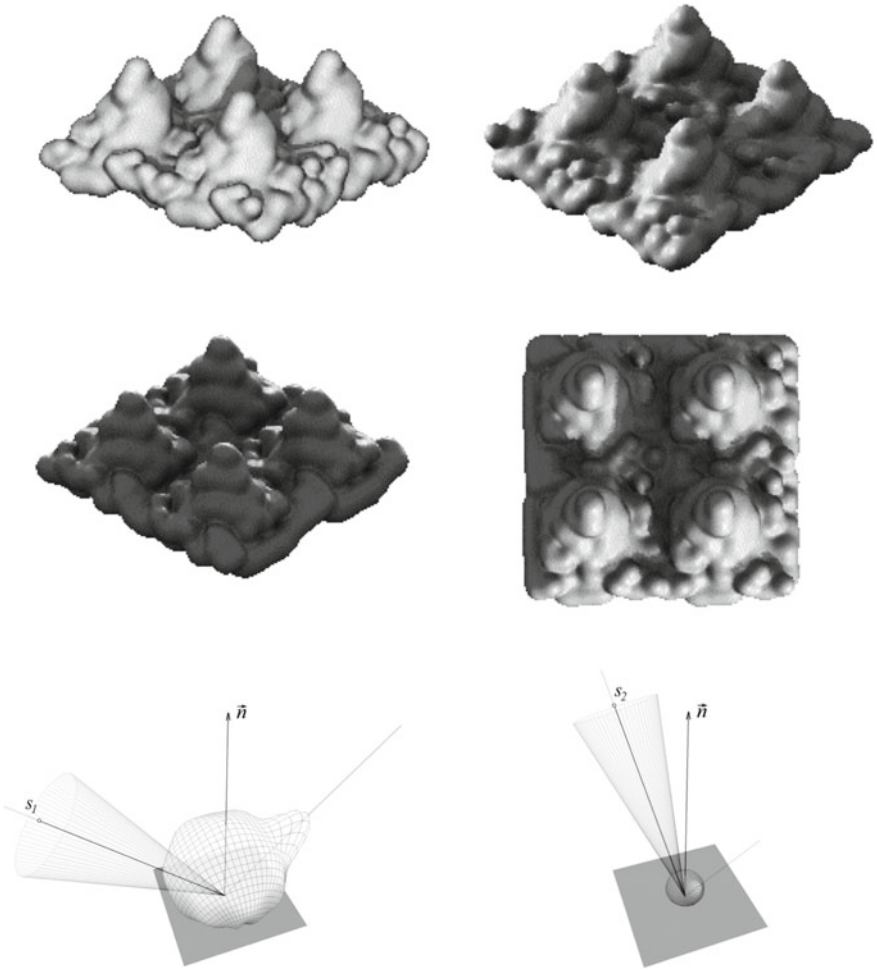

Fig. 22 Brightness variation of a soil surface illuminated unequally with one source of the dominant intensity with reference to others scattered in accordance the quasi-Lambertian function. Below—distribution of light energy coming from sources S_1 and S_2 of the intensity $e_1 > e_2$, respectively, scattered from an elementary fragment f_R of the R surface

3 Soil Albedo

If the bidirectional reflectance is only a part of the reflected radiation from a surface along a given direction, then the albedo of the surface, also called its bihemispherical reflectance (BHR):

$$\mathrm{BHR} = \rho(\theta_i, \phi_i; 2\pi; 2\pi) = \frac{d\Phi_r(\theta_i, \phi_i, 2\pi; 2\pi)}{d\Phi_r^{id}(\theta_i, \phi_i, 2\pi)} \tag{18}$$

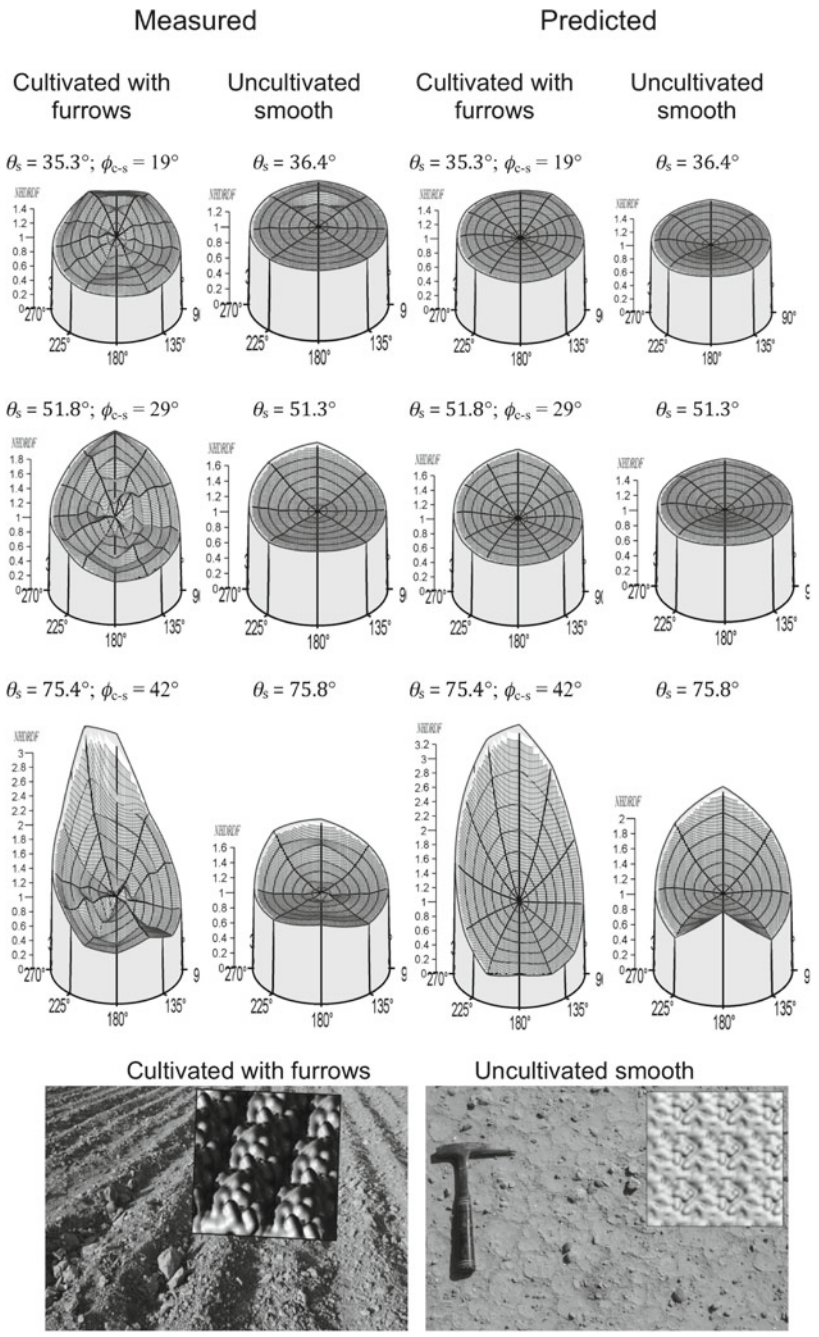

Fig. 23 Distributions of the normalized hemispherical-directional reflectance function of the tested surfaces (cultivated with furrows and the uncultivated relatively smooth), measured and generated for the wavelengths of 0.85 μm for selected illumination conditions defined by the solar zenith angle θ_s and the angle ϕ_{c-s} describing a distance angle between the direction of the furrows and the sun position. Below—view of the surfaces with their virtual equivalents

is influenced by the combined diffuse and direct irradiance and integrates the surface reflectance over all view directions. The albedo is precisely defined as the ratio of the radiant flux reflected from a unit surface area into the whole hemisphere to the incident radiant flux of hemispherical angular extended in the solar reflective radiation range of 0.3–3 μm (Schaepman-Strub et al. 2006). Martonchik et al. (2000) emphasized the distinction between the terms "broadband albedo" and "narrowband (spectral) albedo" depending on whether the albedo is characterized by the entire wavelength range or only a part of it, respectively. The blue-sky albedo refers to the albedo measured in outdoor conditions, where a surface is illuminated by the direct solar irradiance and diffuse irradiance scattered by the atmosphere.

3.1 Variation of Soil Albedo

The broadband blue-sky albedo (α) overall level of arable lands in the mid-latitudes varies substantially between seasons. It reaches the highest values of 0.8–0.95 in the winter due to deep fresh snow cover, and the lowest ones, 0.05–0.15, in the spring when the snow abruptly melts on dark-colored, wet rough soils before the emergence of crops (Oke 1987; Dobos 2017). The α level of arable lands gradually increases during crop maturation (Dexter 2004). Throughout the growing season, the α level of cereals increases as a function of plant height, leaf area and canopy cover. After maturation, during senescence, their α level increases again. In lower latitudes, especially on dry bare arable lands with light-colored soils, their α level reaches 0.35–0.4 and is higher than that of lands covered with crops. The growing share of crop cover increases the α level of arable lands with dark-colored soils (Rechid et al. 2005). The α level of dark-colored soils can also be increased by the presence of light-colored residues (Horton et al. 1996).

The α of arable lands, as well as other Earth objects depend not only on their intrinsic properties, but also on their illumination conditions, described by the θ_s, the proportion of the diffuse radiance and the cloud cover. In clear-sky conditions, the α of bare arable lands increases with increasing θ_s, mainly due to irregularities in their surfaces. Monteith and Szeicz (1961) already reported in the 1960s that α a increased from 0.16 to 0.19 in the afternoon when θ_s increased from 30° to 70°. Kondratyev (1969) found that in the morning, when θ_s decreased from 80° to 25°, α of dry stony and loamy soils dropped from 0.22 to 0.14 and from 0.34 to 0.21, respectively. Much later, a similar relationship between θ_s and the narrowband and broadband α of bare soils was reported by Pinty et al. (1989), Lewis and Barnsley (1994), Oguntunde et al. (2006). The lowest α values of bare arable lands are recorded at local solar noontime when θ_s reaches its minimum. However, the soils attained their highest α values of about 1 at sunrise and sunset. Diurnal graphs of the soils' α versus θ_s are U-shaped (Roxy et al. 2010). This dependency can be asymmetrical around solar noon due to the formation of dew or changes in atmospheric conditions during the day (Fraser 1975). The larger part of the diffuse radiation component (which also

can be the effect of greater cloud cover), the weaker the effect of the θ_s variation on α of soils.

3.2 *Soil Albedo as a Parameter for Modeling Changes in the Climate of the Earth*

The α values of many components of the Earth's surface are fundamental input parameters in modeling the energy flow between them and the atmosphere, and thus in global modeling of the Earth's climate (Ben-Gai et al. 1998; Davin et al. 2007). Smoothing rough, deeply plowed soils with, for example, Hs increases their albedo, which lowers the amount of shortwave radiation absorbed by their surface layer. Those surfaces emit less longwave radiation, reducing their temperature, and when areas of them are large, their reflectance can affect the climate of the Earth (Schneider and Dickinson 1974; Desjardins 2009; Farmer and Cook 2013). The appreciation of soil α variation is particularly important in the view of (Sellers et al. 1995), who defined an acceptable α error of the Earth's surfaces for modeling climate change on a global scale at $\pm 2\%$. The use of average diurnal α_d values (α_d) for such modeling seems more useful than the use of instantaneous values (Grant et al. 2000; Cierniewski et al. 2013).

Nowadays, the α of the Earth's surfaces or their components, such as bare soils, are obtained by means of satellite observation. Because satellite radiometers collect shortwave radiance of the surfaces at one or several directions inside their small field of view, in a number of separate narrowband channels, measuring it at the top of the atmosphere (TOP), the approximation of the α of the surfaces by this raw satellite data needs to be corrected (Pinty and Szejwach 1985; Gutman 1988; Tsvetsinskaya et al. 2006). The estimation of the accuracy of broadband α estimation using satellite data has been made using albedometers mounted on towers from a height of several dozen meters (Liang et al. 2002; Cescatti et al. 2012).

Anticipating that the elimination of even one of these corrective procedures can reduce the error of this approximation, Cierniewski and Gdala (2010) and Cierniewski et al. (2013) considered how correction of the bidirectional reflectance of soils only taking into account the specific direction of satellite viewing (i.e., without taking into account the sun position) can affect the achievement of the soil α values with an error lower than $\pm 2\%$. Cierniewski et al. (2013) analyzed how strongly the roughness of soil surfaces (smooth, moderately rough and very rough) and their latitudinal position affects the optimal time (To) for the soil observation by a satellite in sun-synchronous orbit at selected dates with this acceptable error. It was found that the morning To is expected earliest for the very rough soil, and latest for the smooth soil. In the afternoon this trend is reversed. In certain latitude ranges, the difference between To for smooth soils and for moderately rough soils can be just below 40 min, while the difference between To for very rough and moderately rough soils can be about 15 min. The usefulness of an orbit during the analyzed dates was expressed by the

length along which observation of the soils was available with an acceptable error of ±2%. The longest parts of the orbits—larger than 90°—were predicted for the morning in mid-April, while the shortest, reaching only about 20°, were found for the afternoon in the beginning of the astronomical summer. An attempt was also made to compare the usefulness of satellite orbits crossing the equator at local solar time 7:30 and 10:30, such as for the NOAA-15 and the MODIS Cierniewski (2012). The earlier orbit proved to be much more useful for soil observation in the middle of April and at the end of August in the range larger than 90°, and least useful at the beginning of the astronomical summer in the Northern Hemisphere in the range lower than 30°. The earlier orbits turned out to be much less useful for observing bare soils than the later one.

3.3 *Measurements of Diurnal Blue-Sky Albedo Variation of Soils*

When investigating the diurnal α variation of cultivated and uncultivated surfaces developed from the same soil material in the Israeli Negev desert Cierniewski et al. (2013) found that the soil's roughness not only affects its overall α level under clear-sky conditions, but also the steepness of its α from θ_s at the local solar noon to about 75°. The α values of the surfaces that were deeply plowed barely increased in this θ_s range, while the α values of the soils that were the same but with smoothed surfaces gradually increased. Such an effect of soil roughness on their diurnal α variation (Fig. 24) was confirmed on 81 sets of data collected on arable lands in the southern and central districts in Israel and in the Wielkopolska region of Poland (Cierniewski et al. 2015). Each of these sets, which describe the half-diurnal α distributions of soils and that were collected as in the previous case by LP PYRA 06 albedometers from 1.5–2 m, was accompanied by data characterizing the shape of the soil surfaces formed by such farming tools as planters (Fp), plows (Pd) and disk

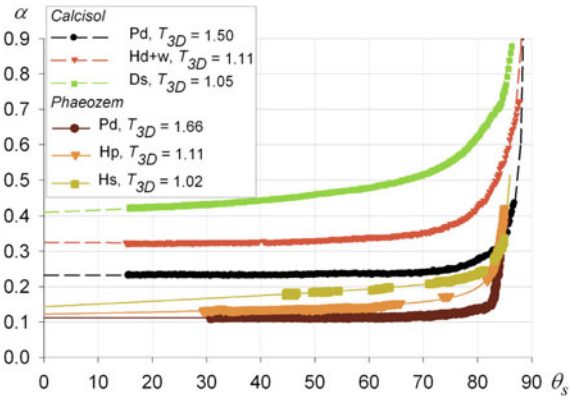

Fig. 24 Variation of the half diurnal broadband blue-sky albedo of a light-colored *Calcisol* formed by a plow (Pd), a disc harrow and modified by sprinkler irrigation (Hd + w) and not cultivated (Ds), as well as a dark-colored *Phaeozem* formed by a plow (Pd), a spike-tooth harrow (Hp), and smoothing harrow (Hs). Shape of the surfaces was quantified by the T_{3D} roughness index

harrows (Hd), pulverizing harrows (Hp) and smoothing harrows (Hs). Modifications of these surfaces due to rainfall or sprinkler irrigation were also taken into account. The shape of the surfaces was measured using stereo-photographs taken by cameras that moved along a leveled construction supported by two tripods, and then as attached to a monopod that, moving around a measured surface, recorded its image from many directions. Additionally, each studied soil's reflectance spectrum in the range 0.35–2.5 μm was measured in the laboratory by a FieldSpec spectroradiometer with a Hi-Brite Muglight receptor, using the procedure that is recommended to collect soil reflectance spectra stored in soil databases in the world (Ben-Dor et al. 2015).

3.4 Equations Predicting Diurnal Blue-Sky Albedo Variation of Soils Taking into Account Their Roughness

The above data, supplemented with values characterizing the contents of soil organic carbon (SOC) and $CaCO_3$ of the studied soils enabled us to determine the following equations (Cierniewski et al. 2015):

$$\alpha_0 = 0.301 - 0.042 \cdot \mathrm{SOC} + 0.007 \cdot \mathrm{CaCO_3} - 0.088 \cdot T_{3\mathrm{D}} \tag{19}$$

$$s_\alpha = 0.0054 \cdot (HSD)^{-1.535}, \tag{20}$$

which enable us to predict the half-diurnal α of a soil surface from the solar noon to $\theta_s = 75°$ depending on its roughness expressed by the *HSD* and T_{3D} indices, where α_0 relates to its theoretical α at $\theta_s = 0°$, and s_α describes the linear slope of the α increase from the solar noon to θ_s of 75°. The correctness of the equations, expressed by the coefficient of determination (R^2) and the root mean square error (RMSE), was estimated at 0.90 and 0.03, respectively.

Carrying out the research project 2014/13/B/ST10/02111, which is supported by the Polish National Science Centre and aims to quantify the annual dynamics of shortwave radiation reflected from arable lands on a global scale taking into account their roughness, the diurnal α distributions of a much larger number of soil units were needed than it was possible to obtain by measuring them directly in the field. Analyzing the correctness of predicting such diurnal α distributions through the aforementioned soil laboratory spectra, it was attempted to determine whether the necessary soil diurnal α distributions could be additionally obtained by their laboratory reflectance spectra stored in the spectral libraries of soils in the world.

The global library of soil reflectance spectra has been being developed since 2008 as a voluntary collaborative project (Viscarra Rossel 2009). By about 2015, this library contained soil reflectance spectra accompanied by chemical and physical attribute data from over 90 countries on seven continents (Viscarra Rossel et al. 2016). This global soil database includes spectra from soil in the World Soil Information collection recorded by the World Agroforestry Centre and also other national,

multinational and continental soil databases. The largest continental database, the European Use and Cover Area frame Statistical Survey (LUCAS), was initiated by a decision of the European Parliament and the Council of the European Union in 2007 (Stevens et al. 2013). The Global Soil Spectral Library and the LUCAS library combined contain over 20,000 such soil spectra of geo-referenced topsoil samples with their chemical and physical attribute data (Viscarra Rossel et al. 2016).

The first set of equations, which predicted the half-diurnal α distributions of a soil surface taking into account its roughness using its soil reflectance spectrum obtained in laboratory conditions, was established on the basis of 108 sets of soil data collected in Poland and Israel (Cierniewski et al. 2017a) in similar way as those mentioned above. The first equation:

$$a_{45} = 0.454 - 0.112T_{3D} + 6952.66d_{474} + 13108.37d_{705} + 12470.20d_{952} - 11597d_{1650} \quad (21)$$

predicts the overall α level of the soil of a given roughness at $\theta_s = 45°$, where d together with its associated number relates to the soil reflectance data transformed to its second derivative for specified wavelength in nm. The second equation:

$$\alpha_{\theta_s} = \alpha_{45}[1 + s_\alpha(\theta_s - 45)], s_\alpha = 0.0008 + 0.00108(T_{3D})^{-20.75} \quad (22)$$

describes its α under $0° < \theta_s > 75°$. The R^2 and RMS values for these equations reached 0.89 and 0.03, respectively. Then, these equations were improved based on number of these data sets being increased to 153 and the improved quality of a newly tested soil population in the northern district of Israel and in three southern regions of France, Mid Pyrenees, Languedoc and Provence (Cierniewski et al. 2018a). These equations, finally determined by examining soils belonging to 22 soil units according to the World Reference Base (WRB) for Soil Resources (IUSS Working Group 2014), were formulated as:

$$a_{45} = 0.33 - 0.1099T_{3D} - 5795.4d_{574} - 510.2d_{1087} + 7787.2d_{1355} + 12161d_{1656} + 6932.8d_{698}, \quad (23)$$

and

$$\alpha_{\theta_s} = \alpha_{45}[1 + s_\alpha(\theta_s - 45)], s_\alpha = 6.26 \cdot 10^{-7} + 0.0043(HSD)^{-1.418} \quad (24)$$

The studied surfaces with the highest roughness formed by Fp and Pd (with average *HSD* and T_{3D} values of 56 mm and 1.4, and 32 mm and 1.6, respectively) were characterized by averaged s_α values of 0.00008 and 0.00005, respectively. On the other hand, average s_α values of the surfaces with the lowest roughness formed by Hs (with average *HSD* of 6 mm and T_{3D} of 1.1) were ten times greater, reaching about 0.0003. The surfaces modified by water drops had a lower roughness than the surfaces formed only by agricultural tools. These modified surfaces in relation to

those originally shaped by Fp and Pd (with average *HSD* and T_{3D} of about 40% and 15% lower, respectively) had averaged s_α values of about 25% and 5% higher, respectively. The surfaces modified by water drops in relation to those originally treated by Hs (described by 40% and 5% lower *HSD* and T_{3D}, respectively) were characterized by s_α value of about 50% higher. The R^2 and RMSE of the last set of the equations were estimated at 0.91 and 0.03, respectively.

For the half-diurnal α variation of soils in the full θ_s range from 0° to 90°, the fitting formulas:

$$\alpha_{\theta_s} = \exp\left(\frac{\mathrm{a} + \mathrm{c}\theta_s}{1 + b\theta_s + d(\theta_s)^2}\right) \tag{25}$$

and

$$\alpha_{\theta_s} = \frac{\mathrm{a} + c(\theta_s)^{0.5}}{1 + b(\theta_s)^{0.5}} \tag{26}$$

were used for data obtained through Eqs. 19 and 20 (Cierniewski et al. 2015, 2018b; Cierniewski and Ceglarek 2018) and Eqs. 21–24 (Cierniewski et al. 2017b, 2018a), respectively, where a, b, c, and d are fitting parameters.

3.5 *Use of Laboratory Data to Predict the Annual Variation of Shortwave Radiation Reflected from Bare Arable Lands Taking into Account Their Roughness*

Equations 19, 20 and 26 were used for estimating the annual dynamics of shortwave radiation reflected from bare air-dried soil surfaces at clear-sky conditions as a consequence of smoothing previously plowed and harrowed arable lands in Poland (Cierniewski et al. 2017b). The input data used for these equations was data describing the contents of SOC and $CaCO_3$ of arable lands in Poland stored in the Land Use/Cover Area Frame Survey (LUCAS) (Tóth et al. 2013) and in the database created for monitoring the properties of arable lands in Poland (Terelak et al. 2008). Equations 21, 22 and 26 were used to quantify the annual variation of shortwave radiation reflected, including in clear-sky conditions from air-dried arable lands in Israel, using reflectance spectra of soils stored in the Israeli Soil Database Library (Cierniewski et al. 2018b). The annual variations of the arable land areas in Poland and Israel were determined with the help of Landsat 8 images recorded for the countries in 2013–2014 and 2013–2015, respectively. The images, recorded by the Operational Land Imager (OLI) instrument of the satellite, included two sample surfaces within two scenes of the satellites located in the eastern and western parts of Poland and the entire territory of Israel within there scenes of the satellite. The

images without snow and with up to 10% of cloud cover were radiometrically calibrated to top-of-atmosphere reflectance (TOA) using metadata, and normalized from different illumination conditions by dividing TOA by the cosine of θ_s. A surface was identified as a bare soil by analyzing the shape of its reflectance (RB) recorded in the following bands (B) of the OLI, i.e., if they fulfilled the following conditions: R2 < R3 < R4 < R5 < R6; R6 > R7; R5/R3 > 1.8; R6 − R5 > 0 in the case of arable lands in Poland, and R3 < R4 < R5 < R6; R6 > R7; R6 − R5 < 1 within the lands in Israel. The above sets of the reflectance conditions were established based on the shape of the spectrum of the dominant soil units located within the contours of arable lands, using digital maps of land use and soils of these countries. The half-diurnal α distributions of the studied soil units generated in the θ_s using the aforementioned sets of equations with the assumption that they have a roughness corresponding to those formed by a Pd, an Hd and an Hs. It was assumed that the roughness, expressed by *HSD* and T_{3D}, was 25 mm and 1.5 for the surfaces shaped by Pd, 10 mm and 1.15 for Hd, and 5 mm and 1.05 for Hs (Cierniewski et al. 2014). The distributions were first matched with θ_s variation for each day of the year from local noon to sunset. Then the distributions were stated in a function of time, replacing θ_s by solar local time. This allowed the average diurnal α value (α_d) to be calculated for each day of the year for averaged air-dried arable lands in the studied countries after using the aforementioned agricultural tools. The examples of average soils located in Poland and Israel show how different their diurnal α distributions can be depending on latitude, date and roughness, and how these variables affect their average diurnal values (Fig. 25). Using an Hs to smoothing soil previously shaped by a Pd in Poland increases its α_d at the beginning of the astronomical winter by about 100% and at the beginning of the astronomical summer by about 65%. For average soils in Israel, located at a lower latitude of about 20°, their α_d increase for the first date is about 45%, and 30% for the second.

The diurnal amounts of shortwave radiation reflected from the lands were estimated by multiplying the total amount of shortwave radiation coming to the lands under clear-sky conditions (formulated by formulas contained in Allen et al. 1998) by the α_d of the lands and their areas. It was found that these areas reached two maxima in spring and late summer in Poland (at the beginning of the second decade of March and the end of the first decade of September) and one maximum in summer until early autumn in Israel (between the end of the second decade of July and the end of the first decade of September). The maxima of shortwave radiation (Rr_d) reflected under the clear-sky from these dried arable lands in Poland formed by Pd and Hs were assessed at about 200 and 320 PJ/day in spring, respectively, and in late summer at 220 and 350 PJ/day (Fig. 26). The Rr_d maximum values for air-dried bare arable lands formed by Pd and Hs in Israel were estimated at about 16 and 23 PJ/day, respectively. These values were approx. 14–15 times lower than the corresponding values for lands in Poland mainly because the total area of these lands in Poland was about 35 times larger, but their α_d and Ri_d values were almost 1.5 times and 1.2 times lower in spring and late summer, respectively, than those in Israel in summer until early autumn.

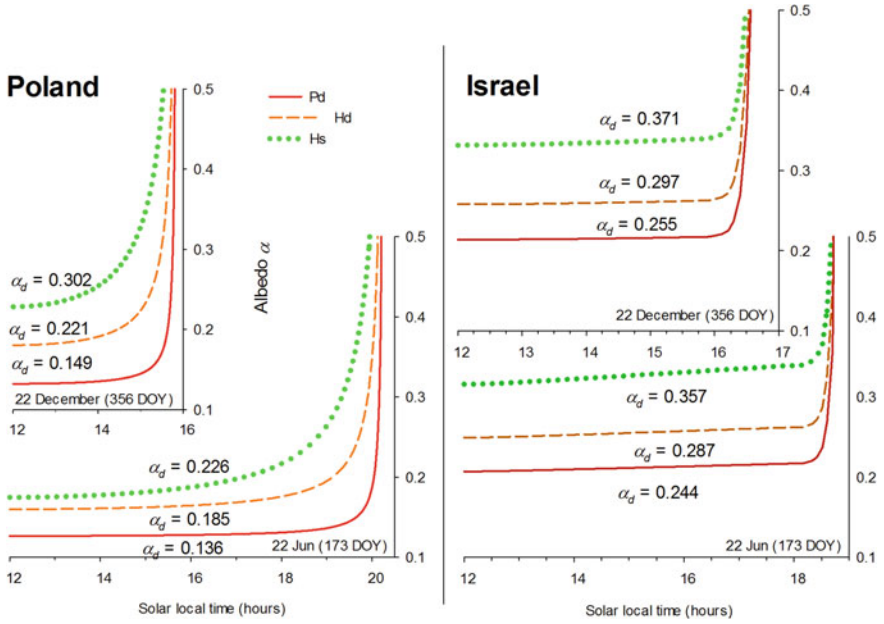

Fig. 25 Half-diurnal albedo distribution of average bare arable lands in Poland and Israel formed by a Pd, an Hd, and an Hs, generated for the shortest (22 December) and the longest (22 June) days, respectively, in relation to the local solar time

In order to estimate the annual dynamics of the shortwave radiation reflected from the bare arable lands on the scale of the European continent Eq. 23, 24 and 25 were used, where thousands of soil reflectance spectra stored in the LUCAS soil database provided input data for these equations to calculate the half-diurnal α variation of the tested lands assuming that they are formed by Pd and Hs and illuminated under clear-sky conditions (Cierniewski et al. 2018c). The use of satellite data from a Spinning Enhanced Visible and Infrared Imager instrument (SEVIRI) (König et al. 2001) made it possible to estimate these dynamics not only under clear-sky conditions, but also in the real changing cloud conditions in the selected year of 2011. The annual variation of the areas of arable lands and periods when they are not covered with crops in such large terrain has been established in a different way than in Poland and Israel. Vectorized and rasterized geostatistical data related to the European Agricultural Region (USDA 1994), divided into three sub-regions limited to member countries of the European Union (EU) together with its associated countries (Switzerland and Norway) were used. The spatial distribution and area of the major crops cultivated there (barley, wheat, maize, potato, rye, sugar beet and rapeseed) was established on the basis of the datasets (Monfreda et al. 2008) in the form of a raster image with a pixel size of 5 × 5 arcmin. The Crop Calendar Dataset (Sacks et al. 2010), containing digitized and georeferenced observation of crop planting and harvesting days (also with the same resolution of 5–5 arcmin) was used to find the date when the crops

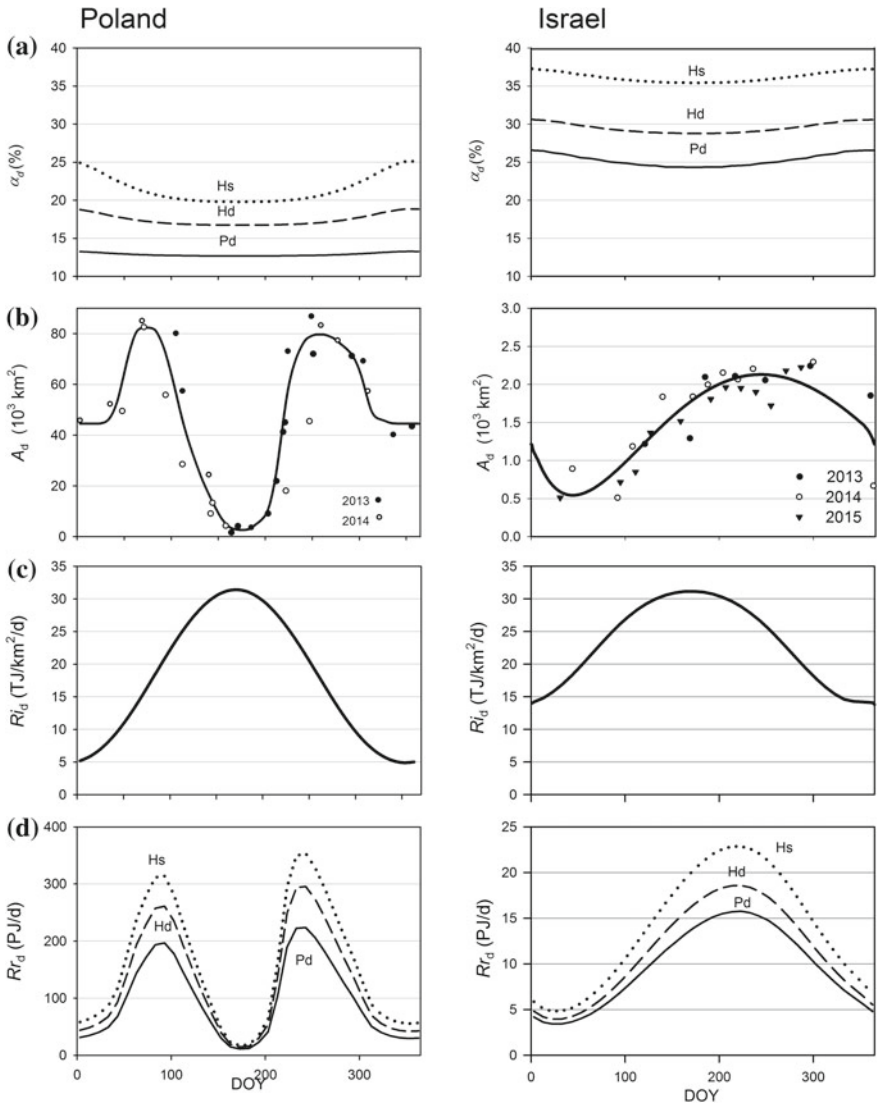

Fig. 26 Annual variation in: **a** average diurnal albedo (α_d) of the average bare arable lands in Poland and Israel, formed by a plow (Pd), a disk harrow (Hd), and a smoothing harrow (Hs); **b** areas of bare arable lands in Poland and Israel extracted from Landsat 8 images; **c** amount of shortwave radiation (Ri_d) reaching the lands in clear-sky conditions; **d** amount of shortwave radiation reflected from all the bare arable lands (Rr_d) within Poland and Israel

were planted. Growing degree days, being a tool for measuring heat accumulation in order to predict the rate of plant development (Miller et al. 2001; Worthington and Hutchinson 2005), was used to determine the period in which crop cover does not exceed 15%, so it could not lose its spectral characteristic as bare soil. To determine the soil units that the delineated arable areas belong to, a digital soil map classified as WRB major reference groups and a land-cover map (GlobCover 2009) were used (Arino et al. 2012). The α_d values of averaged arable lands were generated for each day of the year using half-diurnal α distributions of the air-dried lands in the function of solar local time in the same way as those calculated for these two different size countries—Poland and Israel. Due to the variability of climatic conditions in such a wide area within the EU, α_d values were calculated separately for its western (W), central (C), and southern (S) parts (Fig. 27). Spring peaks of the bare soil areas, about 85,000 and 60,000 km^2, were found within W and C in the middle of first decade of April and in the middle of the first decade of May, respectively. The largest spring peak, reaching 95,000 km^2, was established within S at the turn of the second and the third decade of April. Significantly smaller autumn peaks of the bare soil areas within W, C, and S, reaching 10,000, 20,000, and less than 5000 km^2, respectively, were found at the end of the first decade of October. Within S in summer around the end of the third decade of July an additional area of bare soils was found measuring 10,000 km^2. The average diurnal amount of shortwave radiation reaching the EU's arable lands under changing cloudiness in the selected years of 2011 varied from about 2 TJ/km^2 around the beginning of the astronomical winter to 17, 19, and 21 TJ/km^2 for C, W, and S, respectively, at the beginning of the astronomical summer. It was found finally that the greatest amount of radiation could be reflected from the arable lands of the EU from the beginning of April to the end of May. This instantaneous radiation amount of the soil shaped by a Hs and a Pd was estimated at 250 and 220 PJ/day, respectively, for W, 190 and 150 PJ/day for C, and 330 and 280 PJ/day for S.

In estimating the annual dynamics of short-wave radiation reflected from bare arable lands on a global scale (Cierniewski and Ceglarek 2018), such a procedure for determining the variation of their areas was applied as in the case of the European continent previously discussed, using vectorized and rasterized geostatistical data sets. However, without having the satellite data referring to the real amount of short-wave radiation reaching these lands in this global scale, the estimation was limited only to clear-sky conditions without any clouds. The estimation has been referred to the highest radiation level of the lands, which under conventional tillage (Derpsch et al. 2010) were bare for at least a few days after the day of planting and were air-dried in two extreme roughness states—those shaped by a Pd and those shaped by a Hs. The estimation was carried out on the examples of the thirty-three most extensive agricultural regions on six of the Earth's continents, where thirteen major crops are cultivated (barley, cassava, cotton, groundnut, maize, millet, potato, rapeseed, rye, sorghum, soybean, sugar beet and wheat). This estimate was made using soil units classified as major soil groupings according to the Digital Soil Map of the World (FAO/UNESCO 2007) located within the tested arable lands according to a global land cover map (GlobCover 2009). It was established that the highest peak

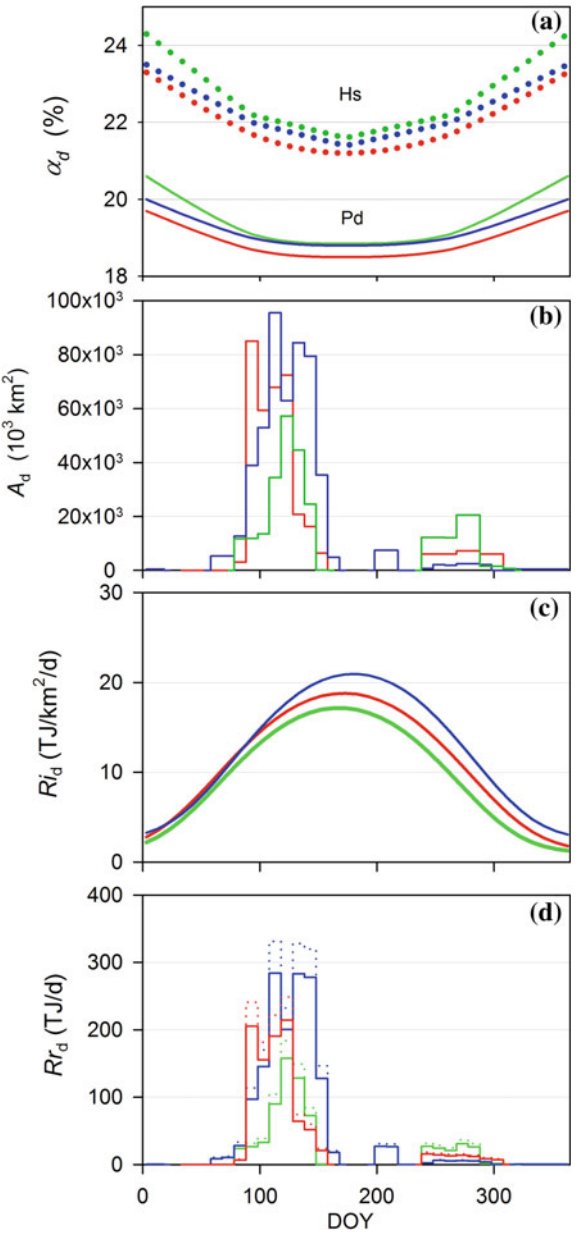

Fig. 27 Annual variation in: **a** average diurnal albedo (α_d) of the average bare arable lands in western (red line), central (green line), and southern (blue line) parts of the European Union (EU), formed by a plow (Pd) and a smoothing harrow (Hs); **b** areas of bare arable lands in these parts of the EUs; **c** real amount of shortwave radiation (Ri_d) reaching the lands in the EU; **d** amount of shortwave radiation reflected from all the bare arable ands (Rr_d), formed by a plow (solid lines) and a smoothing harrow (dashed lines) within these parts of the EU

of shortwave radiation reflected from the lands (Rr_d) formed by a Pd and an Hs in Africa occur in the summer in the middle of the first decade of July, reaching there around 3.5 EJ/day and 4 EJ/day, respectively, when their bare areas reached about 350,000 km^2. In Asia, Europe and North America, the highest Rr_d peaks appear in spring between the beginning and the end of the third decade of May, and in South America at the beginning of the second decade of December. It was found that in this period the total areas of bare arable lands on these continents were about 700,000 km^2, 450,000 km^2, 300,000 km^2, and 500,000 km^2, respectively (Fig. 28). The Rr_d peaks for these extreme roughness states, formed by a Pd and Hs, were evaluated at about 8.5 EJ/day and 10 EJ/day, 5 EJ/day and 8.5 EJ/day, 7 EJ/day and 8.5 EJ/day, and 5.5 EJ/day and 6.3 EJ/day, respectively (Fig. 29). This Rr_d peak appears in Oceania in autumn, in the middle of the first decade of June, reaching

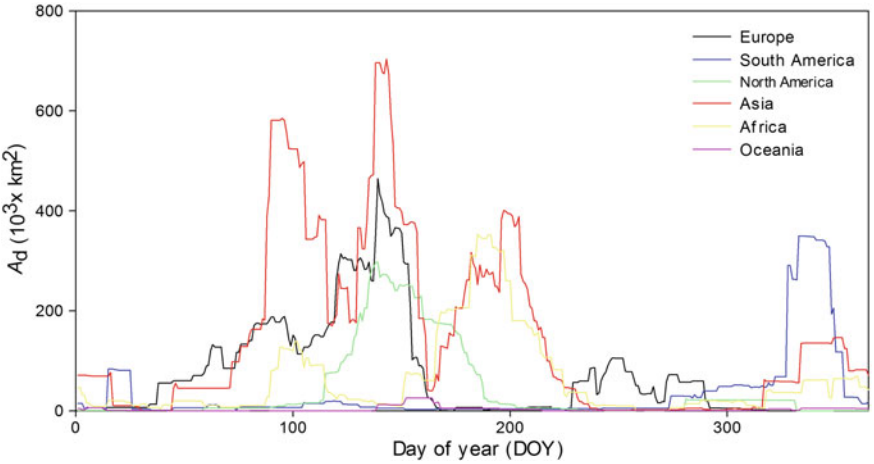

Fig. 28 Annual variation of bare arable land areas (A_d) within six continents of the Earth

Fig. 29 Annual variation of amount of shortwave radiation reflected from all the bare arable lands formed by a smoothing harrow (Rr_d) within six continents of the Earth

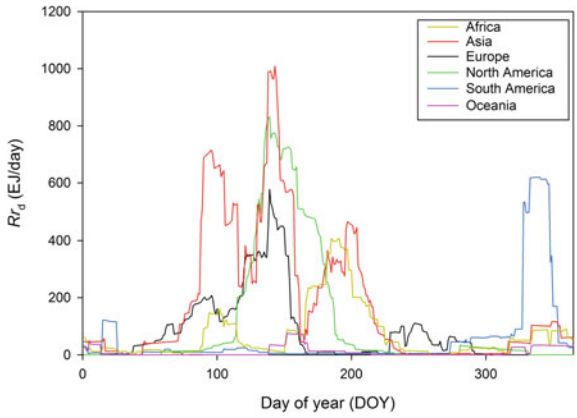

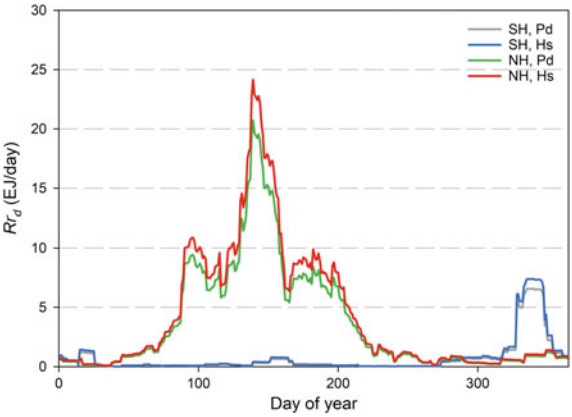

Fig. 30 Annual variation of shortwave radiation reflected from all the bare arable lands (Rr_d), and reflected from bare arable lands formed by a plow (Pd) and a smoothing harrow (Hs) within the Northern Hemisphere (NH) and Southern Hemisphere (SH)

0.15 EJ/day and 0.25 EJ/day. Figure 29 shows the Rr_d values related to these lands formed by a Hs. Aggregating the Rr_d values predicted for the tested agricultural regions located in the Northern Hemisphere, it was found that their highest value occurred at the beginning of the third decade of May reaching 21 EJ/day for soils treated by a Pd, and 24 EJ/day when they are treated by an Hs (Fig. 30).

We suppose that these above values of shortwave radiation reflected and absorbed by bare arable lands in specified periods of the year with their changing areas throughout the year may have a noticeable effect on the Earth's climate on a global scale, depending on the land roughness being the effect of agricultural practices under conventional tillage. Due to the evidently progressive global warming of the climate, forming arable lands under conventional cultivation with the use of agricultural tools that create the lowest possible roughness seems to be one action against this warming. It is assumed that although the annual variation of shortwave radiation reflected from bare arable lands on a global scale is limited to specific conditions, it may facilitate climatologists in more reliable assessment of the impact of these lands on the Earth's climate.

4 Concluding Remarks

This paper discussed the impact of soil properties—those stable in time and those changing dynamically—that have the strongest influence on the bidirectional reflectance (ρ) of soils and their broadband blue-sky albedo (α). However, the impact of soil surface roughness on these physical quantities was discussed here most widely. Models that describe the ρ of soils in changing their illumination and observation condition taking into account this surface feature were used for this purpose.

It is assumed that bare soil surfaces, although appearing in relatively short periods within conventionally cultivated arable lands may, due to their large total areas, can significantly affect the energy transfer between soil, vegetation and the atmosphere,

depending on their spectral reflectance properties (expressed by their α). It is assumed that only one of these properties, which is the roughness of the arable lands, can sufficiently strongly determine this impact. Smoothing rough arable lands that have been previously deeply plowed with, for example, a smoothing harrow increases their α, resulting in a lower amount of shortwave radiation being absorbed by their surface layer. Those surfaces emit less long-wave radiation, leading to reduction in their temperature, which can modify the Earth climate.

This paper presents the sets of equations that make it possible to predict with the satisfactory accuracy the diurnal α using their reflectance spectra obtained under laboratory conditions, which are stored in soil spectral libraries. This variation allows for more precise calculation of the average diurnal α values of soils and, on this basis, also their average α values over longer periods of several days, a month, a season or a year. It is assumed that the application of the procedures for determining the annual variation of shortwave radiation amount reflected from arable lands at such time intervals can improve the accuracy of modeling the Earth's climate change.

Because the surface moisture of arable lands under conventional tillage affects their spectral reflectance as strongly and dynamically as their surface roughness, it would appear important to consider soil moisture as a variables in the newly developed soil reflectance models working in the optical domain.

Estimating the amount of radiation reflected from bare soils on a global scale would be much more realistic if it concerned not only clear-sky conditions, but also the changing cloud conditions on a much larger area than the EU, as has been done thus far using satellite data from the SEVIRI instrument.

In view of the rapid progress of satellite technology, it seems increasingly feasible that a research project can be implemented to confirm the suitability of observation of soil surfaces and other components of the Earth's surface using satellite technology at the optimal time to determine their average diurnal α value.

Acknowledgements This work was supported by the Polish National Science Centre as part of the framework of project no. 2014/13/B/ST10/02111. The author also thanks Jakub Ceglarek for his help in preparation of the figures for this paper.

References

Al-Abbas AH, Swain PH, Baumgardner MF (1972) Relating organic matter and clay content to the multispectral radiance of soils. Soil Sci 114:477–485

Allen RG, Pereira LS, Raes D, Smith M (1998) Crop evapotranspiration: guidelines for computing crop requirements. Irrig Drain Pap No. 56, FAO 300. https://doi.org/10.1016/j.eja.2010.12.001

Andronikov VL (1979) Teoricheskiye osnovy deshifrirovaniya kak metoda izucheniya pochv. Kolos, Moscov (in Rusian)

Arino O, Ramos Perez JJ, Kalogirou V et al (2012) Global land cover map for 2009 (GlobCover 2009). Eur Sp Agency Univ Cathol Louvain

Bachmann CM, Eon R, Ambeau B et al (2017) Modeling and intercomparison of field and laboratory hyperspectral goniometer measurements with G-LiHT imagery of the Algodones Dunes. J Appl Remote Sens 12:1. https://doi.org/10.1117/1.jrs.12.012005

Bauer ME, Vanderbilt VC, Robinson BP, Daugtry CST (1981) Spectral properties of agricultural crops and soils measured space, aerial. In: Field and laboratory sensors. Purdue University

Baumgardner MF, Silva LF, Biehl LL, Stoner ER (1986) Reflectance properties of soils. Adv Agron 38:1–44. https://doi.org/10.1016/s0065-2113(08)60672-0

Ben-Dor E (2002) Quantitative remote sensing of soil properties. 2113:173–243. https://doi.org/10.1016/s0065-2113(02)75005-0

Ben-Dor E, Irons JR, Epema G. (1999) Soil reflectance. In: Rencz E (ed) Remote sensing for earth science: manual of remote sensing. Wiley & Sons Inc, New York, p 111

Ben-Dor E, Goldlshleger N, Benyamini Y et al (2003) The spectral reflectance properties of soil structural crusts in the 1.2 to 2.5 mm spectral region. Soil Sci Soc Am J 67:289–299

Ben-Dor E, Ong C, Lau IC (2015) Reflectance measurements of soils in the laboratory: standards and protocols. Geoderma 245–246:112–124. https://doi.org/10.1016/j.geoderma.2015.01.002

Ben-Gai T, Bitan A, Manes A et al (1998) Spatial and temporal changes in rainfall frequency distribution patterns in Israel. Theor Appl Climatol 61:177–190. https://doi.org/10.1007/s007040050062

Bertuzzi P, Caussignac JM, Stengel P et al (1990) An automated, noncontact laser profile meter for measuring soil roughness in situ. Soil Sci 149:169–178

Białousz S (1978) Zastosowanie Fotointerpretacji do wykonywania map stosunków wodnych gleb. PTG, Pr Kom Nauk 35:1–143 (in Polish)

Białousz S, Girard MG (1978) Wspołczynniki odbicia spectralngo gleb w pasmach pracy satelity landsat. Fotointerpr Geogr 3:111–117 (in Polish)

Biliouris D, Verstraeten WW, Dutré P et al (2007) A Compact Laboratory Spectro-Goniometer (CLabSpeG) to Assess the BRDF of Materials. Presentation, Calibration and Implementation on Fagus sylvatica L. Leaves. Sensors 7:1846–1870. https://doi.org/10.3390/s7091846

Boiffin J (1986) Stages and time-dependency of soil crusting in situ. In: Callebaut F, Gabriels D, De Boodt M (eds) Assessment of soil surface sealing and crusting. University of Ghent, Ghent, Belgium, pp 91–98

Boiffin L, Monnier G (1986) Workshop on erosion assessments for EEC. Methods and models. In: International symposium on assessment of soil surface sealing and crust. Ghent, Belgium, p 4

Bowers SA, Hanks RJ (1965) Reflection of radiant energy from soils. Soil Sci 100:130–138. https://doi.org/10.1097/00010694-196508000-00009

Bowers SA, Smith SJ (1972) Spectrophotometric determination of soil water content. Soil Sci Soc Am J 36:978–980

Brennan B, Bandeen WR (1970) Anisotropic reflectance characteristics of natural earth surfaces. Appl Opt 9:405. https://doi.org/10.1364/ao.9.000405

Cescatti A, Marcolla B, Santhana Vannan SK et al (2012) Intercomparison of MODIS albedo retrievals and in situ measurements across the global FLUXNET network. Remote Sens Environ 121:323–334. https://doi.org/10.1016/j.rse.2012.02.019

Cierniewski J (1985) Relation between soil moisture tension and spectral reflectance of different soils in the visible and near-infrared range. In: Proceedings 3rd international colloquium on spectral signatures of objects in remote sensing. (ESA SP-247), pp 429–432

Cierniewski J (1987) A model for soil surface roughness influence on the spectral response of bare soils in the visible and near-infrared range. Remote Sens Environ 23:97–115. https://doi.org/10.1016/0034-4257(87)90073-3

Cierniewski J (1988) An influence of soil surface moisture and roughness on the spectral response of soil in the visible and near-infrared range, and a mathematical modelling of the relation. Rozpr Nauk Rocz Akad Rol w Pozn 178:1–79 (in Polish)

Cierniewski J (1989) The influence of the viewing geometry of bare rough soil surfaces on their spectral response in the visible and near-infrared range. Remote Sens Environ 27:135–142. https://doi.org/10.1016/0034-4257(89)90013-8

Cierniewski J (1993) Soil moisture tension and soil spectra reflectance on the example of Koscian plain soils. Fotointerpr Geogr 105:107–122
Cierniewski J (1999) Geometrical modeling of soil bi-directional reflectance in the optical domain. Bogucki Sci Publ, Pozn, p 148
Cierniewski J (2001) The bidirectional reflectance model from cultivated soils taking into account soil aggregates and micro-relief. Bogucki Sci Publ, Pozn, p 150 (in Polish)
Cierniewski J (2012) Satellite observation of bare soils for their average diurnal albedo approximation. In: Ist international conference on sensor networks. Rome, Italy, 24–26 February
Cierniewski J, Ceglarek J (2018) Annual dynamics of shortwave radiation of bare arable lands on a global scale incorporating their roughness. Environ Earth Sci 77. https://doi.org/10.1007/s12665-018-7956-7
Cierniewski J, Gdala T (2010) Calculating the optimal time when albedo approximates its daily average: an example using soil surfaces with various roughnesses at different latitudes. Int J Remote Sens 31:2697–2708. https://doi.org/10.1080/01431160903093200
Cierniewski J, Guliński M (2009) Furrow microrelief influence on the directional hiperspectral reflectance of soil at various illumination and observation conditions. IEEE Trans Geosci Remote Sens 48:4143–4148
Cierniewski J, Kuśnierek K (2010) Influence of several soil properties on soil surface reflectance. Quaest Geogr 29:13–25. https://doi.org/10.2478/v10117-010-0002-9
Cierniewski J, Verbrugghe M (1993) A geometrical model of soil bidirectional reflectance in the visible and near-infrared. Fotointerpr Geogr 23:37–51 (in Polish)
Cierniewski J, Verbrugghe M (1994) A geometrical model of soil bidirectional reflectance in the visible and near-infrared range. In: Proceeding 6th international symposium on physical measurements and signatures in remote sensing. Val d'Isére, France, 17–21 January 1994, pp 635–642
Cierniewski J, Verbrugghe M (1997a) Influence of soil surface roughness on soil bidirectional reflectance. Int J Remote Sens 18:1277–1288. https://doi.org/10.1080/014311697218412
Cierniewski J, Verbrugghe M (1997b) Inferring soil surface roughness from soil bidirectional reflectance data. Int Agrophys 11:147–157
Cierniewski J, Verbrugghe M, Marlewski A (2002) Effects of farming works on soil surface bidirectional reflectance measurements and modelling. Int J Remote Sens, 23:1075–1094
Cierniewski J, Kijowski A, Mizgajski A (1988) The influence of soil moisture on spectral response of soil cover in the sensitive region of infrared film. In: Proceeding 3rd symposium of the ISSS Working Group on Remote Sensing for Soil Survey. Prace Komisji Naukowych PTG, Jablonna, Poland 1981, pp 45–59
Cierniewski J, Baret F, Verbrugghe M et al (1996) Geometrical modelling of soil bidirectional reflectance incorporating specular effects. Int J Remote Sens 17:3691–3704. https://doi.org/10.1080/01431169608949178
Cierniewski J, Gdala T, Karnieli A (2004) A hemispherical–directional reflectance model as a tool for understanding image distinctions between cultivated and uncultivated bare surfaces. Remote Sens Environ 90:505–523. https://doi.org/10.1016/j.rse.2004.01.004
Cierniewski J, Karnieli A, Herrmann I et al (2010) Soil surface illumination at micro-relief scale and soil BRDF data collected by a hyperspectral camera. Int J Remote Sens 31:2151–2157. https://doi.org/10.1080/01431161003610281
Cierniewski J, Karnieli A, Kuśnierek K et al (2013) Approximating the average daily surface albedo with respect to soil roughness and latitude. Int J Remote Sens 34:3416–3424. https://doi.org/10.1080/01431161.2012.716530
Cierniewski J, Karnieli A, Kaźmierowski C, Ceglarek J (2014) A tool for predicting diurnal soil albedo variation in Poland and Israel. In: EARSeL eProceedings, Special Issue: 34th EARSeL Symposium, pp 36–40
Cierniewski J, Karnieli A, Kazmierowski C et al (2015) Effects of soil surface irregularities on the diurnal variation of soil broadband blue-sky albedo. IEEE J Sel Top Appl Earth Obs Remote Sens 8:493–502. https://doi.org/10.1109/jstars.2014.2330691

Cierniewski J, Ceglarek J, Karnieli A et al (2017a) Predicting the diurnal blue-sky albedo of soils using their laboratory reflectance spectra and roughness indices. J Quant Spectrosc Radiat Transf 200:25–31. https://doi.org/10.1016/j.jqsrt.2017.05.033

Cierniewski J, Królewicz S, Kaźmierowski C (2017b) Annual dynamics of shortwave radiation as consequence of smoothing of previously plowed and harrowed soils in Poland. J Appl Meteorol Climatol 56:735–743. https://doi.org/10.1175/jamc-d-16-0126.1

Cierniewski J, Ceglarek J, Karnieli A et al (2018a) Shortwave radiation affected by agricultural practices. Remote Sens 10. https://doi.org/10.3390/rs10030419

Cierniewski J, Ceglarek J, Kaźmierowski C (2018b) Predicting the Diurnal Blue-Sky albedo variation of soil with given roughness using their hyperspectral reflectance spectra obtained under laboratory conditions. Remote Sens

Cierniewski J, Ceglarek J, Kaźmierowski C, Roujean JL (2018c) Combined use of remote sensing and geostatistical data sets for estimating the dynamics of shortwave radiation of bare arable soils in Europe. Int J Remote Sens 40:1–16. https://doi.org/10.1080/01431161.2018.1474530

Cipra JE, Baumgardner MF, Stoner ER, MacDonald RB (1971) Measuring radiance characteristics of soil with a field spectroradiometer 1. Soil Sci Soc Am J 35:1014. https://doi.org/10.2136/sssaj1971.03615995003500060043x

Clark RN, Swayze GA, Livo KE et al (2003) Imaging spectroscopy: earth and planetary remote sensing with the USGS Tetracorder and expert systems. J Geophys Res 108:1–2. https://doi.org/10.1029/2002je001847

Coburn CA, Peddle DR (2006) A low-cost field and laboratory goniometer system for estimating hyperspectral bidirectional reflectance. Can J Remote Sens 32:244–253. https://doi.org/10.5589/m06-021

Collinet J, Valentin C (1985) Evaluation of factors influencing water erosion in west Africa using rainfall simulation. Challenges in Africa Hydrology and water resources. IAHS Publ 144:451–461

Cooper KD, Smith JA (1985) A monte carlo reflectance model for soil surfaces with three-dimensional structure. IEEE Trans Geosci Remote Sens GE-23:668–673. https://doi.org/10.1109/tgrs.1985.289385

Coulson KL, Reynolds DW (1971) The spectral reflectance of natural surfaces. J Appl Meteorol 10:1285–1295

Croft H, Anderson K, Kuhn NJ (2012) Reflectance anisotropy for measuring soil surface roughness of multiple soil types. CATENA 93:87–96. https://doi.org/10.1016/j.catena.2012.01.007

Croft H, Anderson K, Brazier RE, Kuhn NJ (2013) Modeling fine-scale soil surface structure using geostatistics. Water Resour Res 49:1858–1870. https://doi.org/10.1002/wrcr.20172

Cruse RM, Linden DR, Radke JK et al (1980) A model to predict tillage effects on soil temperature. Soil Sci Soc Am J 44:378–383. https://doi.org/10.2136/sssaj1980.03615995004400020034x

Curran PJ, Foody GM, Kondratyev K Ya, Kozodyrov VV, Fedchenko PP (1990) Remote sensing of soils and vegetation in the USSR. Taylor & Francis, London, New York Philadelphia

Dalal RC, Henry RJ (1986) Simultaneous determination of moisture, organic carbon, and total nitrogen by near infrared reflectance spectrophotometry 1. Soil Sci Soc Am J 50:120. https://doi.org/10.2136/sssaj1986.03615995005000010023x

Davin EL, de Noblet-Ducoudré N, Friedlingstein P (2007) Impact of land cover change on surface climate: Relevance of the radiative forcing concept. Geophys Res Lett 34. https://doi.org/10.1029/2007gl029678

de Jong SM, Addink EA, van Beek LPH, Duijsings D (2011) Physical characterization, spectral response and remotely sensed mapping of mediterranean soil surface crusts. CATENA 86:24–35. https://doi.org/10.1016/j.catena.2011.01.018

Deering DW, Eck TF, Otterman J (1989) Bidirectional reflectances of three soil surfaces and their characterization through model inversion. In: Proceeding of IGARSS '89. IEEE Publications, New York, Vancouver, pp 670–673

Deering DW, Eck TF, Otterman J (1990) Bidirectional reflectances of selected desert surfaces and their three-parameter soil characterization. Agric For Meteorol 52:71–93. https://doi.org/10.1016/0168-1923(90)90101-b

Derpsch R, Friedrich T, Kassam A, Hongwen L (2010) Current status of adoption of no-till farming in the world and some of its main benefits. Int J Agric Biol Eng 3:1–25. https://doi.org/10.3965/j.issn.1934-6344.2010.01.001-025

Desjardins R. (2009) The impact of agriculture on climate change. In: Eagleshham A, Hardy RWFA (eds) Proceeding of the 21st annual of the NABC conference on adapting agriculture to climate change symposium. National Agricultural Biotechnology Council, Saskatoon, SK, Canada, pp 29–39

Desmet A, Evens H, Gombeer R (1988)). Influence of some factors on the reflectance of bare soils. Pedologie 38:227–247

Dexter R (2004) Diunal and seasonal albedo trends of wheat at the Bratt's Lake Observatory, Saskatchewan. MSc Thesis 125

Di Girolamo L (2003) Generalizing the definition of the bi-directional reflectance distribution function. Remote Sens Environ 88:479–482. https://doi.org/10.1016/j.rse.2003.07.004

Dobos E (2017) Albedo. Encyclopedia of soil science, 3rd edn. Taylor & Francis

Epiphanio JCN, Vitorello I (1984) Inter-relationships between view angles (azimuth) and surface moisture and roughness conditions in field-measured radiometer reflectance of an Oxisol. Colloq l'INRA 23:185–192

Eshel G, Levy GJ, Singer MJ (2004) Spectral reflectance properties of crusted soils under solar illumination. Soil Sci Soc Am J 68:1982. https://doi.org/10.2136/sssaj2004.1982

Evans R (1979) Air photos for soil survey in lowland England: factors affecting the photographic images of bare soils and their relevance to assessing soil moisture content and discrimination of soils by remote sensing. Remote Sens Environ 8:39–63. https://doi.org/10.1016/0034-4257(79)90023-3

FAO/UNESCO (2007) Digital soil map of the world. In: Fao-un—l. Water Div. http://www.fao.org/geonetwork/srv/en/metadata.show?id=14116. Accessed 20 June 2017

Farmer TG, Cook J (2013) Climate change science: a modern synthesis. The physical climate, vol 1

Fedchenko PP (1982) Opredeleniye soderzhaniya gumusa v pochvach po ich cvetu. Pochvoved 10:138–141 (in Russian)

Foody GM (1988) The effects of viewing geometry on image classification. Int J Remote Sens 9:1909–1915. https://doi.org/10.1080/01431168808954989

Fraser RS (1975) Interaction mechanisms within the atmosphere (Chap. 5). In: Manual of remote sensing. American Society of Photogrammetry, Falls Church, VA, pp 181–233

Gerbermann AH, Weber DD (1979) Reflectance of varying mixtures of a clay soil and sand. Photogramm Eng Rem Sens 45:1145–1151

Ghishi G, Morgan RPC (1986) Soil erosion in the European Community. Impact in changing Agriculture. In: Proceedings of a seminar on Land degradation due to to hydrological phenomena in hilly areas. Impact of change of land use and management. Cesena, Italy, p 233

Gilley JE, Kottwitz ER (1995) Random Roughness Assessment by the Pin and Chain Method. Appl Eng Agric 12:39–43. https://doi.org/10.13031/2013.25437

Gilliot J-M, Vaudour E, Michelin J (2017) Soil surface roughness measurement: a new fully automatic photogrammetric approach applied to agricultural bare fields

Girard MC, Białousz S (1989) Characteristics of soils in function of their properties. In: Proceeding 3rd symposium of the ISSS Working Group on remote sensing for soil survey. Prace Komisji Naukowych PTG, Jabłonna, Poland, 1981, pp 105:140–147

Goldshleger N, Ben-Dor E, Benyamini Y, Agassi M (2004) Soil reflectance as a tool for assessing physical crust arrangement of four typical soils in Israel. Soil Sci 169:677–687

Gomez C, Lagacherie P, Coulouma G (2008a) Continuum removal versus PLSR method for clay and calcium carbonate content estimation from laboratory and airborne hyperspectral measurements. Geoderma 148:141–148. https://doi.org/10.1016/j.geoderma.2008.09.016

Gomez C, Viscarra Rossel RA, McBratney AB (2008b) Soil organic carbon prediction by hyperspectral remote sensing and field vis-NIR spectroscopy: an Australian case study. Geoderma 146:403–411. https://doi.org/10.1016/j.geoderma.2008.06.011

Graetz R, Gentle M (1982) The relationships between reflectance in the Landsat wavebands and the composition of an Australian semi-arid shrub rangeland. Photogramm Eng Remote Sens 48:1721–1730

Grant IF, Prata AJ, Cechet RP (2000) The impact of the diurnal variation of albedo on the remote sensing of the daily mean albedo of grassland. J Appl Meteorol 39:231–244. https://doi.org/10.1175/1520-0450(2000)039%3c0231:tiotdv%3e2.0.co;2

Gutman G (1988) A simple method for estimating monthly mean albedo of land surfaces from AVHRR data. J Appl Meteorol 27:973–988. https://doi.org/10.1175/15200450(1988)027%3c0973:ASMFEM%3e2.0.CO;2

Hapke B (1981) Bidirectional reflectance spectroscopy. J Geophys Res 86:3039–3054. https://doi.org/10.1016/j.icarus.2008.01.003

Hapke B (1984) Bidirectional reflectance spectroscopy. 3. Correction for macroscopic roughness. Icarus 59:41–59. https://doi.org/10.1016/0019-1035(84)90054-x

Hapke B (1986) Bidirectional reflectance spectroscopy. 4. The extinction coefficient and the opposition effect. Icarus 67:264–280. https://doi.org/10.1016/0019-1035(86)90108-9

Hapke B (1993) Theory of reflectance and emittance spectroscopy. Cambridge University Press, New York

Hapke B (2002) Bidirectional reflectance spectroscopy. 5. The coherent backscatter opposition effect and anisotropic scattering. Icarus 157:523–534. https://doi.org/10.1006/icar.2002.6853

Hapke B (2008) Bidirectional reflectance spectroscopy. 6. Effects of porosity. Icarus 195:918–926. https://doi.org/10.1016/j.icarus.2008.01.003

Harms JD, Bachmann CM, Ambeau BL et al (2017) Fully automated laboratory and field-portable goniometer used for performing accurate and precise multiangular reflectance measurements. J Appl Remote Sens 11:1. https://doi.org/10.1117/1.jrs.11.046014

Henderson TL, Baumgardner MF, Franzmeier DP et al (1992) High dimensional reflectance analysis of soil organic matter. Soil Sci Soc Am J 56:865. https://doi.org/10.2136/sssaj1992.03615995005600030031x

Horton R, Bristow KL, Kluitenberg GJ, Sauer TJ (1996) Crop residue effects on surface radiation and energy balance—review. Theor Appl Climatol 54:27–37. https://doi.org/10.1007/bf00863556

Huang C, White I, Thwaite EG, Bendeli A (1988) A noncontact laser system for measuring soil surface topography. Soil Sci Soc Am J 52:350–355. https://doi.org/10.2136/sssaj1988.03615995005200020009x

Huete AR (1987) Soil and sun angle interactions on partial canopy spectra. Int J Remote Sens 8:1307–1317. https://doi.org/10.1080/01431168708954776

Hunt GR, Salisbury JW (1970) Visible and near infrared spectra of material and rocks. 1. Silicate minerals. Mod Geol 1:283–300

Idso SB, Jackson RD, Reginato RJ et al (1975) The dependence of bare soil albedo on soil water content. J Appl Meteorol Climatol 14:109–113

Irons JR, Campbell GS, Norman JM et al (1992) Prediction and measurement of soil bidirectional reflectance. IEEE Trans Geosci Remote Sens 30:249–260. https://doi.org/10.1109/36.134075

IUSS Working Group WRB (2014) World reference base for soil resources 2014. International soil classification system for naming soils and creating legends for soil maps

Jackson RD, Moran MS, Slater PN, Biggar SF (1987) Field calibration of reference reflectance panels. Remote Sens Environ 22:145–158

Jackson RD, Teillet PM, Slater PN et al (1990) Bidirectional measurements of surface reflectance for view angle corrections of oblique imagery. Remote Sens Environ 32:189–202. https://doi.org/10.1016/0034-4257(90)90017-g

Jacquemoud S, Baret F, Hanocq JF (1992) Modeling spectral and bidirectional soil reflectance. Remote Sens Environ 41:123–132

Jon Ranson K, Biehl LL, Bauer ME (1985) Variation in spectral response of soybeans with respect to illumination, view and canopy geometry. Int J Remote Sens 6:1827–1842. https://doi.org/10.1080/01431168508948331

Karmanova LA (1981) Vliyaniye Razlichnykh form soedineniy zheleza na spektralnuyu sposobnost i cvet. Pochvoved 9:57–64
King C (1979) Contribution á l'utilisation des micro-ondes pour l'étude des sols. INAPG
Kondratyev KY (1969) Radiacjonnyje Charakteristiki Atmosfery i Zemnoy Powerchnosti. Gidrometeorologiczeskoye Izdatelstwo, Leningrad, Russia
Kondratyev KY, Fedchenko PP (1980) Vlijanije obrabotki na spektralnye otrazatelnye svojstva pochvy. Pochvoved 12:47–53 (in Russ)
König M, Tjemkes S, Kerkmann J (2001) atmospheric instability parameters derived from MSG SEVIRI observations. Amer Meteor Soc Preprints 336–338
Kononova MM (1956) Gumus glavneyshikh tipov pochv SSSR, ego priroda i puti obrazovaniya. In: Dokl. Sovetskikh uchenykh, VI Mezhdunarod. Kongressu Pochvevedov: Khemiya pochv. Izdatelstvo AN SSSR, p 209 (in Russian)
Kononova MM (1963) Organicheskiye veshchestvo pochvy, Ego priroda, cvoystva i metody izucheniya. In: Izdatelstvo AN SSSR, p 314 (in Russian)
Kriebel KT (1976) On the variability of the reflected radiation field due to differing distributions of the irradiation. Remote Sens Environ 4:257–264
Krishna Murti GSR, Satyanarayana KVS (1971) Influence of chemical characteristics in the development of soil colour. Geoderma 5:243–248. https://doi.org/10.1016/0016-7061(71)90013-9
Lagacherie P, Baret F, Feret JB et al (2008) Estimation of soil clay and calcium carbonate using laboratory, field and airborne hyperspectral measurements. Remote Sens Environ 112:825–835. https://doi.org/10.1016/j.rse.2007.06.014
Latz KRA, Weismiller GE, Van Scoyoc GE, Baumgardner MF (1984) Characteristic variation in spectral reflectance of selected Eroded Alfisols. Soil Sci Soc Am J 48:1130–1134
Lekner J, Dorf MC (1988) Why some things are darker when wet. Appl Opt 27:1278. https://doi.org/10.1364/ao.27.001278
Lewis P, Barnsley MJ (1994) Influence of the sky radiance distribution on various formulations of the earth surface albedo. In: Proceedings of 6th international symposium physical measurements and signatures in remote sensing. Val d'Is.re, pp 707–716
Liang S, Fang H, Chen M et al (2002) Validating MODIS land surface reflectance and albedo products: methods and preliminary results. Remote Sens Environ 83:149–162. https://doi.org/10.1016/s0034-4257(02)00092-5
Lillesand TM, Kiefer RW, Chipman JW (2004) Remote sensing and image interpretation, 5th edn. New York
Linden DR (1979) A model to predict soil water storage as effected by tillage practices. Ph.D. Dissertation. University of Minnesota
Martonchik JV, Bruegge CJ, Strahler AH (2000) A review of reflectance nomenclature used in remote sensing. Remote Sens Environ 19:9–20
Matthias ADD, Fimbres A, Sano EEE et al (2000) Surface roughness effects on soil albedo. Soil Sci Soc Am J 64:1035–1041. https://doi.org/10.2136/sssaj2000.6431035x
Mikhajlova NA, Orlov DS (1986) Opticheskie Svoystva Pochv i Pochvennych Komponentov. Russ Nauk 118
Milfred CJ, Kiefer RW (2010) Analysis of soil variability with repetitive aerial photography1. Soil Sci Soc Am J 40:553. https://doi.org/10.2136/sssaj1976.03615995004000040028x
Miller P, Lanier W, Brandt S (2001) Using growing degree days to predict plant stages. Mont State Univ Ext Serv 9:MT00103 AG 7/2001
Milton EJ, Webb JP (1987) Ground radiometry and airborne multispectral survey of bare soils. Int J Remote Sens 8:3–14. https://doi.org/10.1080/01431168708948611
Mitchell JK, Jones BAJ (1978) Micro-relief surface depression storage: changes during rainfall events and their application to rainfall-runoff models. Can Water Resour J 14:777–802. https://doi.org/10.4296/cwrj0401121
Monfreda C, Ramankutty N, Foley JA (2008) Farming the planet: 2. Geographic distribution of crop areas, yields, physiological types, and net primary production in the year 2000. Global Biogeochem Cycles 22:1–19. https://doi.org/10.1029/2007gb002947

Monteith JL, Szeicz G (1961) The radiation balance of bare soil and vegetation. Q J R Meteorol Soc 87:159–170. https://doi.org/10.1002/qj.49708737205
Moreno RG, Requejo AS, Alonso AMT, Barrington S, Alvarez MCD (2008) Shadow analysis: a method for measuring soil surface roughness. Geoderma 146:201–208. https://doi.org/10.1016/j.geoderma.2008.05.026
Morgan RPC (1985) Soil degradation and soil erosion in the loamy belt of northern Europe. Soil erosion. In: Ghishi & Morgan. Balkema, pp 165–172
Morra MJ, Hall MH, Freeborn LL (1991) Carbon and nitrogen analysis for soil fractions using near-ifrared reflectance spectroscopy. Soil Sci Soc Am J 55:288–291
Mulders MA (1987) Remote Sensing in Soil Science
Music H, Pelletier R (1986) Response of some Thematic Mapper band rations to variation in soil water content. Photogramm Eng Remote Sens 52:1661–1668
Nicodemus F, Richmond J, Hsia J (1977) Geometrical considerations and nomenclature for reflectance. Sci Technol 60:1–52. https://doi.org/10.1109/lpt.2009.2020494
Norman JM, Welles JM, Walter EA (1985) Contrasts among bidirectional reflectance of leaves, canopies, and soils. IEEE Trans Geosci Remote Sens GE-23:659–667. https://doi.org/10.1109/tgrs.1985.289384
Obukhov AI, Orlov DS (1964) Spektralnaya otrazhatelnaya sposobnost glavneysych tipov pochv i vozmoznost ispolzovaniya diffuznogo otrazhenija pri pochvennych issledovaniyach. Pochvoved 28:83–94
Oguntunde PG, Ajayi AE, van de Giesen N (2006) Tillage and surface moisture effects on bare-soil albedo of a tropical loamy sand. Soil Tillage Res 85:107–114. https://doi.org/10.1016/j.still.2004.12.009
Oke TR (1987) Boundary layer climates. Routledge
Onstad CA (1984) Depressional storage on tilled soil surfaces. Trans ASAE 27:729–732. https://doi.org/10.13031/2013.32861
Orlov DS (1966) Kalichestvennye zakony otrazhenija sveta ot pochvy. Vlijanie razmera chasti na otrazheniye. Nauch Dokl Vys Sk Biol Nauk 4:206–210
Orlov DS (1969) Kalichestvennye zakony otrazhenija sveta ot pochvy. Vlijanie razmera chasti na otrazheniye. Nauch Dokl Vys Sk Biol Nauk 4:26–210
Orlov DS, Sukhanova NI (1983) Vliyanije gumusa na otrazhatelnuyu sposobnost pochv podzony yuzhnoy taygi. Pochvoved 10:43–51
Orlov DS, Bidabayeva RM, Sadovnikov YN (1976) Kalichestvennye zakony otrazheniya sveta ot pochvy. VII.Spektralnye otrazheniye glavnykh pochv Kazakhstana. Nauchnye Dokl Vyss Shkoly Biol Nauk 20:109–113
Otterman J (1981) Reflection from soil with sparse vegetation. Adv Sp Res 1:115–119. https://doi.org/10.1016/0273-1177(81)90387-2
Otterman J (1985) Bidirectional and hemispheric reflectivities of a bright soil plane and a sparse dark canopy. Int J Remote Sens 6:897–902. https://doi.org/10.1080/01431168508948512
Palmer JM (1982) Field standards of reflectance. Photogramm Eng Remote Sensing 48:1623–1625
Peter Heng BC, Chandler JH, Armstrong A (2010) Applying close range digital photogrammetry in soil erosion studies. Photogramm Rec 25:240–265. https://doi.org/10.1111/j.1477-9730.2010.00584.x
Philpot WD (2010) Spectral reflectance of wetted soils. Art Sci Appl Reflectance Spectrosc 1–11. https://doi.org/10.13140/2.1.2306.0169
Piech KR, Walker JE (1974) Interpretation of soils. Photogramm Eng 40:87–94
Pinty B, Szejwach G (1985) A new technique for inferring surface albedo from satellite observations. J Clim Appl Meteorol 24:741–750. https://doi.org/10.1175/1520-0450(1985)024%3c0741:antfis%3e2.0.co;2
Pinty B, Verstraete MM, Dickinson RE (1989) A physical model for predicting bidirectional reflectances over bare soil. Remote Sens Environ 27:273–288. https://doi.org/10.1016/0034-4257(89)90088-6

Potter KN, Horton R, Cruse RM (1987) Soil surface roughness effects on radiation reflectance and soil heat Flux1. Soil Sci Soc Am J 51:855. https://doi.org/10.2136/sssaj1987.03615995005100040003x

Pratt PF (1961) Effect of pH on the cation-exchange capacity of surface soils. Soil Sci Soc Am J 25:96–98. https://doi.org/10.2136/sssaj1961.03615995002500020008x

Rechid D, Jacob D, Hagemann S, Raddatz TJ (2005) Vegetation effect on land surface albedo: method to separate vegetation albedo from the underlying surface using satellite data. Geophys Res Abstr 7:07153

Rieke-Zapp DH, Nearing MA (2005) Digital close range photogrammetry for measurement of soil erosion. Photogramm Rec 20:69–87. https://doi.org/10.1111/j.1477-9730.2005.00305.x

Römkens MJM, Wang JY (1986) Effects of tillage on surface roughness. Trans ASAE 29:429–433

Rosa DJ, Cooper M, Darboux F, Medeiros JC (2012) Soil roughness evolution in different tillage systems under simulated rainfall using a semivariogram-based index. Soil Tillage Res 124:226–232. https://doi.org/10.1016/j.still.2012.06.001

Roxy MS, Sumithranand VB, Renuka G (2010) Variability of soil moisture and its relationship with surface albedo and soil thermal diffusivity at astronomical observatory, Thiruvananthapuram, South Kerala. J Earth Syst Sci 119:507–517. https://doi.org/10.1007/s12040-010-0038-1

Sacks WJ, Deryng D, Foley JA, Ramankutty N (2010) Crop planting dates: an analysis of global patterns. Glob Ecol Biogeogr 19:607–620. https://doi.org/10.1111/j.1466-8238.2010.00551.x

Sandmeier SR (2000) Acquisition of bidirectional reflectance factor data with field goniometers. Remote Sens Environ 73:257–269. https://doi.org/10.1016/s0034-4257(00)00102-4

Schaepman-Strub G, Schaepman ME, Painter TH et al (2006) Reflectance quantities in optical remote sensing-definitions and case studies. Remote Sens Environ 103:27–42. https://doi.org/10.1016/j.rse.2006.03.002

Schneider SH, Dickinson RE (1974) Climate modeling. Rev Geophys 12:447. https://doi.org/10.1029/rg012i003p00447

Schwanghart W, Jarmer T (2011) Linking spatial patterns of soil organic carbon to topography—a case study from south-eastern Spain. Geomorphology 126:252–263. https://doi.org/10.1016/j.geomorph.2010.11.008

Selige T, Böhner J, Schmidhalter U (2006) High resolution topsoil mapping using hyperspectral image and field data in multivariate regression modeling procedures. Geoderma 136:235–244. https://doi.org/10.1016/j.geoderma.2006.03.050

Sellers PJ, Meeson BW et al (1995) Remote sensing of the land surface for studies of global change: models algorithms experiments. Remote Sens Environ 4257:3–26

Shoshany M (1993) Roughness-reflectance relationship of bare desert terrain: an empirical study. Remote Sens Environ 45:15–27. https://doi.org/10.1016/0034-4257(93)90078-c

Stevens A, Nocita M, Tóth G et al (2013) Prediction of Soil Organic Carbon at the European Scale by Visible and Near InfraRed Reflectance Spectroscopy. PLoS One 8. https://doi.org/10.1371/journal.pone.0066409

Stevens A, Udelhoven T, Denis A, Tychon B, Lioy R, Hoffmann L, van Wesemael B (2010) Measuring soil organic carbon in croplands at regional scale using airborne imaging spectroscopy. Geoderma 158:32–45

Stoner ER, Baumgardner MF, Biehl LL, Robinson BF (1980) Atlas of soil reflectance properties. Agricultural Experiment Statio, Purdue University, West Lafayette, Indiana (Res Bull 962)

Swain PH (1978) Remote sensing: the quantitative approach. Mc-Graw Hill, New York

Taconet O, Ciarletti V (2007) Estimating soil roughness indices on a ridge-and-furrow surface using stereo photogrammetry. Soil Tillage Res 93:64–76. https://doi.org/10.1016/j.still.2006.03.018

Terelak H, Stuczynski T, Motowicka-Terelak T et al (2008) Monitoring of chemistry of arable soils in Poland in 2005–2007. In: Inspection of Environmental Protection. Warsaw, Rep, p 135 (in Polish)

Thomsen LM, Baartman JEM, Barneveld RJ, Starkloff T, Stolte J (2015) Soil surface roughness: comparing old and new measuring methods and application in a soil erosion model. Soil 1:399–410. https://doi.org/10.5194/soil-1-399-2015

Tolchelnikov I (1974) Opticheskiye svoystva landshafta. Leningrad
Tóth G, Jones A, Montanarella L (2013) The LUCAS topsoil database and derived information on the regional variability of cropland topsoil properties in the European Union. Environ Monit Assess 185:7409–7425. https://doi.org/10.1007/s10661-013-3109-3
Tsvetsinskaya EA, Schaaf CB, Gao F et al (2006) Spatial and temporal variability in moderate resolution imaging spectroradiometer-derived surface albedo over global arid regions. J Geophys Res Atmos 111:1–10. https://doi.org/10.1029/2005jd006772
Twomey SA, Bohren CF, Mergenthaler JL (1986) Reflectance and albedo differences between wet and dry surfaces. Appl Opt 25:431. https://doi.org/10.1364/ao.25.000431
Ulaby FT, Moore RK, Fung AK (1982) Microwave remote sensing active and passive. Addison-Wesley, Reading, Massachusetts
UN Sustainable Development Knowledge Platform (2015) Open working group proposal for sustainable development goals
USDA (1994) Major world crop areas and climatic profiles. In: agricultural handbook. World Agricultural Outlook Board
Van der Heide G, Koolen AJ (1980) Soil surface albedo and multispectral reflectance of short-wave radiation as a function of degree of slacking. NethJ Agric Sci 28:252–258
Vermang J, Norton LD, Baetens JM et al (2013) Quantification of soil surface roughness evolution under simulated rainfall. Am Soc Agric Eng 56:505–514. https://doi.org/10.13031/2013.42670
Vinogradov BV (1976) Issledovaniye pochvennovo pokrova. In: Kosmicheskiye metody izucheniya sredy. (in Russian). Mysl, Moscov
Vinogradov BV (1981) Distancyonnaya indikaciya soderzhaniya gumusa v pochvach. Pochvoved 11:114–123
Vinogradov BV (1983) Kolichesvennoya vyrazheniye funkci distacyonnoy indikacii vlazhnostii pochv. Dokl Akad Nauk SSR 272:247–250
Viscarra Rossel R (2009) The Soil Spectroscopy Group and the development of a global soil spectral library. NIR News 20:14. https://doi.org/10.1255/nirn.1131
Viscarra Rossel RA, Behrens T, Ben-Dor E et al (2016) A global spectral library to characterize the world's soil. Earth Sci Rev 155:198–230. https://doi.org/10.1016/j.earscirev.2016.01.012
Walthall CL, Norman JM, Welles JM et al (1985) Simple equation to approximate the bidirectional reflectance from vegetative canopies and bare soil surfaces. Appl Opt 24:383. https://doi.org/10.1364/ao.24.000383
Wang Z, Coburn CA, Ren X, Teillet PM (2012) Effect of soil surface roughness and scene components on soil surface bidirectional reflectance factor. Can J Soil Sci 92:297–313. https://doi.org/10.4141/cjss2011-069
White JL (1971) Interpretation of infrared spectra of soil minerals. Soil Sci 112:22–29
Worthington C, Hutchinson C (2005) Accumulated growing degree days as a model to determine key developmental stages and evaluate yield and quality of potat. Proc Fla State Hort Soc 1:98–101
Zobeck TM, Onstad CA (1987) Tillage and rainfall effects on random roughness: a review. Soil Till Res 9:1–20

Asymptotic Methods in the Theory of Light Scattering by Nonspherical Particles

Aleksey Malinka

Abstract The method of stationary phase is applied to calculate the amplitudes of scattering by nonspherical particles that are much larger than the wavelength. The method is valid for scattering angles outside the narrow cone around the forward direction ($\theta > 1/x$, x is the dimensionless particle size). The scattering amplitudes, and therefore the scattering phase functions, can be calculated using Stokes' theorem for the cases when the field inside the particle is known. These cases match different approximations of physical optics: Fraunhofer diffraction, the Rayleigh-Gans and Wentzel-Kramers-Brillouin approximations. The integral of the field over the particle is converted to the integral over its boundary and then, considering the particles much larger than the wavelength, is calculated with the method of stationary phase that assumes that the essential contribution to the integral comes from the points of the constructive interference, i.e. where the phase of the wave is stationary. The differential cross-section of scattering by an ensemble of chaotically oriented particles is calculated by the non-coherent averaging over particles orientation. Simple approximating formulas are given that relates the scattering properties in the abovementioned cases directly to the microphysical characteristics of the particle ensemble.

1 Introduction

In this work the term 'asymptotic' refers to methods known in mathematics as the methods of stationary phase (Bleistein and Handelsman 1986; Born and Wolf 1968). These methods consider the integrals of fast oscillating functions with a factor of the kind $\exp[ikf(\mathbf{r})]$, where x is a constant parameter, and give the asymptotic behavior of these integrals at large x. The core of the approach is that the fast oscillations destruct each other after integration and the non-vanishing values, contributing to the

A. Malinka (✉)
Institute of Physics, National Academy of Sciences of Belarus, 220072 pr. Nezavisimosti 68-2, Minsk, Belarus
e-mail: a.malinka@ifanbel.bas-net.by

A. Kokhanovsky (ed.), *Springer Series in Light Scattering*,
Springer Series in Light Scattering,
https://doi.org/10.1007/978-3-030-38696-2_5

integral, come from the points where the phase is stationary. In physics, this effect is called the positive interference of waves. So, because of such a close analogy, these methods can be efficiently applied to light scattering by particles whose size significantly exceeds the wavelength of radiation. Hereinafter we will only consider particles that are much larger than the wavelength:

$$x \gg 1, \tag{1}$$

where $x = kD$ is the dimensionless particle size (k is a wavenumber and D is a typical particle dimension). This approach originates from the classical Huygens–Fresnel principle and Kirchhoff diffraction formula, however considers the scattering angles θ that satisfy the relation:

$$x\theta \gg 1. \tag{2}$$

It is a well-known fact that only few problems in the theory of light scattering have a strict solution, like the Mie solution for spherical scatterers. However, the spherical particles are quite rare in nature. These are, e.g., droplets in warm clouds or liquid aerosols, air bubbles in water and ice, fat globules in milk. But most natural particles, such as crystals in cirrus clouds and solids in some aerosols—dust, smokes, or volcanic ashes—in the atmosphere, phytoplankton in seawaters, cells in biological tissues are generally nonspherical. Tons of literature are dedicated to the questions of scattering by nonspherical particles and we cannot mention here any significant part of these works (see Macke et al. 1996; Yang and Liou 1996; Kokhanovsky and Macke 1997; Shcherbakov et al. 2006; Borovoi et al. 2014; Rother and Kahnert 2014; Liou and Yang 2016 for some examples).

The methods of calculation of the characteristics of light scattering by nonspherical particles are very complicated and time consuming. At the same time, such classical approaches as Fraunhofer diffraction, Rayleigh–Gans and Wentzel–Kramers–Brillouin approximations proved their efficiency in a number of problems. The Fraunhofer diffraction theory has high accuracy for optically hard particles, much larger than the wavelength, i.e. when

$$|m - 1|x \gg 1, \tag{3}$$

where $m = n + i\kappa$ is the complex relative refractive index of the particle.

Fraunhofer diffraction completely determines the small-angle scattering by such particles (Bohren and Huffman 1983; van de Hulst 1957), which is extremely important in a number of optical problems (Wells 1973), such as image transfer (Zege et al. 1991) or remote sensing, including particle sizing and lidar sounding (Baum et al. 2005; Bissonnette and Hutt 1990; Roy et al. 1997; Malinka and Zege 2007).

In the case of spherical particles, the Fraunhofer diffraction pattern is an asymptotic behavior of the Mie solution when the particle size approaches infinity (van de Hulst 1957). However, the Fraunhofer diffraction theory is not restricted by the circular shape of an obstacle. The diffraction by regular structures (gratings) or single

obstacles of regular shape (slit, rectangle, or circle) is the commonly known classical problem of optics. However, the question of light diffraction by particles of random shape or, at least, for chaotically oriented nonspherical ones is not investigated properly. Abramyan (1981) considered very small diffraction angles, so the obtained results cannot be used outside the Poisson spot region. The case of very small deviations of a particle shape from a sphere was examined by Abdelazecz (1983). Shifrin et al. (1984) considered the strictly random shape of an obstacle when its contour was described by a random monotypic function $R(\varphi)$ in polar coordinates. Their approach required an a priori knowledge of the correlation function $\langle R(\varphi)R(\varphi+\psi)\rangle$ of a random contour. In the work (Jones 1987) this correlation function was investigated experimentally for different kinds of particles. In Sect. 2 of this work the simple approximating formula and its derivation are given for Fraunhofer diffraction by an ensemble of randomly oriented nonspherical particles. These results were originally published in (Malinka and Zege 2009; Malinka 2010a, b).

Another approach, which unlike Fraunhofer diffraction is used for optically soft particles, is the Rayleigh–Gans (RG) approximation (an equivalent of the 1st Born approximation in quantum mechanics). It works when the phase shift of the electromagnetic wave inside a particle is negligible and the inner field is approximately equal to the incident one. The condition for the phase shift looks as:

$$|m-1|x \ll 1. \tag{4}$$

Although having a different physical meaning, mathematically this problem is fully equivalent to Fraunhofer diffraction. It is just a 3-dimensional analog, where the initial integral is taken over the particle volume, while in the Fraunhofer diffraction approach it is taken over the screen area.

Most biological particles, such as phytoplankton in seawaters (Kopelevich 1983), erythrocytes in blood or other cells in biological tissues (Duck 1990), and some particles of non-living origin, like brine inclusions in sea ice (Light 2010), are optically soft, i.e. meet the condition

$$|m-1| \ll 1. \tag{5}$$

Unfortunately, conditions (1) and (4) are rarely fulfilled in practice together, because the above mentioned optically soft particles that meet Eq. (5) are usually too large to match simultaneously Eq. (4). For this reason the RG approximation has quite narrow application area in the light scattering practice and is considered, first of all, due to its methodological worth.

An approximation that accounts for the phase shift $\mathrm{Re}(m-1)x = (n-1)x$ in optically soft large particles is the Wentzel–Kramers–Brillouin (WKB) approximation, which is often called the approximation of physical optics and is closely related to the eikonal approximation in geometrical optics. It neglects the reflection and refraction by the particle boundary and thus requires condition (5) only, imposing no restriction on the phase shift $(n-1)x$. The WKB approximation provides a more accurate solution for large optically soft particles than the RG approximation and has

the wider application scope. The solutions for the ensembles of randomly shaped or chaotically oriented nonspherical particles within these two approximations are given in Sects. 3 and 4, respectively. These results were originally published in Malinka (2011, 2015a) and were applied to the description of phytoplankton (Malinka and Zege 2011; Malinka 2015b) and sea ice inherent optical properties (Malinka et al. 2018; Zege et al. 2018), as well as to remote sensing of the sea ice cover (Zege et al. 2015; Istomina et al. 2015a, b).

2 Fraunhofer Diffraction

2.1 Statement of the Problem

Fraunhofer diffraction implies that an optically hard particle, i.e. the particle with the refractive index that meets condition (3), just obscures the part of the front of the incident wave. Let the incident wavefront be parallel to the xy-plane and the wavevector $\mathbf{k}_0$ be perpendicular to it. The wavevector of the diffracted wave is $\mathbf{k}_s$. As the obstacle is much larger than the wavelength [see Eq. (1)], the diffracted light is concentrated at the small angles:

$$\theta \ll 1. \tag{6}$$

Due to Eq. (6) we can assume that the projection of vector $\mathbf{k}_s$ onto the xy-plane is equal to the difference

$$\Delta\mathbf{k} = \mathbf{k}_s - \mathbf{k}_0 = (k\theta\cos\varphi, k\theta\sin\varphi), \tag{7}$$

where k is the wavenumber, θ is the diffraction angle, φ is the azimuth. So that

$$\Delta k = |\Delta\mathbf{k}| = k\theta = \frac{2\pi}{\lambda}\theta, \tag{8}$$

where λ is the wavelength.

Within approximation (6) $\Delta\mathbf{k}$ is perpendicular to $\mathbf{k}_0$ and lies in the xy-plane.

Let the contour (the edge of the screen) be described by the two-dimensional vector function

$$\mathbf{r} = \mathbf{r}(l) = (x(l), y(l)). \tag{9}$$

The derivative of this function is a tangent vector to the contour:

$$\frac{d\mathbf{r}}{dl} = \mathbf{t}(l) = (\cos\psi(l), \sin\psi(l)), \tag{10}$$

where ψ is the angle between the tangent line at the point $\mathbf{r}(l)$ and the x-axis, l is the natural parameter of the contour (the length along the curve).

The amplitude scattering function of Fraunhofer diffraction is (see e.g. van de Hulst 1957; Born and Wolf 1968):

$$f = \frac{1}{\lambda} \iint\limits_S e^{i\,\Delta\mathbf{k}\cdot\mathbf{r}} d^2\mathbf{r}, \tag{11}$$

the integral is taken over the area of the screen S. Formula (11) realizes the Huygens principle in the far field zone, when the secondary sources are distributed uniformly over the area S.

The differential cross-section is

$$\frac{dC_{sca}}{d\Omega} = |f|^2. \tag{12}$$

It meets the normalization

$$\int \frac{dC_{sca}}{d\Omega}\, d\Omega = \int\limits_0^{2\pi} \int\limits_0^{\infty} |f|^2 \theta d\theta d\varphi = S, \tag{13}$$

where S is the area of the obstacle, which is equal to the total scattering cross-section in Fraunhofer diffraction.

2.2 Solution for a Single Obstacle

By Stokes' theorem the integral over the screen area (11) can be rewritten through the integral over the contour bordering the screen:

$$f = \frac{-i}{\lambda\,\Delta k^2} \oint e^{i\,\Delta\mathbf{k}\cdot\mathbf{r}}\, \Delta\mathbf{k} \times d\mathbf{r}, \tag{14}$$

where the sign $\times$ in this (two-dimensional) case denotes

$$\mathbf{a} \times \mathbf{b} = a_x b_y - b_x a_y. \tag{15}$$

Passing to the integration over l, we have

$$f = \frac{-i}{\lambda\,\Delta k^2} \oint e^{i\,\Delta\mathbf{k}\cdot\mathbf{r}}\, \Delta\mathbf{k} \times \mathbf{t}\, dl, \tag{16}$$

where $\mathbf{t}$ is a tangent vector introduced in Eq. (10). Formula (16) transforms the surface-distributed secondary sources to those distributed along the contour. Function $\Delta\mathbf{k} \times \mathbf{t}$ describes the contribution of the these sources to integral (16).

Now we consider the case when the obstacle is much larger than the wavelength. This means that the typical size of the obstacle D satisfies the condition

$$D \gg \lambda. \tag{17}$$

Let us consider first the region of the diffraction angles that are far outside the main diffraction peak. The main diffraction peak is concentrated near the forward direction at angles ranging from 0 to about $1/x$, $x = \pi D/\lambda$ being the Fraunhofer diffraction parameter or the dimensionless obstacle size. If the diffraction angle is far outside the main peak, then

$$\Delta k\, D = \frac{\pi}{\lambda}\theta\, D = x\,\theta \gg 1. \tag{18}$$

Note that simultaneously the diffraction angle θ meets condition (6).

With this regard, to calculate integral (16) we can use the method of stationary phase. Under condition (18) the nonvanishing contribution to integral (16) is due only to the points where the phase is stationary:

$$\frac{d\,\Delta\mathbf{k}\cdot\mathbf{r}}{dl} = \Delta\mathbf{k}\cdot\mathbf{t} = 0, \tag{19}$$

because the waves from the vicinity of these points have the same phase and thus undergo positive (constructive) interference. The waves from the other points have the different phases and thus they destruct each other, because of the fast oscillations of the exponential function.

Condition (19) is satisfied when vectors $\Delta\mathbf{k}$ and $\mathbf{t}$ are orthogonal (see Fig. 1). At these points the product $\Delta\mathbf{k} \times \frac{d\mathbf{r}}{dl}$ equals

$$\Delta\mathbf{k} \times \frac{d\mathbf{r}}{dl} = \Delta\mathbf{k} \times \mathbf{t} = \pm\Delta k, \tag{20}$$

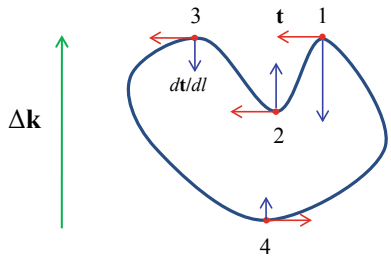

Fig. 1 Example of a contour and the points where the tangent line is perpendicular to $\Delta\mathbf{k}$. The green arrow is vector $\Delta\mathbf{k}$, the red arrows are tangent vectors $\mathbf{t}$, and the blue arrows are vectors $d\mathbf{t}/dl$

where sign '+' is taken for point 4, and sign '–' for points 1–3. Thus, the contribution of every stationary point $\mathbf{r}_s$ [the solution of Eq. (19)] to the integral in Eq. (16) is

$$I_s = \int\limits_{\delta r_s} e^{i\,\Delta\mathbf{k}\cdot\mathbf{r}}\,\Delta\mathbf{k}\times\mathbf{t}\,dl = \int\limits_{-\infty}^{\infty} \exp\left(i\,\Delta\mathbf{k}\cdot\mathbf{r}_s + i\,\Delta\mathbf{k}\cdot\frac{d^2\mathbf{r}_s}{dl^2}\,\frac{l^2}{2}\right)(\pm\Delta k)dl, \tag{21}$$

where δr_s is the vicinity of point $\mathbf{r}_s$ and the phase is expanded to the second order of l [the first order is equal to zero due to condition (19)]. Integral (21) is equal to (see, e.g., Bleistein and Handelsman 1986):

$$I_s = \exp\left(i\,\Delta\mathbf{k}\cdot\mathbf{r}_s + \frac{\pi i}{4}\mathrm{sgn}_s\right)(\pm\Delta k)\sqrt{\frac{2\pi}{\left|\Delta\mathbf{k}\cdot\frac{d^2\mathbf{r}_s}{dl^2}\right|}}. \tag{22}$$

The second derivative $d^2\mathbf{r}_s/dl^2$ is the first derivative of $\mathbf{t}$ and thus it is perpendicular to $\mathbf{t}$ and parallel or antiparallel to $\Delta\mathbf{k}$:

$$\Delta\mathbf{k}\cdot\frac{d^2\mathbf{r}_s}{dl^2} = \Delta\mathbf{k}\cdot\frac{d\mathbf{t}}{dl} = \pm\Delta k\left|\frac{d\mathbf{t}}{dl}\right|. \tag{23}$$

Value sgn_s denotes the sign in Eq. (23): $\mathrm{sgn}_s = 1$ (sign +), if $\Delta\mathbf{k}$ and $d\mathbf{t}/dl$ are parallel, and $\mathrm{sgn}_s = -1$ (sign −), if they are antiparallel. An example of the contour is represented in Fig. 1. There $\mathrm{sgn}_s = 1$ in points 2 and 4, and $\mathrm{sgn}_s = -1$ at points 1 and 3.

The absolute magnitude of vector $d\mathbf{t}/dl$ equals to the curvature of the contour:

$$\left|\frac{d\mathbf{t}}{dl}\right| = \frac{1}{R_s}, \tag{24}$$

where R_s is the contour curvature radius at point $\mathbf{r}_s$. Hence, integral (21) is equal to

$$I_s = \exp\left(i\,\Delta\mathbf{k}\cdot\mathbf{r}_s + \frac{\pi i}{4}\mathrm{sgn}_s\right)(\pm\Delta k)\sqrt{\frac{2\pi R_s}{\Delta k}}. \tag{25}$$

For function f we get:

$$f = \frac{-i}{\lambda\,\Delta k^2}\sum_s I_s = \frac{\mp i}{\lambda\,\Delta k^2}\sum_s \exp\left(i\,\Delta\mathbf{k}\cdot\mathbf{r}_s + \frac{\pi i}{4}\mathrm{sgn}_s\right)\sqrt{2\pi\,\Delta k R_s}. \tag{26}$$

The differential cross-section is

$$|f|^2 = \frac{2\pi}{\lambda^2 \Delta k^3} \sum_q \sum_s \exp\left(i\, \Delta\mathbf{k} \cdot (\mathbf{r}_q - \mathbf{r}_s) + \frac{\pi i}{4} (\mathrm{sgn}_q - \mathrm{sgn}_s) \right) \sqrt{R_q R_s}. \quad (27)$$

Formula (27) gives the solution for a single arbitrary-shaped screen with a piecewise-smooth boundary.

Let us separate the terms with $q = s$ and $q \neq s$ in Eq. (27):

$$|f|^2 = \frac{2\pi}{\lambda^2 \Delta k^3} \sum_s R_s + Int. \quad (28)$$

In Eq. (28) the first term (for $q = s$) describes incoherent addition of the intensities of the waves diffracted by every stationary point. The second term, *Int* (for $q \neq s$), describes the interference of the waves diffracted by the different stationary points.

2.3 Randomly Oriented Obstacles

If the medium is isotropic then the particles are randomly oriented in the plane of a wavefront. So, let us average function (28) over the contour orientation (the same, over φ, the azimuth of $\Delta\mathbf{k}$). As seen in Fig. 1, rotation of $\Delta\mathbf{k}$ on $d\varphi$ shifts points 1–4 along the contour to dl and rotates the tangent vectors on $d\psi = d\varphi$, as the tangent vectors are always perpendicular to $\Delta\mathbf{k}$.

The curvature radius by definition is

$$R = \frac{dl}{d\psi}. \quad (29)$$

Hence, azimuth averaging gives

$$\frac{dC_{sca}}{d\Omega} = \overline{|f|^2} = \frac{1}{2\pi} \int_0^{2\pi} |f|^2 d\varphi = \frac{2\pi}{\lambda^2 \Delta k^3} \sum_s \int_0^{\pi} R_s \frac{d\psi}{\pi} + \overline{Int}. \quad (30)$$

A contour can always be divided into arcs, where function $\psi(l)$ is monotonic, so that the inverse function $l(\psi)$ is monotypic. Every arc has only one stationary point. The integral

$$\int R_s d\psi = \int \frac{dl}{d\psi} d\psi = l_s \quad (31)$$

is the length of the arc. So the sum of the arc lengths

$$\sum l_s = L, \quad (32)$$

where L is the length of the entire contour.

That is:

$$\int_0^{\pi} \sum_s R_s \frac{d\psi}{\pi} = \frac{L}{\pi}. \tag{33}$$

Formula (33), in fact, means that the average curvature radius of the contour is the contour length divided by 2π, and the sum of radii at points with parallel tangent lines on average is equal to the doubled average radius of the contour (this statement is obvious for a circle: there are always two points with parallel tangent lines and they are diametrically opposed).

Therefore, we get for Eq. (30):

$$\frac{dC_{sca}}{d\Omega} = \frac{2L}{\lambda^2 \Delta k^3} + \overline{Int} = \frac{2\lambda L}{(2\pi)^3 \theta^3} + \overline{Int}. \tag{34}$$

Equation (34) shows that the main term in the differential cross-section of a randomly oriented obstacle far outside of the main diffraction peak behaves as θ^{-3} and depends on the perimeter of the obstacle only.

The differential cross-section of Fraunhofer diffraction by a rectangular screen averaged over orientation in the xy-plane and the first term of function (34) are plotted in Fig. 2. The differential cross-section of the rectangle was calculated by a straight-

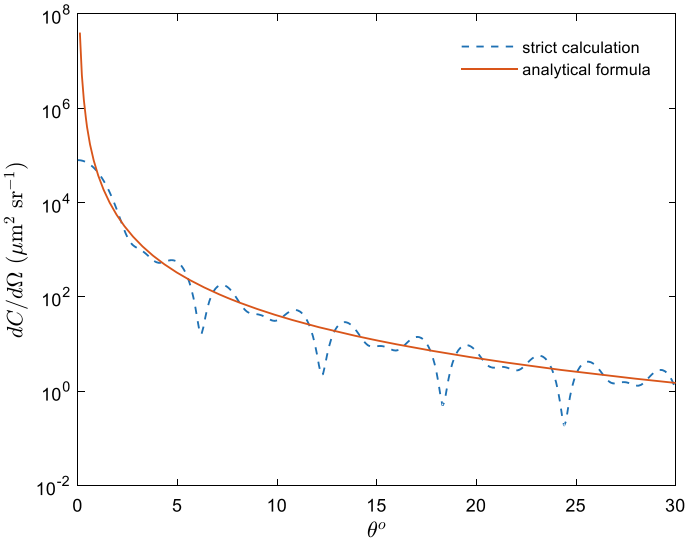

Fig. 2 Differential cross-section of Fraunhofer diffraction by a randomly oriented rectangular screen with sides of 10 and 15 μm (dashes) and the first term of Eq. (34) (curve). Wavelength is equal to 532 nm

forward integration of the basic formula [Eq. (11)] and by numerical averaging over the azimuth. The oscillations on the plot mirror the interferential term $\overline{Int}$ in Eq. (34) and are around the average value given by the first term.

The critical angular value λ/L that defines the first diffraction peak is about ~0.6° in this case. It is seen that for smaller angles formula (34) does not work, approaching infinity at zero. However, for angles larger than critical, the first term of formula (34) correctly describes the angular behavior of the differential cross-section except for oscillations.

2.4 Particular Case of Spherical Particles

The foregoing results for the general case could be easily gotten in the particular case of spherical particles, i.e. circular obstacles. The diffraction differential cross-section on a circular screen is (e.g., van de Hulst 1957)

$$\frac{dC}{d\Omega}^{circ} = r^2 \frac{J_1^2(x\theta)}{\theta^2}, \tag{35}$$

where r is the radius, $J_1(z)$ is the Bessel function, and

$$x = \frac{2\pi r}{\lambda}. \tag{36}$$

Considering the limit

$$x\theta \to \infty, \tag{37}$$

which corresponds to Eq. (18), and writing the asymptotic expression for the Bessel function

$$J_1(z \gg 1) = \sqrt{\frac{2}{\pi z}} \cos\left(z - \frac{3\pi}{4}\right), \tag{38}$$

we can write Eq. (35) as

$$\frac{dC}{d\Omega}^{circ} = \frac{2r^2}{\pi x\theta^3} \cos^2\left(x\theta - \frac{3\pi}{4}\right). \tag{39}$$

We get

$$\frac{dC}{d\Omega}^{circ} = \frac{2\lambda(2\pi r)}{(2\pi)^3\theta^3}\left(1 + \cos\left(2x\theta - \frac{3\pi}{2}\right)\right). \tag{40}$$

So the first term of formula (40) for a large circle coincides with the first term of formula (34) for a screen of arbitrary shape and the cosine function in Eq. (40) represents the interferential term.

2.5 Size-Distributed Obstacles

For an ensemble of size-distributed obstacles the differential cross-section is

$$\frac{dC_{sca}}{d\Omega} = \frac{2\lambda\langle L\rangle}{(2\pi)^3\theta^3} + \langle\overline{Int}\rangle, \tag{41}$$

where sign $\langle\ \rangle$ denotes averaging over the ensemble.

Assuming that averaging over orientation and over size are commutative, we can write:

$$\langle\overline{Int}\rangle = \overline{\langle Int\rangle} = \frac{2\pi}{\lambda^2\Delta k^3}$$
$$\frac{1}{2\pi}\int_0^{2\pi} d\varphi \sum_{q\neq s}\left\langle \exp\left(i\,\Delta\mathbf{k}\cdot(\mathbf{r}_q-\mathbf{r}_s)+\frac{\pi i}{4}(\mathrm{sgn}_q-\mathrm{sgn}_s)\right)\sqrt{R_q R_s}\right\rangle = 0. \tag{42}$$

This term reaches zero due to the fast oscillations of the exponential function if the size distribution is smooth enough, i.e., if it does not have peaks with the width comparable to the wavelength.

Finally, we have

$$\frac{dC_{sca}}{d\Omega} = \frac{2\lambda\langle L\rangle}{(2\pi)^3\theta^3}. \tag{43}$$

Particle size-distribution smoothes the diffraction pattern, such that one cannot distinguish between the first and the higher-order peaks. We will refer to the region

$$\theta < \frac{\lambda}{\langle L\rangle} \tag{44}$$

as a main peak. Equation (43) claims that far outside the main diffraction peak the differential cross-section depends on the average contour length $\langle L\rangle$ only and is independent of the obstacles' shape.

As it can be easily seen from Eqs. (11) and (12), the value of the differential cross-section in the strictly forward direction $\theta = 0$ equals S^2/λ^2. The total scattering cross-section, i.e. the integral of the differential cross-section over θ, is equal to the obstacle area S [see (13)]. None of these values depends on the shape. So, for size-distributed

obstacles the differential cross-section meets three conditions independently of the obstacles shape:

$$\left.\frac{dC_{sca}}{d\Omega}\right|_{\theta=0} = \frac{\langle S^2\rangle}{\lambda^2}, \quad \left.\frac{dC_{sca}}{d\Omega}\right|_{\theta>\lambda/\langle L\rangle} = \frac{2\lambda\langle L\rangle}{(2\pi)^3\theta^3}, \quad \int \frac{dC_{sca}}{d\Omega}d\Omega = S. \tag{45}$$

These conditions mean that the diffraction-angle patterns of two ensembles of chaotically oriented large particles, differing in shape and/or size distribution, will be identical if the 1st and 2nd moments of the obstacle area distribution, $\langle S\rangle$ and $\langle S^2\rangle$, and the average perimeter $\langle L\rangle$ are the same.

2.6 Approximating Formula

The statement made in the previous paragraph pushes an idea to find one universal phase function that would satisfy conditions (45) to describe the Fraunhofer diffraction pattern of any ensemble, regardless of the particle shape or size distribution.

Let us define the scattering phase function of Fraunhofer diffraction as

$$p(\theta) = \frac{2\pi}{\langle S\rangle}\frac{dC_{sca}}{d\Omega}, \tag{46}$$

with the normalization, followed from (13) in the framework of the small-angle scattering approach

$$\int_0^\infty p(\theta)\theta\, d\theta = 1. \tag{47}$$

Conditions (45) become

$$p(\theta)|_{\theta\gg\lambda/\langle L\rangle} = \frac{a}{\theta^3}, \quad a = \frac{\lambda\langle L\rangle}{2\pi^2\langle S\rangle}, \tag{48}$$

$$p(0) = \frac{2\pi\langle S^2\rangle}{\lambda^2\langle S\rangle}. \tag{49}$$

Condition (48) gives the asymptotical behavior, while condition (49) gives the strict forward value.

If the particle size distribution is wide enough (i.e., its width is much greater than the wavelength—which is the case of most of the natural scattering media) the diffraction phase function must be monotonic, because the oscillations destruct each

other. So we have the monotonic function that has the given value at zero, the given asymptotical behavior, and its integral equals unity.

Because Eq. (48) is unphysical at $\theta \to 0$, the Wells function (Wells 1973) can be used for the approximation: it satisfies asymptotic condition (48) and normalization (47) and takes finite values over the entire range. The Wells function (50) is a small-angle analog of the widely-used Henye–Greenstein function and is often used in hydro-optics (Wells 1973; McLean and Voss 1991). However, function (50) does not describe the main diffraction peak; in particular, it does not satisfy Eq. (49). To describe the main diffraction peak, let us take an equal-weighted mixture of (50) and a Gaussian function: this will adjust the near-zero value and will not change the asymptotic behavior:

$$p(\theta) = \frac{\rho^2}{\left(1 + \rho^2\theta^2\right)^{3/2}} \tag{50}$$

$$p(\theta) = \frac{1}{2V}\exp\left(-\frac{\theta^2}{2V}\right) + \frac{\rho^2}{2\left(1 + \rho^2\theta^2\right)^{3/2}}. \tag{51}$$

Function (51) satisfies the normalization (47) automatically. From conditions (48)–(49) we have:

$$\rho = \frac{1}{2a}, \quad V = \frac{4a^2}{8p(0)a^2 - 1}. \tag{52}$$

Thus, only two microphysical parameters of the ensemble, $\langle S^2\rangle/\langle S\rangle$ and $\langle L\rangle/\langle S\rangle$, define the diffraction phase function regardless of particle shape; the former characterizes the width of the size distribution (it is the 2nd moment of the cross-sectional area distribution), the latter determines the deviation from spherical shape. The average contour length $\langle L\rangle$ in the particular case of a convex particle is proportional to the average particle thickness $\langle T\rangle$ (Kendall and Moran 1963):

$$\langle L\rangle = \pi\langle T\rangle. \tag{53}$$

However, in general, Eq. (53) is not valid.

Qualitatively, the first term in (51) describes the main diffraction peak and the second one refers to the peaks of higher orders. The latter is obtained within the stationary phase method, while the former is just approximated by Gaussian function. It is to note that these two terms have equal energy—a half of the total one. Moreover, the second term—outside the zero diffraction peak—may become more important than the first one in some situations where a receiver does not have sufficient resolution and the first term cannot be distinguished from the direct light.

2.7 Hexagonal Prisms

Let us compare formula (51) with the strict solution for Fraunhofer diffraction by an ensemble of randomly oriented hexagonal prisms—this model is widely used for modeling the microphysical and optical properties of crystal clouds. Let D be the maximum dimension of a hexagon and H be the prism height. Prism orientation is determined by three angles: φ, the angle of rotation around the main prism axis, θ, the angle between the main prism axis and the incident light direction, and ψ, the angle of rotation around the incident light direction (see Fig. 3).

We are to find average values of $\langle S \rangle$, $\langle S^2 \rangle$, and $\langle L \rangle$. Averaging over the ensemble means averaging over angles φ, θ, and ψ. Averaging over ψ is trivial, because none of the above mentioned values depends on ψ.

So, averaging is:

$$\langle f(\theta, \varphi) \rangle = \frac{6}{\pi} \int_0^{\pi/6} d\varphi \int_0^{\pi/2} f(\theta, \varphi) \sin(\theta) d\theta. \tag{54}$$

The prism cross-sectional area is

$$S(\theta, \varphi) = S_{base} \cos\theta + S_{side} \sin\theta \cos\varphi, \tag{55}$$

where S_{base} is the hexagon area and S_{side} is the maximal area of the side projection:

$$S_{base} = \frac{3\sqrt{3}}{8} D^2, \quad S_{side} = DH. \tag{56}$$

So we have

$$S(\theta, \varphi) = \frac{3\sqrt{3}}{8} D^2 \cos\theta + HD \sin\theta \cos\varphi. \tag{57}$$

From (54) and (57) it is easy to find:

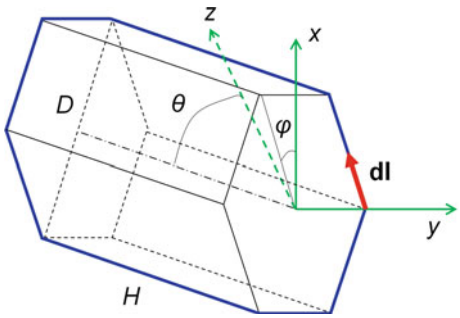

Fig. 3 Hexagonal prism

$$\langle S\rangle = \frac{3\sqrt{3}}{16}D^2 + \frac{3}{4}DH, \qquad \left\langle S^2\right\rangle = \frac{9}{64}D^4 + \frac{3\sqrt{3}}{4\pi}D^3H + \frac{2\pi + 3\sqrt{3}}{6\pi}D^2H^2. \tag{58}$$

Note that the average cross-sectional area $\langle S\rangle$ is equal to one fourth of the prism surface area, as for any convex particle.

It is somewhat more complicated to find the average length of the contour, bordering the particle projection, $\langle L\rangle$. The projection contour comprises of two halves of the hexagon moved apart by lateral edges. The length of the projection of the lateral edges is equal to $2H\sin\theta$, so its average value is

$$L_{lat} = \int_0^{\pi/2} 2H\sin^2\theta d\theta = \frac{\pi}{2}H. \tag{59}$$

In order to find the average length of the base perimeter, let us consider the length element dl (see Fig. 3). Let vector **dl** have elements ($dl\cos\varphi_0$, $dl\sin\varphi_0$, 0) when the principal prism axis is parallel to the z-axis. Then after two consecutive rotations—the 1st one by angle φ around the z-axis and the 2nd one by angle θ around the x-axis—vector **dl** will have elements

$$(dl\cos(\varphi_0+\varphi), dl\sin(\varphi_0+\varphi)\cos\theta, dl\sin(\varphi_0+\varphi)\sin\theta).$$

The length of its projection onto the xy-plane is

$$dl\sqrt{\cos^2(\varphi_0+\varphi) + \sin^2(\varphi_0+\varphi)\cos^2\theta}. \tag{60}$$

Averaging this element over all possible angles, we have:

$$\begin{aligned}\langle dl\rangle &= dl\frac{1}{2\pi}\int_0^{\pi/2}\sin\theta d\theta\int_0^{2\pi}\sqrt{\cos^2(\varphi_0+\varphi) + \sin^2(\varphi_0+\varphi)\cos^2\theta}\,d\varphi \\ &= dl\frac{2}{\pi}\int_0^{\pi/2}\mathbf{E}(\sin^2\theta)\sin\theta d\theta = \frac{\pi}{4}dl,\end{aligned} \tag{61}$$

where $\mathbf{E}(m)$ is the elliptic integral. Then, integrating dl over the prism base perimeter,

$$\oint dl = L_{base}, \tag{62}$$

we have for the prism:

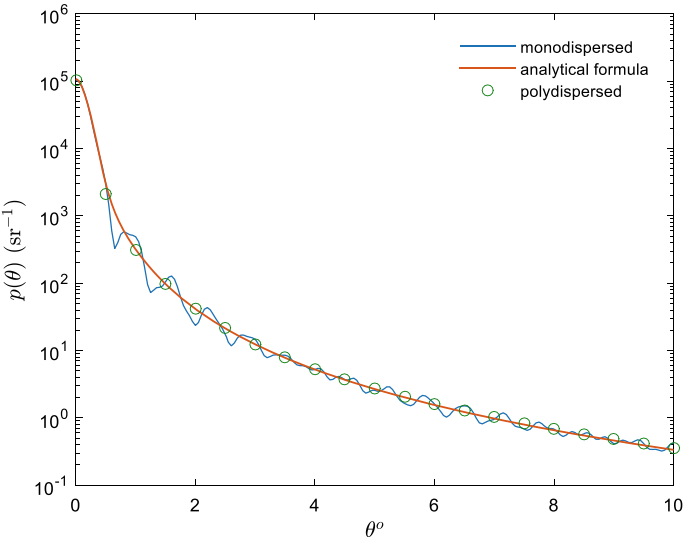

Fig. 4 Diffraction phase function calculated strictly for the mono- (thin curve) and polydispersed (circles) ensembles of randomly oriented prisms and its approximation by formula (51) (thick curve)

$$\langle L\rangle = \frac{\pi}{4}L_{base} + \frac{\pi}{2}H. \tag{63}$$

Note that Eq. (63) is valid not only for the hexagonal prism, but for any prism with a convex base. For a hexagonal prism we have:

$$\langle L\rangle = \frac{3\pi}{4}D + \frac{\pi}{2}H. \tag{64}$$

Figure 4 presents the phase function of diffraction calculated directly by numerical integration of the phase of a wavefront over the particle projection and its approximation by formula (51) with parameters given by Eqs. (58) and (64).

The direct calculations are given for two cases: the monodispersed ensemble of randomly oriented prisms with $D = 50\,\mu\text{m}$, $H = 100\,\mu\text{m}$ and the polydispersed ensemble of randomly oriented prisms with $H/D = 0.9$ and Gamma size distribution for D:

$$\frac{dp}{dD} = \frac{D^\gamma}{D_0^{\gamma+1}\gamma!}\exp\left(-\frac{D}{D_0}\right) \tag{65}$$

with $\gamma = 15$ and $D_0 = 3.68\,\mu\text{m}$. These distribution parameters provide the same values of $\langle S^2\rangle/\langle S\rangle$ and $\langle L\rangle/\langle S\rangle$. The wavelength is 532 nm. Note that there are the oscillations in the thin curve, because the ensemble is monodispered. As was mentioned above, in the case of a polydispersion the phase function is monotonic.

Thus, the universal function (51) approximates the Fraunhofer diffraction peak of randomly oriented particles of any shape. The approximating formula includes two simple functions, which are widely used in the radiation transfer theory. This universal function depends on two microphysics parameters only: the average area squared and perimeter length per average area of the projection: $\langle S^2 \rangle / \langle S \rangle$ and $\langle L \rangle / \langle S \rangle$. The latter describes the deviation of the particle shape from sphere, while the former depends both on the deviation from sphere and the particle size distribution width. The obtained approximation is simple and allows one to avoid the time consuming and rather complicated strict calculations of the diffraction pattern. It may be useful for description of laser bream propagation and lidar return from cirrus clouds or strongly nonspherical aerosols, such as volcano ashes.

3 Rayleigh–Gans Approximation

3.1 Statement of the Problem

As it was mentioned the Rayleigh–Gans (RG) approximation is valid when the field inside a particle is approximately equal to the incident field. This condition is met when the phase shift inside the particle is negligible, Eq. (4). But though this demand is opposite to the conditions of Fraunhofer diffraction, Eq. (3), mathematically these approaches are completely analogous, dealing with a two-dimensional surface or a three-dimensional volume.

Let the wavevector of the incident wave $\mathbf{k}_0$ be again perpendicular to the xy-plane. The wavevector of the scattered wave is $\mathbf{k}_s$:

$$|\mathbf{k}_s| = |\mathbf{k}_0| = k = \frac{2\pi}{\lambda} n_0, \tag{66}$$

where n_0 is the refractive index of the surrounding medium, λ is the wavelength in vacuum.

The difference between wavevectors of the scattered and initial wave is

$$\Delta k = |\Delta \mathbf{k}| = |\mathbf{k}_s - \mathbf{k}_0| = 2k \sin \frac{\theta}{2}, \tag{67}$$

where θ is the scattering angle.

Let the particle surface be described by the three-dimensional vector function

$$\mathbf{r} = \mathbf{r}(u, v) = (x(u, v), y(u, v), z(u, v)), \tag{68}$$

where u and v are the natural parameters, which determine the point on the two-dimensional surface and are equal to the distances measured along the surface. The derivatives of this function are the unit tangent vectors to the surface:

$$\frac{\partial \mathbf{r}}{\partial u} = \mathbf{u}(u, v), \quad \frac{\partial \mathbf{r}}{\partial v} = \mathbf{v}(u, v). \tag{69}$$

The physical reason for the RG approximation is that the electromagnetic field inside the particle is assumed to be approximately equal to the incident field and every point inside the particle is a secondary source for the scattered field. The amplitude matrix elements within the RG approximations are (van de Hulst 1957; Bohren and Huffman 1983):

$$S_1 = -i\frac{k^3}{2\pi}(m-1)\int\limits_V \exp(i\,\Delta\mathbf{k}\cdot\mathbf{r})d^3\mathbf{r}, \quad S_2 = S_1\cos\theta. \tag{70}$$

where $m = n + i\kappa$ is the relative refractive index of the particle. The integral is taken over the particle volume V. The differential cross-section is

$$\frac{dC_{sca}}{d\Omega} = \frac{|S_1|^2 + |S_2|^2}{2k^2} = \frac{1+\cos^2\theta}{2k^2}|S_1|^2. \tag{71}$$

3.2 Solution for a Single Particle

By the Ostrogradsky–Gauss divergence theorem, which is the 3-d version of the Stokes theorem, the integral over the particle volume (70) can be written through the integral over its surface:

$$S_1 = -\frac{k^3}{2\pi\ \Delta k^2}(m-1)\int\limits_S \exp(i\,\Delta\mathbf{k}\cdot\mathbf{r})\Delta\mathbf{k}\cdot\mathbf{n}dS, \tag{72}$$

where $\mathbf{n}$ is the outer-pointing normal to the surface. Multiplier $\Delta\mathbf{k}\cdot\mathbf{n}$, proportional to the cosine of the angle between vectors $\Delta\mathbf{k}$ and $\mathbf{n}$, describes the contribution of a secondary source to the resulting field.

Now, as we consider the case when the obstacle is much greater than the wavelength, we can use the method of the stationary phase, similar to the way we did it in Sect. 2.2. Analogously to Eq. (18), we will consider here the region of angles, far outside of the forward direction peak, i.e.

$$2x\sin\frac{\theta}{2} \gg 1. \tag{73}$$

Under condition (73) only the points, where the phase is stationary, i.e.

$$\frac{\partial\,\Delta\mathbf{k}\cdot\mathbf{r}}{\partial u} = \Delta\mathbf{k}\cdot\mathbf{u} = \frac{\partial\,\Delta\mathbf{k}\cdot\mathbf{r}}{\partial v} = \Delta\mathbf{k}\cdot\mathbf{v} = 0, \tag{74}$$

make the nonvanishing contribution to the integral in Eq. (72). These are the points where $\Delta\mathbf{k}$ is perpendicular to the surface (collinear to its normal $\mathbf{n}$), because the waves from the vicinity of these points undergo the positive interference. The waves from the other points destruct each other, because of the fast oscillations of the exponential function. At these points product $\Delta\mathbf{k} \cdot \mathbf{n}$ equals

$$\Delta\mathbf{k} \cdot \mathbf{n} = \pm\Delta k. \tag{75}$$

Thus, the contribution of each stationary point $\mathbf{r}_s$ to the integral in Eq. (72) is (Bleistein and Handelsman 1986):

$$\begin{aligned} I_s &= \int\limits_{\delta r_s} \exp(i\,\Delta\mathbf{k}\cdot\mathbf{r})\Delta\mathbf{k}\cdot\mathbf{n}dS \\ &= \int\limits_{-\infty}^{\infty}\int\limits_{-\infty}^{\infty} \exp\left(i\,\Delta\mathbf{k}\cdot\mathbf{r}_s + i\,\frac{1}{2}\Delta\mathbf{k}\cdot\left[\frac{\partial^2\mathbf{r}_s}{\partial u^2}\,u^2 + 2\frac{\partial^2\mathbf{r}_s}{\partial u\partial v}\,uv + \frac{\partial^2\mathbf{r}_s}{\partial v^2}\,v^2\right]\right)(\pm\Delta k)dudv \end{aligned} \tag{76}$$

where the phase is expanded to the second order of u and v. Integral (76) is equal to

$$I_s = \pm\exp\left(i\,\Delta\mathbf{k}\,\cdot\mathbf{r}_s + \frac{\pi i}{4}\mathrm{sgn}_s\right)\frac{2\pi\,\Delta k}{\sqrt{|J_s|}}, \tag{77}$$

where sgn_s is the signature of the surface metrics at point $\mathbf{r}_s$ (in the general case it equals the number of positive radii minus the number of negative radii) and J_s is the Jacobian:

$$J_s = \begin{vmatrix} \Delta\mathbf{k}\cdot\frac{\partial^2\mathbf{r}_s}{\partial u^2} & \Delta\mathbf{k}\cdot\frac{\partial^2\mathbf{r}_s}{\partial u\partial v} \\ \Delta\mathbf{k}\cdot\frac{\partial^2\mathbf{r}_s}{\partial u\partial v} & \Delta\mathbf{k}\cdot\frac{\partial^2\mathbf{r}_s}{\partial v^2} \end{vmatrix}. \tag{78}$$

Jacobian J_s is proportional to the Gaussian curvature at point $\mathbf{r}_s$.

Indeed, we can always choose the local coordinate system, in which the surface equation in the vicinity of point $\mathbf{r}_s$ has the form

$$\mathbf{r} - \mathbf{r}_s = \mathbf{u}u + \mathbf{v}v - \mathbf{n}\left(\frac{u^2}{2R_s^u} + \frac{v^2}{2R_s^v}\right), \tag{79}$$

where R_s^u and R_s^v are the principal curvature radii. From Eq. (79) it straightforwardly follows that

$$J_s = \frac{\Delta k^2}{R_s^u R_s^v}. \tag{80}$$

Hence, integral (76) is equal to

$$I_s = \pm \exp\left(i\ \Delta\mathbf{k}\ \cdot \mathbf{r}_s + \frac{\pi i}{4} \mathrm{sgn}_s \right) 2\pi \sqrt{\left| R_s^u R_s^v \right|}. \tag{81}$$

For function S_1 we get:

$$\begin{aligned} S_1 &= \mp \frac{k^3}{2\pi\ \Delta k^2} (m-1)\, I_s \\ &= \mp \frac{k^3}{\Delta k^2} (m-1) \sum_s \exp\left(i\ \Delta\mathbf{k}\ \cdot \mathbf{r}_s + \frac{\pi i}{4} \mathrm{sgn}_s \right) \sqrt{\left| R_s^u R_s^v \right|}. \end{aligned} \tag{82}$$

Its squared magnitude is

$$\begin{aligned} |S_1|^2 = \frac{k^6}{\Delta k^4} |m-1|^2 \\ \sum_s \sum_q \exp\left(i\ \Delta\mathbf{k}\ \cdot (\mathbf{r}_s - \mathbf{r}_q) + \frac{\pi i}{4} (\mathrm{sgn}_s - \mathrm{sgn}_q) \right) \sqrt{\left| R_s^u R_s^v R_q^u R_q^v \right|}. \end{aligned} \tag{83}$$

Formula (83) gives the solution for a single arbitrary-shaped large particle with the piecewise-smooth surface.

Let us again separate the terms with $s = q$ and $s \neq q$ in Eq. (83):

$$|S_1|^2 = \frac{k^6}{\Delta k^4} |m-1|^2 \sum_s \left| R_s^u R_s^v \right| + Int. \tag{84}$$

In Eq. (84) the first term (for $s = q$) describes the 'incoherent' scattering, which is simply the sum of the intensities of the waves scattered by every stationary point. The second term, Int (for $s \neq q$) describes the interference of the waves from different stationary points.

3.3 *Randomly Oriented Particles*

The case when the particles are randomly oriented in space is of practical interest. So, let us average function (84) over the particle orientation.

In the vicinity of point $\mathbf{r}_s$ the surface equation has the form (79). The particle rotation around vector $\mathbf{n}$ does not change function $|S_1|^2$. Two other rotations (around u- and v-axes) on angles $d\psi_u$ and $d\psi_v$, respectively, are equivalent to the appropriate tilt of $\mathbf{n}$:

$$d\mathbf{n} = (d\psi_u, d\psi_v). \tag{85}$$

As $\mathbf{n}$ is normal to the surface, point $\mathbf{r}_s$ due to a tilt of $\mathbf{n}$ drifts by

$$d\mathbf{r}_s = (R_s^u d\psi_u, R_s^v d\psi_v). \tag{86}$$

This means that the integration element in the space of rotations equals

$$d\psi_u d\psi_v = \frac{dudv}{|R_s^u R_s^v|} = \frac{dS}{|R_s^u R_s^v|}, \tag{87}$$

where dS is the surface area element. Thus, averaging function $|S_1|^2$ over orientations gives:

$$\begin{aligned}\overline{|S_1|^2} &= \frac{k^6|m-1|^2}{\Delta k^4}\int\limits_{4\pi}\sum_s |R_s^u R_s^v|\frac{d\psi_u d\psi_v}{4\pi} + \overline{Int} \\ &= \frac{k^6|m-1|^2}{\Delta k^4}\int\limits_{S}\frac{2dS}{4\pi} + \overline{Int} = \frac{k^6(m-1)^2}{\Delta k^4}\frac{S}{2\pi} + \overline{Int},\end{aligned} \tag{88}$$

where S is the particle surface area. Multiplier 2 appears because every point of the surface contributes twice to the integral, in accordance with signs '+' and '–' in Eq. (75).

In natural media, an ensemble of particles always has some size distribution that usually does not have peaks with a width comparable to the wavelength. With averaging over the size distribution, the term $\overline{Int}$ vanishes due to the fast oscillations of the exponential function and, finally, we have

$$\left\langle\overline{|S_1|^2}\right\rangle = \frac{k^6(m-1)^2}{\Delta k^4}\frac{\langle S\rangle}{2\pi}, \tag{89}$$

where $\langle\ \rangle$ denotes the averaging over the ensemble.

Therefore, for the differential cross-section (71) we have:

$$\begin{aligned}\frac{dC_{sca}}{d\Omega} &= \frac{k^4|m-1|^2}{\Delta k^4}\frac{1+\cos^2\theta}{2}\frac{\langle S\rangle}{2\pi} \\ &= |m-1|^2\frac{1+\cos^2\theta}{32\sin^4\theta/2}\frac{\langle S\rangle}{2\pi}.\end{aligned} \tag{90}$$

Equation (90) shows that the differential cross-section of an ensemble of randomly oriented soft particles, except for the near forward direction, behaves as Δk^{-4} and depends on the average particle surface area only. Let us note that, unlike Eqs. (43) and (51) derived within Fraunhofer diffraction, formula (90) is also valid for scattering into the backward hemisphere.

3.4 Approximating Formula

As in the case of Fraunhofer diffraction, Eq. (90) has been derived under assumption (73), where the method of stationary phase is valid, and it is incorrect in the vicinity of the forward direction, where the function approaches infinity. This behavior can be corrected by introducing an approximating function with the same asymptotic behavior:

$$\begin{aligned}\frac{dC_{sca}}{d\Omega} &= \frac{k^4|m-1|^2}{2\pi}\langle S\rangle\frac{1+\cos^2\theta}{2}\frac{r_{eff}^4}{\left(1+r_{eff}^2\Delta k^2\right)^2}\\ &= \frac{|m-1|^2}{2\pi}\langle S\rangle\frac{1+\cos^2\theta}{2}\frac{x^4}{\left(1+4x^2\sin^2\theta/2\right)^2}\\ &= \frac{|m-1|^2}{2\pi}\langle S\rangle\frac{1+\mu^2}{2}\frac{x^4}{\left(1+2x^2(1-\mu)\right)^2},\end{aligned} \tag{91}$$

where $x = kr_{eff}$ and r_{eff} is the effective size parameter, which is to be defined. The function in Eq. (91) is given in three forms, where $\mu = \cos\theta$. Strictly the same dependence was derived by Debye and Bueche (1949) and Debye et al. (1957) for scattering by small random fluctuations of the refractive index in solids. In that case r_{eff} was the correlation length of the fluctuations.

Integrating Eq. (91) over all directions $d\Omega = d\varphi d\mu$, we have:

$$C_{sca} = |m-1|^2\langle S\rangle\frac{2x^2+1}{2}\left[\frac{2x^2+1}{4x^2+1} - \frac{\ln(4x^2+1)}{4x^2}\right]. \tag{92}$$

Taking into account Eq. (1), we can write for large x:

$$C_{sca} = \frac{1}{2}|m-1|^2\langle S\rangle x^2. \tag{93}$$

Equation (93) has a difference with Eq. (92) of less than 1% for $x \geq 17$ and less than 0.1% for $x \geq 65$. So, implying that particles we consider are much larger than the wavelength, we will employ Eq. (93) to express x:

$$x = \frac{1}{|m-1|}\sqrt{\frac{2C_{sca}}{\langle S\rangle}}. \tag{94}$$

As in the RG approximation the scattering cross-section is proportional to $|m-1|^2$, the effective size depends on the microphysical characteristics only.

The scattering phase function $p(\theta)$ is defined as

$$p(\theta) = \frac{4\pi}{C_{sca}} \frac{dC_{sca}}{d\Omega}. \tag{95}$$

Employing Eqs. (91) and (92) we get:

$$p(\theta) = \frac{1}{N} \frac{2x^2\left(1+\cos^2\theta\right)}{\left(1+4x^2\sin^2\theta/2\right)^2} = \frac{1}{N} \frac{2x^2\left(1+\mu^2\right)}{\left(1+2x^2(1-\mu)\right)^2}, \tag{96}$$

where N is the normalization factor, which equals

$$N = 1 + \frac{1}{x^2} - \frac{1}{4x^2+1} - \frac{2x^2+1}{4x^4}\ln(4x^2+1). \tag{97}$$

It approaches 1 with x approaching infinity. According to Eq. (95) the phase function meets normalization

$$\frac{1}{2}\int_0^\pi p(\theta)\sin\theta d\theta = 1. \tag{98}$$

Let us note that the phase function in the RG approximation, as well as the effective size x, depends on the microphysical characteristics of a particle—size and shape—only, but not on its refractive index. This result obviously follows from the fact that the scattering amplitude in the RG approach is approximated by the first-order term of $m-1$.

3.5 Total Scattering Cross-Section

The total scattering cross-section in the RG approximation is not easy to find. Firstly, because the optical theorem yields the extinction cross-section equal to the absorption one:

$$C_{ext} = \frac{4\pi}{k^2}\mathrm{Re}[S_1(0)] = 2\mathrm{Re}\left[-ik(m-1)\int_V d^3\mathbf{r}\right] = 2k\kappa V = C_{abs}, \tag{99}$$

so the scattering cross-section vanishes. This occurs, as well, because of the approximation of the scattering amplitude by the first order of $m-1$, while the scattering cross-section is proportional to the second one.

Secondly, the straightforward calculation of the integral in Eq. (71) cannot be made in the general case. However, the method of stationary phase can help here as well, if one considers particles much larger than the wavelength.

Let us start with the initial Eq. (70) and write Eq. (71) in the form:

$$\frac{dC_{sca}}{d\Omega} = \frac{1+\cos^2\theta}{2}\frac{k^4|m-1|^2}{(2\pi)^2}\int\limits_{V'}\int\limits_{V}\exp\bigl(i\,\Delta\mathbf{k}\cdot(\mathbf{r}-\mathbf{r}')\bigr)d^3\mathbf{r}d^3\mathbf{r}'$$
$$= \frac{1+\cos^2\theta}{2}\frac{k^4|m-1|^2}{(2\pi)^2}\int\limits_{V'}\int\limits_{V}\exp\bigl(ik|\mathbf{r}-\mathbf{r}'|\cos\eta - ik(z-z')\bigr)d^3\mathbf{r}d^3\mathbf{r}', \tag{100}$$

where η is the angle between $\mathbf{k}_s$ and vector $\mathbf{r}-\mathbf{r}'$. The scattering cross-section equals the integral

$$C_{sca} = \int\limits_{4\pi}\frac{dC_{sca}}{d\Omega}d\Omega. \tag{101}$$

The integration of Eq. (100) is easier to make in coordinates (η, ψ), where ψ is the azimuth around vector $\mathbf{r}-\mathbf{r}'$, counted from the plane produced by vectors $\mathbf{r}-\mathbf{r}'$ and $\mathbf{k}_0$, so that $d\Omega = \sin\eta d\eta d\psi$.

Let us first transform the polarization term. By the geometry of the sphere

$$\cos\theta = \cos\eta\cos\zeta + \sin\eta\sin\zeta\cos\psi,$$

where ζ is the angle between vectors $\mathbf{r}-\mathbf{r}'$ and $\mathbf{k}_0$. The cosine square is

$$\cos^2\theta = \cos^2\eta\cos^2\zeta + 2\cos\eta\cos\zeta\sin\eta\sin\zeta\cos\psi + \sin^2\eta\sin^2\zeta\cos^2\psi. \tag{102}$$

The integral of Eq. (102) over ψ yields the factor of 2π for the first term, 0 for the second one, and π for the third one, so:

$$\int\limits_0^{2\pi}\frac{1+\cos^2\theta}{2}d\psi = \pi + \pi\cos^2\eta\cos^2\zeta + \frac{\pi}{2}\sin^2\eta\sin^2\zeta$$
$$= \frac{\pi}{2}\bigl(2+\sin^2\zeta\bigr) + \frac{\pi}{2}\bigl(2-3\sin^2\zeta\bigr)\cos^2\eta. \tag{103}$$

So we need to calculate the integrals:

$$I_{1,2} = \int\limits_0^{\pi}\begin{pmatrix}1\\ \cos^2\eta\end{pmatrix}\exp\bigl(ik|\mathbf{r}-\mathbf{r}'|\cos\eta\bigr)\sin\eta d\eta.$$

These integrals equal

$$I_1 = 2\frac{\sin k|\mathbf{r}-\mathbf{r}'|}{k|\mathbf{r}-\mathbf{r}'|},$$

$$I_2 = 2\frac{2k|\mathbf{r}-\mathbf{r}'|\cos k|\mathbf{r}-\mathbf{r}'| + (k^2|\mathbf{r}-\mathbf{r}'|^2 - 2)\sin k|\mathbf{r}-\mathbf{r}'|}{k^3|\mathbf{r}-\mathbf{r}'|^3}. \tag{104}$$

If we omit in Eq. (104) the terms with orders of $1/k$ greater than 1, we will find that

$$I_2 = I_1 = 2\frac{\sin k|\mathbf{r}-\mathbf{r}'|}{k|\mathbf{r}-\mathbf{r}'|}. \tag{105}$$

Now, let us get back to the initial coordinate system (x, y, z). We need to find the integral:

$$\int\limits_{S_\perp} \pi\left(1 + \frac{(z-z')^2}{|\mathbf{r}-\mathbf{r}'|^2}\right) 2\frac{\sin k|\mathbf{r}-\mathbf{r}'|}{k|\mathbf{r}-\mathbf{r}'|} dx'dy', \tag{106}$$

where $S_\perp$ stands for the particle projection onto the xy-plane. The expression in the parentheses originates from Eq. (103). Let us find the integrals

$$\int\limits_{S_\perp} \frac{\exp(\pm ik|\mathbf{r}-\mathbf{r}'|)}{|\mathbf{r}-\mathbf{r}'|^b} dx'dy'. \tag{107}$$

Here we can use the method of stationary phase. The phase $k|\mathbf{r}-\mathbf{r}'|$ is stationary at the points where

$$\frac{\partial|\mathbf{r}-\mathbf{r}'|}{\partial x'} = \frac{\partial|\mathbf{r}-\mathbf{r}'|}{\partial y'} = 0.$$

These points are $x' = x,\ y' = y$. The matrix of the second derivatives is

$$\left(\begin{array}{cc} \pm k\frac{\partial^2|\mathbf{r}-\mathbf{r}'|}{\partial x'^2} & \pm k\frac{\partial^2|\mathbf{r}-\mathbf{r}'|}{\partial x'\partial y'} \\ \pm k\frac{\partial^2|\mathbf{r}-\mathbf{r}'|}{\partial x'\partial y'} & \pm k\frac{\partial^2|\mathbf{r}-\mathbf{r}'|}{\partial y'^2} \end{array}\right)\Bigg|_{\substack{x'=x \\ y'=y}} = \left(\begin{array}{cc} \pm\frac{k}{|z-z'|} & 0 \\ 0 & \pm\frac{k}{|z-z'|} \end{array}\right),$$

So the Jacobian $J = k^2|z-z'|^{-2}$ and integral (107) equals

$$\int\limits_{S_\perp} \frac{\exp(\pm ik|\mathbf{r}-\mathbf{r}'|)}{|\mathbf{r}-\mathbf{r}'|^b} dx'dy' = \frac{2\pi\exp\left(\pm ik|z-z'| \pm i\frac{\pi}{2}\right)}{k|z-z'|^{b-1}}. \tag{108}$$

With use of Eq. (108) we can write integral (106) as

$$\frac{8\pi^2}{k^2}\cos(k(z-z')). \tag{109}$$

Thus, for the scattering cross-section we have:

$$C_{sca} = 2k^2|m-1|^2 \int\limits_{S_\perp} dxdy \int\limits_{Z_1(x,y)}^{Z_2(x,y)} dz' \int\limits_{Z_1(x,y)}^{Z_2(x,y)} \cos(k(z-z')) \exp\bigl(-ik(z-z')\bigr)dz, \tag{110}$$

where functions $Z_1(x, y)$ and $Z_2(x, y)$ determine the lower and upper particle surfaces. The integral in Eq. (110) equals

$$\begin{aligned} &\int\limits_{Z_1}^{Z_2} \int\limits_{Z_2}^{Z_2} \cos(k(z-z')) \exp\bigl(-ik(z-z')\bigr)dzdz' \\ &\quad = \frac{2k^2(Z_2-Z_1)^2 + 1 - \cos(2k(Z_2-Z_1))}{4k^2}. \end{aligned} \tag{111}$$

Omitting again terms with k^{-2}, we finally get:

$$C_{sca} = k^2|m-1|^2 \int\limits_{S_\perp} [Z_2(x,y) - Z_1(x,y)]^2 dxdy. \tag{112}$$

The line segment connecting points $Z_1(x, y)$ and $Z_2(x, y)$ is the particle chord in the z-axis direction; its length ξ is $Z_2(x, y) - Z_1(x, y)$. (In the case when the particle is not convex, a chord may consist of several segments. In this case the sum of lengths should be taken.) The integral in Eq. (112) stands for averaging over the particle projection (see Kendall and Moran 1963 for more information on geometrical statistics):

$$\int\limits_{S_\perp} \xi^2 dxdy = \bigl\langle \xi^2 \bigr\rangle_{\mathbf{k}_0} S_\perp(\mathbf{k}_0), \tag{113}$$

where sign $\bigl\langle \xi^2 \bigr\rangle_{\mathbf{k}_0}$ denotes the square of the chord length averaged over the particle projection in direction $\mathbf{k}_0$ and $S_\perp(\mathbf{k}_0)$ is the projection area. So Eq. (112) can be written as

$$C_{sca} = k^2|m-1|^2 \bigl\langle \xi^2 \bigr\rangle_{\mathbf{k}_0} S_\perp(\mathbf{k}_0). \tag{114}$$

If the particles are randomly oriented, then the scattering cross-section is the average over the direction of incidence $\mathbf{k}_0$:

$$C_{sca} = k^2|m-1|^2 \bigl\langle \xi^2 \bigr\rangle \overline{S_\perp}, \tag{115}$$

where $\langle \xi^2 \rangle$ is the average chord length squared and $\overline{S_\perp}$ is the mean particle projection area.

Comparing Eqs. (115) and (93) we can write the expression for the effective particle size:

$$x^2 = k^2 r_{eff}^2 = 2k^2 \langle \xi^2 \rangle \frac{\overline{S_\perp}}{S}. \tag{116}$$

For a convex particle the average projection area is equal to the one fourth of its surface area, i.e. $S = 4\overline{S_\perp}$, so in this case we get:

$$x^2 = k^2 r_{eff}^2 = \frac{1}{2} k^2 \langle \xi^2 \rangle. \tag{117}$$

As the scattering efficiency Q_{sca} by definition is the ratio of the scattering cross-section to the average projection area, it equals

$$Q_{sca} = |m-1|^2 k^2 \langle \xi^2 \rangle, \tag{118}$$

or for a convex particle:

$$Q_{sca} = 2|m-1|^2 x^2. \tag{119}$$

Equation (119) coincides with that given by van de Hulst (1957) for a spherical scatterer with the refractive index close to 1.

Let us note that value $\langle \xi^2 \rangle$ depends on the geometrical characteristics (size and shape) of the particle only. So Eqs. (91), (93), (94), and (117) describe the scattering properties of the soft particle in terms of its refractive index and microphysical characteristics.

3.6 *Chaotically Oriented Cylinder and Size-Distributed Spheres*

Here we will consider an example of a finite cylinder and compare its scattering properties to those of a polydispersion of spheres with the same dimensionless effective size x.

Let the cylinder have diameter $D = 10\,\mu\text{m}$ and height $H = 50\,\mu\text{m}$, the wavelength be 532 nm, and the refractive index be $m = 1.001$. The differential cross-section of a finite cylinder is (van de Hulst 1957):

$$\frac{dC_{sca}}{d\Omega} = \left(\frac{m-1}{2\pi}\right)^2 k^4 V^2 \frac{1+\cos^2\theta}{2} F^2\left(kD \sin\frac{\theta}{2} \sin\beta\right) E^2\left(kH \sin\frac{\theta}{2} \cos\beta\right),$$

$$\cos\beta = -\cos\eta \sin\frac{\theta}{2} + \sin\eta \cos\frac{\theta}{2}\cos\varphi,$$
$$F(u) = \frac{2}{u} J_1(u),$$
$$E(u) = \frac{1}{u}\sin u, \tag{120}$$

where $V = \pi D^2 H/4$ is the cylinder volume, η and φ are the polar angle and azimuth of the cylinder axis. The differential cross-section is then averaged numerically over the cylinder orientation $\sin\eta\, d\eta\, d\varphi$. Then the total scattering cross-section is calculated by the numerical integration over θ and the phase function $p(\theta)$ is found according to (95).

As for any convex shape the mean projection area of a cylinder is equal to 1/4 of the surface area, i.e. $\overline{S_\perp} = \pi D(D + 2H)/8$. The average chord length squared $\langle \xi^2 \rangle$ is calculated numerically. For a cylinder with the aspect ratio $H/D = 5$ it equals

$$\langle \xi^2 \rangle \approx 4.208\,(D/2)^2 \approx 105.2\,\mu\text{m}^2. \tag{121}$$

Then we calculated these values for a polydispertion of spheres with the gamma size distribution given by Eq. (65) with $\gamma = 6$. For a single sphere of radius r the mean square of the chord length $\langle \xi^2 \rangle$ equals

$$\langle \xi^2 \rangle = \frac{1}{\pi r^2} \int_0^r 4(r^2 - \rho^2) 2\pi\rho\, d\rho = 2r^2. \tag{122}$$

For a polydispersion of spheres it is

$$\langle \xi^2 \rangle = \frac{\langle 2r^4 \rangle}{\langle r^2 \rangle} \tag{123}$$

and for the Gamma size distribution it gives

$$\langle \xi^2 \rangle = 2(\gamma + 3)(\gamma + 4) r_0^2. \tag{124}$$

The value of r_0 derived from Eq. (124) for $\langle \xi^2 \rangle$ given by Eq. (121) and $\gamma = 6$ is 0.76449 μm.

The scattering properties of the polydispersion are calculated with a Mie code with parameters given above. The final values of the scattering efficiency Q_{sca} are 1.4636×10^{-2} for the cylinders and 1.4644×10^{-2} for the spherical polydispersion, while the approximate value given by Eq. (118) is 1.4674×10^{-2}.

Figure 5 shows the phase functions in these two cases (chaotically oriented cylinders and polydispersed spheres) and the analytical approximation by Eq. (96).

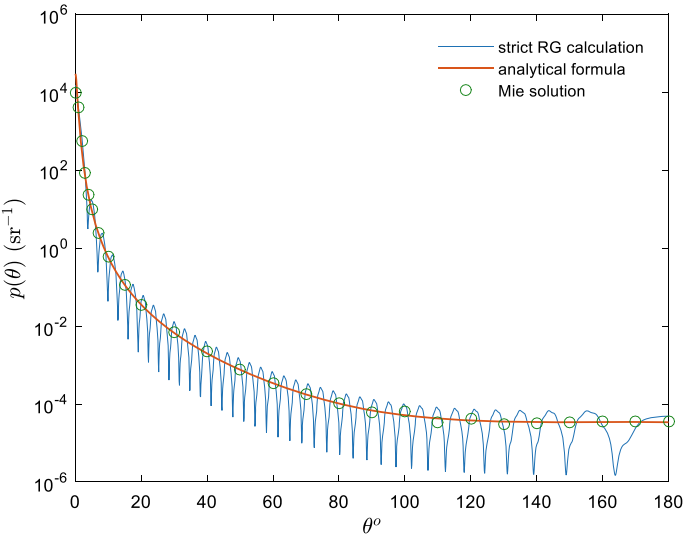

Fig. 5 Phase functions of the chaotically oriented cylinders calculated numerically within the RG approximation (thin curve), the polydispersion of spheres calculated within the Mie solution (circles), and the analytical approximate formula (thick curve)

Let us note that the phase function in the form (96) has the analytical expansion in the Legendre polynomials:

$$\frac{1}{2}\int_{-1}^{1} p(\mu)P_n(\mu)d\mu = -\frac{2}{N_c}\left[(c^2+1)Q_n'(c) + 2cQ_n(c)\right] \qquad \text{for } n \geq 1, \tag{125}$$

where $P_n(\mu)$ and $Q_n(c)$ are the Legendre polynomials of the 1st and 2nd kind, respectively (the latter are defined with a cut in the complex plane from $-\infty$ to $+1$), and

$$c = \frac{2x^2+1}{2x^2}. \tag{126}$$

Also with the use of Eq. (126) the phase function (96) can be written as

$$p(\theta) = \frac{2}{N_c}\frac{1+\mu^2}{(c-\mu)^2}, \tag{127}$$

with the normalization factor

$$N_c = \frac{4c^2}{c^2-1} - 2c\ln\frac{c+1}{c-1}. \tag{128}$$

3.7 Inherent Optical Properties

It is useful to find the inherent optical properties of a medium with optically soft particles embedded in it. The scattering coefficient σ of a turbid medium equals the average total scattering cross-section by one particle multiplied by the particle number density C_N:

$$\sigma = C_{sca} C_N. \tag{129}$$

The product of the mean particle surface area by the number density gives the specific particle surface area s: the area of the particles–medium interface per unit volume:

$$s = \langle S \rangle C_N. \tag{130}$$

According to Eq. (130) the scattering coefficient becomes

$$\sigma = \frac{1}{2} |m - 1|^2 s\, x^2. \tag{131}$$

The transport—or reduced—scattering coefficient σ_{tr} is often used in the radiative transfer theory and its reduction to the theory of photon diffusion:

$$\sigma_{tr} = \sigma (1 - g), \tag{132}$$

where g is the mean cosine of the scattering phase function:

$$g = \frac{1}{2} \int_0^{\pi} p(\theta) \cos\theta \, \sin\theta d\theta. \tag{133}$$

The transport scattering coefficient mainly determines the apparent optical properties of a scattering layer: two different layers with the identical absorption and transport scattering coefficients will have the similar apparent optical properties (van de Hulst 1980; Zege et al. 1991). The transport approximation has higher accuracy in the case when scattering is strongly peaked in the forward direction and is smooth in the backward hemisphere. This is the case of the phase function given by Eq. (96). The mean cosine equals

$$g = \frac{1}{N} \left[\frac{16x^6 + 32x^4 + 18x^2 + 3}{4x^4(4x^2 + 1)} - \frac{16x^4 + 12x^2 + 3}{16x^6} \ln(4x^2 + 1) \right], \tag{134}$$

where N is the normalization factor defined by Eq. (97).

We have for large particles:

$$1 - g = \frac{\ln 2x - 1}{x^2}. \tag{135}$$

So, in this case the transport scattering coefficient equals

$$\sigma^{tr} = \frac{1}{2}|m-1|^2 s\,(\ln 2x - 1). \tag{136}$$

It is seen that the transport scattering coefficient has a much weaker dependence on x than the total one.

Another important parameter, often used in the radiative transfer theory, is the fraction of light scattered into the forward or backward hemisphere, F or $1 - F$, respectively:

$$F = \frac{1}{2}\int_0^{\pi/2} p(\theta)\,\sin\theta d\theta. \tag{137}$$

Integration of (91) gives

$$F = \frac{1}{2N}\left[1 + \frac{1}{x^2} + \frac{2x^2}{2x^2+1} - \frac{2x^2+1}{2x^4}\ln(2x^2+1)\right]. \tag{138}$$

For large particles the backscattering fraction is

$$1 - F = \frac{1 - \ln 2}{2x^2}. \tag{139}$$

The backward scattering coefficient $\sigma_b = \sigma(1-F)$ for large particles is equal to

$$\sigma_b = \frac{1 - \ln 2}{4}|m-1|^2 s \tag{140}$$

and depends on the specific area s only.

In lidar/radar sounding, the lidar/radar backscattering coefficient σ_π and lidar/radar ratio L is often used. They are defined as:

$$\sigma_\pi = 4\pi\frac{dC_{sca}(\pi)}{d\Omega}C_N, \qquad L = \frac{\sigma}{\sigma_\pi} = \frac{1}{p(\pi)}. \tag{141}$$

It straightforwardly follows from Eqs. (91) and (96) that these values are equal to

$$\sigma_\pi = 2|m-1|^2 s\frac{x^4}{\left(1+4x^2\right)^2}, \quad L = N\frac{(1+4x^2)^2}{4x^2}. \tag{142}$$

It is easy to see that for large particles

$$\sigma_\pi = \frac{1}{8}|m-1|^2 s, \quad L = 4x^2. \tag{143}$$

Both backscattering coefficient σ_π and lidar ratio L depend on one microphysical parameter only, the former on the particle specific area s and the latter on x. It is to note that the former is exactly the value measured in lidar or radar sounding.

4 Wentzel–Kramers–Brillouin (WKB) Approximation

The WKB approximation, or quasi-classical approximation, is called after Wentzel (1926), Kramers (1926), and Brillouin (1926), who made a quantum-mechanical application of the method developed by Liouville (1837) and Green (1837) as an approach in mathematical physics. Ironically, for the first time this method was applied to optics by Rayleigh (1912) and Gans (1915), so it should have been named 'the Rayleigh–Gans approximation,' however, it so happened that this name is traditionally applied to the method described in the previous section. So we will keep calling it 'the WKB approximation' to avoid confusion and distinguish it from other very similar methods.

In optics, the WKB approximation is related closely to the eikonal approximation (see, e.g. Born and Wolf 1968). It has an intuitively clear physical meaning and a much wider range of applicability, e.g. liquid crystals (Loiko et al. 2016), than the RG approximation. Its utility has been noted by many authors. Particularly, it has been shown that some useful and acknowledged approaches, such as the RG approximation, van de Hulst anomalous diffraction, and Fraunhofer diffraction, follow from the WKB approximation in various limiting cases (Klett and Sutherland 1992; Lopatin and Shepelevich 1996). In spite of that, the WKB approximation is not so widely used as could be expected.

4.1 Statement of the Problem

The physical meaning of the WKB approximation is very simple. It supposes that the wave inside the particle does not change its direction and propagates with the phase corresponding to the optical path length in the substance. The electric field inside the particle $\mathbf{E}_{in}$ is expressed in the WKB approximation as (we omit the term $e^{-i\omega t}$):

$$\mathbf{E}_{in} = \mathbf{E}_0 \frac{1}{\sqrt{m}} \exp\left[i \int \mathbf{k}_0 m(\mathbf{r}) d\mathbf{r} \right], \tag{144}$$

where $\mathbf{E}_0$ is the initial field amplitude, $\mathbf{k}_0$ is the initial wavevector, $m = n + i\kappa$ is the complex refractive index that, in general, depends on the coordinate $\mathbf{r}$.

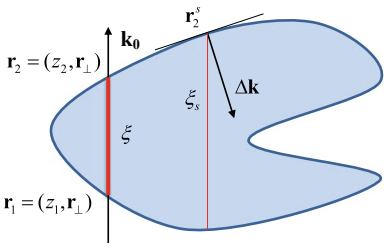

Fig. 6 Diagram of a scattering particle

The WKB approximation is valid for particles with the refractive index close to 1, see Eq. (5), and accounts correctly for the phase shift. Additionally, the factor $1/\sqrt{m}$ responds for the slow changes of the wave amplitude. In the context of optics, some authors use factor $2/(m+1)$ instead of $1/\sqrt{m}$ (Ishimaru 1978; Klett and Sutherland 1992). These two factors are equal to the first order of $(m-1)$, but factor $2/(m+1)$ has a simple physical interpretation: it is the Fresnel transmission coefficient thought the boundary with the relative refractive index m at normal incidence. We will follow the classical form of the WKB formulation, Eq. (144), but will remember that due to condition (5)

$$\frac{2}{m+1} \approx \frac{1}{\sqrt{m}}. \tag{145}$$

In what follows we will only consider homogeneous particles with $n > 1$.

For the homogeneous particle the integral in Eq. (144) takes the form:

$$\mathbf{E}_{in} = \mathbf{E}_0 \frac{1}{\sqrt{m}} \exp[i\, \mathbf{k}_0 m \cdot (\mathbf{r} - \mathbf{r}_1) + i\, \mathbf{k}_0 \cdot \mathbf{r}_1], \tag{146}$$

where $\mathbf{r}_1$ is the point of the intersection of the particle surface with the ray drawn from point $\mathbf{r}$ in the direction $-\mathbf{k}_0$ (see Fig. 6).

As we take the coordinate system with the z-axis parallel to $\mathbf{k}_0$, expression (146) will become

$$\mathbf{E}_{in} = \mathbf{E}_0 \frac{1}{\sqrt{m}} \exp[i\, k\, m\, (z - z_1(\mathbf{r}_\perp)) + i\, k\, z_1(\mathbf{r}_\perp)], \tag{147}$$

where k is a wavenumber, sign $\perp$ denotes the projection of a vector onto the xy-plane, and function $z_1(\mathbf{r}_\perp)$ determines the lower part of the particle surface (see Fig. 6).

The strict expression for the amplitude scattering function $\mathbf{f}$ is (Ishimaru 1978):

$$\mathbf{f} = \frac{1}{4\pi} \int_V \{-\mathbf{k}_s \times [\mathbf{k}_s \times \mathbf{E}_{in}(\mathbf{r})/E_0]\}\left[m^2(\mathbf{r}) - 1\right] e^{-i\, \mathbf{k}_s \cdot \mathbf{r}} dV \tag{148}$$

where the integral is taken over the particle volume V.

The amplitude scattering matrix in the WKB approximation is derived from Eqs. (147) and (148):

$$S_1 = -i\frac{k^3}{2\pi}(m-1)\int\limits_V \exp\left[i\,k\,m\,(z-z_1) + i\,k\,z_1 - i\,k\,z\,\mu - i\,\mathbf{k}_\perp^s \cdot \mathbf{r}_\perp\right] dV,$$

$$S_2 = S_1\,\mu \tag{149}$$

where $\mu = \cos\theta$ is the cosine of the scattering angle θ. In transition to Eq. (149) we used the approximate equality (145).

Unlike the RG approach that approximates the field inside the particle by the incident wave and therefore requires that the phase shift inside the particle must be negligible, the WKB approximation considers the phase shift correctly and, therefore, does not make a restriction on the particle size. Formally, the RG approximation follows from the WKB approximation as the first-order term of $(m-1)x$ in the field characteristics and as the second order one in the intensity.

Another approximation widely used for soft particles, namely, the anomalous diffraction by van de Hulst (1957), is a small-angle limit of the WKB approximation. The formulas of the anomalous diffraction for the scattering matrix elements are derived from Eq. (149) if one put $\mu = 1$, i.e. these approximations coincide in the strictly forward direction.

4.2 Extinction and Absorption

The extinction cross-section can be easily got from Eq. (149) through the optical theorem:

$$C_{ext} = \frac{4\pi}{k^2}\mathrm{Re}[S_1(\theta = 0)]. \tag{150}$$

As the WKB approximation coincides with the anomalous diffraction in the strictly forward direction, so the expressions for extinction derived within these two approximations are the same. Jacquier and Gruy (2008) derived the expression for the scattering cross-section of clusters of non-absorbent spheres within the anomalous diffraction, using the notion of chord length distribution (CLD)—the density of probability that the length of a random chord inside the particle lies between ξ and $\xi + d\xi$:

$$C_{sca} = 2\overline{S_\perp}\int (1 - \cos[k(m-1)\xi])\,f(\xi)\,d\xi, \tag{151}$$

where $\overline{S_\perp}$ is the average geometrical cross-section of the particle, $f(\xi)$ is the CLD, m is real.

Despite this equation is valid not only for clusters of spheres but for particles of any shape, the significant restriction of Eq. (151) is the absence of absorption. Malinka (2015a) has shown that the general expression for extinction when both scattering and absorption are present is

$$C_{ext} = 2\overline{S_\perp}\mathrm{Re}\int (1 - \exp[ik(m-1)\xi])\, f(\xi)\, d\xi. \tag{152}$$

In the absence of absorption—when m is real—the scattering cross-section is equal to the extinction one and Eq. (152) turns to Eq. (151). If absorption is present, the absorption cross-section is

$$C_{abs} = \overline{S_\perp}\int \left(1 - e^{-2k\kappa\xi}\right) f(\xi) d\xi, \tag{153}$$

where α is the absorption coefficient of the substance:

$$\alpha = 2k\kappa. \tag{154}$$

The scattering cross-section is obviously given by the difference

$$C_{sca} = C_{ext} - C_{abs}. \tag{155}$$

4.3 Scattering Phase Function

The anomalous diffraction can describe correctly the near-forward scattering; however it cannot be used for large scattering angles, particularly in the backward hemisphere. On the contrary, the WKB approximation is valid all over the scattering angle range, so for large particles—in fact, when the WKB approximation is really useful—we can consider the term $\exp[i\,(\mathbf{k}_0 - \mathbf{k}_s)\cdot\mathbf{r}]$ as a fast oscillating function and apply the method of stationary phase, exactly as it was done in the previous section. In addition, we are interested in dielectric particle that have small imaginary part of the refractive index $\kappa < 10^{-3}$ (van de Hulst 1957). As the phase function is weakly dependent on the imaginary part of the refractive index, we will neglect the effect of absorption on the phase function and put there $\kappa = 0$.

Term $\exp[i\,(\mathbf{k}_0 - \mathbf{k}_s)\cdot\mathbf{r}]$ can be considered as fast oscillating if the particle size is much greater than the wavelength ($x \gg 1$) and the scattering is not very close to the forward direction [Eq. (73)]. Thus, the method of stationary phase is valid in the range of scattering angles

$$\frac{1}{x} < \theta \leq \pi. \tag{156}$$

(To describe correctly the near-forward scattering one needs to use another approximation, e.g., anomalous diffraction.)

Let us rewrite Eq. (149) in the following way:

$$
\begin{aligned}
S_1 &= \frac{k^2}{2\pi}(m-1)\int\limits_V e^{i\,k\,(m-\mu)\,z - i\,k\,(m-1)z_1 - i\,\mathbf{k}_\perp^s\cdot\mathbf{r}_\perp} dV \\
&= \frac{k^2}{2\pi}(m-1)\int\limits_{S_\perp} d^2\mathbf{r}_\perp e^{-i\,\mathbf{k}_\perp^s\cdot\mathbf{r}_\perp}\int\limits_{z_1}^{z_2} e^{i\,k\,(m-\mu)\,z - i\,k\,(m-1)z_1} dz \\
&= \frac{-ik}{2\pi}\frac{(m-1)}{(m-\mu)}\int\limits_{S_\perp}\left\{e^{i\,k\,(m-\mu)\,z_2 - i\,k\,(m-1)z_1} - e^{i\,k\,(1-\mu)\,z_1}\right\}e^{-i\,\mathbf{k}_\perp^s\cdot\mathbf{r}_\perp}\, d^2\mathbf{r}_\perp \\
&= \frac{-ik}{2\pi}\frac{(m-1)}{(m-\mu)}\int\limits_{S_\perp}\left\{e^{i\,k\,(1-\mu)\,z_2 + i\,k\,(m-1)\xi} - e^{i\,k\,(1-\mu)\,z_1}\right\}e^{-i\,\mathbf{k}_\perp^s\cdot\mathbf{r}_\perp}\, d^2\mathbf{r}_\perp \\
&= \frac{-ik}{2\pi}\frac{(m-1)}{(m-\mu)}(I_2 - I_1), \qquad (157)
\end{aligned}
$$

where $\xi = z_2 - z_1$.

First consider integral I_1

$$
I_1 = \int\limits_{S_\perp}\exp\left[i\,k\,(1-\mu)\,z_1 - i\,\mathbf{k}_\perp^s\cdot\mathbf{r}_\perp\right]d^2\mathbf{r}_\perp = \int\limits_{\cup}\exp[i\,\Delta\mathbf{k}\cdot\mathbf{r}]n_z dS, \qquad (158)
$$

where n_z is the z-component of the normal to the surface $\mathbf{n}$ at the point $\mathbf{r}$; sign $\cup$ denotes the integration over the lower part of the surface. Integral I_1 is completely analogous to that in Eq. (76), except the integrands n_z in Eq. (158) and $\Delta\mathbf{k}\cdot\mathbf{n}$ in Eq. (76). At the stationary point, where $\Delta\mathbf{k}\|\mathbf{n}$, $\Delta\mathbf{k}\cdot\mathbf{n} = \Delta k = 2k\sin\theta/2$ and

$$
n_z = \frac{\Delta k_z}{\Delta k} = \frac{1-\cos\theta}{2\sin\theta/2} = \sin\theta/2. \qquad (159)
$$

So, integral I_1 at the stationary point s is equal to the integral in Eq. (76) divided by $2k$:

$$
I_1^s = \pm\frac{\pi}{k}\exp\left(i\,\Delta\mathbf{k}\cdot\mathbf{r}^s + \frac{\pi i}{4}\mathrm{sgn}_s\right)\sqrt{R_1^s R_2^s}. \qquad (160)
$$

After squaring and averaging over orientations as it was done in the previous section we find that the contribution of the integral I_1 to the differential cross-section is

$$\left\langle |I_1|^2 \right\rangle = \frac{\pi^2}{k^2} \left\langle \sum_s R_1^s R_2^s \right\rangle = \frac{\pi^2}{k^2} \frac{S}{4\pi}, \tag{161}$$

where S is the particle surface area.

Integral I_2 differs from I_1 in the term $e^{i\,k\,(m-1)\xi}$, which we consider as slow-oscillating, as compared to the term $e^{i\,k\,(1-\mu)z_2}$, because of conditions (5) and (156). Therefore, integral I_2^s equals

$$I_2^s = \frac{\pi}{k} \exp\left(i\,\Delta\mathbf{k}\cdot\mathbf{r}_2^s + \frac{\pi\, i}{4}\mathrm{sgn}_s + i\,k\,(m-1)\xi_s \right) \sqrt{R_1^s R_2^s}, \tag{162}$$

where $\mathbf{r}_2^s$ is the stationary point on the upper part of the surface and $\xi_s = z_2^s - z_1$ (see Fig. 6). As it was mentioned above, we neglect the effect of absorption on the phase function, so we assume here that m is real. In this case, the modulus of I_2 equals the modulus of I_1 and, therefore, the contribution of I_2 to scattering is equal to that of I_1. (Guessing again that different stationary points from the upper and lower parts of the surface do not correlate, we neglect the interference of I_1 and I_2: $\langle I_1^* I_2 \rangle = 0$.) We finally get for the differential cross-section:

$$\frac{dC_{sca}}{d\Omega} = \frac{1}{8\pi} \left| \frac{m-1}{m-\mu} \right|^2 \frac{1+\mu^2}{2} S. \tag{163}$$

As was mentioned above, Eq. (163) does not hold true in the forward direction. Therefore, it also does not meet the normalization (101).

In the range of applicability, given by Eq. (156), the accuracy of Eq. (163) increases when the scattering angle θ approaches π, because the oscillations in the term $e^{i\,k\,(1-\mu)z_2}$ become faster. In view of this, we can slightly change the behavior of the phase function near the forward direction to get the approximate function that will coincide with the derived value at $\theta = \pi$ and meet the normalization condition (101). The suitable phase function is given by Eqs. (96) and (127). We are only to redefine parameter x (or c). Let us put

$$p(\pi) = \frac{4x^2}{N\left(1+4x^2\right)^2} = \frac{S}{2C_{sca}} \left| \frac{m-1}{m+1} \right|^2. \tag{164}$$

Assuming that the particle is large ($x \gg 1$), we can easily get that

$$x = \left| \frac{m+1}{m-1} \right| \sqrt{\frac{C_{sca}}{2S}}. \tag{165}$$

Recalling that for a convex particle $S = 4\overline{S_\perp}$, we can write in this case:

$$x = \left|\frac{m+1}{m-1}\right|\sqrt{\frac{Q_{sca}}{8}}. \tag{166}$$

The phase function given by Eq. (96) with the effective particle size (165) is a simple analytical approximation valid for soft particles, much larger than the wavelength. Note that although Eq. (165) formally coincides with Eq. (94) for m close to 1, the effective size x in the WKB approximation has the different physical meaning: it depends not only on the geometrical but also on optical properties of the particle, as the cross-section C_{sca} in the WKB approximation, given by Eqs. (152)–(155), is quite different from that in the RG approximation, given by Eq. (115). Particularly, for non-absorbing large particle the scattering efficiency has a known limit $Q_{sca} = 2$ and the effective size has a limit value

$$x = \frac{1}{2}\frac{n+1}{n-1} \approx \frac{1}{n-1}, \tag{167}$$

while in the RG approximation the effective size x has no upper limit for large particles.

4.4 Comparison to the Discrete Dipole Approximation

Let us now compare numerically the derived analytical formula to the results given by a more strict method, namely, the discrete dipole approximation (DDA). The DDA code used here has been developed by Yurkin and Hoekstra (2011) and is available at https://code.google.com/p/a-dda.

As an object of comparison we took the ensembles of randomly oriented spheroids, prolate (axes ratio 4:1) and oblate (axes ratio 1:4), both with maximum dimension $kD_{\max} = 100$. Table 1 shows the size parameters for both ensembles: the principal axes, the mean chord $\langle\xi\rangle$, and the WKB-size x, defined by Eq. (165), for various refractive indices.

Figure 7 presents the differential scattering efficiencies $Q_{sca}(\theta) = Q_{sca}\,p(\theta)$ for both ensembles. As it is seen the approximate formula (96) with Eq. (166) represents the scattering phase function quite well, at least for the refractive index values of up to 1.1. Besides, although initially the considered range of scattering angles excludes

Table 1 Size parameters (dimensionless) of the two ensembles of spheroids

kD_x, kD_y, kD_z	$k\langle\xi\rangle$	n			
		1.001	1.01	1.05	1.1
		x			
25, 25, 100	20.7	16.3	16.3	14.8	11.8
100, 100, 25	29.4	24.2	24.0	18.6	11.9

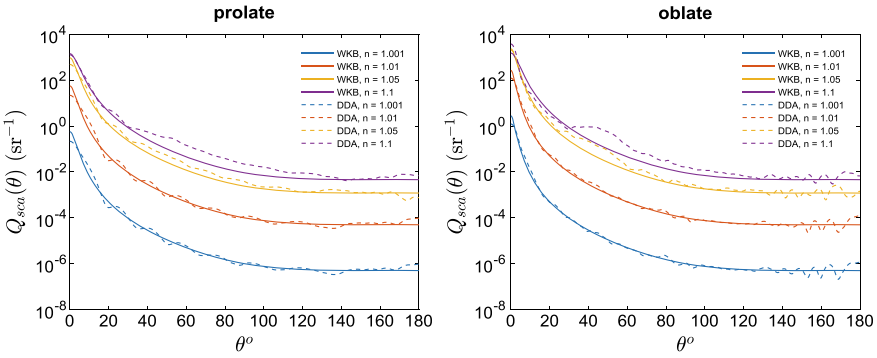

Fig. 7 Differential scattering efficiencies of prolate (left) and oblate (right) spheroids for various refractive indices

the forward direction [Eq. (156)], the corrected phase function approximates the strict one not only at large angles but also for some cases at angles near the direction $\theta = 0$.

5 Conclusion

We have shown how asymptotic methods, namely, the method of stationary phase, can help in the study of light scattering by large particles, especially nonspherical ones when there are no strict analytical solutions and numerical methods are tremendous, sophisticated, and resource intensive. This approach is particularly useful when an ensemble of randomly shaped or chaotically oriented particles is of interest. Moreover, the asymptotic solutions provide a simple physical insight to the problem and help us understand what microphysical parameter of an ensemble is leading.

For example, the differential cross-section of Fraunhofer diffraction far outside the main peak has the angular dependence of θ^{-3} with the total energy, equal to that of the main peak. In this angular range the differential cross-section depends on the obstacle perimeter L only, regardless of its shape. It could be also noted that if a non-circular obstacle has the same area as a circle, its perimeter will be greater than the circumference of the circle. As a result, the non-circular obstacle will diffract more light to large angles and the main peak will be narrower. This can result in overestimating particles size in problem of particle sizing with use of Fraunhofer diffraction. This fact was underlined by Bohren and Koh back in (1985).

One more conclusion from the asymptotic solution is that different ensembles diffract light almost identically if they have the same average values of area $\langle S \rangle$, area squared $\langle S^2 \rangle$, and perimeter $\langle L \rangle$.

Scattering by an ensemble of large soft particles is considered within the Rayleigh–Gans approximation. It has been shown that the scattering pattern does not depend on particle shape or size distribution. The differential cross-section at large scattering

angles has the form $\langle S \rangle \Delta k^{-4}\left(1 + \cos^2 \theta\right)$. Also it is shown that the total scattering cross-section is determined by the average chord length squared $\langle \xi^2 \rangle$. It is shown that the inherent optical properties, such as the total, transport, and backward scattering coefficients of a medium with optically soft particles are mainly determined by the specific particle surface area, the backward scattering coefficient being dependent on this microphysics parameter only. The spectral dependence of the inherent optical properties appears to be the following: the total scattering coefficient depends on wavelength as λ^{-2}, not λ^{-4}, as in pure Rayleigh case. The dependence of the transport scattering coefficient is even weaker, as $\ln \lambda$, and the backward scattering coefficient is spectrally neutral. We have to note that the last conclusion is the most trustworthy, because approximating formula (91) has higher accuracy for the backward hemisphere.

The simple analytical formulas that include the microphysical ensemble parameters are proposed to approximate the phase function within the framework of these three approximations—Fraunhofer diffraction, the RG approximation, and the WKB approximation—and are shown to have high accuracy. This finding could be very useful in the problem of calculating the scattering properties of large particles of complex shape and their remote sizing with optical methods.

References

Abdelazecz MK (1983) Wave scattering from a large sphere with rough surface. IEEE T Antenn Propag AP-31:375–377

Abramyan GL (1981) Theory of the diffraction by an opaque disk with a randomly rough edge. Radiophys Quantum El 24:132–138. https://doi.org/10.1007/BF01034798

Baum BA, Heymsfield AJ, Yang P, Bedka ST (2005) Bulk scattering models for the remote sensing of ice clouds. 1: microphysical data and models. J Appl Meteor 44:1885–1895

Bissonnette L, Hutt D (1990) Multiple scattering lidar. Appl Opt 29:5045–5046

Bleistein N, Handelsman RA (1986) Asymptotic expansions of integrals. Dover, New York

Bohren CF, Huffman DR (1983) Absorption and scattering of light by small particles. Wiley, New York

Bohren CF, Koh G (1985) Forward-scattering corrected extinction by nonspherical particles. Appl Opt 24:1023–1029

Born M, Wolf E (1968) Principles of optics. Pergamon Press, Oxford

Borovoi A, Konoshonkin A, Kustova N (2014) The physical-optics approximation and its application to light backscattering by hexagonal ice crystals. Journal of Quantitative Spectroscopy and Radiative Transfer. J Quant Spectrosc Radiat 146:181–189. https://doi.org/10.1016/j.jqsrt.2014.04.030

Brillouin L (1926) La mécanique ondulatoire de Schrödinger: une méthode générale de resolution par approximations successives. Comptes Rendus de l'Academie des Sciences 183:24–26

Debye P, Bueche AM (1949) Scattering by an inhomogeneous solid. J Appl Phys 20:518–525

Debye P, Anderson HR Jr, Brumberger H (1957) Scattering by an inhomogeneous solid. II. The correlation function and its application. J Appl Phys 28:679–683

Duck FA (1990) Physical properties of tissue: a comprehensive reference book. Academic Press, London

Gans R (1915) Fortpflantzung des Lichts durch ein inhomogenes Medium. Ann Phys 47:709–736. https://doi.org/10.1002/andp.19153521402

Green G (1837) On the motion of waves in a variable canal of small depth and width. Trans Cambridge Philos Soc 6:457–462
Ishimaru A (1978) Wave propagation and scattering in random media. Academic Press, New York
Istomina L, Heygster G, Huntemann M, Schwarz P, Birnbaum G, Scharien R, Polashenski C, Perovich D, Zege E, Malinka A, Prikhach A, Katsev I (2015a) Melt pond fraction and spectral sea ice albedo retrieval from MERIS data—Part 1: validation against in situ, aerial, and ship cruise data. Cryosphere 9:1551–1566. https://doi.org/10.5194/tc-9-1551-2015
Istomina L, Heygster G, Huntemann M, Marks H, Melsheimer C, Zege E, Malinka A, Prikhach A, Katsev I (2015b) Melt pond fraction and spectral sea ice albedo retrieval from MERIS data—Part 2: case studies and trends of sea ice albedo and melt ponds in the Arctic for years 2002–2011. Cryosphere 9:1567–1578. https://doi.org/10.5194/tc-9-1567-2015
Jacquier S, Gruy F (2008) Anomalous diffraction approximation for light scattering cross section: case of ordered clusters of non-absorbent spheres. J Quant Spectrosc Radiat 109:789–810
Jones AL (1987) Fraunhofer diffraction by random irregular particles. Part Charact 4:123–127
Kendall MG, Moran PAP (1963) Geometrical probabilities. Griffins statistical monographs and courses, No 5, C. Griffin, London
Klett JD, Sutherland RA (1992) Approximate methods for modeling the scattering properties of nonspherical particles: evaluation of the Wentzel–Kramers–Brillouin method. Appl Opt 31:373–386
Kokhanovsky AA, Macke A (1997) Integral light scattering and absorption characteristics of large nonspherical particles. Appl Opt 36:8785–8790
Kopelevich OV (1983) Low-parametric model of seawater optical properties. In: Monin AS (ed) Ocean optics I: physical ocean optics. Nauka, Moscow, pp 208–234 (in Russian)
Kramers HA (1926) Wellenmechanik und halbzählige Quantisierung. Z Phys 39:828–840. https://doi.org/10.1007/BF01451751
Light B (2010) Theoretical and observational techniques for estimating light scattering in first-year Arctic sea ice. In: Kokhanovsky A (ed) Light scattering reviews 5. Single light scattering and radiative transfer. Springer, pp 331–391
Liou KN, Yang P (2016) Light scattering by ice crystals: fundamentals and applications. Cambridge University Press, Cambridge. https://doi.org/10.1017/CBO9781139030052
Liouville J (1837) Sur le développement des fonctions et series. J Math Pure Appl 1:16–35
Loiko VA, Konkolovich AV, Miskevich AA (2016) Light scattering by a nematic liquid crystal droplet: Wentzel–Kramers–Brillouin Approximation. J Exp Theor Phys+ 122:176–192
Lopatin VN, Shepelevich NV (1996) Consequences of the integral wave equation in the Wentzel–Kramers–Brillouin approximation. Opt Spectrosc+ 81:103–106
Macke A, Mueller J, Raschke E (1996) Single scattering properties of atmospheric ice crystals. J Atmos Sci 53:2813–2825
Malinka A (2010a) Approximation of the Fraunhofer diffraction peak, produced by particles of arbitrary shape. Opt Lett 35:3411–3413
Malinka A (2010b) Analytical approximation of the phase function, specified by Fraunhofer diffraction by cloud ice crystals. In: Proceedings of the 25th international laser radar conference (ILRC 2010), 5–9 July 2010, St. Petersburg, Russia, CD-ROM
Malinka A (2011) Light scattering by optically soft large particles of arbitrary shape. J Opt Soc Am A 28:2086–2090
Malinka A (2015a) Analytical expressions for characteristics of light scattering by arbitrarily shaped particles in the WKB approximation. J Opt Soc Am A 32:1344–1351. https://doi.org/10.1364/JOSAA.32.001344
Malinka A (2015b) Analytical description of light scattering by phytoplankton particles in the WKB approximation. In: Proceedings of the VIII international conference "Current Problems in Optics of Natural Waters" (ONW-2015), 8–12 Sept 2015, St.-Petersburg, Russia/Nauka, St.-Petersburg, pp 113–118
Malinka A, Zege E (2007) Possibilities of warm cloud microstructure profiling with multiple-field-of-view Raman lidar. Appl Opt 46:8419–8427

Malinka A, Zege E (2009) Fraunhofer diffraction by arbitrary-shaped obstacles. J Opt Soc Am A 26:1763–1767
Malinka A, Zege E (2011) Phase function of light scattering by phytoplankton particles. In: Proceedings of the VI international conference "Current Problems in Optics of Natural Waters" (ONW-2011), 6–10 Sept 2011, D.S. Rozhdestvensky Optical Society, St.-Petersburg, Russia, pp 90–94
Malinka A, Zege E, Istomina L, Heygster G, Spreen G, Perovich D, Polashenski C (2018) Reflective properties of melt ponds on sea ice. Cryosphere 12:1921–1937. https://doi.org/10.5194/tc-12-1921-2018
McLean JW, Voss KJ (1991) Point spread function in ocean water: comparison between theory and experiment. Appl Opt 30:2027–2030
Rother T, Kahnert M (2014) Electromagnetic wave scattering on nonspherical particles: basic methodology and simulations. Springer, Berlin Heidelberg
Rayleigh JWS (1912) On the propagation of waves through a stratified medium, with special reference to the question of reflection. Proc Royal Soc London A86:207–223. https://doi.org/10.1098/rspa.1912.0014
Roy G, Bissonnette L, Bastille C, Vallee G (1997) Estimation of cloud droplet-size density distribution from multiple-field-of-view lidar returns. Opt Eng 36:3404–3415
Shcherbakov V, Gayet J-F, Baker B, Lawson P (2006) Light scattering by single natural ice crystals. J Atmos Sci 63:1513–1525
Shifrin KS, Shifrin YS, Mikulinsky IA (1984) Diffraction of electromagnetic wave on a screen of a random shape. Tech Phys Lett+ 10:68–72 (in Russian)
van de Hulst HC (1957) Light scattering by small particles. Wiley, New York
van de Hulst HC (1980) Multiple light scattering: tables, formulas, and applications. Academic Press, New York
Wells WH (1973) Theory of small angle scattering. AGARD lecture series, No 61 (NATO)
Wentzel G (1926) Eine Verallgemeinerung der Quantenbedingungen für die Zwecke der Wellenmechanik. Z Phys 38:518–529. https://doi.org/10.1007/BF01397171
Yang P, Liou KN (1996) Geometric-optics–integral-equation method for light scattering by nonspherical ice crystals. Appl Opt 35:6568–6584
Yurkin MA, Hoekstra AG (2011) The discrete-dipole-approximation code ADDA: capabilities and known limitations. J Quant Spectrosc Radiat 112:2234–2247
Zege E, Ivanov A, Katsev I (1991) Image transfer through a scattering medium. Springer, Heidelberg
Zege EP, Malinka AV, Katsev IL, Prikhach AS, Heygster G, Istomina L (2015) Algorithm to retrieve the melt pond fraction and the spectral albedo of Arctic summer ice from satellite optical data. Remote Sens Environ 163:153–164. https://doi.org/10.1016/j.rse.2015.03.012
Zege E, Malinka A, Katsev I, Prikhach A, Istomina L, Heygster G, Spreen G (2018) Reflective properties of summer Arctic sea ice in visible and near infrared. Fundamentalnaya i Prikladnaya Gidrofizika 11:17–25. https://doi.org/10.7868/S2073667318030024

Index

A. Kokhanovsky (ed.), *Springer Series in Light Scattering*,
Springer Series in Light Scattering,
https://doi.org/10.1007/978-3-030-38696-2